Investigation of Atmospheric Clouds and Boundary Layer Characteristics over the Western Indian Region

A thesis submitted in partial fulfilment of
the requirements for the degree of

Doctor of Philosophy

by

Dharmendra Kumar Kamat

(Roll No. 20330007)

Under the guidance of

Prof. Som Kumar Sharma
Space and Atmospheric Sciences Division
Physical Research Laboratory, Ahmedabad, India

Discipline of Physics
Indian Institute of Technology Gandhinagar, India
2025

Dedicated to

My beloved grandparents,

parents, and family

Declaration

I hereby declare that this thesis is a representation of my original ideas, expressed in my own words. Wherever I have incorporated ideas or words from others, I have duly cited and referenced the original sources. I affirm that I have upheld the principles of academic honesty and integrity, ensuring that no ideas, data, facts, or sources have been misrepresented, fabricated, or falsified in this work. I acknowledge that any violation of these principles may result in disciplinary action by the Institute and could also lead to legal consequences from improperly cited sources or those for whom necessary permissions were not obtained.

Date: 30 December 2025

Place: Ahmedabad

Dharm

Dharmendra Kumar Kamat

(Roll No: 20330007)

CERTIFICATE

I am pleased to certify that the thesis titled **"Investigation of Atmospheric Clouds and Boundary Layer Characteristics over the Western Indian Region"** by Mr. Dharmendra Kumar Kamat (Roll No. 20330007), has been conducted under my supervision. I confirm that this work has not been submitted elsewhere for any degree or diploma.

Date: 30 December 2025
Place: Ahmedabad

Prof. Som Kumar Sharma
(Thesis supervisor)
Physical Research Laboratory
Ahmedabad-380009, Gujarat, India

Acknowledgments

I am deeply grateful for the invaluable experiences, personal growth, and cherished memories I have gained during my five-year Ph.D. journey at PRL. With heartfelt appreciation, I extend my sincere thanks to all those who have been part of this remarkable chapter of my life.

First and foremost, I express my profound and heartfelt gratitude to my supervisor, Prof. Som Kumar Sharma, for being far more than just a guide in my academic journey. His unwavering support, guidance, and constant encouragement have been the cornerstone of my growth as a researcher. I consider myself truly blessed to have had a mentor who not only believed in my abilities but also inspired me to aim higher and persevere through challenges. His distinctive approach to scientific problems, sharp analytical thinking, and ability to draw deep insights from observations have greatly shaped my research. His constructive criticism has refined my work, while his appreciation during moments of achievement has been an enduring source of motivation. What I admire most is that his mentorship extended well beyond academics. From the very first day I joined him for my Ph.D., he has shown genuine care for my well-being, offering practical advice, and sharing thoughtful tips to maintain balance in life. His kindness, humility, and generosity have made a lasting impression on me. I will always remember how he made me feel like part of his family. The warmth and affection of Aarti Ma'am, the cheerful presence of Ansh and Anshi, and the many delightful meals and conversations at their home have created memories I will forever cherish.

A very important mention, to whom I owe my deepest thanks, is Dr. Prashant Kumar (SAC, Ahmedabad). His insightful suggestions have consistently strengthened my research and improved the quality of my work. Despite his demanding schedule, he always found time for in-depth scientific discussions, patiently listening to my basic queries, and providing thoughtful feedback. I am especially grateful for his meticulous review of my thesis, which helped refine it considerably. His constant encouragement, clear guidance, and unwavering support have been invaluable during challenging phases of my Ph.D. journey. His friendly nature and willingness to help at every stage have left a lasting impression on me, and I extend my heartfelt thanks for being such a steady source of motivation and direction.

I also wish to express my sincere gratitude to Dr. Kondapalli Niranjan Kumar (NCMRWF, Noida) for his invaluable guidance and encouragement throughout my Ph.D. journey. His support in shaping my scientific writing, especially during the preparation of research papers, has been immensely beneficial. He has always been approachable, generous with his time, and keen to share his expertise. His patience, insightful advice, and positive attitude have not only improved my research but have also helped me grow as a more confident and independent researcher. I am truly thankful for the inspiration and mentorship he has provided during this journey.

I am deeply thankful to Ms. Sourita Saha (Scripps Institution of Oceanography, California) for her invaluable support during the early stages of my Ph.D. At a time when I was still finding my footing, she guided me in understanding the instrumentation. She greatly contributed to my scientific communication skills by providing feedback on manuscripts, helping structure presentations, and offering insightful suggestions that strengthened my research papers. Her encouragement was instrumental in preparing for review seminars, enabling me to present my work with clarity and confidence. I am truly grateful for her patience, expertise, and willingness to help, which enriched my skills and instilled in me a lasting sense of discipline and professionalism.

I would like to express my sincere gratitude to my Doctoral Studies Committee (DSC) members: Prof. Harish Gadhavi, Dr. Narendra Ojha, Prof. Neeraj Rastogi, and Prof. Brajesh Kumar, for their constant support, thoughtful questions, and constructive comments, which have significantly enhanced my understanding of the subject. Their insightful feedback during review meetings not only deepened my conceptual clarity but also encouraged me to think critically and explore new perspectives in my research. The stimulating discussions and valuable suggestions they shared have been instrumental in refining my work and strengthening the overall quality of this thesis. I am truly grateful for the time, effort, and expertise they invested in guiding me throughout my doctoral journey.

I would like to take this opportunity to express my heartfelt gratitude for the immense support I have received from PRL. I am deeply thankful to the Department of Space, Government of India, for providing the research grant that supported my tenure at PRL. My sincere thanks go to Prof. Anil Bharadwaj, Director of PRL, for his un-

wavering support and for ensuring access to world-class research facilities. I am also grateful to Prof. Pallamraju, Dean of PRL and former Head of the SPASC division, and to Prof. Dibyendu Chakrabarty, current Head of SPASC division, for their consistent encouragement and invaluable support throughout my thesis work. I extend my thanks to all members of the Academic Committee for their insightful comments and constructive suggestions, which have greatly contributed to my growth as a researcher. I would also like to acknowledge the former Registrar of PRL, Prof. R. D. Deshpande, as well as Prof. Shyam Lal and Prof. Harish Chandra, for their kindness, support, and thoughtful gestures.

I am sincerely grateful to all my colleagues in the Space and Atmospheric Sciences (SPASC) division: Prof. S. Ramachandran, Prof. L. Sahu, Prof. H. Gadhvi, Dr. R. P. Singh, Dr. A. Guharay, Dr. T. A. Rajesh, Dr. K. Venkatesh, Mr. S. Venkataramani, Mr. A. Manke, Mr. T. K. Sunil Kumar, Mr. M. Bhavsar, Ms. Sneha, Mr. A. Sarda, Mr. Malaidevan P., Mr. A. K. Yadav, Mr. S. Urmalia, Mr. P. S. Suryawanshi, Mr. R. Pathak, Mr. P. K. Kushwaha, Ms. C. Raghavan, Mr. M. K. Soni, Mr. T. Tamrakar, Mr. V. K. Dhaker, Mr. J. Sebastian, Mr. A. Kumar, Mr. M. Jain, Mr. D. Khonde, and Mr. Chirag, for creating such a friendly, supportive, and motivating work environment. I have greatly enjoyed interacting and collaborating with both seniors and juniors in the division, including Nidhi, Subir, Sovan, Ankit, Tanzil, Meghna, Yogesh, Sunil, Kshitiz, Gourav, Bijoy, Kiran, Komal, Nitin, Aakash, Sandeep, Ankita, Shivam, Bhavesh, Samarpan, Abhishek, Dibyani, and Harsh. The camaraderie and shared moments within the SPASC division, whether in professional settings or through informal interactions, have been a cherished part of my journey. Taking part in division activities such as badminton, cricket, volleyball, and Hindi Pakhwada with my colleagues has been both exciting and memorable, leaving me with experiences I will fondly remember long after my time at PRL. I would like to express my heartfelt gratitude to Meghna, Mansi, and Haritha for creating such a warm, engaging, and intellectually stimulating atmosphere in our shared office. The insightful discussions, collaborative spirit, and moments of laughter we shared have not only made the workspace enjoyable but have also been a valuable source of learning.

I am also thankful to Aniket and Arun for their valuable support and the many en-

gaging discussions we have shared on a wide range of topics, both scientific and otherwise. Their friendly and cheerful nature, along with their sense of humour, brought positivity and light-heartedness to the workplace, making even the busiest days enjoyable. In addition, I would like to express my gratitude to Dr. Ruchita Shah for her kind support and care during the critical phase of my thesis writing. Our discussions were immensely helpful in refining my ideas and maintaining clarity of thought.

Life becomes truly joyful and vibrant when accompanied by friends, and I have been fortunate to be surrounded by some of the best. First and foremost, I would like to express my heartfelt thanks to my Lobby B friends: Kamran, Debashis, and Gurucharan, who have been a constant source of energy, laughter, and positivity during my stay at PRL. From the very beginning, their cheerful spirit and boundless enthusiasm turned everyday moments into unforgettable memories. Whether it was our lively breakfast, lunch, and dinner gatherings at the hostel, the countless jokes and humorous banter that filled the air, or our spontaneous trips together, their companionship made hostel life far more colorful and enjoyable. They are the true powerhouses of fun, always living life to the fullest, and together we enjoyed every moment to its absolute maximum. I will always cherish the warmth, support, and countless happy moments we shared, which made my time at PRL not just productive but truly memorable. I also convey my heartfelt thanks to my batchmates, the crazy and enthusiastic batch of 2020: Arup (AC), Wafikul, Sanjay, Trinesh, Sandeep, Arup, Aditya, Mansi, Akanksha, Malika, Chandrima, and Ananya, for the wonderful memories we created together on various occasions. Being my first hostel experience, it was a delight to share hostel life with such spirited and fun-loving people. Playing cricket, badminton, and volleyball at the PRL Navrangpura Hostel with seniors (Atif, Amit, Ankit, Sovan, Praveen, Ramanuj, Shidharth, Devaprasad, Arijit, Gaurav, Bijoy, Kshitiz) and juniors (Rahul, Sandeep, Akash, J.T., Shivam, Bhavesh, Samarpan, Abhishek, Namit, Bhavya, Aditya, Fahad) has been an absolute pleasure, adding an extra dimension of joy to my stay. I am also thankful to the members of our lunch group: Saurabh, Supriyo, Bharthi, Kamran, Debashis, Gurucharan, Arup (AC), Sougata, Chinmoy, Shubhanka, Monal, Chandrima (THEPH), Achintyaa, and Dibyani, for the endless humor, engaging discussions, and lighthearted debates over a range of topics, which made our lunchtime a refreshing *and delightful break every day.*

I extend my sincere thanks to Nishtha and Pragya Ma'am and the entire library staff for their efficient management of the library, including organizing book fairs and maintaining journal subscriptions. I am also thankful to Dr. Bhushit Vaishnav, Head of Academics, for his invaluable support and guidance in academic matters. My gratitude goes to the Computer Centre (CNIT) team at PRL for ensuring seamless internet connectivity and providing prompt software support whenever required. I am deeply appreciative of all the faculty members of PRL for fostering an excellent research environment that has greatly enriched my learning experience. I would like to express my heartfelt thanks to Richa Ma'am for her support during times of need and to Ganesh Sir for ensuring the smooth functioning of the hostel. I am also grateful to the PRL medical facility, particularly Dr. Samir Dani and Dr. Sheetal Patel, for their availability and assistance whenever needed. My thanks also go to the administration, canteen, accounts, dispensary, CMG, purchase section, CISF, and housekeeping staff of PRL for their cooperation and for providing various facilities that made day-to-day life comfortable. Furthermore, I extend my appreciation to the academic and administrative staff of IIT Gandhinagar for facilitating official formalities and providing the necessary resources. Their support has been instrumental in ensuring the smooth progression of my work. I acknowledge the various research agencies, institutions, and organizations that generously made various datasets and models publicly available. Their contributions have provided both supporting and crucial information for this thesis work.

I am truly grateful to my brother-like friend, Ammu, whose constant encouragement played a pivotal role in my decision to pursue a Ph.D. Since our Master's days, we have shared countless moments together and supporting each other through challenges. His love, trust, and belief in my abilities have been a source of strength throughout my Ph.D. journey, motivating me to strive for excellence in all my work. Beyond academics, we have created a treasure trove of memories, watching movies, going on tours, exploring new places, and sharing endless conversations filled with laughter. His presence has made this journey far more joyful, and I cherish the bond we share, which goes far beyond friendship. I would also like to convey my deepest gratitude *to my dearest friends: Deepanshu, Ujjwal, Diwakar, Harsh, Ojasvi, Shubham, Akash, Nishant, Kanchan, and Sharwani. Even though we may not meet often, our long and lively conversations over calls, the laughter we share, and their love and support have always brought warmth and happiness into my life. The moments we've spent together, whether in person or virtually, have been a reminder that true friendship transcends distance and time.*

Pursuing and completing Ph.D. would not have been possible without the unwavering support of my family, who have been my true backbone. Expressing my gratitude to them could fill an endless list: it is so deep and heartfelt that words alone cannot do justice. Yet, I wholeheartedly and affectionately convey my sincere appreciation to my parents, whose love, guidance, and sacrifices gave me the gift of education. Nothing would have been possible without their constant presence, their hand always over my head as a source of strength and reassurance. My heartfelt respect and thanks also go to my grandparents for their immense love, care, trust, and blessings, which have been my silent shield through every challenge. I extend my warmest appreciation to my energetic and wonderfully mischievous siblings and cousins: Virendra bhaiya, Ravinder bhaiya, Reena Di, Vibha Di, Satendra, Jitendra, Sikander, Shailendra, and Aman, who have brought boundless joy, laughter, and affection into my life and who have stood beside me in every situation. I am equally grateful to my badepapa and badimummy, mamaji and mamiji, fufaji and buaji, bhaiya and bhabhi, and the adorable little ones in the family for their love, constant encouragement, and heartfelt blessings.

I would also like to extend my gratitude to every single person who, in some way, helped, supported, or inspired me through this five-year-long Ph.D. journey.

And finally, this moment belongs to me, too. I want to sincerely thank myself for staying strong and resilient, for facing every obstacle with courage and a smile. Over these years, I have become my own motivator, cheering myself on, keeping the positive energy alive, and balancing research with moments of joy in the gym, on the sports field, or simply in little everyday pleasures. Here's to the perseverance that kept me going and to the optimism that never let me give up. Well done, self-keep shining!

- Dharmen

Abstract

Atmospheric clouds are the fundamental components of the Earth's climate system, intricately linked to weather patterns, hydrological cycles, and the global energy balance. Clouds influence climate by modulating radiative transfer, exerting both cooling and warming effects through their albedo and greenhouse roles, respectively. On the other hand, the atmospheric boundary layer (ABL), the lowest part of the troposphere directly influenced by the Earth's surface on diurnal time scales, governs turbulent mixing and vertical exchange of heat, momentum, moisture, and trace gases. The interactions between clouds and the ABL drive key processes such as the initiation of convective flow, the formation of fog and mist, the dispersion of pollutants, and the development of precipitation. Despite their central role, the coupled variability of clouds and the ABL in semi-arid and topographically complex environments, such as the Western India, remains insufficiently understood due to a scarcity of high-resolution and long-term ground-based observations. This knowledge gap limits the ability to accurately represent these processes in weather and climate models, with downstream consequences for forecasting, water resource management, and climate adaptation strategies.

This thesis seeks to address this gap by conducting a comprehensive investigation into the spatiotemporal characteristics of clouds and the ABL over three climatically and geographically distinct locations in the Western India: Ahmedabad, Mt. Abu, and Udaipur. Ahmedabad, a highly polluted urban city in Gujarat, experiences a hot semi-arid climate; Mount Abu, located in the Aravalli range of Rajasthan, represents a high-altitude, forested terrain; and Udaipur, situated near the eastern edge of the Thar Desert, is surrounded by lakes and also exhibits a hot semi-arid climate. The study integrates continuous ground-based remote sensing of clouds and ABL using Lidar, complemented with satellite datasets and reanalysis products. The study focuses on quantifying the seasonal and diurnal variability of cloud base height (CBH), cloud occurrence, and boundary layer height (BLH) across the three sites; examining the physics of cloud formation below and near the lifting condensation level (LCL); exploring event-scale interactions between the ABL and cloud processes during phe-

nomena such as dust storms, fog events, and intense convective activity; and improving model predicted BLH estimates through statistical and machine learning based bias correction techniques anchored in observational data.

Results show pronounced seasonal cycles in both CBH and BLH across all three regions, reflecting the combined influence of surface heating, moisture availability, and synoptic-scale circulation. During the monsoon season, CBH values frequently fall in the range of 1.5-2.5 km due to moist atmospheric profiles and reduced sensible heat fluxes, while BLH is similarly suppressed (1.0-1.5 km) under cloudy, humid conditions. In contrast, the pre-monsoon period exhibits elevated CBH values exceeding 6 km, driven by intense thermal convection and dry conditions, with BLH frequently surpassing 3 km. The post-monsoon and winter seasons are characterized by lower CBH events linked to radiation fog, mist, and shallow convective clouds, especially during early morning hours. Notably, Mt. Abu records more frequent "full-sky obscuration" events ($\sim$12% of days), predominantly during the monsoon, caused by orographic cloud formation and persistent mist, a feature much less common at Ahmedabad ($\sim$3%) and Udaipur ($\sim$5%). Cloud occurrence statistics reveal that Udaipur experiences the highest overall cloud frequency ($\sim$32%), followed by Mt. Abu ($\sim$28%) and Ahmedabad ($\sim$21%). Rainy-cloud occurrence, when considered separately, shows an increasing trend in September over Ahmedabad, indicating possible late-monsoon dynamical changes. These trends suggest a potential link between aerosol loading and shifts in cloud microphysical properties, warranting further investigation into aerosol-cloud-radiation feedbacks in the region.

The characteristics of clouds forming near and below LCL are also presented. The low clouds, developing within the mixed layer under moderate humidity and enhanced latent heat flux, point to complex land-atmosphere feedbacks in semi-arid environments. Furthermore, this thesis provides insights into clouds and ABL dynamics during extreme events. A pre-monsoon case study over Ahmedabad demonstrated how moist convection, followed by intense dust storm activity, can markedly alter boundary layer evolution and drive rapid cloud development. Complementing this, a wintertime investigation over Delhi, selected for its chronic and severe air quality deterioration and

fog formation, revealed how persistent pollution and fog episodes are closely governed by suppressed BLH and limited dispersion. Together, these case studies emphasize the pivotal role of boundary layer dynamics in shaping both cloud evolution and atmospheric composition during extreme meteorological and air quality events.

Furthermore, the study evaluated the Weather Research and Forecasting (WRF) model's skill in representing BLH and demonstrated improvements using a machine learning (ML) bias-correction approach. The hybrid WRF-ML framework significantly reduced errors, improved detection of low-to-moderate BLH regimes, and better captured diurnal variability. The largest improvements were observed for low-to-moderate BLH ranges, which are critical for air quality forecasting and fog prediction. These findings demonstrate the utility of observationally constrained model improvements and highlight the potential of such frameworks for operational weather prediction in India. The results from this thesis also serve as ground truth for evaluating cloud property retrievals from geostationary platforms, where spatial and temporal resolution often limit cloud type discrimination and vertical profiling accuracy. This thesis work has important implications for regional climate assessments. The identification of systematic BLH biases in models and their successful correction also paves the way for more accurate simulation of pollutant dispersion and fog hazards, enhancing public safety and transportation reliability.

Overall, this thesis advances the understanding of clouds and ABL processes in the semi-arid Western Indian region by linking observational climatology, process-level mechanisms, extreme event analysis, and model improvement strategies. The results provide valuable insights for enhancing weather and climate model representations, improving satellite retrieval validation, and strengthening hazard prediction capabilities in complex terrain and transitional boundary layer regimes.

Keywords: Clouds, atmospheric boundary layer, fog, mist, semi-arid region, Western India, Lidar, cloud base height, boundary layer height, lifting condensation level, extreme events

List of Abbreviations

ABL	Atmospheric Boundary Layer
AOD	Aerosol Optical Depth
AMS	American Meteorological Society
AWS	Automated Weather Station
BC	Black Carbon
BLH	Boundary Layer Height
CAMS	Copernicus Atmosphere Monitoring Service
CBH	Cloud Base Height
CCN	Cloud Condensation Nuclei
CER	Cloud Effective Radius
CGT	Cloud Geometrical Thickness
CI	Capping Inversion
COT	Cloud Optical Thickness
CTH	Cloud Top Height
CTT	Cloud Top Temperature
CWP	Cloud Water Path
DALR	Dry Adiabatic Lapse Rate
DES	Delhi Earth Station
ECMWF	European Center for Medium-Range Weather Forecasts
ELR	Environmental Lapse Rate
ERA5	Fifth generation ECMWF Atmospheric Reanalysis
EZ	Entrainment Zone
FA	Free Atmosphere
GPS	Global Positioning System
HYSPLIT	Hybrid Single Particle Lagrangian Integrated Trajectory
IGP	Indo-Gangetic Plain
IMD	India Meteorological Department

INSAT	Indian National Satellite System
ISCCP	International Satellite Cloud Climatology Project
ISM	Indian Summer Monsoon
ISRO	Indian Space Research Organization
IST	Indian Standard Time
IQR	Inter Quartile Range
LCL	Lifting Condensation Level
LES	Large Eddy Simulation
Lidar	Light Detection and Ranging
LLJ	Low Level Jets
LWC	Liquid Water Content
LWP	Liquid Water Path
MALR	Moist Adiabatic Lapse Rate
ML	Machine Learning
ML	Mixed Layer
MODIS	Moderate Resolution Imaging Spectroradiometer
MSLP	Mean Sea Level Pressure
NBL	Neutral Boundary Layer
NOAA	National Oceanic and Atmospheric Administration
NWP	Numerical Weather Prediction
PBL	Planetary Boundary Layer
RF	Radiative Forcing
RH	Relative Humidity
RL	Residual Layer
SBL	Stable Boundary Layer
SNPP	Suomi National Polar-orbiting Partnership
UTC	Coordinated Universal Time
VC	Ventilation Coefficient
VIIRS	Visible Infrared Imaging Radiometer Suite

VV	Vertical Visibility
WD	Wind Direction
WMO	World Meteorological Organization
WRF	Weather Research and Forecasting
WS	Wind Speed
WVMR	Water Vapor Mixing Ratio

Contents

List of Figures

List of Tables

Chapter 1

Introduction

The Earth's atmosphere is a gaseous envelope composed primarily of nitrogen (78%), oxygen (21%), and argon (0.93%), along with trace amounts of other gases such as carbon dioxide, water vapor, methane, and noble gases (Salby, 1996). It supports life by shielding the planet from harmful solar radiation, regulating temperature, sustaining the water cycle, and driving weather and climate processes. The atmosphere behaves as a complex fluid system, and the chaotic motion within the atmosphere manifests as weather (Stull, 2017). The complexity arises from the feedback between the various physical and chemical processes at different locations. The study of the physics and chemistry of this complex fluid system, which aims to explain the physical phenomenon occurring in the atmosphere with a focus on weather forecasting, is known as meteorology.

The state of the air in the atmosphere is governed by thermodynamic variables such as temperature, pressure, and density (or volume), and the equation that describes how these variables affect each other is the ideal gas law: $P = \rho R_d T$, where P is pressure, ρ is air density, T is temperature, and R_d is the specific gas constant for dry air ($\sim 287\ \mathrm{J\,kg^{-1}\,K^{-1}}$) (Caballero, 2014). In the real atmosphere with moisture present, the ideal gas law transforms to $P = \rho R_{\text{moist}} T$, where $R_{\text{moist}} = (1-q)R_d + qR_v$, and R_v represents the specific gas constant of water vapor ($\sim 461\ \mathrm{J\,kg^{-1}\,K^{-1}}$), and q is specific humidity (mass of water vapor divided by total mass of moist air).

This thermodynamic relationship describes the behavior of air parcels and helps understand how atmospheric properties vary with altitude. The atmospheric pressure decreases consistently with height and follows an approximately exponential decay. The barometric equation mathematically represents the variation in atmospheric pressure: $\frac{dP}{dz} = -\rho g$, where $\frac{dP}{dz}$ is the rate of pressure change with height, ρ is the air density, and g is the acceleration due to gravity. By combining the barometric equation with the ideal gas law $P = \rho RT$ and assuming an isothermal atmosphere, the pressure variation with altitude can be derived as $P = P_0 \exp(-z/H)$, where P_0 is surface pressure, z is altitude, and $H = \frac{RT}{g}$ is the scale height (Lente and Ősz, 2020).

The atmosphere is vertically stratified into distinct layers based on the temperature gradient with altitude (Flohn and Penndorf, 1950). From the surface upward, these layers are the troposphere, stratosphere, mesosphere, and thermosphere (Andrews, 2010). The temperature remains constant near the boundaries of two layers; these boundaries are called "pauses" (e.g., tropopause, stratopause, mesopause), where the trend of temperature change with altitude reverses. The physical, chemical, and dynamic processes in these layers govern the temperature variations. The temperature change rate with altitude in the atmosphere is known as the lapse rate. This parameter determines the atmosphere's stability and the vertical motion of air parcels (Daidzic, 2019). The environmental lapse rate (ELR) is the actual rate of temperature decrease in the atmosphere (approximately 6.3 $\mathrm{K\,km^{-1}}$ in the troposphere). In contrast, the dry adiabatic lapse rate (DALR) (approximately 9.8 $\mathrm{K\,km^{-1}}$) is the rate at which the temperature of a dry (unsaturated) air parcel changes as it ascends or descends adiabatically (Brunt, 1933). When an air parcel contains moisture and becomes saturated (relative humidity reaches 100%), it cools at the moist adiabatic lapse rate (MALR), which is lower than the DALR and typically ranges between $4-7$ $\mathrm{K\,km^{-1}}$, depending on temperature and pressure. The comparison between the ELR and adiabatic lapse rates determines the stability of the atmosphere: if ELR $>$ DALR, the atmosphere is unstable, promoting vertical motion and cloud development. If ELR $<$ MALR, the atmosphere is stable, suppressing vertical movement. If MALR $<$ ELR $<$ DALR, the atmosphere is conditionally unstable, i.e., vertical motion depends on whether the air is saturated. Atmospheric instability provides the uplift to the air parcels crucial for cloud formation. When the rising air cools to its dew point, the contained water vapor condenses onto aerosols, forming cloud droplets. The type, height, and extent of clouds depend on factors such as humidity, lapse rates, and the vertical velocity of air parcels. The cloud formation process initiates in the lower part of the atmosphere, where interactions between the Earth's surface and the overlying air are most intense. This lowest portion is known as the atmospheric (or planetary) boundary layer (ABL or PBL).

This chapter presents a detailed discussion of the ABL, its structure and dynamics, and atmospheric clouds and their role in the weather and climate. Furthermore, the chapter explores the interactions between ABL and clouds. Lastly, current advances in observational and modeling studies of the ABL and clouds will be reviewed with an aim to identify the key research gaps in understanding the complex processes governing these systems.

1.1 The atmospheric boundary layer (ABL)

The ABL is the lowermost part of the troposphere in direct contact with the Earth's surface, where significant fluxes of heat, momentum, and moisture are transported by turbulent motions (Stull, 2012). This region responds rapidly to surface forcings such as heating, cooling, and friction (Garratt, 1994). The ABL plays a crucial role in energy exchange, moisture transport, pollutant dispersion, and cloud dynamics. It influences weather patterns and the hydrological cycle and is often associated with the formation of low-level clouds. The ABL is unique due to its complex spatial and temporal structure and its position as a transitional zone between the Earth's surface and the free troposphere. Its structure exhibits both diurnal and seasonal variability, shaped by surface conditions, atmospheric stability, and large-scale synoptic weather systems.

The ABL plays a central role across various disciplines, including meteorology, hydrology, air pollution, agricultural meteorology, aeronautical and mesoscale meteorology, weather forecasting, and climate studies (Garratt, 1994). Understanding the ABL's structure and dynamics is essential for interpreting weather and climate systems, pollutant dispersion, and the exchange of heat, moisture, and momentum between the surface and atmosphere. As a transitional zone between the biosphere and the free troposphere, the ABL is critically important for air quality and climate-related research (Li et al., 2017; Yuval et al., 2020). Since most atmospheric pollutants and trace gases are confined within this layer, their concentrations directly affect air quality. Consequently, variations in the boundary layer height (BLH) significantly influence air quality assessments and the performance of numerical weather prediction (NWP) models.

1.1.1 ABL structure and diurnal evolution

The ABL typically extends from approximately 100 m to 3000 m above the surface and is the most responsive part of the troposphere to surface forcings such as friction, heating, and moisture fluxes (Garratt, 1994; Stull, 2012). The ABL depth or BLH, is highly variable in both space and time, governed by the diurnal cycle of solar radiation, land-surface characteristics, and larger-scale atmospheric dynamics (Seibert et al., 2000; Stull, 2012). The top of the ABL is usually capped by a strong temperature inversion or a statically stable layer, which separates it from the overlying free atmosphere (FA) (Garratt, 1994). This inversion acts as a lid, suppressing vertical turbulence and confining most boundary-layer processes below it. On average, the troposphere exhibits static stability, with a typical vertical gradient in potential temperature ($\partial\theta/\partial z = 3.3$ K/km), making turbulent mixing across the ABL top energetically unfavourable (Wallace and Hobbs, 2006). Consequently, the air within the ABL becomes well-mixed, forming a mixed layer (ML) with nearly uniform potential temperature and moisture characteristics beneath the stabilizing inversion (Arya, 2001; Wyngaard, 2010).

Over land, under anticyclonic conditions with light winds, the diurnal cycle of solar heating produces a strong daily variation in the ABL (Figure 1.1). During

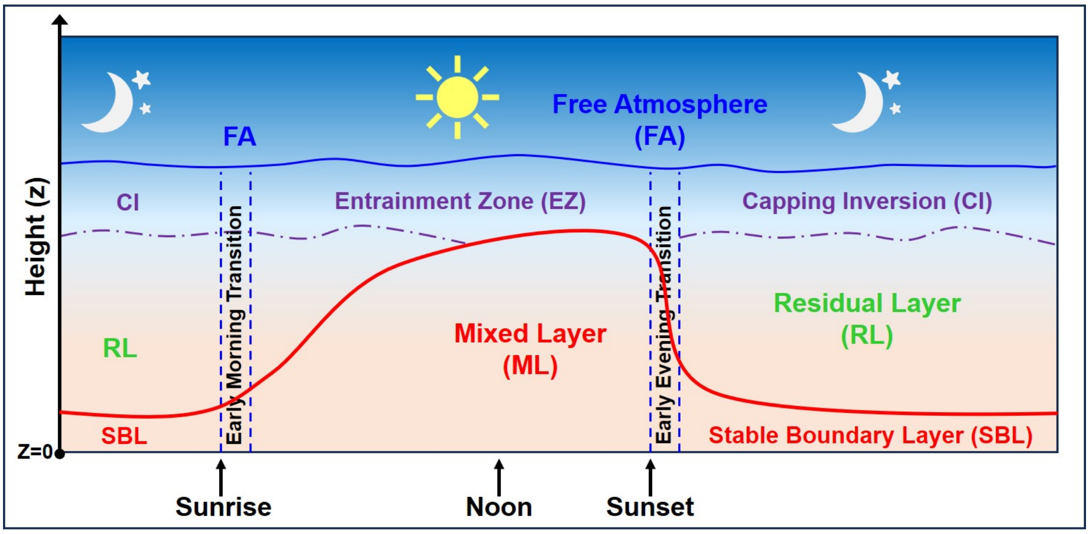

Figure 1.1: Diurnal evolution of the ABL under clear-sky conditions (adapted from Stull (2012)). The solid red line represents the BLH, while the dashed violet line indicates the top of the residual layer.

the day, a convective ML forms and evolves through three stages: a slow morning growth as surface heating warms the nocturnally cooled air; a rapid deepening during late morning and early afternoon as the ML entrains air from the residual layer; and a relatively steady afternoon phase where the ML typically reaches depths of 1 to 3 km, with entrainment balanced by large-scale subsidence (Stull, 2012). Turbulence is generated thermally by convection and mechanically by wind shear. The upper boundary of the ML, characterized by a temperature inversion through which entrainment occurs, is known as the entrainment zone (EZ). Near sunset, longwave radiative cooling at the surface suppresses thermal convection, causing turbulence to decay and leaving behind a residual layer (RL) aloft, while a stable boundary layer (SBL) begins forming near the ground. The interface between these layers is marked by the capping inversion (CI). Overnight, shear-driven turbulence within the SBL facilitates downward heat transfer to the cooling surface. This diurnal cycle typically repeats daily unless disrupted by synoptic-scale systems such as storms. In real atmospheric conditions, horizontal advection also plays a significant role and can even dominate ABL evolution. The vertical structure of temperature (T), potential temperature (θ), and specific humidity (q) in the lower troposphere during day and nighttime is schematically illustrated in Figure 1.2.

Turbulence in the ABL is primarily controlled by flow stability. Unstable conditions, such as those caused by surface heating or wind shear, promote turbulence, while stable conditions suppress it and favour laminar flow (Garratt, 1994; Stull, 2012). The key forms of stability are static (buoyancy-related) and dynamic (shear-related). Turbulence tends to reduce instabilities through mixing but dissipates if not continuously forced (Arya, 2001). The gradient Richardson Number is commonly used to quantify local stability; values below ∼0.25 generally indicate turbulent conditions (Stull, 2012). When multiple stability criteria disagree, the presence of any instability is usually taken as dominant. Diurnal changes in stability control the vertical extent and intensity of turbulent mixing, shaping the ABL's internal structure over time.

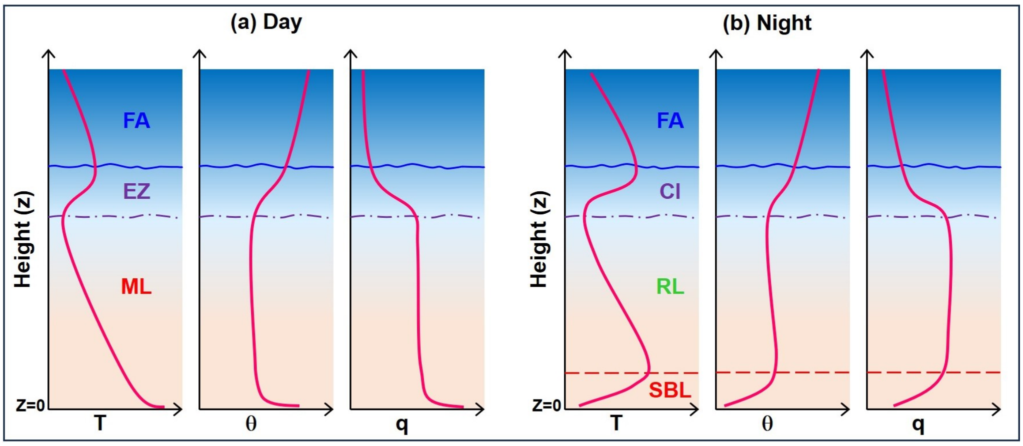

Figure 1.2: Typical vertical profiles of temperature (T), potential temperature (θ), and specific humidity (q) in the lower troposphere (adapted from Stull (2012)).

Air from the free atmosphere enters the ABL primarily via turbulent entrainment at the top of the ML. This process is driven by turbulent motions within the ABL that erode and incorporate air from above, resulting in an increase in ABL depth and volume (Deardorff, 1979; Sullivan et al., 1998). However, this entrainment is typically one-way; pollutants, moisture, and aerosols already within the ABL tend to remain trapped unless removed by deep convective processes (Seinfeld and Pandis, 2016). Clouds and storms play a critical role in vertically redistributing ABL air, either by convective venting, frontal lifting, or downdrafts (Emanuel, 1994; Houze, 2014). Precipitation from these systems can further modify the thermal and moisture structure of the ABL.

The coupling between the ABL and the free atmosphere is often intermittent, spatially localized, and nonlinear (Mahrt, 1991; Stull, 2012). A useful conceptual model treats the ABL as a reservoir of air that interacts actively with the surface but remains largely isolated from the FA above (Garratt, 1994). However, episodic processes such as convection, frontal passage, and large eddies act as vents or conduits, intermittently transporting ABL air upward and exchanging it with the overlying atmosphere (Stull, 2012; Wyngaard, 2010). From the perspective of the free atmosphere, the ABL appears as a nearly frictionless, non-penetrative lower boundary.

Mixed layer (ML)

The concept of ML was originally identified in the upper ocean and later adapted to atmospheric studies by Ball (1960). Foundational contributions by Deardorff (1972, 1974); Deardorff and Willis (1985) significantly advanced the understanding and established the modern framework of atmospheric ML dynamics. Within the ML, the virtual potential temperature remains nearly constant throughout most of its depth, indicating strong turbulent mixing (Hibberd and Sawford, 1994).

Turbulence in the ML is strongly anisotropic, with most of the turbulent kinetic energy concentrated in the vertical component. Temperature and density fluctuations are minimal within the ML core, and vertical fluxes (e.g., of heat or moisture) typically vary linearly with height to maintain the structure of mean scalar profiles such as potential temperature. On small spatial scales, individual thermals intermittently rise above the mean ML top, deforming the inversion layer before sinking back, although the mean entrainment zone remains relatively sharp and well-defined when averaged over time. Its alignment with complex terrain (e.g., valleys and ridges) depends on the intensity of convection and the bulk buoyancy within the ML. Under sufficiently moist conditions, rising thermals can reach their LCL before encountering the inversion, forming cumulus clouds (Schrieber et al., 1996). The latent heat release from condensation enhances buoyancy, allowing some clouds to penetrate the inversion and extend into the FA, thereby ventilating boundary-layer air and trace gases into higher atmospheric levels.

Capping inversion (CI) and entrainment zone (EZ)

The CI is a layer of stable stratification that typically forms at the top of the convective ML and marks the upper boundary of the ABL. It is characterized by a sharp increase in temperature with height, a reversal from the adiabatic or near-adiabatic lapse rate in the ML, thus suppressing vertical mixing and turbulent transport into the FA (Stull, 2012). The CI arises primarily due to two mechanisms: subsidence warming from large-scale anticyclonic conditions and entrainment processes at the ML top, where warmer, drier air from the free atmosphere is intermittently mixed downward (Garratt, 1994). This inversion acts as a lid, restricting the vertical development of boundary-layer thermals and shallow cumulus clouds, and plays a significant role in controlling ABL depth, cloud formation, and pollutant dispersion.

Within the CI, a thin region known as the EZ forms, where dynamic interactions between the convective ML and the overlying stable layer occur. This zone is marked by strong gradients in temperature, humidity, and turbulence. Turbulent eddies from below can intermittently break into the EZ, but the inversion largely prevents their full penetration into the free atmosphere (Sullivan et al., 1998). The strength and persistence of the capping inversion vary diurnally and seasonally. During the day, especially under strong solar heating, thermals may erode or lift the inversion, allowing deeper boundary layers or even cumulus-topped boundary layers to develop. At night, with radiative surface cooling, the inversion often strengthens, further stabilizing the boundary layer and promoting the development of a SBL beneath it (Mahrt, 2010). In air quality studies, the CI is of particular importance, as it traps pollutants within the ABL and limits their vertical dispersion. Consequently, a shallow boundary layer capped by a strong inversion often correlates with high near-surface pollutant concentrations, especially in urban environments.

Stable boundary layer (SBL)

The SBL typically forms during nighttime over land as a result of radiative cooling of the surface, which cools the adjacent air and creates a stable stratification. Unlike the convective daytime boundary layer, the SBL is characterized by weak, patchy, and often intermittent turbulence, making it especially challenging to observe, model, and parameterize accurately (Mahrt, 1999; Poulos and Burns, 2003). The suppression of turbulence under stable conditions leads to strong vertical anisotropy, with turbulence often confined to very shallow layers near the ground. The vertical transport of momentum, heat, and scalars in the SBL is significantly reduced due to static stability, which inhibits vertical motions and mixing. As a result, the timescale for surface-released tracers or perturbations to reach the top of the SBL can exceed the length of the night, particularly at midlatitudes during the cool season (Holtslag and Boville, 1993). This limited vertical mixing contributes to the accumulation of pollutants and the formation of radiation fog under favorable humidity conditions.

Turbulence in the SBL may be sustained or modulated by various mechanisms, including mechanical shear near the surface, gravity (buoyancy) waves, drainage flows along sloping terrain, and subsidence from large-scale high-pressure systems (Fernando and Weil, 2010). In complex terrain, katabatic flows, downslope winds driven by cooling near slopes, are common features that further complicate SBL structure and evolution. Additionally, low-level jets (LLJs) can generate turbulence in the upper portion of the SBL through shear instabilities, even when the surface remains decoupled (Banta et al., 2002). Due to the variety of physical processes at play and their intermittent and localized nature, the SBL remains a significant challenge for both NWP and climate models, where simplified parameterizations often fail to capture its complexity and variability.

Residual layer (RL)

The RL forms during the evening transition when surface radiative cooling leads to the development of the SBL near the ground, effectively decoupling the formerly well-mixed convective boundary layer from the surface. The air above this stable surface layer, formerly part of the daytime ML, becomes the RL. Though no longer actively turbulent, the RL retains the thermodynamic and kinematic characteristics of the daytime ML (Stull, 2012). Turbulence in the RL is typically very weak, isotropic, and decaying, as there is little or no forcing to maintain it. However, inertial oscillations, shear instabilities, or interaction with LLJ can occasionally reinitiate turbulence within this layer (Mahrt, 2010).

The RL is important for pollutant dispersion and tracer transport, as it can carry residual moisture, aerosols, or chemical species horizontally over long distances. Due to the decoupling from the SBL, wind speed and direction in the RL often differ significantly from those in the layer below. This mismatch in flow regimes can result in differential advection: tracers in the RL and SBL may originate from different regions and travel along different trajectories. Consequently, when the next day's ML re-forms, it entrains both the locally influenced SBL air and advected RL air, thereby integrating air masses with potentially different thermodynamic properties and pollutant loads. Over multiple diurnal cycles, this leads to splitting and merging of air parcel trajectories below the capping inversion, contributing to atmospheric heterogeneity and impacting regional air quality, boundary-layer predictability, and cloud development. Understanding the RL is thus crucial for initializing and validating NWP models, especially in clear-sky, light-wind conditions.

Neutral boundary layer (NBL)

The neutral boundary layer (NBL) occurs under conditions where surface heating is negligible, such as during overcast, windy days or nights, resulting in minimal buoyancy effects. In these cases, turbulence is maintained primarily by mechanical shear generated by wind velocity gradients near the surface, rather than by convective processes (Garratt, 1994; Stull, 2012). Because there is little or no net heating or cooling at the surface, the virtual potential temperature remains nearly constant with height, leading to near-neutral static stability. Although termed "neutral," the boundary layer is still dynamically active, with turbulence being driven by surface-layer wind shear and modulated by surface roughness and large-scale geostrophic winds (Wyngaard, 2010). The depth of the NBL typically ranges from a few hundred meters to over 1 km, depending on wind speed and surface drag, but remains limited by the presence of a capping inversion.

Turbulence within the NBL is slightly anisotropic, with greater energy in the horizontal (especially in the along-wind) direction than in the vertical, though generally more isotropic than in strongly convective boundary layers. The turbulent kinetic energy budget in the NBL is governed by shear production, turbulent transport, and viscous dissipation, with buoyancy playing a minimal role (Moeng and Sullivan, 1994). Despite the absence of strong surface heating, the NBL plays an important role in pollutant dispersion, LLJ formation, and momentum transport, especially in urban and coastal environments, where mechanical turbulence dominates and interacts with mesoscale circulations (Fernando et al., 2001). Moreover, neutral layers are common during transitional periods (e.g., sunrise or sunset) or during frontal passages, making them important for modeling weather and air quality dynamics.

1.1.2 Significance of the ABL

The ABL plays a pivotal role in connecting the Earth's surface with the overlying free troposphere, making it a critical region for various atmospheric, environmental, and societal processes. Its dynamic nature governs the exchange of momentum, heat, moisture, and trace gases between the surface and the atmosphere, influencing weather, climate, air quality, and ecosystem functioning (Figure 1.3). From a meteorological perspective, the ABL regulates the formation and development of clouds, fog, and precipitation, particularly through processes like convective mixing, turbulent transport, and surface energy fluxes (Garratt, 1994; Stull, 2012). The depth and structure of the ABL control the vertical extent of surface-based convection and the initiation of boundary-layer clouds, which in turn affect the Earth's radiation budget and hydrological cycle (Holtslag and Nieuwstadt, 1986).

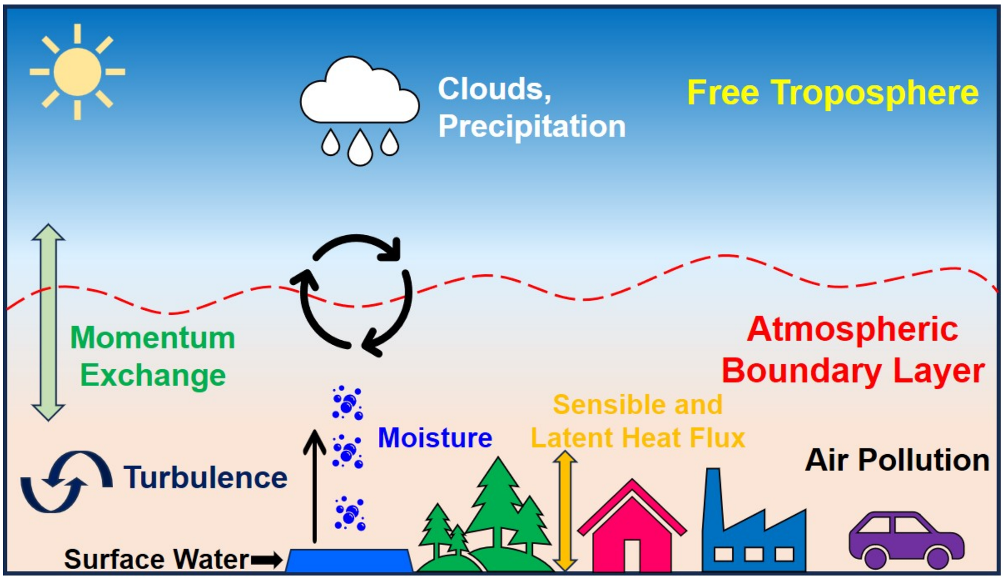

Figure 1.3: Schematic representation of the significance of the ABL. The ABL acts as a dynamic interface between the Earth's surface and the free troposphere, facilitating critical processes such as turbulent mixing, moisture transport, momentum exchange, and cloud and precipitation formation. Surface features, including vegetation, urban structures, and water bodies, contribute to the generation of turbulence and surface fluxes. The ABL also plays a central role in air pollution dispersion, as most pollutants are confined within this layer. The red dashed line indicates the variable top of the ABL, which influences vertical mixing and interactions with the overlying atmosphere.

In the context of air pollution and urban meteorology, the ABL acts as a dilution volume for pollutants emitted at the surface. A shallow boundary layer, often capped by a strong temperature inversion, can trap pollutants near the ground, leading to degraded air quality and increased health risks in urban areas (Seibert et al., 2000). The height and stability of the ABL are thus key parameters in atmospheric chemistry models and air quality forecasting systems. From the standpoint of climate and land-atmosphere interactions, the ABL serves as a key feedback region. Surface conditions, such as soil moisture and vegetation cover, can influence boundary-layer development, which in turn modulates cloud formation, precipitation, and surface energy partitioning (Santanello et al., 2009). Accurate simulation of ABL processes is therefore essential in NWP and climate models, where errors in ABL representation often propagate to larger spatial and temporal scales.

The ABL also has practical importance in areas such as aviation safety, wind energy, and agriculture. For instance, the variability of wind speed and turbulence within the ABL influences wind turbine performance and load stress, while thermal stratification and inversion conditions affect frost risk and pesticide dispersion in agricultural fields (Arya, 2001). Overall, the ABL serves as the interface between the Earth's surface and atmospheric dynamics, controlling near-surface meteorology and the initial conditions for deeper atmospheric processes. As such, it is a critical zone for observation, modeling, and prediction, and a focus area for both fundamental research and applied environmental studies.

1.2 Atmospheric clouds

Clouds cover more than 60% of the globe, with more clouds over the ocean than land (Eastman et al., 2011; Stubenrauch et al., 2013). They play a vital role in the Earth's hydrological cycle as atmospheric water reservoirs and significantly influence the radiation budget through interactions with shortwave and longwave radiation (Ramanathan et al., 1989; Randall and Tjemkes, 1991; Slingo, 1990; Stephens and Greenwald, 1991). While clouds are among the most familiar and easily observed features of the atmosphere, articulating a precise scientific definition is more complex than it might initially appear (Hirsch et al., 2014; Spänkuch et al., 2022). The World Meteorological Organization (WMO) defines a cloud as an aggregate of tiny water droplets, ice crystals, or a combination of both, suspended in the atmosphere with its base situated above the Earth's surface and observable from the ground. On the other hand, the American Meteorological Society (AMS) describes clouds as visible accumulations of minute water droplets and/or ice particles formed through the condensation of water vapor in rising air currents. The AMS's extended definition of "cloud" also encompasses any dense, visible atmospheric concentration of particulate matter, such as dust or smoke. Using optical thickness as the primary defining criterion, Spänkuch et al. (2022) proposed the following definition of a cloud: a meteorological cloud is an aggregate of minute particulate matter (solid, liquid, or mixed) suspended in the atmosphere above ground, which becomes visible from the ground when the line-of-sight optical depth reaches approximately 0.03 during the day and 0.05 at night. Clouds are mainly found in the troposphere and occasionally occur in the lower stratosphere, while clouds near polar latitudes in the stratosphere and mesosphere are seasonal phenomena (Garcia, 1989; Thomas and Olivero, 2001; Tolbert, 1994; Tritscher et al., 2021). Clouds, while ubiquitous and easily observable, display a wide range of morphologies depending on atmospheric conditions and geographical locations. Figure 1.4 presents representative examples of different cloud types, captured over plains, urban areas, coastal regions, and mountainous terrain, highlighting their diversity and occurrence in the atmosphere.

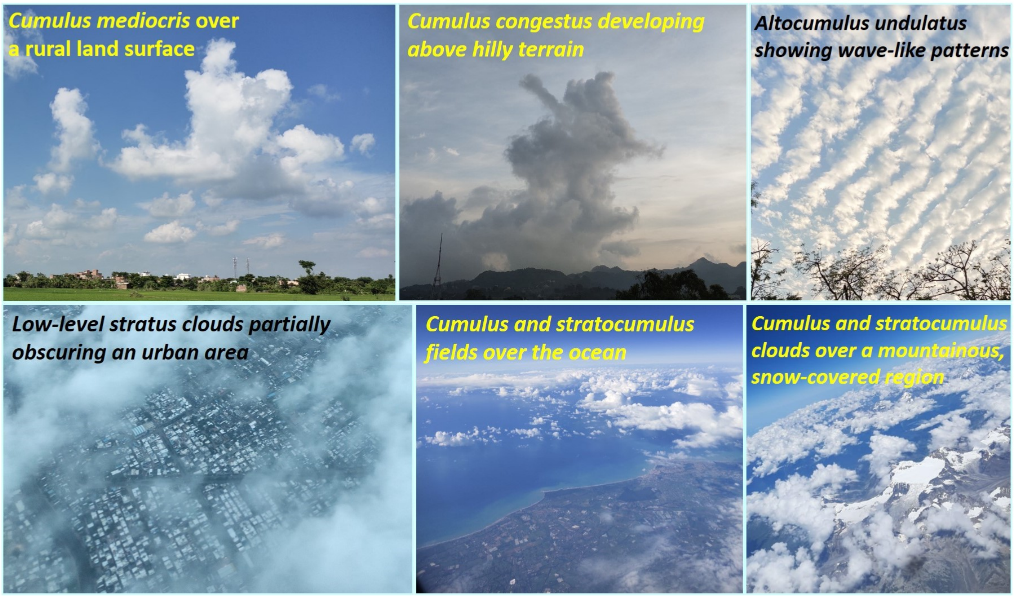

Figure 1.4: Representative pictures of different cloud types captured over land, ocean, and mountainous regions, illustrating the variability in cloud morphology and occurrence.

1.2.1 Cloud formation processes

Clouds form through the condensation of water vapor onto tiny atmospheric particles known as cloud condensation nuclei (CCN), which can include sea salt, dust, pollutants, and other aerosols (Pruppacher and Klett, 2012). This process begins when air cools to its dew point, leading to saturation. Hence, the two fundamental prerequisites for cloud formation are sufficient atmospheric moisture and mechanisms that induce cooling. Moisture is continuously cycled through the Earth-atmosphere system via the hydrological cycle, in which water exists in all three physical states: vapor, liquid, and solid. Cooling of air, typically achieved through vertical lifting, promotes condensation and cloud development. The primary lifting mechanisms include frontal, orographic, and convective lifting, and convergence (Figure 1.5).

1. **Frontal lifting:** Occurs when warm and cold air masses meet, forcing the warmer, less dense air upward.
2. **Orographic lifting:** Caused by air ascending over topographical barriers such as mountains.
3. **Convective lifting:** Results from localized surface heating, leading to the buoyant rising of air.
4. **Convergence:** When airflows meet and are forced to rise due to horizontal compression.

Apart from vertical motion, clouds and fog can also form through advection and radiational cooling, which cool the lower atmosphere under specific conditions. In advection, moist air flows horizontally over cooler surfaces (e.g., snowpacks or cold-water bodies), potentially reaching saturation from below and forming fog (Barry and Chorley, 2009). Radiational cooling, on the other hand, is common on clear, calm nights, where surface cooling lowers the temperature of air near the ground to its dew point, resulting in ground or radiation fog.

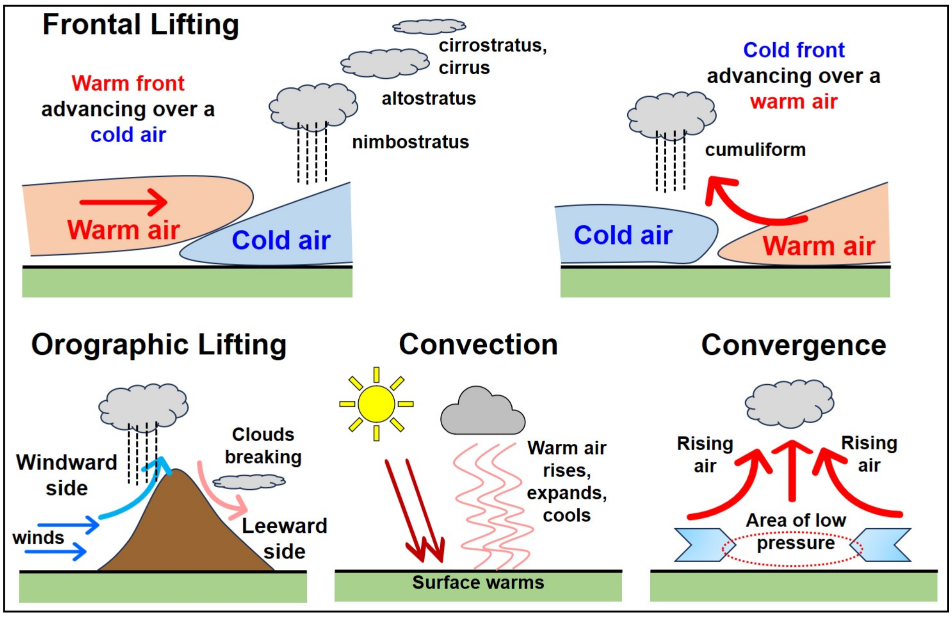

Figure 1.5: Schematic of cloud formation mechanisms, including frontal, orographic, and convective lifting, and convergence.

Saturation refers to the state where the rates of water vapor condensing and evaporating are equal, establishing a dynamic equilibrium. At this point, the vapor and the condensed phase (liquid or ice) reach thermal equilibrium, sharing the same temperature (Rogers and Yau, 1989). The Kelvin effect explains how the saturation vapor pressure increases over curved surfaces. A convex surface, such as that of a small droplet, requires a higher vapor pressure to maintain equilibrium than a flat one. This underscores the role of CCN, which lowers the energy barrier needed for droplet formation (Wallace and Hobbs, 2006).

The Kelvin equation mathematically expresses this phenomenon:

$$\ln\left(\frac{p}{p_{\text{sat}}}\right) = \frac{2\gamma V_m}{rRT} \tag{1.1}$$

where p represents the vapor pressure over a curved droplet surface, p_{sat} is the saturation vapor pressure over a flat surface, γ denotes the surface tension of the liquid, V_m is the molar volume of the liquid, R stands for the universal gas constant, r is the radius of the droplet, and T is the absolute temperature. Equation 1.1 highlights how smaller droplets, with higher curvature, require a greater vapor pressure to remain in equilibrium, underscoring the importance of condensation nuclei in initiating droplet growth.

The Köhler theory combines the Kelvin effect with Raoult's law to describe the activation of cloud droplets. It postulates that each aerosol particle requires a certain amount of water vapor and a threshold supersaturation to become an active cloud droplet (Wallace and Hobbs, 2006).

The Köhler equation is given by:

$$\ln\left(\frac{p_w(D_p)}{p^0}\right) = \frac{4M_w\sigma_w}{RT\rho_w D_p} - \frac{6n_s M_w}{\pi\rho_w D_p^3} \tag{1.2}$$

where $p_w(D_p)$ is the vapor pressure over a droplet of diameter D_p, p^0 is the saturation vapor pressure over a flat surface, σ_w is the droplet surface tension, ρ_w is the density of pure water, n_s is the number of moles of solute, and M_w is the molecular weight of water.

Köhler's equation is visually represented by the Köhler curve. It shows the supersaturation at which the cloud drop is in equilibrium with the environment over a range of droplet diameters. Once supersaturation exceeds a critical value, rapid condensation ensues, leading to cloud development. However, the resulting clouds can vary widely in appearance, structure, altitude, and associated weather phenomena. These differences arise due to variations in atmospheric stability, temperature, moisture content, and vertical air motion. To systematically study and describe this diversity, clouds are categorized into distinct types based on their form and the altitude at which they occur.

1.2.2 Cloud classification and morphology

Clouds are typically classified based on their altitude and morphological characteristics, following the international system developed by Luke Howard in the early 19th century and formalized by the World Meteorological Organization (WMO) (Hamblyn, 2022). This classification groups clouds into four main genera: high-level, mid-level, low-level, and vertically developed clouds (Table 1.1). Each category includes distinct cloud types based on appearance, height, and physical processes.

Table 1.1: Cloud classification summary (based on WMO)

Level	**Cloud Types**	**Typical Altitude**
High (cirro-)	Cirrus, Cirrostratus, Cirrocumulus	$>$ 6,000 m
Mid (alto-)	Altostratus, Altocumulus	2,000–6,000 m
Low	Stratus, Stratocumulus, Nimbostratus	$<$ 2,000 m
Vertical	Cumulus, Cumulonimbus	Surface to $>$ 12,000 m

1. **High-level clouds (cirro-)**

   These clouds form in the upper troposphere, typically above 6,000 m (20,000 ft). They consist mostly of ice crystals due to the cold temperatures at these altitudes.

   - **Cirrus (Ci)**: Thin, wispy clouds that appear white and fibrous. They often indicate fair weather but can also signify an approaching frontal system or upper-level jet stream.
   - **Cirrostratus (Cs)**: Transparent, sheet-like clouds that cover large portions of the sky and can produce halo phenomena around the sun or moon.
   - **Cirrocumulus (Cc)**: Small, white patches or ripples without shadows, often appearing in rows. Unlike other cirrus types, they may indicate atmospheric instability at upper levels.

2. **Mid-level clouds (alto-)**

   These clouds usually occur between 2,000 and 6,000 m (6,500 to 20,000 ft) and consist of water droplets, supercooled droplets, and sometimes ice crystals.

   - **Altostratus (As)**: Gray or bluish sheets of cloud that cover the sky, often preceding a warm front. They can produce light precipitation.

- **Altocumulus (Ac)**: White or gray patches with a wave-like structure, sometimes resembling a field of cotton balls. They may signal changing weather or convection aloft.

3. **Low-level clouds**

   Found below 2,000 m (6,500 ft), these clouds are predominantly composed of liquid water droplets, though snow or ice may occur in cold conditions.

   - **Stratus (St)**: Featureless, gray layers that cover the entire sky, resembling fog but not touching the ground. They often bring drizzle or light mist.
   - **Stratocumulus (Sc)**: Low, lumpy clouds with gaps of clear sky in between. They are common in stable atmospheric conditions and may form in the wake of cold fronts.
   - **Nimbostratus (Ns)**: Thick, dark clouds that cover the sky and produce continuous, widespread precipitation. They often originate from thickening altostratus layers.

4. **Vertically developed clouds**

   These clouds span multiple levels of the troposphere and are associated with strong vertical air motion. They can grow from the surface to altitudes over 12,000 m (39,000 ft).

   - **Cumulus (Cu)**: Fluffy, white clouds with flat bases and domed tops. Fair-weather cumulus forms in response to localized surface heating.
   - **Cumulonimbus (Cb)**: Towering, anvil-shaped clouds associated with severe weather, including thunderstorms, hail, and sometimes tornadoes. These clouds can reach the tropopause and are driven by strong convection (Houze, 2014).

1.2.3 Role of clouds in weather and climate

Clouds are integral to the Earth's atmospheric system, exerting strong influences on both weather processes and climate dynamics. Through their interactions with incoming solar and outgoing terrestrial radiation, clouds play a dual role: they cool the planet by reflecting sunlight (*cloud albedo effect*) and warm it by trapping outgoing longwave radiation (*cloud greenhouse effect*) (Ramanathan et al., 1989). Even minor variations in cloud coverage, type, or altitude can significantly alter the Earth's radiation budget and, consequently, affect both regional weather and global climate patterns. A useful metric for assessing these impacts is *radiative forcing* (RF), defined as the change in net radiative flux at the tropopause after stratospheric temperature adjustment, with surface and tropospheric temperatures held fixed (Ramaswamy et al., 2001). RF is typically expressed in watts per square meter ($\mathrm{W\,m^{-2}}$) and provides insight into how different atmospheric components, including clouds, influence the Earth's energy balance.

Cloud-related RF is governed by a cloud's microphysical properties (e.g., effective droplet radius, liquid water content) and macrophysical attributes (e.g., cloud cover, cloud base, and top heights). These factors determine how much solar radiation is reflected or absorbed and how much terrestrial radiation is retained (Luebke et al., 2022). Given their complexity and variability, clouds remain a critical yet challenging component in understanding and predicting both weather phenomena and climate change (Stephens, 2005). The representation of clouds in climate models has remained one of the largest sources of uncertainty in climate projections over the past several decades (Arakawa, 2004; Bony and Dufresne, 2005; Cess et al., 1989; Randall et al., 2003). Among the various anthropogenic and natural drivers of RF, cloud-related processes linked to aerosols are especially important sources of uncertainty. Aerosols interact with clouds both directly and indirectly: they scatter and absorb solar radiation (aerosol-radiation interactions) and modify cloud microphysical properties such as droplet size, lifetime, and albedo (aerosol-cloud interactions). These processes generally exert a negative radiative forcing (cooling effect), as indicated by the blue bars in Figure 1.6, offsetting part of the warming caused by greenhouse gases.

Figure 1.6 highlights that the effective radiative forcing from aerosol-cloud interactions is estimated at $-0.22\ \mathrm{W\,m^{-2}}$ (with a range from -0.47 to $+0.04$), while

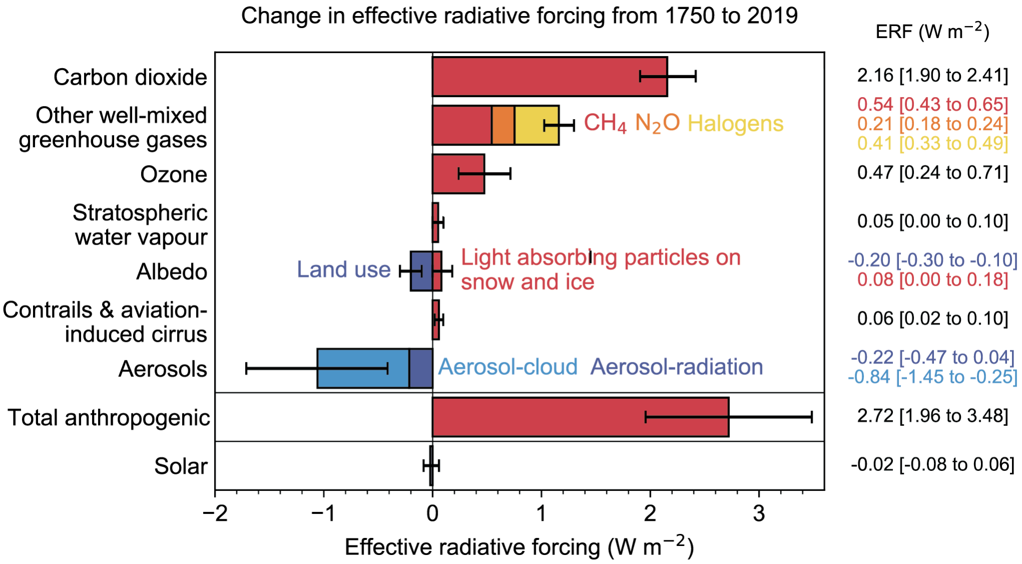

Figure 1.6: Effective RF due to major anthropogenic and natural drivers from 1750 to 2019. Positive values indicate warming, while negative values indicate cooling. Notably, aerosol-cloud and aerosol-radiation interactions contribute the largest negative forcing, with a high associated uncertainty (Forster et al., 2021).

aerosol-radiation interactions contribute about $-0.84\ \mathrm{W\,m^{-2}}$ (range -1.45 to -0.25). This substantial negative forcing underscores how clouds, through their interaction with aerosols, act to moderate anthropogenic warming. However, the wide uncertainty ranges emphasize the difficulty in quantifying cloud processes, given their dependence on complex microphysical and dynamical factors. In contrast, other cloud-related processes exert smaller but non-negligible positive forcings. For example, contrails and aviation-induced cirrus add a warming effect of about $+0.06\ \mathrm{W\,m^{-2}}$, while light-absorbing particles on snow and ice contribute $+0.08\ \mathrm{W\,m^{-2}}$ by reducing surface albedo and enhancing local warming.

Clouds and weather

Clouds play a pivotal role in shaping short-term weather phenomena, particularly through their influence on precipitation formation, atmospheric composition, and vertical transport processes. A significant portion of global precipitation originates from ice and mixed-phase clouds, where the glaciation process, particularly via the Bergeron–Findeisen mechanism, plays a decisive role in precipitation efficiency (Rogers and

Yau, 1989). In convective cloud systems, the presence of ice particles enhances precipitation pathways, leading to more intense weather events (Houze, 2014). Beyond precipitation, clouds act as effective mediators in atmospheric cleansing through wet deposition, which is one of the principal pathways for removing aerosols and soluble gaseous pollutants. During cloud formation, aerosol particles serve as CCN, upon which water vapor condenses to form cloud droplets. These droplets incorporate the aerosols, and upon coalescence and precipitation, remove them from the atmosphere (Pruppacher and Klett, 2012). This scavenging process is crucial for regulating air quality and influencing the lifetime of atmospheric pollutants. Furthermore, clouds contribute to the vertical redistribution of atmospheric constituents. Deep convective clouds, characterized by intense updrafts, can transport boundary-layer air, including moisture, aerosols, and trace gases, into the upper troposphere and even the lower stratosphere. This vertical transport modifies the chemical composition of upper atmospheric layers, affects radiative transfer processes, and alters the residence time of pollutants. However, the extent to which these materials persist at higher altitudes after the decay of convective systems is still an open question and continues to be a focus of ongoing research (Stohl et al., 2005).

Clouds and climate

From a climatological perspective, clouds play a dominant role in shaping the Earth's radiation budget. They cover nearly 60–70% of the Earth's surface and influence both shortwave (solar) and longwave (infrared) radiative fluxes. On average, clouds reflect about 26% of incoming solar radiation, accounting for more than 70% of the total planetary albedo and yielding a net cooling effect estimated between -42 and $-74\ \mathrm{W\,m^{-2}}$ (Stephens et al., 2012). This cooling is most pronounced in mid- and low-level stratiform clouds due to their high optical thickness. Over oceans, this effect is particularly significant given the ocean's inherently low surface albedo. Simultaneously, clouds absorb and re-emit longwave radiation emitted from the Earth's surface. This greenhouse-like warming effect varies with cloud altitude and temperature. The high-level cirrus clouds, although thinner and less reflective, trap outgoing infrared radiation efficiently due to their cold temperatures, contributing a warming effect estimated at $+22$ to $+55\ \mathrm{W\,m^{-2}}$ (Hartmann et al., 1992). The global net effect of clouds is a modest cooling of approximately $-15\ \mathrm{W\,m^{-2}}$, though this value is subject to spatial and temporal variability and significant uncertainty (Masson-Delmotte et al., 2021).

Cloud-climate interactions are further complicated by feedback mechanisms. Changes in global temperature can alter cloud formation, type, and distribution, thereby modifying cloud radiative properties in a process known as *cloud feedback*. For example, a warmer atmosphere may promote higher water vapor content and shift cloud types, which could either amplify (positive feedback) or mitigate (negative feedback) warming. Accurate quantification of these feedbacks is essential for robust climate projections (Bony and Dufresne, 2005).The microphysical properties of clouds, particularly droplet size and concentration, also play a pivotal role in radiative behavior. A cloud composed of numerous small droplets reflects more solar radiation than one with fewer, larger droplets, even if both contain the same liquid water content. This principle underpins the *aerosol indirect effect*, wherein anthropogenic aerosols serve as additional CCN, increasing cloud albedo and potentially extending cloud lifetime by suppressing precipitation formation (Twomey, 1977; Albrecht, 1989). In addition to the first aerosol indirect effect (enhanced cloud reflectivity), aerosols may also modify cloud dynamics and thermodynamics, especially in ice and mixed-phase clouds. However, the full extent of aerosol–cloud interactions remains uncertain due to the complexity of feedback loops and the spatial heterogeneity of aerosol distributions (Fan et al., 2016; Masson-Delmotte et al., 2021).

1.3 Observational and modeling studies of ABL and clouds

Understanding the evolution of the ABL and its interaction with clouds requires a combination of *in situ* observations, remote sensing, and numerical modeling (Seibert et al., 2000). Observations provide the essential baseline for characterizing ABL thermodynamics, turbulence, and cloud properties, while models enable controlled experimentation and extrapolation to larger spatial and temporal scales. Over recent decades, advances in measurement technologies and computational capabilities have enhanced our ability to investigate ABL dynamics and cloud microphysics at fine temporal and spatial scales (Bony et al., 2015). These advancements allow for detailed analyses of cloud occurrence, diurnal variability, and boundary layer processes. Numerical models, ranging from large-eddy simulations (LES) to global and regional climate models, complement these observations by simulating the coupled dynamics of turbulence, convection, and cloud formation under varying environmental conditions. Despite these advances, there remains several challenges. The ABL-cloud system is inherently complex due to the nonlinear coupling between radiation, turbulence, microphysics, and surface fluxes. These processes are strongly modulated by local factors such as topography, land use heterogeneity, and soil moisture variability, as well as by synoptic and mesoscale forcing (Pino et al., 2006; Santanello et al., 2009). Capturing this multiscale variability poses significant difficulties for both observations and models, often leading to uncertainties in cloud representation and boundary layer parameterizations in weather and climate simulations.

1.3.1 Observational approaches

Field campaigns and long-term ground-based observations form the backbone of empirical research on the ABL and cloud processes. A wide range of instruments are employed to capture the thermodynamic and dynamical state of the atmosphere. Radiosondes provide vertical profiles of temperature, humidity, and wind, which are essential for diagnosing stability regimes and convective potential (Seidel et al., 2010). Ground-based remote sensing instruments, such as Lidars and wind profilers, offer continuous measurements of BLH, CBH, and wind structure (Stull, 2012). Microwave radiometers complement these systems by providing column-integrated water vapor and temperature profiles, while eddy-covariance flux towers supply direct estimates of surface energy and momentum fluxes. Collectively, these measurements allow for the diagnosis of turbulent mixing processes and surface-atmosphere exchanges, which are critical to ABL evolution and cloud initiation.

Satellite-based sensors extend this capability to the global scale by providing detailed information on cloud macro- and microphysical properties. Instruments such as MODIS, CALIPSO, and CloudSat have revolutionized the ability to monitor cloud occurrence, cloud optical thickness, effective droplet radius, cloud-top pressure, and liquid water path across diverse regions and seasons (Stephens and Kummerow, 2007; King et al., 2013). However, satellite observations typically lack the fine vertical resolution and temporal sampling required to directly resolve ABL structure and sub-cloud turbulence (Wood, 2012). This limitation constrains their utility for studying diurnal ABL dynamics or near-surface cloud processes.

To overcome these observational gaps, integrated ground-based monitoring networks are required. The long-term, continuous observations of ABL evolution, cloud formation, and surface–atmosphere coupling are indispensable for advancing process-level understanding, improving turbulence and cloud parameterizations in weather and climate models, and validating satellite retrievals. Together, multi-platform observational strategies from localized field campaigns to global satellite missions enable a more complete picture of ABL processes and their coupling with clouds, despite the persistent challenges posed by scale mismatches and observational limitations.

1.3.2 Modeling studies

Numerical modeling is indispensable for investigating ABL and cloud processes under controlled, repeatable conditions. Models provide the ability to isolate individual processes, perform sensitivity experiments, and explore scenarios that are difficult to capture with observations alone. LES models explicitly resolve the largest turbulent eddies while parameterizing only the subgrid-scale motions. This approach has proven especially powerful for studying cloud-topped boundary layers, entrainment at the inversion, and convective mixing processes (Moeng et al., 1996; Sullivan et al., 1998). LES experiments have been instrumental in advancing our understanding of shallow cumulus convection, stratocumulus-to-cumulus transitions, and aerosol-cloud-radiation interactions. They also serve as "virtual laboratories" for testing turbulence closure schemes and microphysical parameterizations used in larger-scale models.

At regional scales, mesoscale models such as the Weather Research and Forecasting (WRF) model operate at horizontal resolutions of 1–10 km and are widely employed to simulate diurnal ABL evolution, fog events, sea-breeze circulations, and convective cloud systems (Skamarock et al., 2019). These models incorporate detailed physics, including surface-layer schemes, PBL parameterizations, cloud microphysics, and radiation transfer modules. Despite their versatility, substantial uncertainties remain due to the need to parameterize subgrid turbulence, microphysics, and land-atmosphere exchanges, particularly over heterogeneous terrain, complex topography, and urban regions (Santanello et al., 2009).

At global scales, general circulation models (GCMs) aim to represent ABL and clouds in a climate context, but coarse horizontal resolution necessitates heavily parameterized treatments of turbulence and cloud processes. These simplifications contribute to one of the largest sources of uncertainty in climate projections: the representation of low clouds and their radiative (Bony and Dufresne, 2005). To address this, recent developments include variable-resolution models, superparameterization, and machine-learning-based parameterizations that attempt to bridge scales between LES and GCMs. Together, LES, mesoscale, and global modeling approaches provide complementary insights into ABL and cloud dynamics. However, bridging the scale gap between process-resolving LES studies and global-scale climate simulations remains a central challenge in atmospheric science.

1.4 Gaps in regional understanding of ABL and clouds

Despite considerable progress in advancing our understanding of the ABL and cloud systems through observational campaigns, satellite datasets, and numerical modeling, significant regional disparities remain. While global and continental-scale studies provide important insights, they often fail to capture the complexity and heterogeneity of processes that operate on smaller spatial and temporal scales. Consequently, regular vertically and temporally high-resolution observations and regionally tuned modeling efforts are essential for addressing the following key scientific aspects of the ABL cloud system:

- Diurnal, seasonal, and long-term variability of ABL and cloud dynamics, and their influence on local and regional weather-climate interactions. For instance, the diurnal growth of the ABL strongly regulates the onset of convection, while seasonal variability influences monsoon circulation and precipitation patterns
- Influence of regional and large-scale circulations on ABL dynamics and cloud formation, particularly in areas impacted by complex terrain, land-sea interactions, or monsoonal flows. These interactions are often poorly constrained in current models
- Transition dynamics between convective and stable boundary layer states, which remain a key uncertainty in understanding boundary layer turbulence, pollutant dispersion, and cloud initiation
- Boundary layer cloud formation under aerosol-laden conditions, especially over rapidly urbanizing regions where high aerosol loading can alter cloud microphysics, lifetime, and radiative properties
- Cloud and ABL responses to extreme weather events. Such extremes are expected to intensify under climate change, but their impact on ABL and clouds is not fully understood at the regional scale

These knowledge gaps are particularly critical in regions like Western India, where a unique combination of intense monsoonal variability, high aerosol concentrations, rapid land-use changes, and urban expansion directly impacts ABL and cloud processes. The region's vulnerability to air quality deterioration, extreme weather, and hydrological stresses underscores the importance of building a robust scientific understanding of these interactions.

Moreover, accurate characterization of ABL and cloud processes in this region is fundamental for a range of applications, including:

- Improved weather and air quality prediction, particularly for short-term forecasts of haze, fog, and convective storms
- Reliable climate impact assessments, which depend on better representation of ABL–cloud–aerosol feedbacks in regional climate models
- Hydrological and water resource management, as boundary layer processes and cloud properties directly influence precipitation efficiency and distribution

Bridging these gaps requires integrated observational strategies, combining ground-based remote sensing, in-situ measurements, and satellite retrievals with high-resolution numerical simulations. Strengthening regional networks and enhancing long-term datasets are crucial for reducing uncertainties and building a more comprehensive understanding of ABL and cloud processes in this vulnerable part of the world.

1.5 Objectives of the thesis

The semi-arid regions of Western India present a complex and understudied environment, characterized by heterogeneous land cover, rugged topography, sparse vegetation, and strong diurnal variability in surface energy balance (Raja et al., 2016; Satyanarayana et al., 2003). These characteristics make the region particularly sensitive to land–atmosphere coupling, especially under monsoonal and pre-monsoonal conditions. Despite this sensitivity, the current understanding of ABL dynamics and cloud processes in this region remains limited due to a lack of focused observational and modeling studies (Turner et al., 2020).

Studies have shown that the performance of numerical weather and climate models in capturing ABL development and cloud formation are strongly dependent on the choice of model physics, PBL schemes, land surface models (LSMs), and initial and boundary conditions (Rai and Pattnaik, 2019; Santanello et al., 2009). These sensitivities are magnified in semi-arid environments, where the interaction between soil moisture availability, surface flux partitioning, and boundary-layer thermodynamics plays a critical role in governing cloud initiation, convective development, and precipitation efficiency (Sanchez-Mejia and Papuga, 2017).

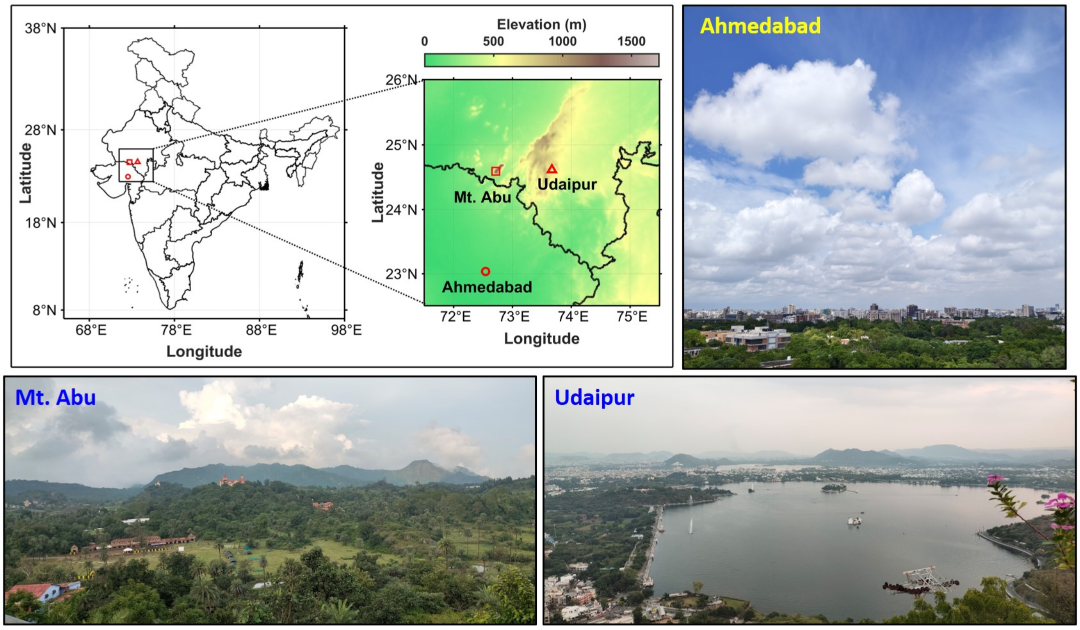

Figure 1.7: Geographical location of the study region. The top left panel shows the map of India with the study areas marked over Western India, along with a zoomed-in view of the selected region highlighting the three observational sites: Ahmedabad (red circle), Mt. Abu (red square), and Udaipur (red triangle). The background shading represents terrain elevation (in meters). The right panels present site photographs from Ahmedabad (top right), Mt. Abu (bottom left), and Udaipur (bottom right).

Given that ABL and cloud processes and their interactions directly affect regional climate feedbacks, air quality, and hydrological responses, it becomes essential to investigate these processes over semi-arid terrains like Western India. However, limited availability of high-resolution observations and the absence of systematic model evaluations have hindered efforts to accurately represent ABL evolution and cloud processes in this region. Furthermore, the uncertainty introduced by model configuration choices, particularly under weak synoptic forcing and strong local heterogeneity, poses a challenge for representing key phenomena such as fog, convective precipitation, low-level cloud formation, and pollution dispersion.

The three selected study regions, Ahmedabad, Mt. Abu, and Udaipur (Figure 1.7), offer a natural testbed due to their diverse land-surface characteristics, which include urban basins, forested hills, and lake-dominated valleys. Ahmedabad, a highly polluted urban city in Gujarat, experiences a hot semi-arid climate; Mount Abu, located in the Aravalli range of Rajasthan, represents a high-altitude, forested terrain; and Udaipur, situated near the eastern edge of the Thar Desert, is surrounded by lakes and also exhibits a hot semi-arid climate. High-resolution, ground-based Lidar observations at these locations, supported by satellite and reanalysis datasets, will allow for a more accurate characterization of ABL dynamics and cloud development. Therefore, the overarching objective of this thesis is to improve our understanding of cloud formation and ABL dynamics over the Western Indian region through an integrated observational and modeling approach.

The specific objectives are as follows:

- To characterize the seasonal and diurnal variability of ABL and clouds over the three regions, Ahmedabad, Mt. Abu, and Udaipur, in Western India, using ground-based Lidar, satellite, and reanalysis datasets
- To investigate the formation mechanism and characteristics of clouds forming below and near the LCL
- To investigate the influence of local meteorological and thermodynamic conditions on boundary layer cloud formation
- To analyze the thermodynamic and dynamic behavior of the ABL and associated cloud features during extreme events such as dust storms and severe air pollution episodes
- To evaluate the performance of the WRF model in simulating boundary layer characteristics under varying atmospheric conditions.

By addressing these objectives, this thesis aims to fill the existing knowledge gaps and contribute to the improved representation of ABL and cloud interactions in weather and climate models over semi-arid regions of India.

1.6 Organization of the thesis

This thesis is organized into seven chapters. It begins with a foundational overview in Chapter 1, which introduces the core concepts related to clouds and the ABL, summarizes the current state of knowledge, and outlines the motivation and objectives of the study. Chapter 2 presents the methodology, detailing the instruments and observational datasets (Lidar, radiosonde, etc.), as well as satellite and reanalysis products.

The central investigation is carried out across Chapters 3 to 6, which collectively explore the physical processes governing ABL dynamics and cloud formation over semi-arid regions. These chapters examine the influence of local meteorology, thermodynamics, extreme events, and model sensitivities on ABL and cloud characteristics. Finally, Chapter 7 concludes the thesis by summarizing the key findings and discussing their broader implications, along with directions for future research.

Following the introductory chapter, below are concise descriptions of the remaining chapters of the thesis:

- **Chapter 2** presents a detailed account of the observational datasets and instruments used in this study. It includes the technical specifications and operational principles of ground-based Lidars, particularly the Ceilometer and Raman Lidar systems. Additionally, the chapter outlines the satellite-based observations (e.g., INSAT, MODIS) and reanalysis datasets (e.g., ERA5, CAMS) that support the analysis.
- **Chapter 3** focuses on the seasonal and diurnal variability of the ABL and cloud properties over Ahmedabad, Mt. Abu, and Udaipur in western India. It utilizes

ground-based Lidar observations, satellite products, and reanalysis data. The chapter also investigates long-term trends in cloud occurrence and precipitation over the Ahmedabad region.

- **Chapter 4** examines the formation mechanisms and characteristics of clouds that form below or near the lifting condensation level (LCL). An analytical expression for estimating the LCL based on surface temperature and relative humidity is derived and applied to analyze seasonal and diurnal variations in the Ahmedabad region.
- **Chapter 5** analyzes the thermodynamic and dynamic behavior of the ABL and associated cloud during extreme events, such as dust storms and severe air pollution episodes. The chapter highlights how such events influence ABL development and cloud properties.
- **Chapter 6** investigates the role of local meteorological and thermodynamic conditions in boundary-layer cloud formation. It also evaluates the performance of the Weather Research and Forecasting (WRF) model in simulating ABL characteristics under varying atmospheric conditions.
- **Chapter 7** provides a comprehensive summary of the research findings, followed by the main conclusions drawn from the work. It also identifies key scientific questions that remain open and proposes directions for future research to advance the understanding of ABL–cloud interactions in semi-arid environments.

****

Chapter 2

Methodology: Instruments and Datasets

The study of ABL and cloud dynamics relies on a combination of *in situ* measurements, remote sensing instruments, numerical modeling, and reanalysis datasets. Each of these approaches offers distinct advantages in terms of spatial coverage, temporal resolution, and the type of atmospheric variables retrieved. Over the past few decades, a variety of methods have been employed to understand ABL structure, cloud evolution, and their interactions with surface and synoptic-scale forcings (Dang et al., 2019; Kotthaus et al., 2023; Mahajan and Fataniya, 2020; Smith et al., 2021; Stephens and Kummerow, 2007). Traditionally, radiosondes have been the backbone of upper-air atmospheric profiling, providing vertical profiles of temperature, relative humidity, and wind up to the stratosphere (Seidel et al., 2010). While valuable for large-scale weather diagnostics, radiosondes are typically launched only twice daily and offer limited temporal resolution, which restricts their utility for studying rapidly evolving boundary layer and cloud processes. To overcome these limitations, a variety of ground-based remote sensing instruments have been deployed, including microwave radiometers, Doppler Sodars, and Lidars. These systems allow for continuous, high-resolution monitoring of ABL dynamics and CBH (Emeis, 2010; Wiegner et al., 2014). In particular, Raman and Doppler Lidar have proven especially useful for retrieving aerosol backscatter, vertical motion, and moisture profiles, offering detailed insights into mixing layer dynamics and aerosol–cloud interactions (Summa et al., 2023). At regional to global scales, satellite-based remote sensing platforms have transformed the ability to monitor cloud properties. Satellite-based sensors such as MODIS (onboard *Terra* and *Aqua*), CALIOP (on *CALIPSO*), CPR (on *CloudSat*), and the imager and sounder instruments on *INSAT-3D/3DR* provide key parameters such as cloud optical thickness (COT), cloud top pressure (CTP), cloud top temperature (CTT), effective droplet radius (CER), and cloud phase (John et al., 2019; Platnick et al., 2003; Stubenrauch et al., 2013). Complementary to direct observations, reanalysis datasets such as ERA5 (Hersbach et al., 2020) and CAMS (Inness et al., 2019) offer gridded, physically consistent datasets of meteorological and chemical variables. These have been widely used to study ABL climatology, cloud trends, and radiative effects over long periods, especially in regions where continuous ground-based observations are limited.

Recent studies have demonstrated the strength of multi-platform integration, where ground-based instruments, satellite retrievals, and reanalysis products are used in synergy to improve our understanding of ABL and cloud processes (Turner et al., 2020). This integrated approach allows to resolve diurnal and seasonal variability, detect extreme events, and validate model simulations under diverse meteorological conditions. Given the semi-arid and topographically complex nature of Western India, such a multi-instrumental strategy becomes crucial. In this thesis, high-resolution ground-based Lidar measurements are employed alongside satellite and reanalysis datasets to provide a detailed characterization of ABL and cloud evolution across three climatically distinct locations. The following sections describe the individual instruments and datasets used in this thesis work, with a major focus on Lidar systems, satellite observations, and reanalysis products.

2.1 Lidars

Light Detection and Ranging (Lidar) is a remote sensing technique that uses laser pulses to measure atmospheric constituents and structures by detecting backscattered signals from aerosols, molecules, and cloud particles. The lidar system determines the distance to atmospheric targets by measuring the time delay between the emission of a laser pulse and the detection of its backscattered signal, based on the relation $h = \frac{ct}{2}$, where h is the height, c is the speed of light, and t is the round-trip time (Figure 2.1).

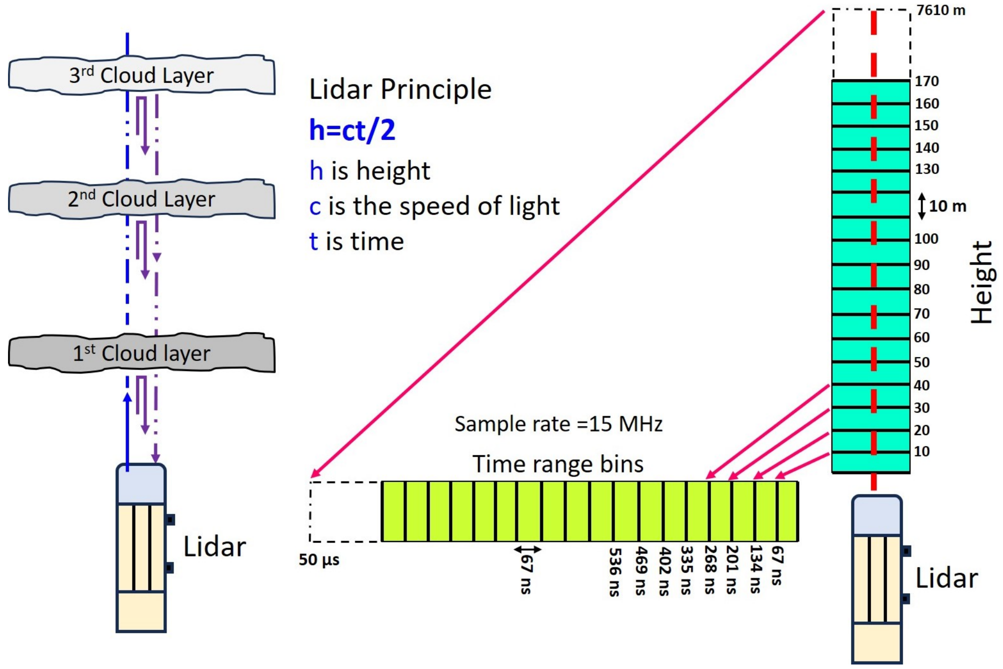

Figure 2.1: Schematic illustration of the lidar measurement principle for cloud detection. The left panel shows how vertically emitted laser pulses from a ground-based lidar are backscattered by different cloud layers. The backscattered signal is used to determine the height (h) of cloud layers using the time delay (t) between emission and detection, based on the equation $h = \frac{ct}{2}$, where c is the speed of light. The right panel demonstrates the conversion of return times into height bins, with a sample rate of 15 MHz corresponding to a vertical resolution of approximately 10 meters. Multiple time bins (in nanoseconds) are mapped to corresponding atmospheric heights, enabling the construction of vertical profiles of clouds and aerosols.

Over the past few decades, Lidar has emerged as a critical tool for high-resolution profiling of ABL and cloud properties, providing valuable insights into vertical atmospheric structure at fine temporal and spatial scales. The development of Lidar technology began in the early 1960s, following the invention of the laser (Maiman, 1960). The first atmospheric Lidar observations were demonstrated shortly thereafter

(Fiocco and Smullin, 1963). By the 1970s, Lidar systems were already being used to detect cloud layers and aerosol distributions (She and Friedman, 2022). Advances in laser technology, detector sensitivity, and signal processing over the next few decades led to the development of various Lidar configurations, including elastic backscatter Lidar, Raman Lidar, differential absorption Lidar (DIAL), and Doppler Lidar, each optimized for specific atmospheric targets. Lidars are widely used in cloud detection and profiling. They can detect CBH with high accuracy, and under certain configurations (e.g., Raman or high-spectral-resolution Lidars), they can estimate liquid water content, cloud optical depth, and phase information (Schmidt et al., 2013). Due to their sensitivity to optically thin layers, Lidars are particularly effective at identifying sub-visual cirrus and shallow cumulus clouds, which are often underestimated in passive satellite retrievals.

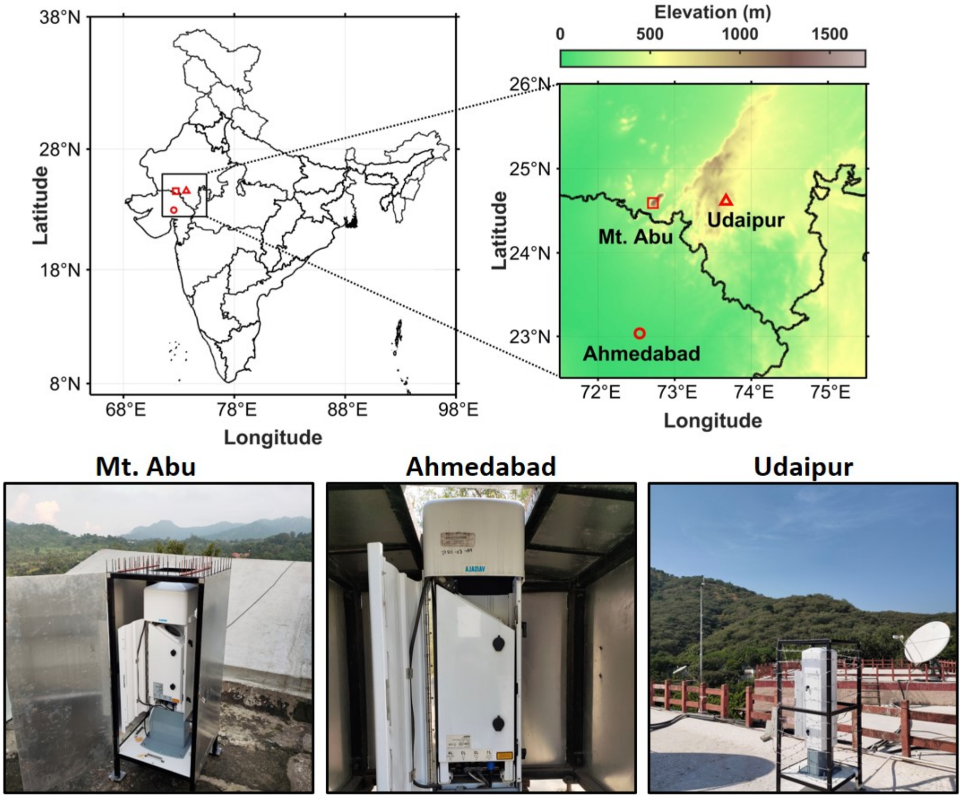

Figure 2.2: Ground-based Ceilometer Lidar systems deployed at the three study locations-Ahmedabad, Mount Abu, and Udaipur.

Lidar has also proven useful in observing the temporal evolution and vertical structure of the ABL. Elastic backscatter Lidars and Ceilometers can detect strong gradients in aerosol concentration, which often coincide with the top of the convective boundary layer, making them effective for determining BLH (Eresmaa et al., 2006; Lammert and Bösenberg, 2006; Menut et al., 1999). Doppler Lidar, on the other hand, measures vertical wind velocity and turbulence within the ABL, enabling assessments of mixing processes and entrainment (Gal-Chen et al., 1992).

Lidar systems are especially valuable due to their ability to operate continuously with high vertical resolution, often down to tens of meters, making them ideal for capturing diurnal variability, nocturnal inversions, and transitional phases that are often missed by radiosonde observations. Their integration into long-term observation networks and field campaigns has substantially enhanced our understanding of ABL dynamics, cloud evolution, and aerosol-cloud interactions. The Ceilometer Lidars installed at Ahmedabad, Mt. Abu, and Udaipur served as key instruments in this thesis work for monitoring boundary-layer and cloud characteristics (Figure 2.2).

Ceilometer Lidar

The Vaisala CL31 Ceilometer Lidar is a compact, eye-safe, and automated Lidar system widely used for atmospheric profiling, particularly for the detection of CBH and vertical visibility. This instrument is based on the elastic backscatter Lidar principle and is capable of operating continuously under diverse weather conditions. The Ceilometer (CL31) uses a low-power indium gallium arsenide (InGaAs) diode laser, which emits short-duration laser pulses ($\sim$110 nanoseconds) at a wavelength of 910 ± 10 nm (at 25°C) with a pulse repetition rate of 10 kHz (Martucci et al., 2010). The maximum detection range of the Ceilometer is approximately 7.6 km, allowing it to profile cloud layers within the troposphere. The laser pulses transmitted into the atmosphere are backscattered by aerosols, hydrometeors, or cloud droplets, and the return signals are collected by a silicon avalanche photodiode detector. This backscattered signal is then processed to derive range-resolved profiles of attenuated backscatter.

An example of such a backscatter profile from the Ceilometer is shown in (Figure 2.3), illustrating the detection of cloud layer and sharp signal returns from cloud base. The CL31 is capable of detecting up to three distinct cloud layers, provided the lowest layer does not fully attenuate the laser beam. In conditions where the sky is fully obscured, such as by fog, haze, or precipitation, the instrument estimates the maximum backscatter altitude, providing information on vertical visibility and the height of the optically densest atmospheric layer. The measurement accuracy for CBH is the greater of $\pm 1\%$ or ± 5 meters, making it suitable for detailed cloud monitoring.

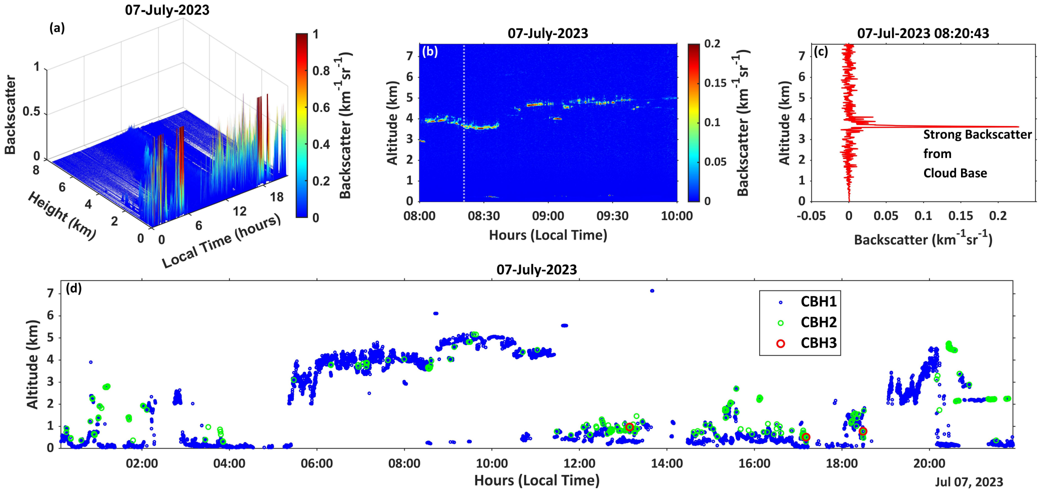

Figure 2.3: (a-b) Time-height cross-section of backscatter derived from the Ceilometer Lidar over Mt. Abu on 07 July 2023, showing cloud layers with strong backscatter signals. (b) Corresponding vertical profile of backscatter at 08:20:43 LT, indicating a sharp increase in backscatter at CBH, representing cloud detection through enhanced signal return. (c) Diurnal variation of CBH over Mt. Abu on 07 July 2023, showing the first (CBH1), second (CBH2), and third (CBH3) detected cloud layers.

The received power at the detector from a target at a distance z is described by the general Lidar equation (Weitkamp, 2005) as shown in Equation 2.1:

$$P_r(z) = \frac{E_0 c}{2} \cdot \frac{A}{z^2} \cdot \beta(z) \cdot \exp\left(-2\int_0^z \sigma(z')\,dz'\right) \tag{2.1}$$

where $P_r(z)$ is the instantaneous power received by the Ceilometer from distance z, E_0 (in Ws) is the effective pulse energy after accounting for optical attenuation, c

is the speed of light (in $\mathrm{m\,s^{-1}}$), A is the receiver aperture (in $\mathrm{m^2}$), $\beta(z)$ is the volume backscatter coefficient (in $\mathrm{m^{-1}\,sr^{-1}}$), and $\sigma(z)$ is the extinction coefficient (in $\mathrm{m^{-1}}$).

The relationship between the backscatter coefficient and extinction coefficient is given by Equation 2.2:

$$\beta(z) = k \cdot \sigma(z) \tag{2.2}$$

Here, k is known as the Lidar Ratio (in $\mathrm{sr^{-1}}$), which depends on atmospheric composition and relative humidity. Under average aerosol-dominated conditions, $k \approx 0.03\,\mathrm{sr^{-1}}$ is typically assumed. This value may decrease to $\sim 0.02\,\mathrm{sr^{-1}}$ in humid environments and increase to $\sim 0.05\,\mathrm{sr^{-1}}$ in dry conditions (Vaisala Oyj, 2024). During precipitation, scattering variability may cause further deviation.

The extinction coefficient is also related to meteorological optical range (MOR) through Koschmieder's law, which under standard atmospheric conditions and a 5% contrast threshold (as defined by the WMO) is given by Equation 2.3:

$$\sigma = \frac{3}{V} \tag{2.3}$$

where V is the MOR in meters. Using this relation, the Ceilometer can estimate vertical visibility from measured extinction profiles. For example, with $k = 0.03\,\mathrm{sr^{-1}}$, a visibility range of 15–150 meters in optically thick clouds corresponds to $\beta(z)$ values between approximately 0.6 and 6 $\mathrm{km^{-1}sr^{-1}}$ (Vaisala Oyj, 2024).

In addition to cloud detection, Ceilometer backscatter profiles are widely used to study the ABL (Münkel et al., 2007). Due to elevated aerosol concentrations in the boundary layer compared to the free troposphere, the backscatter signal typically shows a sharp decrease at the top of the well-mixed layer, enabling estimation of BLH.

In this study, the gradient method (Lo Feudo et al., 2020) is employed for BLH estimation. This method identifies the altitude of the maximum negative gradient in the backscatter profile, representing the transition from the turbulent, aerosol-rich boundary layer to the cleaner free troposphere. The gradient is computed using Equation 2.4:

$$\left.\frac{\partial \beta}{\partial h}\right|_{h_i} = \frac{\beta(h_i + \Delta h) - \beta(h_i - \Delta h)}{2\Delta h} \tag{2.4}$$

where β is the backscattered signal (in $\mathrm{m}^{-1}\,\mathrm{sr}^{-1}$), h_i is the height above the Ceilometer, and Δh is the vertical resolution (10 m). This method is computationally efficient, physically intuitive, and has proven effective in aerosol-rich urban environments, where a distinct gradient often marks the BLH (Caicedo et al., 2017; Haeffelin et al., 2012; Zhang et al., 2022). Figure 2.4 illustrates an example of BLH estimation using this method applied to Ceilometer backscatter data.

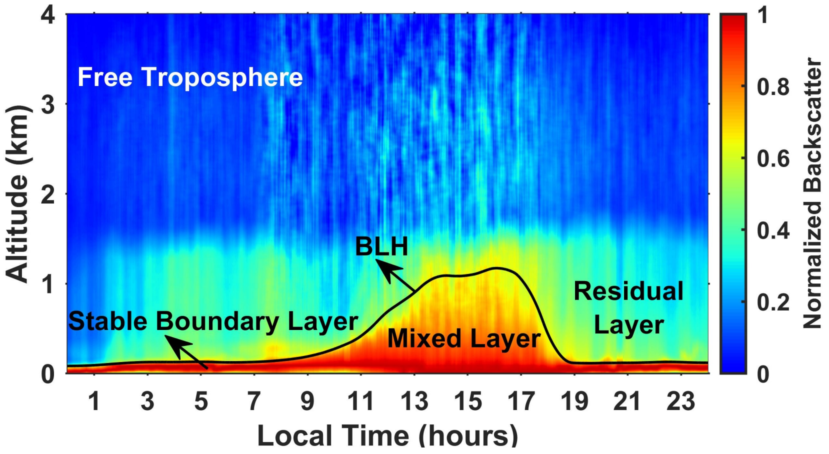

Figure 2.4: Diurnal variation of normalized backscatter from the Ceilometer showing ABL evolution on a clear-sky day. The black line represents the BLH derived using the gradient method overlaid on the backscatter profile.

The Ceilometer Lidar offers a key advantage over traditional profiling instruments due to its high temporal resolution and all-weather autonomous operation, enabling real-time monitoring of diurnal evolution, boundary-layer transitions, and pollutant dispersion. In particular, their utility in urban settings has made them indispensable for understanding pollution dynamics and evaluating model simulations. In this thesis, the Ceilometer Lidar is used to simultaneously retrieve CBH and BLH, forming a core component of the observational framework for characterizing diurnal and seasonal variability in ABL and cloud over semi-arid regions of Western India.

Raman Lidar

The Raman Lidar (RL) system employed in this thesis work utilizes an Nd:YAG laser, which emits linearly polarized pulses at three wavelengths: 1064 nm, 532 nm, and 355 nm. The backscattered signals are received using a high-performance Cassegrain telescope with a 400 mm aperture (Saha et al., 2020, 2021). The detection system is equipped to operate in both analog and photon-counting modes: analog detection is used for capturing strong signals at lower altitudes, while photon-counting mode is optimized for detecting weak backscatter signals from higher altitudes, typically above 8–10 km. The overlap function of the Lidar system reaches full efficiency at approximately 300 m altitude. To enhance signal quality and vertical resolution, data from both detection modes are combined ("glued") during post-processing. Each vertical profile corresponds to an integration time of three minutes. Prior to further analysis, the raw signals are background-subtracted and range-corrected, yielding the Range-Corrected Signal (RCS). Subsequently, the Klett–Fernald inversion algorithm is applied to derive vertical profiles of backscatter and extinction coefficients, assuming the far-end boundary condition (Klett, 1981).

2.2 Radiosonde

Radiosondes are balloon-borne instruments widely used for vertical profiling of the atmosphere. They provide high-resolution, *in-situ* measurements of atmospheric variables such as temperature, pressure, relative humidity, wind speed, and wind direction from the surface up to the lower stratosphere (typically ∼30 km). Radiosonde data play a crucial role in characterizing the thermodynamic structure of the atmosphere and are particularly useful for evaluating ABL properties and cloud formation potential.

In this thesis work, radiosonde data are utilized to:

- Estimate vertical profiles of temperature and humidity to understand atmospheric stability
- Validate the BLH derived using the radiosonde profile with the Lidar-derived BLH (Figure 2.5a)
- Derive thermodynamic parameters such as LCL (Figure 2.5b)

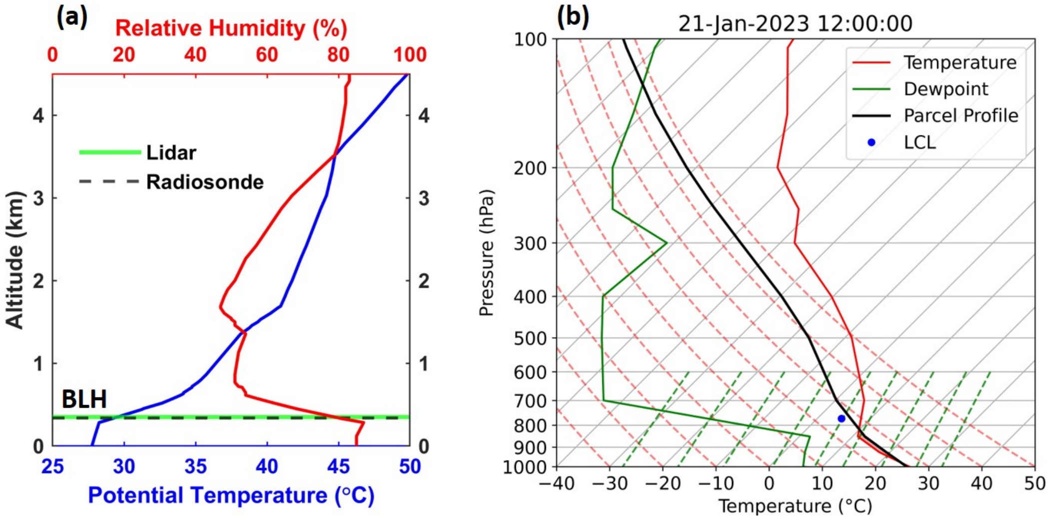

Figure 2.5: (a) Comparison of BLH derived from vertical profiles of potential temperature (blue) and relative humidity (red) with Ceilometer Lidar observation. (b) Skew-T log-p diagram showing the LCL (blue dot) over Ahmedabad.

The vertical profiles of meteorological parameters are obtained from radiosonde observations conducted by the India Meteorological Department (IMD). The IMD employs GPS-based radiosonde systems, which are automated, portable, and designed for ease of operation and maintenance (Ansari et al., 2015).

In this thesis, the radiosonde data for the Ahmedabad and Delhi regions are utilized. The radiosondes are launched twice daily at 0000 UTC and 1200 UTC from Ahmedabad airport (23.07° N, 72.63° E), which is located approximately 13 km from the Ceilometer Lidar site at the Physical Research Laboratory. Similarly, the radiosondes are launched twice daily at 0000 UTC and 1200 UTC from the Safdarjung Airport site (28.58° N, 77.20° E), located approximately 7 km from the Delhi Earth Station, where the Ceilometer Lidar operates.

2.3 Satellites

Satellite-based remote sensing provides large-scale, continuous observations of atmospheric parameters that are critical for analyzing cloud properties, radiation budget, aerosol concentrations, and surface conditions (Kaufman et al., 2002; King et al., 2003; Stephens and Kummerow, 2007). These datasets offer valuable spatial and temporal coverage, especially over regions with sparse *in situ* observations. In this study, satellite datasets were employed to complement ground-based and radiosonde measurements, particularly for assessing spatiotemporal cloud occurrence, cloud top properties, and their interactions with boundary layer dynamics. Cloud properties from satellites are primarily derived using measurements of radiance in the thermal infrared spectrum and reflectance in the visible and near-infrared bands.

Figure 2.6 illustrates the use of radiance and reflectance in deriving satellite-based cloud properties and shows a sample MODIS-derived cloud top height (CTH) over India. Thermal infrared radiance is used to estimate CTT, which can be converted to CTH by referencing atmospheric temperature profiles (e.g., from radiosondes or reanalysis). Meanwhile, visible and near-infrared reflectance data are used to infer COT and cloud phase, based on how clouds scatter and absorb solar radiation. The intensity and spectral distribution of the reflected sunlight vary with cloud type, droplet size, and optical depth, enabling the retrieval of microphysical cloud properties. In this study, INSAT-3D/3DR geostationary observations and MODIS polar-orbiting products have been employed for analyzing cloud characteristics over the study region. A detailed discussion on these datasets, including their specifications and applications, is given below.

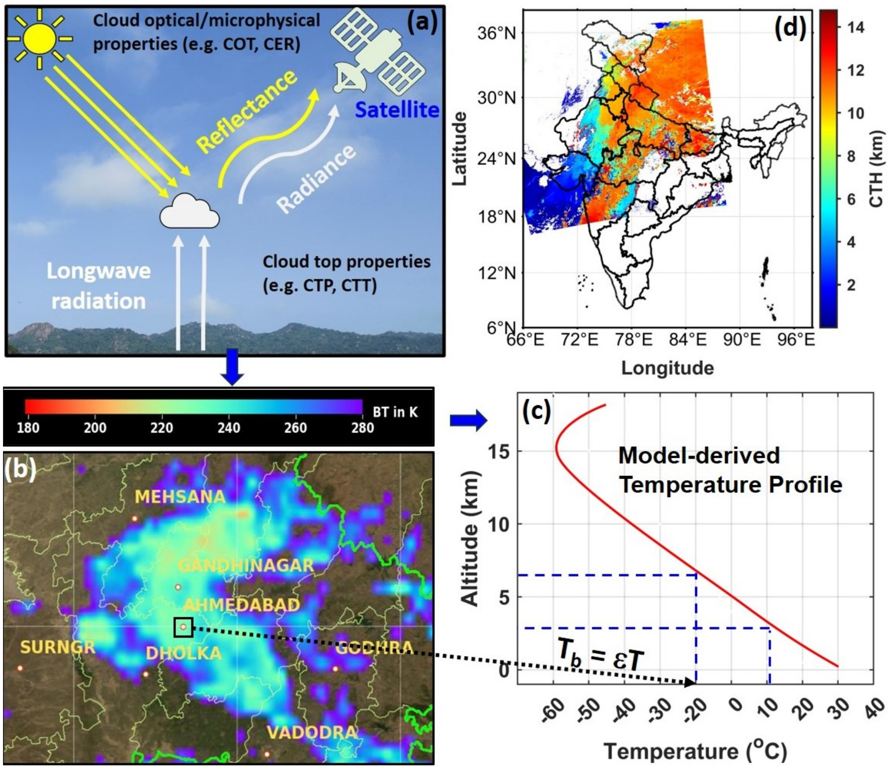

Figure 2.6: (a) Schematic showing satellite-based remote sensing of cloud properties. (b) Brightness temperature map around Ahmedabad and nearby regions. (c) CTH retrieval using the model-derived atmospheric temperature profile by matching observed brightness temperature. (d) Spatial distribution of CTH over India from MODIS.

2.3.1 INSAT 3D/3DR

INSAT-3D and 3DR, part of the *Indian National Satellite System* (INSAT), are geostationary satellites launched by the Indian Space Research Organization (ISRO) on 26 July 2013 and 8 September 2016, respectively (Kumar et al., 2022). These satellites offer continuous, high-temporal-resolution monitoring of atmospheric conditions over the Indian subcontinent (Gopikrishnan et al., 2023). Both satellites are positioned in geostationary orbits at an altitude of approximately 35,786 km, with INSAT-3DR stationed at 74°E and INSAT-3D at 82°E longitude. They carry two instruments: a 6-channel imager and a 19-channel sounder (18 infrared + 1 visible) for meteorological observations and disaster management (Kumar et al., 2022). The 6-channel imager operates in the following spectral bands: Visible (VIS, 0.52–0.72 µm), Short Wave Infrared (SWIR, 1.55–1.70 µm), Mid Wave Infrared (MWIR, 3.80–4.00 µm), Water

Vapor (WV, 6.50–7.00 µm), Thermal Infrared 1 (TIR1, 10.2–11.2 µm), and Thermal Infrared 2 (TIR2, 11.5–12.5 µm). The corresponding spatial resolutions are: 1 km for VIS and SWIR, 4 km for MWIR, 8 km for WV, and 4 km for both TIR-1 and TIR-2. The cloud products from INSAT-3D are available at a temporal resolution of 30 minutes, offering more frequent observations compared to polar-orbiting satellites like MODIS Terra and Aqua. However, the relatively coarse spatial resolution (4–8 km) limits its ability to detect small-scale clouds and fine atmospheric features.

In this thesis, the INSAT-3D/3DR imager brightness temperature data and cloud mask product with 4 km spatial resolution are used to investigate cloud cover over the Western-Indian region (Figure 2.7a). The study also utilizes the fog products from INSAT-3D and 3DR over the Western Indian region (Figure 2.7b). The key specifications of the fog product from these satellites are listed in Table 2.1.

Table 2.1: Key specifications of INSAT-3D and 3DR fog product

Parameters	**Value**
Spatial resolution	$\sim$4 km
Temporal resolution	30 minutes, 15 minutes (combined operation of INSAT-3D with INSAT-3DR)
Instrument used	Six-channel Imager
Key channels for fog detection	TIR-1 ($\sim$11 µm), MIR (3.9 µm), and Visible (0.65 µm)
Nighttime fog detection method	Brightness temperature difference between the TIR-1 and MIR channels (Hunt, 1973)
Daytime fog detection method	Reflectance (visible) combined with TIR-1 temperature (d'Entremont and Gustafson, 2003)

The INSAT-3D and INSAT-3DR satellites play a critical role in monitoring fog events due to their high temporal resolution and broad spatial coverage. The fog product from these satellites is particularly effective for detecting nighttime fog development. Compared to polar-orbiting satellites with limited revisit times or sparse ground-based visibility data, the INSAT-3D and 3DR provide significant advantages. With observations available every 30 minutes, these satellites enable precise tracking of fog initiation, evolution, and dissipation. Additionally, the broad spatial coverage helps to capture regional fog patterns and transport mechanisms, which is not possible through point-based measurements alone.

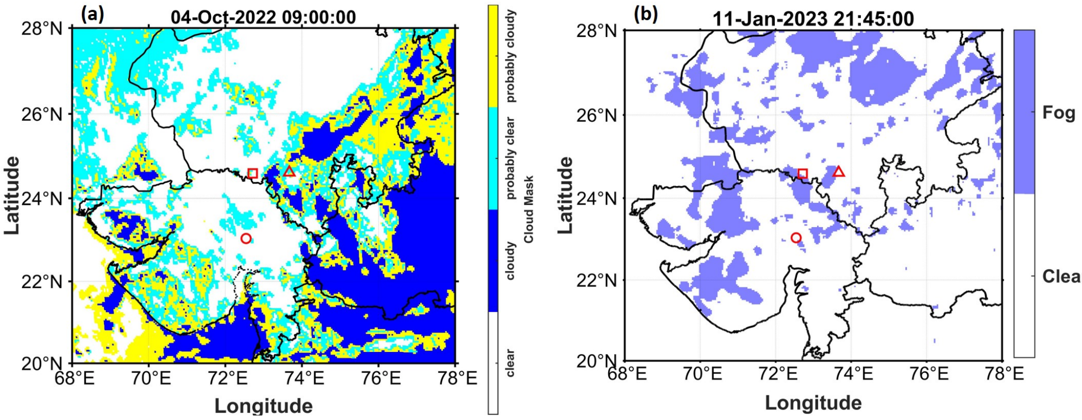

Figure 2.7: (a) Cloud mask over the Western Indian region obtained from INSAT-3D on 04 October 2022 at 09:00 IST. (b) Fog mask Western Indian region obtained from INSAT-3DR on 11 January 2023 at 21:45 IST, indicating fog-affected and clear regions. Red markers (circle, square, and triangle) denote Ahmedabad, Mt. Abu, and Udaipur, respectively.

2.3.2 MODIS

The *Moderate Resolution Imaging Spectroradiometer* (MODIS) is one of the five instruments aboard the Terra and Aqua satellites, which were launched in December 1999 and May 2002, respectively. These satellites operate in near-polar, sun-synchronous orbits at an altitude of approximately 705 km, and provide extensive land, ocean, and atmospheric data (Platnick et al., 2003). Terra observes the Earth during its descending node at 10:30 am, while Aqua does so during its ascending node at 1:30 pm. The MODIS instrument captures the entire Earth every 1–2 days in 36 spectral bands ranging from 0.4 µm to 14.4 µm, facilitating comprehensive studies of terrestrial, oceanic, and atmospheric phenomena. Further information about MODIS is available at https://modis.gsfc.nasa.gov/.

This thesis utilizes the MODIS/Aqua Level-2 cloud properties dataset (L2 5-Min Swath 1 km) to examine cloud characteristics over the Western-Indian region. The MODIS surface reflectance datasets (Liang et al., 2002) are also used to study dust storms in the same region.

2.3.3 VIIRS

The *Visible Infrared Imaging Radiometer Suite* (VIIRS) is onboard two satellites: the NASA *Suomi National Polar-orbiting Partnership* (SNPP) satellite and the *National Oceanic and Atmospheric Administration*-20 (NOAA-20) satellite. The SNPP satellite was launched in 2011, and the NOAA-20 satellite was launched in 2017. Both satellites circle the Earth in the same orbit but are separated in space and time by approximately 50 minutes (Cao et al., 2018). VIIRS is a visible and infrared radiometer comprising 22 spectral bands ranging from 0.41 µm to 12.5 µm, divided into 16 moderate-resolution and 5 imaging-resolution bands (Chen et al., 2021). The spatial resolution of VIIRS is 375 m for imaging bands and 750 m for radiometric bands. This thesis uses cloud properties derived from VIIRS onboard the SNPP and NOAA-20 satellites to study cloud characteristics over the region of interest.

2.4 Reanalysis datasets

Model-generated reanalysis datasets provide consistent, gridded representations of atmospheric variables by assimilating observations into numerical weather prediction (NWP) models. These datasets are particularly useful for filling observational gaps and for studying long-term trends in meteorological and chemical parameters. In this study, two state-of-the-art reanalysis products were utilized: ERA5, produced by the European Centre for Medium-Range Weather Forecasts (ECMWF), and CAMS, developed under the Copernicus Atmospheric Monitoring Service. ECMWF reanalysis products are specifically selected because they offer high spatial and temporal resolution, long-term continuity, and an advanced data-assimilation framework that integrates diverse global observations. These characteristics ensure physically consistent, high-quality atmospheric fields that are widely validated and extensively used in boundary-layer, cloud, and aerosol research. Consequently, these datasets serve as important complementary tools to ground-based, radiosonde, and satellite observations, especially for evaluating ABL characteristics, aerosol concentrations, and the large-scale meteorological conditions influencing cloud formation.

2.4.1 ERA5 reanalysis

The ECMWF is a leading organization in numerical weather prediction and climate modeling, known for producing high-resolution global datasets covering the land surface, atmosphere, and oceans. These datasets support a wide range of applications, from operational forecasting to climate research and policy development. One of ECMWF's most significant contributions to the climate science community is its suite of reanalysis products, which systematically assimilate historical observational data into a consistent modeling framework to reconstruct past atmospheric states. The ERA5 reanalysis, developed under the Copernicus Climate Change Service (C3S), represents the fifth generation of ECMWF's global atmospheric reanalysis (Hersbach et al., 2020). It offers hourly estimates of a broad spectrum of atmospheric, land, and oceanic variables, globally and continuously. ERA5 achieves high spatial resolution, with a horizontal grid of $0.25^\circ \times 0.25^\circ$, and employs 137 vertical model levels extending from the surface to the top of the stratosphere ($\sim$0.01 hPa). Its improvements over previous reanalyses include enhanced data assimilation techniques, better representation of physical processes, and a more extensive use of satellite observations. The ERA5 system blends short-range forecasts from ECMWF's Integrated Forecasting System (IFS) with a wide range of observations, including satellite radiances, ground-based measurements, radiosondes, and aircraft reports, to generate a physically consistent, gridded dataset. These data are freely available through the Climate Data Store (CDS) platform: `https://cds.climate.copernicus.eu`, facilitating widespread use across scientific disciplines.

In this thesis, ERA5 data were utilized to derive several key atmospheric parameters relevant to cloud and boundary layer analysis. Specifically, variables such as cloud cover fraction, CBH, BLH, temperature, surface heat fluxes, and specific/relative humidity at multiple pressure levels were employed. Both single-level and multi-level (pressure level) data ARE incorporated to analyze surface conditions and vertical atmospheric structure, respectively. These products are further processed to derive spatiotemporal patterns of cloud occurrence and to characterize the ABL dynamics across the study regions.

2.4.2 CAMS reanalysis

The ECMWF Atmospheric Composition Reanalysis 4 (EAC4), widely known as the *Copernicus Atmosphere Monitoring Service* (CAMS) reanalysis, represents the fourth and most advanced global reanalysis dataset dedicated to atmospheric composition (Inness et al., 2019). Developed by ECMWF under the Copernicus programme funded by the European Union, CAMS reanalysis provides comprehensive information on aerosols, greenhouse gases, and reactive trace gases by assimilating both satellite observations and ground-based measurements into a global chemistry transport model. CAMS reanalysis is particularly valuable for monitoring and assessing air quality over regions where direct observational data are sparse or unavailable, especially in developing countries or remote areas where ground-based stations are limited. The dataset combines satellite retrievals from instruments such as MODIS, MISR, and IASI with model simulations to produce physically consistent fields of atmospheric constituents. As a result, CAMS offers spatially continuous global coverage, ensuring reliable estimations of aerosol and pollutant concentrations at each grid point. The CAMS reanalysis is provided at a horizontal resolution of $0.75^\circ \times 0.75^\circ$, with a temporal resolution of 3 hours, making it well-suited for both climatological assessments and short-term case studies. CAMS data include a wide range of species such as $PM_{2.5}$, PM_{10}, Aerosol Optical Depth (AOD), ozone, nitrogen dioxide (NO_2), carbon monoxide (CO), and sulphur dioxide (SO_2), among others. The model also categorizes aerosols into different types (e.g., sea salt, dust, organic matter, black carbon), enabling detailed studies of aerosol sources and transport. Recent studies have validated the accuracy and consistency of CAMS aerosol products over various regions of the world (Gueymard and Yang, 2020; Salamalikis et al., 2021). In this thesis, CAMS reanalysis data were used to obtain both hourly and monthly mean concentrations of key aerosol parameters, including $PM_{2.5}$, PM_{10}, and AOD, over the selected study regions. These parameters were further analyzed to examine the spatiotemporal variability of aerosol loading and its potential interactions with cloud properties and boundary layer dynamics. The integration of CAMS data thus provided a valuable complement to satellite observations and ground-based measurements, enabling a more comprehensive understanding of the regional aerosol environment.

****

Chapter 3

Spatial and Temporal Characteristics of Clouds and ABL over Western India

Clouds and the ABL are among the most dynamic and influential components of the Earth's atmosphere. Together, they govern a multitude of processes, from regulating Earth's radiation budget and influencing local weather to modulating global climate feedbacks and hydrological cycles (Arking, 1991; Ramanathan et al., 1989; Randall and Tjemkes, 1991; Stubenrauch et al., 2013). Cloud properties such as CBH, CTH, cloud fraction, and vertical layer structure significantly affect the radiative balance, atmospheric circulations, and other meteorological processes (Lü et al., 2015; Samanta et al., 2020). The spatial and temporal variability of clouds and the ABL plays a critical role in shaping atmospheric thermodynamics, surface energy balance, precipitation formation, and pollutant dispersion. Given their dynamic nature in space and time, accurately representing clouds and ABL in weather and climate models poses significant challenges. Improper representation of these parameters introduces uncertainty in models, making it difficult to accurately predict future weather and climate. Therefore, continuous monitoring and investigation of clouds and ABL are essential for climate diagnosis and forecasting.

Clouds, covering nearly two-thirds of the Earth's surface (King et al., 2013), have significant radiative impacts depending on their type, height, thickness, and microphysical composition. High-level clouds tend to trap outgoing longwave radiation, contributing to a warming effect, while low-level clouds primarily reflect incoming solar radiation, leading to a cooling effect (Stephens and Webster, 1981). The net cloud radiative forcing thus depends on the cloud vertical structure and layering, which vary regionally and seasonally. Accurate quantification of CBH, CTH, and cloud fraction is essential for determining their radiative impacts. However, a persistent challenge in both weather and climate modeling is the poor representation of cloud properties, especially in regions where *in situ* observations are sparse (Bony et al., 2015; Randall et al., 2003).

The ABL, typically extending from the surface up to 1-2 km during daytime, serves as a crucial zone for momentum, energy, moisture, and aerosol exchanges between the surface and the free atmosphere (Stull, 2012). The ABL exhibits pronounced diurnal variability, with strong convective mixing during the day and a stable stratified layer at night. Its structure and evolution are influenced by surface heating, topography, vegetation cover, and cloud radiative feedback. Clouds forming within or just above the boundary layer, particularly stratiform and cumulus clouds, can significantly alter its growth and mixing processes (Stull, 1988). In turn, the height and thermodynamic properties of the ABL affect the development and type of clouds, making cloud and ABL interactions a tightly coupled system.

Over India, significant attention has been devoted to examining the variability of cloud cover and rainfall across various regions, such as the Indo-Gangetic plains, the Arabian Sea coast, and others (Fukushima et al., 2019; Guhathakurta and Revadekar, 2017; Jaswal et al., 2017; Kishore et al., 2016; Kumar et al., 2010b; Roy and Balling, 2005). However, localized studies over regions with complex topography and semi-arid climate, such as Western India, remain limited. This region presents unique challenges and opportunities due to its diverse physiographic features, including urban landscapes (e.g., Ahmedabad), semi-urban lake-dominated terrain (e.g., Udaipur), and elevated mountainous zones (e.g., Mt. Abu). Such diversity induces mesoscale circulations and land–atmosphere interactions that significantly modulate cloud formation and ABL dynamics. Yet, due to a lack of sustained, high-resolution observations, the understanding of clouds and ABL processes in this region remains inadequate.

Satellite-based sensors offer broad spatial coverage but are often limited in their ability to resolve low- and mid-level cloud layers, particularly under multilayer or broken cloud conditions. Ground-based active remote sensing instruments such as Ceilometer Lidar offer a powerful complement, providing continuous, high-resolution vertical profiles of CBH and aerosol backscatter, essential for monitoring both cloud evolution and boundary layer height. Representative examples of such observations over Ahmedabad, Mt. Abu, and Udaipur are shown in Figure 3.1.

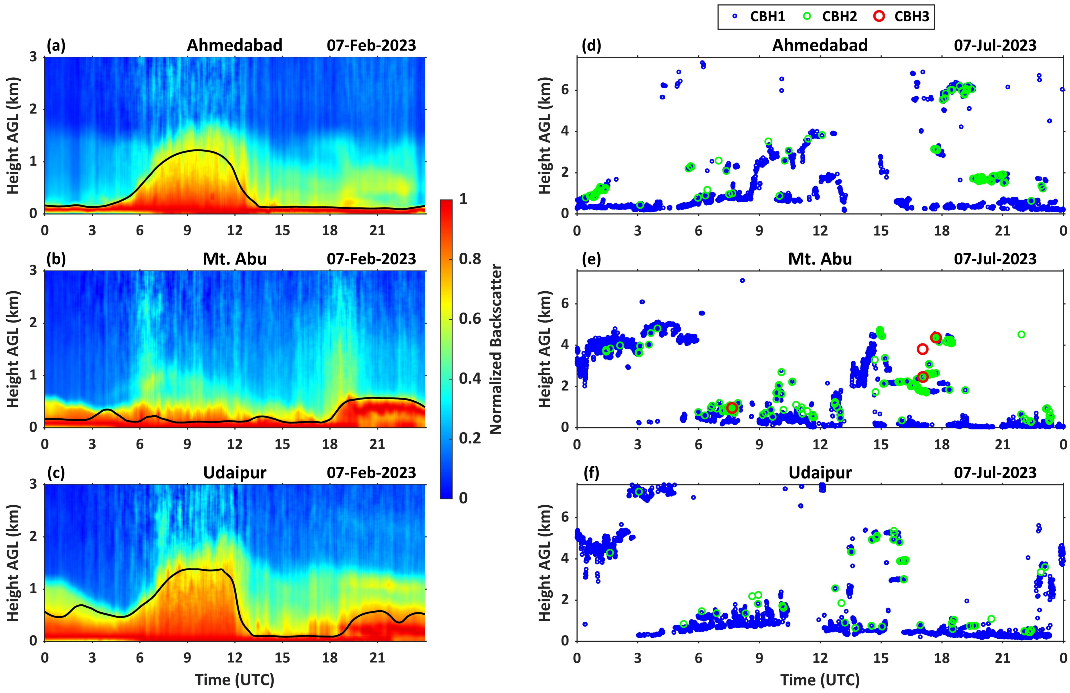

Figure 3.1: Representative examples of ABL and cloud observations over Ahmedabad, Mt. Abu, and Udaipur. Panels (a–c) depict the diurnal evolution of the ABL on 07 February 2023, while panels (d–f) illustrate the variation in cloud base heights (CBH1, CBH2, CBH3) on 07 July 2023, highlighting the contrasting conditions across the three sites.

This chapter presents a comprehensive investigation of the spatial and temporal characteristics of clouds and the boundary layer over three climatically distinct regions of western India, Ahmedabad, Udaipur, and Mt. Abu, representing a continuum from lowland urban environments to high-altitude, forested terrain. The study integrates multi-source datasets including ground-based Lidar measurements, satellite-derived cloud products, and reanalysis outputs to explore cloud frequency, vertical layering, seasonal variability, and clouds and ABL coupling.

3.1 Cloud characteristics over Udaipur

This section presents an analysis of cloud occurrence and layering over Udaipur during 2021–2022 using ground-based Ceilometer Lidar observations. The backscatter from the Ceilometer is used to classify the sky conditions into single- and multi-layer categories, as well as "no cloud" and "full obscuration" cases. Full obscuration refers to conditions where the sky is obscured by haze, fog, dust, smoke, or rain. Figure 3.2 presents the monthly occurrence frequencies of one-, two-, and three-layer clouds, along with full obscuration. The occurrence frequency for a given cloud layer is defined as the ratio of the number of observations containing that layer to the total number of valid observations. "Total Detection" refers to all instances when either clouds or full obscuration were present. During the observation period, total detection was approximately 31%, with cloud frequency (at least one cloud layer) at about 27% and full obscuration at about 4%. Among the total cloud occurrences, single-layer, double-layer, and triple-layer clouds accounted for approximately 26.3%, 0.61%, and 0.006%, respectively.

As shown in Figure 3.2a, single-layer clouds were observed year-round and dominated the total cloud occurrences, with peaks in March and November. The highest frequencies were recorded during the monsoon, reaching approximately 33%, 75%, 64%, and 36% in June, July, August, and September, respectively. Full obscuration was most frequent in winter, particularly in December ($\sim$ 13%), mainly due to fog formation facilitated by local water bodies such as Fateh Sagar Lake ($\sim$ 4 km^2). During the monsoon, full obscuration primarily resulted from rainfall, with frequencies of approximately 10%, 2%, 4.6%, and 1.1% in June through September, respectively. The minimum total detection was found in February ($\sim 8\%$) and March ($\sim 9\%$), while November showed the lowest ($\sim 2\%$), reflecting mostly clear skies.

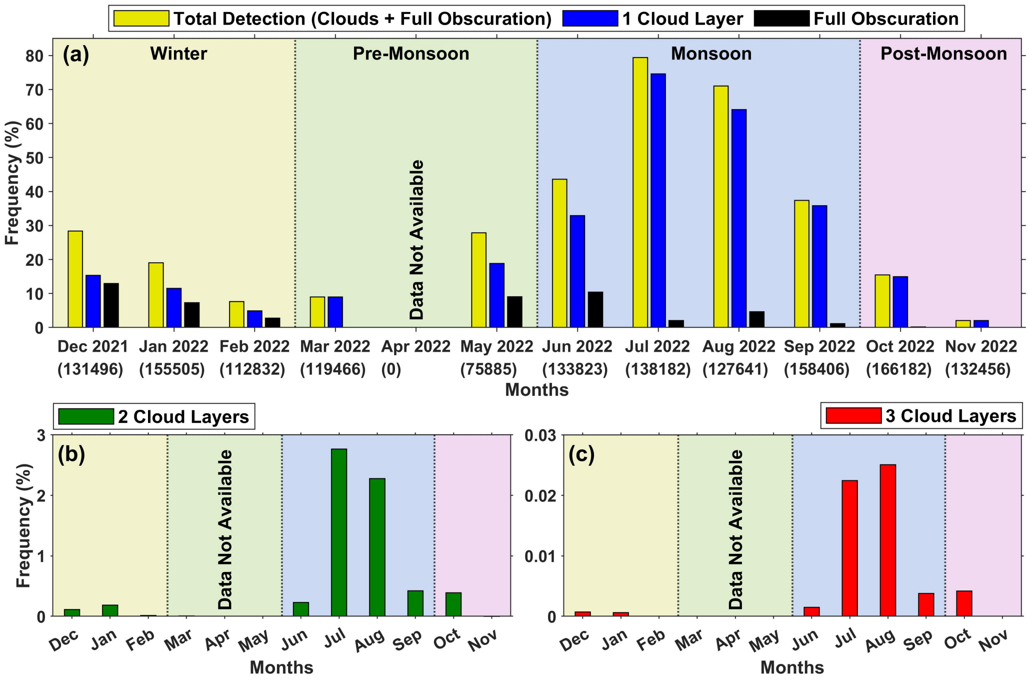

Figure 3.2: (a) Monthly total detection (clouds + full obscuration), frequency of single-layer clouds, and full obscuration (fog, haze, rain, etc.) over Udaipur during 2021-2022. The number in brackets below each month's name indicates the total number of observations from the Ceilometer. (b) Frequency of two-layer clouds. (c) Frequency of three-layer clouds.

Multi-layer clouds occurred primarily during the monsoon season. Double-layer clouds (Figure 3.2b) were most common in July ($\sim 2.7\%$) and August ($\sim 2.2\%$), while triple-layer clouds (Figure 3.2c) were rare, appearing mainly in July ($\sim 0.022\%$) and August ($\sim 0.025\%$). Triple-layer clouds were absent in February, March, May, and November. The overall occurrence of multi-layer clouds in Udaipur was lower than reported for other tropical locations in India. For example, Narendra Reddy et al. (2018) observed multi-layer clouds in all seasons over Gadanki (13.45° N, 79.16° E), with a monsoon maximum. Similarly, Vaishnav et al. (2019) reported peak double-layer occurrence during pre- and post-monsoon periods, and triple-layer peaks during the monsoon, over Ahmedabad.

In addition to cloud occurrence and layering, the CBH is a fundamental property influencing the Earth's radiation balance. The variation in CBH directly affects the amount of shortwave radiation reaching the surface and the longwave radiation emitted back into space. Thick, low-level clouds typically have a cooling effect by reducing incoming shortwave radiation and enhancing the loss of longwave radiation compared to clear-sky conditions (Lee et al., 2001). In contrast, thin, high-level clouds generally contribute to atmospheric warming by increasing downward shortwave radiation and reducing upward longwave radiation (Slingo and Slingo, 1988). Consequently, variations in CBH have notable implications for the radiation budget and, therefore, the climate system.

Figure 3.3 illustrates the monthly statistics of the lowest cloud base height (CBH1) over Udaipur during 2021–2022. During the monsoon season, average CBH1 remains below 4 km, with the lowest values recorded in August. Specifically, the average CBH1 values are approximately 3.4 km, 1.8 km, 1.4 km, and 3.1 km in June, July, August, and September, respectively. In contrast, CBH1 frequently exceeds 5 km during March and May, reflecting a predominance of high-level clouds in these months. Outliers in CBH1 are most prominent in May, July, and August, while no significant outliers are observed in January, March, June, September, and October. The inter-quartile range (IQR) also displays notable seasonal variability, ranging from about 4 km in June to just 0.5 km in May.

The probability distribution of CBH across different altitude ranges reveals distinct patterns for the three cloud layers. CBH1 occurs most frequently below 1 km, whereas CBH2 and CBH3 are most common between 1–2 km. Above 1 km, the occurrence of CBH2 decreases steadily with height, while CBH3 is mainly concentrated within 1–4 km and is not observed above 7 km. Analysis of diurnal variation shows that the frequency of total cloud occurrence and the first cloud layer remains steady at around 4% throughout both day and night, indicating a uniform distribution over the 24-hour cycle. The double-layer clouds are more frequent during nighttime, particularly

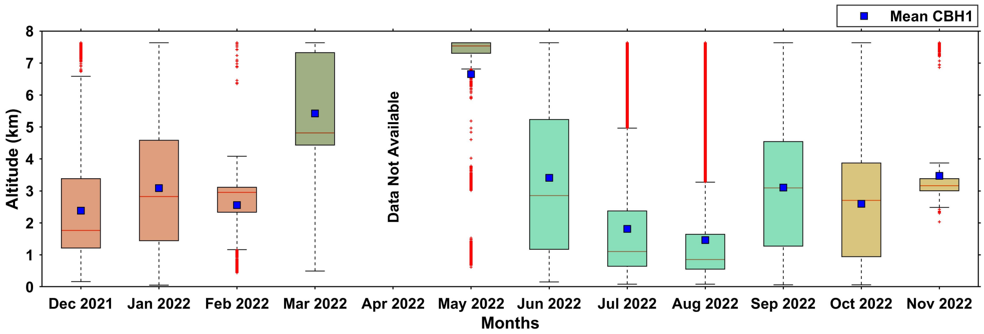

Figure 3.3: Box plot showing CBH1 observed over Udaipur using Ceilometer during 2021-2022. The blue squares in each box represent the average value, the central line is the median, the edges indicate the 25th and 75th percentile values, and the red '+' symbol represents outliers. Whiskers are drawn at 1.5 times the Inter Quartile Range (IQR).

between 22:00 LT and 05:00 LT, while the triple-layer clouds show peaks during early morning, midday, and evening hours. Sky obscuration is also more prevalent at night compared to daytime.

Cloud top properties over Udaipur for 2021–2022 were examined using 735 MODIS observations, of which 270 reported CTH. Most clouds occurred during the monsoon season, with CTH ranging from ∼0.2 km to 16 km. About 14% of clouds were between 0–2 km, 25% between 2–6 km, and 61% above 6 km. For 102 cases, cloud top pressure and cloud optical thickness data enabled classification into nine cloud types based on the ISCCP scheme. Cirrostratus clouds were most frequent (36%), while stratus (<1%) and altocumulus (2%) were rare. Cumulonimbus, altostratus, and cirrus occurred 13%, 17%, and 10% of the time, respectively.

Cloud top properties retrieved from MODIS were used to estimate the CBH. The CBH was calculated using the CTH and cloud geometrical thickness (CGT), where CGT is determined by the microphysical characteristics of the cloud (Seaman et al., 2017):

$$\mathrm{CBH} = \mathrm{CTH} - \mathrm{CGT} \tag{3.1}$$

For liquid-phase clouds, CGT is derived as:

$$\text{CGT} = \frac{\text{LWP}}{\text{LWC}} \tag{3.2}$$

Here, LWP (liquid water path) is a function of COT and CER (Liou, 1992), while LWC (liquid water content) varies by cloud type. In this study, MODIS/Aqua Level-2 cloud property products at 1 km spatial resolution were used. CBH was computed by first classifying clouds using the ISCCP cloud classification scheme, based on cloud top pressure and cloud optical thickness. The LWC values prescribed for each cloud type by ISCCP were then applied to determine CGT (Equation 3.2), followed by CBH estimation (Equation 3.1).

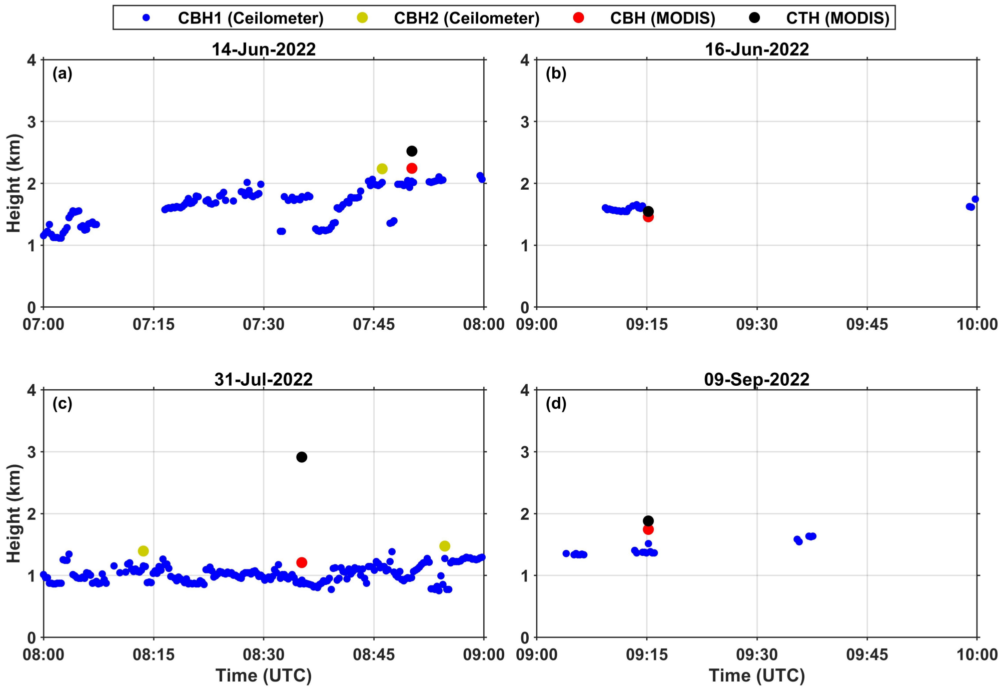

Figure 3.4: MODIS-derived CTH and CBH for low-level clouds compared with the Ceilometer observed CBH over the Udaipur region.

The CBH retrieval from MODIS has certain limitations. It is restricted to daytime observations, as cloud optical thickness and effective radius are derived from sunlight reflected by clouds. Additionally, the algorithm assumes a constant LWC throughout the vertical extent of the cloud (Hutchison, 2002). For direct comparison, the MODIS pixel closest to the Ceilometer site was used for all matched observations in this study. For low-level clouds (below 2 km), the CBH estimates from MODIS show close agreement with ground-based observations (Figure 3.4). In contrast, for clouds above 2 km, the differences between the two measurements become more substantial, indicating that the algorithm exhibits better performance for low-level, optically thick clouds.

This study also evaluates the performance of ERA5 in estimating CBH over the Udaipur region by comparing it with ground-based Ceilometer observations. Since the Ceilometer's vertical detection range is limited to approximately 7.6 km, the analysis is restricted to clouds below this altitude. A total of 3,236 hourly cloud observations from both datasets were analyzed. The Ceilometer detected clouds in 2,844 cases, while ERA5 detected clouds in 2,704 cases. Table 3.1 summarizes the detection statistics. ERA5's detection efficiency, defined as the percentage of cases where ERA5 identified clouds also observed by the Ceilometer, was about 76.42%. In 11.46% of the cases, ERA5 failed to detect clouds present in Ceilometer data.

ERA5 shows a tendency to underestimate mid- and high-level clouds during the monsoon season. Such discrepancies are partly due to the parameterization schemes and coarse spatial resolution of the reanalysis model. Previous studies (Kundu et al., 2023; Wang et al., 2022; Yao et al., 2020a) have reported similar limitations, noting that cloud properties in reanalysis datasets are often parameterized due to the difficulty of assimilating cloud observations (Yao et al., 2020b). These biases introduce uncertainties into weather and climate simulations (Wu et al., 2024), highlighting the importance of continued evaluation and improvement of reanalysis products.

3.2 Cloud characteristics over Mt. Abu

The monthly cloud occurrence over the Mt. Abu region during 2023, as observed by the Ceilometer Lidar, is summarized in Figure 3.5. Data availability exceeded 40% for most months, except in September and October, when power failures and instrument servicing led to significant gaps (Figure 3.5a). In 2023, the total cloud

Table 3.1: Cloud representation by Ceilometer and ERA5 over Udaipur during December 2021 to November 2022.

S.no.	**Ceilometer**	**ERA5**	**Percentage (%)**
1	Cloud detected (Yes)	Cloud detected (No)	11.46
2	Cloud detected (Yes)	Cloud detected (Yes)	76.42
3	Cloud detected (No)	Cloud detected (Yes)	7.14
4	Cloud detected (No)	Cloud detected (No)	4.98

occurrence over Mt. Abu was 22.88%, comprising 22.46% single-layer clouds, 0.42% double-layer clouds, and 0.0021% triple-layer clouds. The full sky obscuration, caused by fog, haze, dust, or rainfall, accounted for 8.67% of observations. As discussed in the previous section, Udaipur experienced a total cloud occurrence of about 27% annually, with an obscured sky frequency of approximately 4%. Although Mt. Abu and Udaipur, both situated in the Aravalli Range of Western India, exhibit similar annual cloud detection rates, Mt. Abu experiences more frequent sky obscuration due to higher rainfall and mist. In contrast, Udaipur records a higher proportion of multi-layer clouds, suggesting stronger vertical wind shear in that region.

Over the Mt. Abu region, cloud frequency peaks during the southwesterly monsoon months, June (35.43%), July (53.94%), August (56.27%), and September (25.84%). The seasonal mean cloud occurrence is 4.1% in winter (December–February), 19.25% in the pre-monsoon (March–April), 42.88% in the monsoon (June–September), and 7.28% in the post-monsoon (October–November). Layer-wise monthly analysis indicates that single-layer clouds dominate year-round (Figure 3.5c). Double-layer clouds are primarily associated with the monsoon season, with minimal occurrences in other months (Figure 3.5d). Triple-layer clouds were detected only in March, June, July, and August, with monthly frequencies ranging from 0–1.49% for double layers and 0–0.01% for triple layers (Figure 3.5e).

Figure 3.6 illustrates the diurnal variation of cloud occurrence frequency over

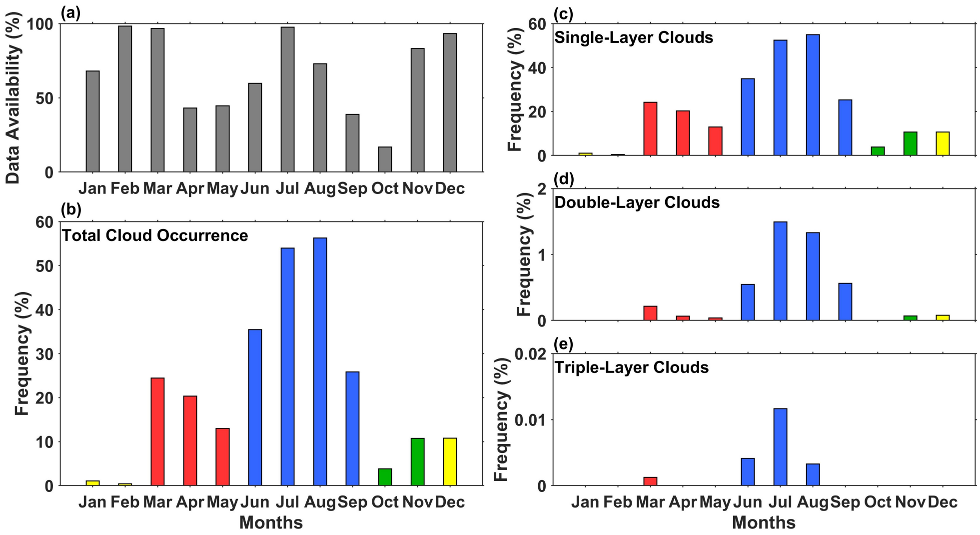

Figure 3.5: (a) Monthly data availability from Ceilometer Lidar over Mt. Abu during 2023. (b) Total cloud occurrence observed during different months. The frequency of single, double, and triple-layer clouds is shown in (c), (d), and (e), respectively. The yellow, red, blue, and green bars represent the winter, pre-monsoon, monsoon, and post-monsoon seasons.

Mt. Abu during 2023, as derived from the Ceilometer Lidar. A pronounced enhancement is observed during the monsoon months (June–September), particularly between 11:00 and 17:00 local time, indicating a strong diurnal pattern (Figure 3.6a). Cloud occurrence frequency peaks in the afternoon, especially in July and August, when values often exceed 60–80%, reflecting abundant moisture availability during the monsoon season. Morning and evening hours exhibit comparatively lower frequencies, while nocturnal cloudiness remains limited outside the monsoon months. Figure 3.6b further quantifies these seasonal patterns. During the monsoon season (blue bars), a distinct diurnal cycle emerges, with cloud frequency peaking between 13:00 and 15:00 local time, surpassing 60%, and remaining elevated during daylight hours (06:00–18:00). This behavior reflects the influence of convective processes enhanced by solar heating, topographic lifting, and mesoscale circulations, which are characteristic of mountainous regions like Mt. Abu. The elevated terrain likely promotes earlier initiation and sustained convective activity compared to the surrounding plains.

In contrast, the pre-monsoon (green bars) and post-monsoon (red bars) seasons exhibit moderate daytime cloud development with smaller amplitudes, peaking around midday but rarely exceeding 25%. These conditions suggest localized convection under transitional atmospheric regimes, with occasional moisture influx, particularly during April and November. Winter months (yellow bars) show minimal diurnal variation, with cloud frequencies remaining below 10% throughout the day, indicative of predominantly clear-sky conditions governed by synoptic-scale subsidence and a dry, stable boundary layer that inhibits vertical cloud growth. A slight nocturnal to early-morning enhancement may be associated with fog, low stratus, or haze layers formed under radiative cooling.

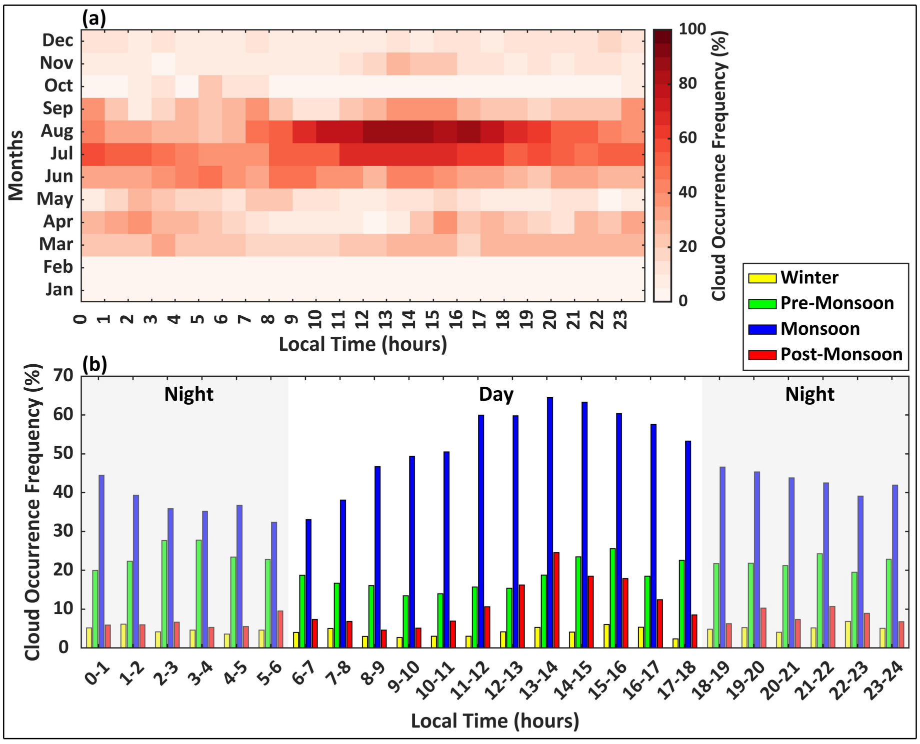

Figure 3.6: (a) Diurnal variation of cloud occurrence frequency over Mt. Abu during January to December 2023. (b) Mean diurnal variation of cloud occurrence frequency (%) during different seasons—winter (yellow), pre-monsoon (green), monsoon (blue), and post-monsoon (red).

The monthly and seasonal statistics of CBH over the Mt. Abu region from January to December 2023, derived from Ceilometer observations are presented in Figure 3.7.

The monthly box plots, with mean CBH indicated by cyan markers, reveal distinct seasonal variations. During the monsoon months (June, July, August, and September), CBH values drop markedly, with mean heights of 1000 ± 1720 m, 880 ± 1470 m, 360 ± 620 m, and 1610 ± 1710 m, respectively, reflecting the prevalence of low-level clouds over Mt. Abu. Similar dominance of low-level clouds during the monsoon in mountainous regions has been documented in earlier studies (Konwar et al., 2014; Kumar et al., 2014; Varghese et al., 2021). The low-level winds during this season predominantly flow perpendicular to the orographic alignment, forcing moisture-laden air to ascend over the mountains and generating vertical motion conducive to cloud formation and precipitation (Houze Jr., 2012; Kumar and Bhat, 2017). The frequent occurrence of outliers during these months indicates the coexistence of deep convective and stratiform cloud layers, suggesting a high prevalence of multilayered cloud structures.

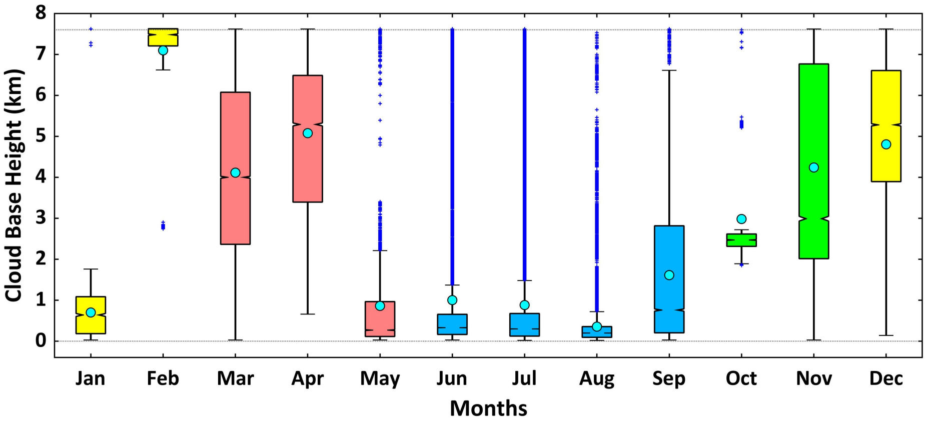

Figure 3.7: Box plots showing monthly CBH statistics for single-layer clouds observed over Mt. Abu during 2023. In each box, the notch represents the median; edges indicate the 25th and 75th percentile values, and the blue '+' symbols denote outliers. Whiskers are drawn at 1.5 times the Interquartile Range (IQR). The cyan-filled circles represent the monthly average CBH. The yellow, red, blue, and green colors correspond to the winter, pre-monsoon, monsoon, and post-monsoon seasons, respectively.

During the winter season, high CBH values are generally observed, 7100 ± 1190 m in February and 4800 ± 2210 m in December. However, an anomalously low CBH of 700 ± 630 m is noted in January. This indicates potential episodes of low-lying stratus clouds or fog, possibly driven by nocturnal inversions and stagnant wintertime meteorological conditions. The distinctly different wintertime behavior over Mt. Abu can be attributed to the very cold and dry air masses that prevail over the Aravalli highlands during this season, which substantially elevate the LCL and lead to cloud formation only at higher altitudes. Limited solar heating and weak ABL development further suppress vertical mixing, allowing high-level clouds to dominate. Occasionally, strong nocturnal inversions trap shallow moisture layers close to the surface, resulting in low-level stratus or fog, as reflected in the unusually low CBH observed in January. Thus, winter exhibits a dual structure, predominantly high CBH due to dry, stable conditions, punctuated by episodic low-level cloud formation driven by inversion strength. The pre-monsoon season (March and April) is characterized by elevated CBH, reaching 4110 ± 2100 m and 5070 ± 1630 m, respectively, driven by dry conditions and convective heating. Interestingly, CBH sharply drops in May (860 ± 1490 m), signalling the early influence of monsoonal moisture influx even before full monsoon onset. In the post-monsoon period, the CBH rises to 2980 ± 1250 m in October and 4240 ± 2470 m in November, marking the transition to drier, stable atmospheric conditions. The interquartile range (IQR) of CBH is narrowest in August and October, with October's limited spread likely influenced by reduced data availability. In contrast, the highest IQR is observed in November, suggesting enhanced variability in cloud formation due to the coexistence of residual moisture and incoming wintertime circulations. Overall, the seasonal mean CBH is highest during winter (4620 ± 2390 m), followed by post-monsoon (4150 ± 2420 m) and pre-monsoon (3830 ± 2330 m), and lowest during monsoon (780 ± 1370 m). These results emphasize the dominant role of monsoon dynamics and orographic influence in governing cloud formation processes over Mt. Abu.

Fog and mist formation over Mt. Abu were examined using Ceilometer Lidar and surface meteorological data. Fog is a low-level cloud in contact with the ground that reduces horizontal visibility to less than 1 km, while mist limits visibility to 1–2 km (Vautard et al., 2009). A representative fog episode occurred on 11–12 January 2023 (Figure 3.8). Ceilometer backscatter profiles showed strong near-surface attenuation from approximately 23:00 LT, indicating dense fog, preceded by low-level clouds with a CBH near 600 m. Vertical visibility (VV) dropped to an average of 35 ± 16 m, and CBH remained at ground level. Meteorological data showed nighttime temperatures of 11–12 °C, dew point matching air temperature, and relative humidity reaching 100% before fog onset. Winds shifted from westerly to north-westerly and increased from approximately 4.5 to 9 m s^{-1}, conditions favorable for radiation fog formation under a stable nocturnal boundary layer. Fog persisted until sunrise, when surface warming and boundary layer mixing led to dissipation.

Mist events, though less studied, were frequent during the monsoon. Identification criteria included: (i) enhanced backscatter below 200 m AGL, (ii) VV $<$ 100 m, (iii) near-zero CBH, and (iv) RH $\sim$ 100% with stable temperatures. Seasonal VV analysis revealed that low-visibility ($<$100 m) conditions peaked during the monsoon—July (21.5%), August (36.8%), and June (7.6%)—primarily due to mist. In winter, such as January (1.2%) and December (0.15%), low visibility was linked to fog under radiative cooling and stable boundary layers. These findings highlight distinct seasonal visibility hazards in Mt. Abu: winter dominated by radiation fog, and monsoon by shallow mist, sometimes compounded by rainfall.

The analysis of cloud types over the Mt. Abu region using MODIS revealed that cirrostratus clouds dominate, comprising about 30% of total cloud coverage during the observation period. These high-level, ice-crystal clouds prevail during satellite passes. Stratocumulus clouds account for roughly 24%, indicating a significant presence of low-level, layered clouds associated with stable atmospheric conditions. Cirrus clouds make up 16%, while altostratus and cumulonimbus contribute 12% and 5%, respectively. Other cloud types, such as cumulus, nimbostratus, stratus, and altocumulus, are less common, each ranging between 2% and 5%. The relatively low frequency of nimbostratus, which typically signals prolonged rain, suggests fewer extended precipitation events during the study period. Overall, high-level clouds constitute nearly half of the observations, with moderate amounts of low-level stratiform clouds and limited convective cloud activity. Comparing MODIS-derived cloud base heights with

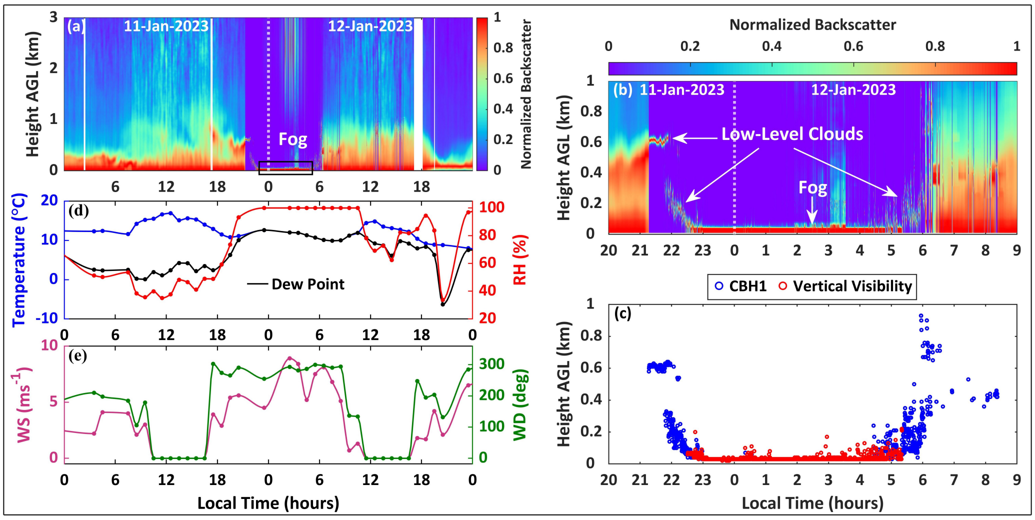

Figure 3.8: (a) Normalized backscatter profiles from the Ceilometer Lidar at Mt. Abu on 11–12 January 2023. White gaps represent missing data. The enhanced near-surface backscatter observed from around 23:00 LT on 11 January indicates the onset of fog. (b) Formation of low-level clouds and fog during the nighttime over Mt. Abu. (c) Temporal variation of the CBH (blue circles) and vertical visibility (red circles) during the fog event. (d) Time series of air temperature and RH, along with dew point temperature. (e) Variation of WS and WD during the same period.

Ceilometer measurements reveals a weak correlation, indicating considerable differences between satellite and ground-based estimates. This underscores the need for enhanced satellite retrieval algorithms that better capture cloud microphysics and vertical structure to improve cloud base height accuracy.

3.3 Long-term trends in clouds and rainfall over Ahmedabad

This section examines the long-term monthly and annual variations of rainfall, CBH, and BLH over Ahmedabad, covering a 22-year period from 2000 to 2021. The total monthly precipitation derived from GSMaP_ISRO and ERA5 datasets reveals that Ahmedabad receives most of its rainfall during the southwest monsoon months of June, July, August, and September (JJAS), consistent with the Indian Summer

Monsoon system (Parthasarathy, 1984). The monsoon typically begins in mid-June and ends by late September in this region. The average monthly rainfall over JJAS from the GSMaP_ISRO dataset is approximately 92 ± 73 mm (June), 302 ± 159 mm (July), 269 ± 161 mm (August), and 125 ± 110 mm (September) (Figure 3.9a). ERA5 tends to underestimate rainfall in June and September but overestimates it during July and August (Figure 3.9b). Both datasets indicate that JJAS accounts for about 96% of the total annual rainfall. The highest annual rainfall occurred in 2006, reaching around 1215 mm (GSMaP_ISRO) and 1664 mm (ERA5), while the lowest was recorded in 2018 with about 400 mm (GSMaP_ISRO) and 394 mm (ERA5).

The monthly average CBH over Ahmedabad between 2000 and 2021 shows values below 2 km during the JJAS period, except for an anomalous peak of 3 km in June 2000 (Figure 3.9c). Outside the monsoon months, CBH generally exceeds 4 km, with maximum values reaching nearly 11 km in December 2011 and 2016. During the pre-monsoon and summer months, boundary layer height (BLH) reaches its peak values, averaging 728 ± 70 m in April, 913 ± 82 m in May, 960 ± 132 m in June, and 717 ± 123 m in July (Figure 3.9d). These elevated BLH values correspond to increased surface heating, which drives the boundary layer higher. In contrast, the lowest BLH values occur in winter months, dropping to around 340 m in December.

Figure 3.10 presents the monthly averages of precipitation and CBH over the period 2000–2021. During the monsoon months (JJAS), the average CBH remains low, typically below 2 km, coinciding with peak rainfall. Outside this period, CBH generally exceeds 2 km. From January through April, the average CBH hovers around 6 km, then gradually decreases from May onward, reaching its lowest point below 1 km in August. Between September and December, CBH shows a marked upward trend, increasing at an approximate rate of 1.5 km per month and reaching a maximum of 7 km by December. The greatest variability in CBH, indicated by the highest standard deviation, occurs during October, November, and December, while the lowest variability is found during the monsoon months when low-level precipitating clouds (below 2 km) dominate. Rainfall is predominantly concentrated during JJAS,

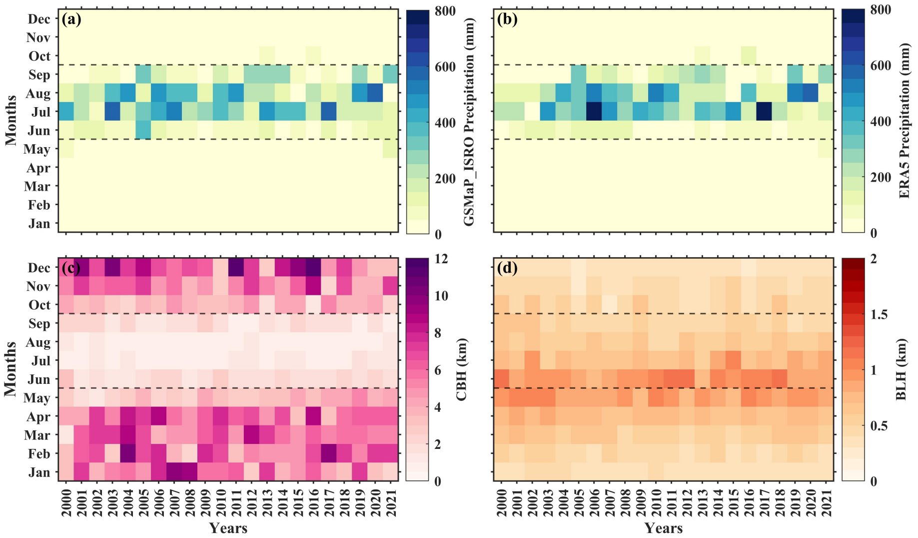

Figure 3.9: Monthly-yearly variation of (a) GSMaP_ISRO precipitation, (b) ERA5 precipitation, (c) CBH, and (d) BLH over Ahmedabad during 2000–2021. The area between the dashed lines represents the Indian Summer Monsoon months (JJAS).

with July experiencing the highest monthly totals. However, light rainfall events also occur during the pre-monsoon (May) and post-monsoon (October) periods, averaging about 8 mm and 11 mm, respectively. Correspondingly, the average CBH during these months falls between 4 and 6 km, reflecting the presence of mid-level clouds.

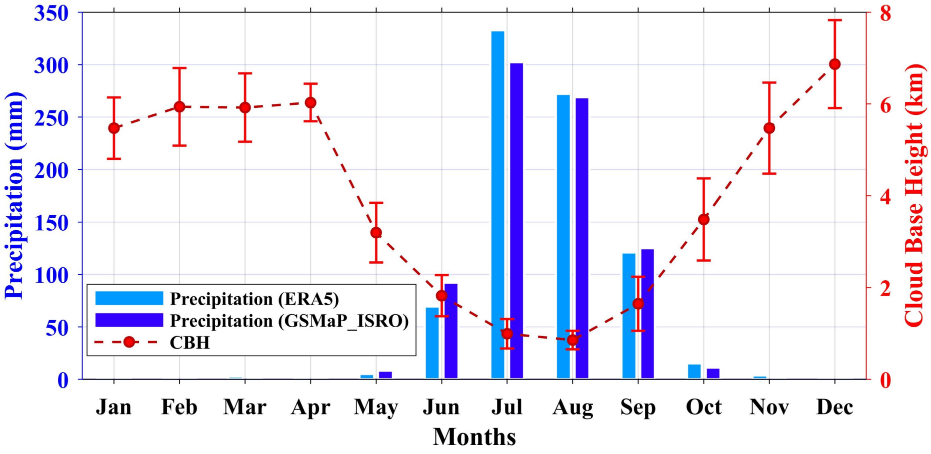

Figure 3.10: Monthly average cloud base height (CBH) and precipitation over Ahmedabad during 2000-2021. The red error bars represent the standard deviation of CBH during different months.

Focusing on the monsoon season, trends and variability in the occurrence of rainy clouds over Ahmedabad are examined. Rainy clouds are defined as those producing rainfall exceeding 0.5 mm per hour. The probability distribution of these rainy clouds shows that they predominantly have CBH below 1 km, with the highest occurrence concentrated between 200 and 250 meters (Figure 3.10a). Comparisons of CBH statistics for rainy and non-rainy clouds during JJAS reveal that most clouds are low-level, with bases under 2 km, though occasional higher cloud bases appear as outliers. The interquartile range (IQR) for non-rainy clouds is wider, indicating a broader vertical distribution, while rainy clouds are largely confined to narrower altitude ranges. On average, rainy clouds exhibit a CBH near 800 meters, compared to roughly 1,350 meters for non-rainy clouds (Figure 3.11).

Throughout the 2000–2021 period, overall cloud cover during the monsoon in Ahmedabad has consistently remained above 90% in most years. However, the frequency of rainy versus non-rainy clouds has shown notable changes. On average, rainy clouds occurred approximately 5%, 16%, 14%, and 8% of the time in June, July, August, and September, respectively, closely matching the monthly rainfall patterns discussed earlier. The trend analysis from September 2000 to 2021 reveals no significant change in rainy cloud frequency during June, July, and August, the monsoon onset and peak months, but shows a statistically significant increasing trend in September (monsoon withdrawal), with rainy cloud frequency rising by 0.49 ± 0.23% per year (RMSE = 6.86; $p < 0.05$, Mann-Kendall test). Alongside this, June has experienced a decline in total rainfall at a rate of 2.72 ± 1.50 mm/year, while September has seen an increase of 5.37 ± 3.52 mm/year. These shifts point to a notable alteration in the monsoon rainfall pattern over Ahmedabad during the last two decades.

Clouds over Ahmedabad during 2000–2001 are classified into low-level (<2 km), mid-level (2–6 km), and high-level (>6 km) categories based on their base heights to analyze their occurrence patterns and temporal trends. The highest total cloud cover occurs in July and August, reaching nearly 99%, while February records the lowest at around 20%. Winter months (December–February) see predominantly high-level

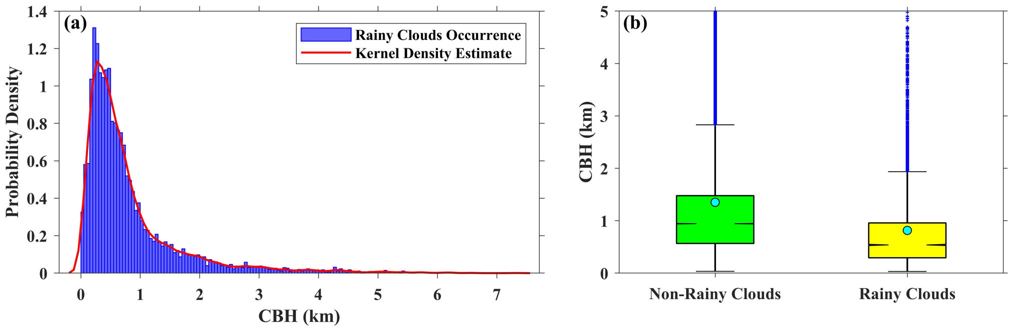

Figure 3.11: (a) Probability density of rainy cloud occurrence in different height ranges over Ahmedabad during JJAS from 2000–2021. (b) Box plot showing the CBH statistics for non-rainy and rainy clouds during JJAS from 2000–2021. In each box, the notch is the median; edges indicate the 25th and 75th percentile values, and the blue '+' symbols are outliers. Whiskers are drawn with 1.5 times the IQR. The cyan-filled circles represent the average CBH.

clouds, though overall cloudiness is low. During the monsoon (June–September), low-level clouds dominate with frequencies between 61% and 95%, while high-level clouds are rare. Mid-level clouds are moderately frequent in June and September and peak during the post-monsoon months of October and November. Trend analysis from 2000 to 2021 reveals a significant increase in low-level cloud occurrence during September at $0.80 \pm 0.39\%$ per year, while mid-level clouds show a decline of $-0.8 \pm 0.36\%$ per year (Figure 3.12). High-level clouds show no notable trend. Since precipitation during the monsoon is mainly associated with low-level clouds, the rise in low-level cloud frequency likely drives the observed increase in rainy clouds in September.

Long-term variations in cloud cover and rainfall during the Indian Summer Monsoon (ISM) appear to be closely linked to rising aerosol concentrations, particularly Black Carbon (BC). The radiative heating effects of BC differ throughout the troposphere, impacting atmospheric stability and cloud formation processes. Specifically, BC induces stronger heating in the upper troposphere compared to the lower troposphere, modifying stability through semi-direct radiative effects (Stjern et al., 2017). Consequently, the vertical cloud distribution shifts, favoring an increase in low-level

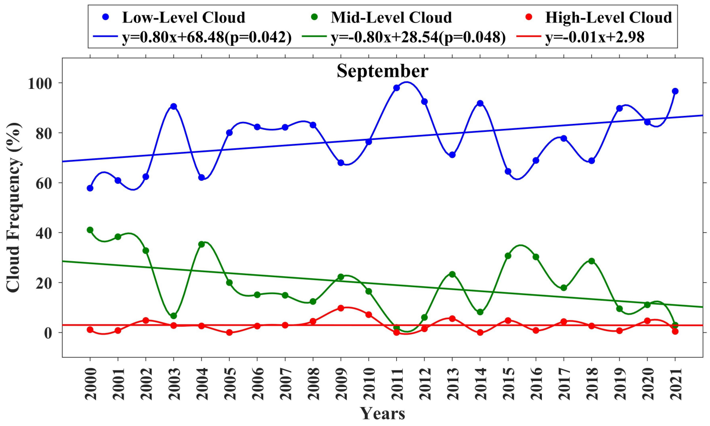

Figure 3.12: Long-term trends in the frequency of low-level (blue line), mid-level (green line), and high-level clouds (red line) during September over Ahmedabad from 2000-2021.

clouds and a reduction in high-level clouds. This pattern is evident over Ahmedabad, where elevated aerosol levels in September correspond to higher temperatures in the upper troposphere. These thermal changes promote enhanced low-level cloud formation while suppressing mid- and high-level clouds, thereby increasing the frequency of rainy clouds. Such aerosol-driven alterations in cloud cover and precipitation patterns, driven by intensified anthropogenic emissions, underscore the regional impacts of climate change.

3.4 Comparison of clouds and ABL characteristics over Ahmedabad, Mt. Abu, and Udaipur

This study presents a detailed comparison of cloud layering frequencies and monthly average CBH across three sites in Western India: Ahmedabad, Mt. Abu, and Udaipur, from December 2021 to March 2025. The analysis reveals significant spatial and seasonal variations influenced by local geography and atmospheric dynamics. The frequency distribution of single-layer, double-layer, and triple-layer clouds and full obscuration reveals notable differences among the three regions. Figure 3.13a shows that the single-layer clouds dominate all three locations, occurring most frequently in Udaipur ($\sim 31.9\%$), followed by Mt. Abu ($\sim 27.0\%$) and Ahmedabad ($\sim 23.8\%$).

Interestingly, full obscuration is considerably more frequent at Mt. Abu ($\sim$ 12.2%) compared to Ahmedabad ($\sim$ 2.6%) and Udaipur ($\sim$ 2.6%). This elevated occurrence is likely due to mist formation over Mt. Abu during the monsoon. Double-layer clouds are quite rare at all sites, with frequencies under 1% (Ahmedabad: 0.29%, Mt. Abu: 0.63%, Udaipur: 0.6%), while triple-layer clouds are negligible, found only at Mt. Abu and Ahmedabad at 0.01%.

Seasonal trends in CBH across the three sites demonstrate the influence of monsoonal dynamics and regional geography. Figure 3.13b shows the monthly mean CBH over the three regions. During winter months (December to February), Udaipur consistently shows the highest average CBH values, reaching approximately 4.4 km in January and November, while Ahmedabad and Mt. Abu have comparatively lower cloud bases, generally below 4 km. This indicates relatively deeper, higher-altitude cloud formations over Udaipur during the cooler, drier months, potentially due to its position within the Aravalli hills affecting local atmospheric stability. During the pre-monsoon season (March to May), CBH increases across all sites, peaking in May, with Udaipur reaching around 6.5 km, the highest among the three locations. Ahmedabad and Mt. Abu also show increases but with larger variability, as indicated by wider error bars. This variability suggests that atmospheric conditions are more heterogeneous during this transitional period, with mixed cloud types and varying stability levels influencing cloud base heights.

During the monsoon months (June to September), CBH decreases markedly at all sites. Ahmedabad and Mt. Abu record their lowest cloud bases, frequently falling below 2 km. These low cloud bases are characteristic of dense, moisture-laden monsoon clouds and deep convective activity typical of the Indian monsoon. Udaipur's cloud bases are also lower but remain somewhat higher than the other sites, reflecting local geographic influences that moderate cloud base altitudes. Post-monsoon months (October and November) show a rebound in CBH, with Udaipur once again exhibiting the highest cloud bases ($\sim$ 4.8 km in November), consistent with a transition toward drier and more stable atmospheric conditions. The error bars during transitional

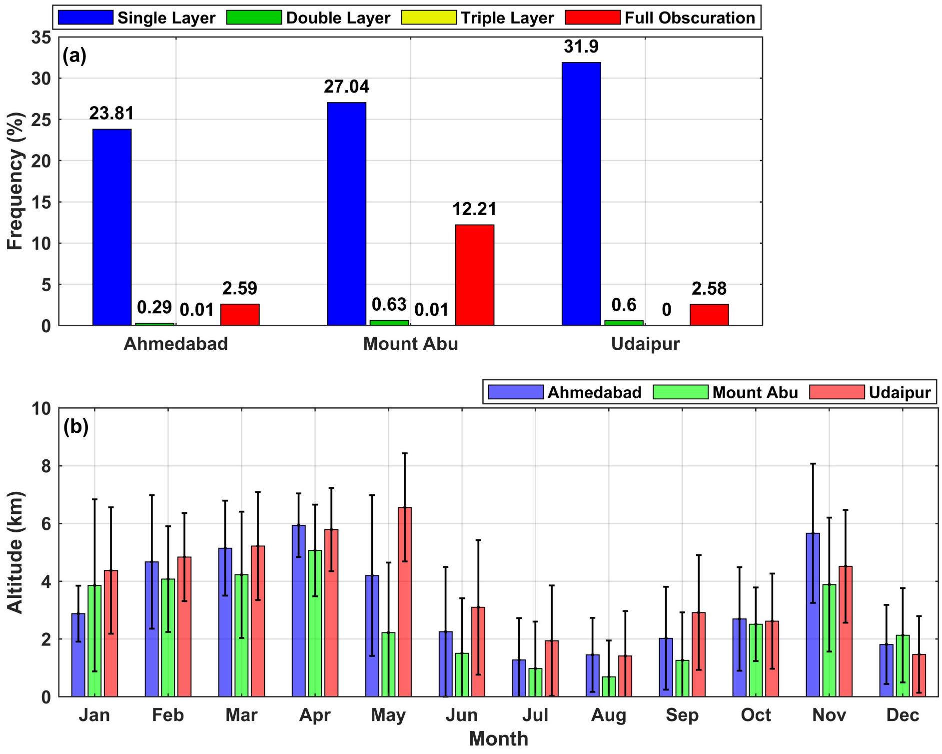

Figure 3.13: (a) Frequency distribution of different sky conditions, single layer, double layer, and triple layer clouds, and full obscuration over Ahmedabad, Mt. Abu, and Udaipur during December 2021 to March 2025. (b) Monthly mean cloud base height (CBH) variations over the three regions.

months (May, September, November) are generally larger, highlighting increased variability in cloud heights due to the dynamic interplay of monsoon withdrawal and the onset of dry season conditions.

Figure 3.14a presents the mean diurnal variation of BLH over Ahmedabad, Mt. Abu, and Udaipur, averaged over the entire observation period. The BLH shows a clear diurnal pattern at all three sites, characterized by low values during nighttime and early morning hours, followed by a steady increase from 03 UTC. Ahmedabad exhibits the highest peak BLH, reaching approximately 1.3 km around 10–11 UTC, which is notably larger than the peak heights observed over Mt. Abu and Udaipur, both of which have peak BLHs below 1 km. The daytime growth of the boundary layer is attributed to surface heating and convective processes, with the height peaking near afternoon. Post 12 UTC, the BLH declines gradually, stabilizing at lower values during the late afternoon and night. The error bars indicate significant variability throughout the day, with Ahmedabad showing the largest spread in BLH during peak hours, reflecting dynamic boundary layer conditions influenced by urban and meteorological factors.

Figure 3.14b illustrates the mean monthly variation of peak BLH at the three sites. Ahmedabad consistently exhibits higher peak BLHs throughout the year, with maxima during the pre-monsoon months of April and May exceeding 2 km. In contrast, Mt. Abu shows the lowest BLH values year-round, likely influenced by its elevated terrain and cooler conditions, with peaks generally below 1.5 km. Udaipur displays intermediate values, with peak BLH ranging roughly between 0.8 and 1.3 km, and somewhat less pronounced seasonal variability compared to Ahmedabad. Seasonal trends show elevated BLH during the warmer months (March to June), consistent with increased solar insolation and stronger convective mixing. The lower BLH values during the monsoon and winter months (July to February) are indicative of increased atmospheric stability and cloud cover, which suppress boundary layer growth. Error bars across months demonstrate substantial inter-month variability, especially over Ahmedabad, reflecting complex meteorological influences including urban heat effects and synoptic conditions.

3.5 Summary and conclusions

This chapter examined the vertical structure and seasonal variability of clouds and BLH over Ahmedabad, Mt. Abu, and Udaipur using ground-based Ceilometer observations. Single-layer clouds were found to dominate at all locations, with the highest frequency at Udaipur, while Mt. Abu showed the greatest occurrence of full obscuration events due to orographic lifting and persistent moisture. The CBH climatology revealed a clear seasonal cycle: monsoon months exhibited the lowest CBHs (1.5–2 km), pre-monsoon months showed the highest values (up to 6.5 km over Udaipur), and winter months displayed moderately elevated CBHs with occasional

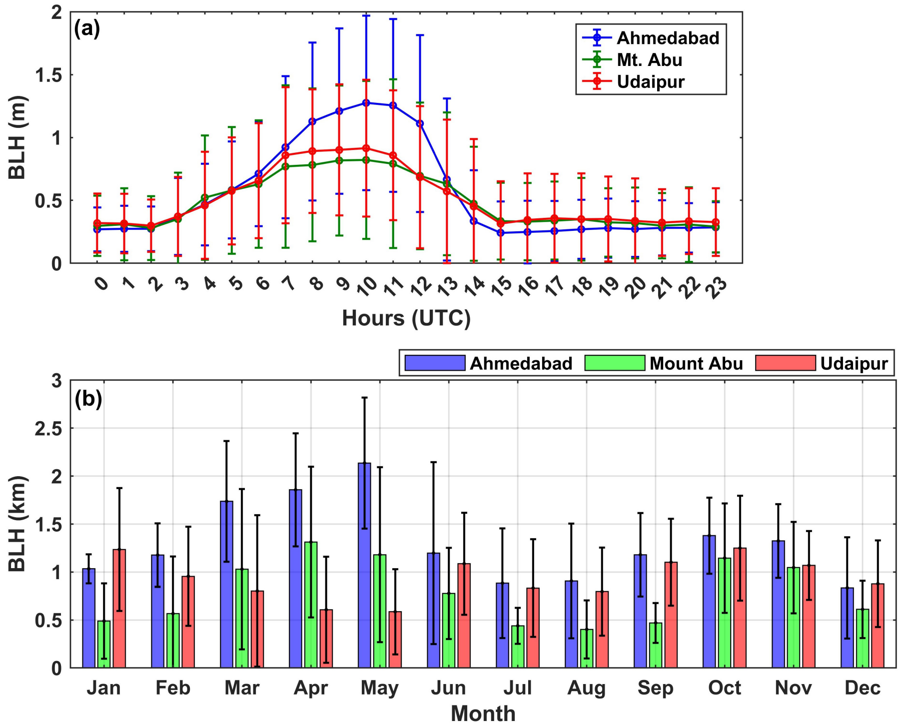

Figure 3.14: (a) Mean diurnal variation of boundary layer height (BLH) over Ahmedabad (blue), Mt. Abu (green), and Udaipur (red) during the observation period. Error bars represent the standard deviation at each hour. (b) Monthly mean peak BLH with standard deviation for the three regions.

low-level stratus or fog linked to strong nocturnal inversions. A 22-year analysis over Ahmedabad further indicated that rainfall is most intense during July–August, with rainy clouds typically associated with CBHs below 1 km. A significant increasing trend in September rainfall, along with a rise in low-level cloud occurrence, suggests a shift toward late-monsoon intensification.

BLH characteristics across the three sites showed strong seasonal and diurnal dependence. Pre-monsoon months exhibited the deepest boundary layers (above 2.5–3 km), driven by intense surface heating, while monsoon and winter seasons showed reduced BLHs due to enhanced moisture and stable atmospheric conditions. Ahmedabad consistently recorded the highest BLH, influenced by urban heat island effects and stronger daytime convective mixing, whereas Mt. Abu exhibited the lowest values due to its elevated and cooler terrain. Overall, the chapter highlights the dominant roles of local topography, seasonal meteorology, and moisture availability in modulating CBH and BLH variability across the three regions, providing a strong observational basis for the analyses presented in subsequent chapters.

****

Chapter 4

Clouds Below and Near the LCL: Dynamics and Thermodynamic Influences

Atmospheric convection refers to the vertical movement of air, including updrafts and downdrafts, which plays a crucial role in transporting mass, heat, and momentum in the atmosphere. This process is often linked to the phase changes of water, contributing to cloud formation and influencing weather patterns (Lin et al., 2022). Convective clouds are formed by the adiabatic rise of warm air parcels near the Earth's surface, which expand and cool, causing water vapor to condense into cloud droplets. These clouds, prevalent in mid to low latitudes, include cumulus (fair-weather clouds), cumulus congestus, and cumulonimbus, reaching their greatest depth in the tropics (Murray and Liu, 2022; Williams and Hacker, 1992). Convective clouds are integral to the Earth's energy balance and hydrological cycle, with any variations in their distribution or initiation timing potentially exerting substantial influence on the climate system (Stocker et al., 2013). Despite their critical role, small convective cumulus clouds remain challenging to measure and model due to their complex spatial distribution, which has a pronounced effect on the radiative budget (Benner and Curry, 1998). These clouds are intricately linked to the dynamics of the ABL, which mediates the exchange of heat, moisture, and momentum between the surface and the atmosphere (Stull, 1988).

The coupling between the ABL and cloud processes remains a fundamental and actively explored topic due to its pivotal role in cloud initiation and evolution. The ABL governs the thermodynamic and dynamic environment in which clouds initiate, especially during transitions from stable to unstable regimes. Recent studies have highlighted that cloud-surface interactions can significantly influence the structure and timing of ABL transitions. For example, Su et al. (2023) demonstrated that cloud-surface coupling during the morning hours can alter the transition from a stable nocturnal boundary layer to an unstable convective boundary layer, thereby modifying the timing and conditions for convective cloud formation. Similarly, Nowak et al. (2021) investigated turbulence characteristics in coupled and decoupled stratocumulus-topped boundary layers and found that the nature of this coupling strongly affects cloud properties, entrainment rates, and the vertical structure of turbulence. These findings underscore the importance of considering ABL and cloud coupling dynamics when investigating cloud formation processes, especially in regions with intense surface heating and boundary layer variability.

The formation of convective clouds begins when a rising air parcel reaches the LCL, the critical altitude at which it becomes saturated, leading to cloud development (Stackpole, 1967). The LCL is vital for various applications, including weather forecasting, air quality assessments, and ensuring flight safety (Wilde et al., 1985). Furthermore, the interaction between the LCL and land surface fluxes plays a vital role in a region's climate, where inaccuracies in its parameterization can introduce biases in weather and climate models (Emanuel and Živković-Rothman, 1999; Wei et al., 2021). The first formula for LCL was introduced by Espy in 1836. Since then, numerous studies have been dedicated to calculating the analytical formula for LCL height through various methodologies (Bolton, 1980; Craven et al., 2002; Daidzic, 2019; Lawrence, 2005; Romps, 2017; Stackpole, 1967). Furthermore, Wilde et al. (1985) discovered that the LCL height can vary within small altitude ranges within a region, termed the LCL zone. The spatial relationship between this zone and the entrainment zone is crucial for cloud formation.

Despite the LCL being the recognized minimum height for cloud formation, studies by Hirsch et al. (2017) and Altaratz et al. (2021) indicate that under certain atmospheric conditions, clouds can form below the LCL height. Specifically, Hirsch et al. (2017) showed through air parcel simulations that in a humid boundary layer capped by a strong inversion layer, clouds could form beneath the LCL height due to humidity perturbations in the boundary layer. Similarly, Altaratz et al. (2021) outlined conditions under which sub-LCL clouds could develop in the lower troposphere, noting that the presence of the LCL above the BLH and the relative humidity near the BLH top are critical conditions for the formation of such clouds. In addition to thermodynamic factors, the presence of hygroscopic aerosols within such confined layers can facilitate droplet activation below saturation. Hygroscopic aerosol particles act as CCN and can activate droplets at relative humidities below 100%, driven by Köhler theory (Petters and Kreidenweis, 2007). This process, observed in urban polluted environments, can enhance the likelihood of shallow, sub-LCL clouds even under subsaturated ambient conditions (Kawana et al., 2014). Moreover, aerosol-cloud interactions can significantly affect the cloud height. Khatri et al. (2023) reported that in polluted continental atmospheres, increased aerosol loading enhances sub-cloud stability and promotes collision-coalescence processes, which leads to larger droplet sizes and reduced cloud top heights. Therefore, the processes driving cloud formation below the LCL involve a complex interplay between boundary layer moisture perturbations and aerosol-induced microphysical mechanisms.

This chapter investigates the characteristics and formation mechanisms of convective clouds developing below LCL over a subtropical semi-arid region, Ahmedabad (23.02° N, 72.57° E), using ground-based Lidar (Figure 4.1a). Furthermore, the chapter also presents a case study on boundary layer clouds and their response to surface forcings. Ahmedabad, an urban area in the western Indian state of Gujarat, experiences a hot semi-arid climate with four distinct seasons: winter (December–February), pre-monsoon (March–May), monsoon (June–September), and post-monsoon (October–November). The highest temperatures are recorded in April (31.9 ± 4.2 °C), May (34 ± 4.6 °C), and June (32.4 ± 3.8 °C), with daily maximum temperatures often exceeding 40 °C (Figures 4.1b–c). In contrast, the coldest months are January and December, with mean temperatures of 20.2 ± 4 °C and 21.7 ± 3.6 °C, respectively. The most humid months are July, August, and September, with daily relative humidity reaching up to 100% (Figures 4.1d–e).

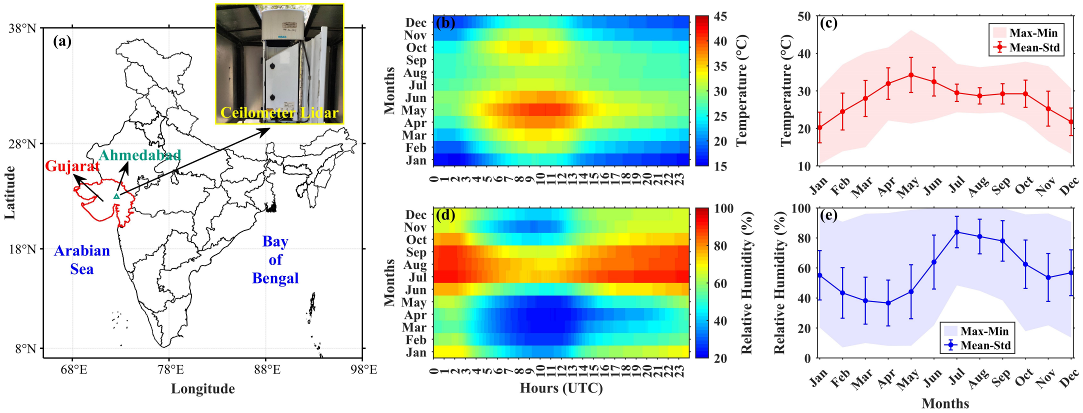

Figure 4.1: (a) Map highlighting the study region, Ahmedabad, located in the western Indian state of Gujarat, along with an image of the Ceilometer Lidar. (b, d) Monthly mean diurnal variations of temperature and relative humidity for different months over Ahmedabad during 2023-2024. (c, e) Monthly mean temperature and relative humidity, with shaded regions indicating the minimum and maximum values.

4.1 Derivation of an analytical expression for the LCL

The first historically recorded definition for the LCL was given by the famous meteorologist James Pollard Espy in 1836. Since then, many analytical expressions have been proposed to approximate LCL. A summary of various LCL formulations proposed in previous studies is provided in Table 4.1. This study uses a simple approach to estimate the LCL from the surface temperature and relative humidity.

The pressure at the LCL height (P_{LCL}) is obtained from the equation below (Georgakakos and Bras, 1984):

$$P_{\text{LCL}} = \frac{P}{\left[\frac{T-T_d}{223.15}+1\right]^{3.5}} \tag{4.1}$$

where P is the pressure at the surface and T_d is the dew point temperature, calculated as (Lawrence, 2005):

$$T_d = \frac{T}{1-\frac{T\ln(\text{RH}/100)}{L_v/R_v}} \tag{4.2}$$

Here, T is surface temperature, RH is surface relative humidity, L_v is the latent heat of vaporization, and R_v is the gas constant for water vapor.

Given the pressure at the LCL, we can estimate the LCL height using the barometric formula. This study uses an improved barometric formula that incorporates temperature changes in the atmosphere (Lente and Ősz, 2020):

$$P(h) = P_0\left(1-\frac{\alpha}{T}h\right)^{\frac{Mg}{\alpha R}} \tag{4.3}$$

where α is the change in temperature with altitude (lapse rate), M is the molecular mass of air, g is the acceleration due to gravity, R is the universal gas constant, and T is the surface temperature.

Rearranging Equation 4.3 and substituting the pressure at the LCL from Equation 4.1, we obtain an expression for the LCL height:

$$h = \frac{T}{\alpha}\left[1-\left(\frac{1}{\left(\frac{T-T_d}{223.15}+1\right)^{3.5}}\right)^{\frac{\alpha R}{Mg}}\right] \tag{4.4}$$

By inserting the surface temperature and relative humidity observed from the AWS into the above equation, the LCL can be calculated.

Table 4.1: Analytical expressions for estimating the Lifted Condensation Level (LCL) from various studies.

Method	Analytical Expression for LCL
J. P. Espy, 1836	$z_{\mathrm{LCL}} = z + 165\,\mathrm{mK}^{-1}(T - T_d)$
Davis, 1889	$z_{\mathrm{LCL}} = z + 137\,\mathrm{mK}^{-1}(T - T_d)$
Mc Donald, 1963	$z_{\mathrm{LCL}} = z + 123\,\mathrm{mK}^{-1}(T - T_d)$
Bolton, 1980	$z_{\mathrm{LCL}} = z + \frac{c_p}{g}\left\{T - 55K - \left[\frac{1}{T - 55K} - \frac{\log(RH)}{2840K}\right]^{-1}\right\}$
Lawrence, 2005	$z_{\mathrm{LCL}} = z + \left(20 - \frac{T - 273.15K}{5K}\right)(100\,\mathrm{m})(1 - RH)$
Romps, 2017	$T_{\mathrm{LCL}} = c\left[W_{-1}\left(RH^{1/a}ce^{c}\right)\right]^{-1} T,$ $z_{\mathrm{LCL}} = z + \frac{c_p}{g}(T - T_{\mathrm{LCL}})$
Daidzic, 2019	$z_{\mathrm{LCL}} = z_0 + \frac{c_{pd}}{g_0}(1 + 0.856q)\left[T - 55 - \left(\frac{1}{T - 55} - \frac{\ln(RH)}{2840}\right)^{-1}\right]$

4.2 Comparison of various analytical expressions for LCL

The analytical expression for the LCL derived in this study is compared against previously established formulations using radiosonde observations as the reference (Figure 4.2). It is important to note that radiosonde profiles are available only at 0000 UTC and 1200 UTC, which may limit the temporal resolution of validation. Consistent with earlier studies, all analytical LCL formulations, including the new expression derived here, tend to underestimate LCL heights relative to those observed from radiosonde data. This underestimation is primarily attributed to the simplified assumptions used in analytical approaches, such as constant lapse rates and idealized moist adiabatic processes, which do not fully capture the complexity of real atmospheric profiles. Despite this inherent bias, all methods exhibit strong correlations with radiosonde observations, indicating their capability to capture the temporal variability and trends in LCL. The correlation coefficient (R) is approximately 0.89 for all methods, with the new formulation yielding the highest R value of 0.893, indicating a marginally better fit (Figure 4.2d). However, notable

Table 4.2: Definitions of symbols used in the equations in Table 4.1.

Symbol	**Definition**
z, z_0	Surface or initial height (m)
z_{LCL}	Height of the lifted condensation level (m)
T	Air temperature (K)
T_d	Dew point temperature (K)
T_{LCL}	Temperature at the LCL (K)
RH	Relative humidity (unitless, i.e., 0–1 or as a %)
c_p	Specific heat at constant pressure ($\approx 1004\,\mathrm{J/kg{\cdot}K}$)
c_{pd}	Specific heat of dry air ($\approx 1004\,\mathrm{J/kg{\cdot}K}$)
g, g_0	Gravitational acceleration ($\approx 9.81\,\mathrm{m/s^2}$)
q	Specific humidity (kg/kg)
ln	Natural logarithm
W_{-1}	Lower branch of the Lambert W function
a, c	Empirical constants in Romps (2017) formula

differences arise in the error metrics among the four methods. The Lawrence (2005) formulation exhibits the highest root mean square error (RMSE) and mean absolute error (MAE) values, 1493.1 m and 1161.4 m, respectively, indicating comparatively lower accuracy, especially for higher LCL values (Figure 4.2b). In contrast, the Romps (2017) and Bolton (1980) methods demonstrate similar performance, with RMSE values of approximately 1226 m and 1242 m and MAE values around 989 m and 1004 m, although both tend to slightly overestimate lower LCL values and underestimate higher ones (Figure 4.2a,c). The newly proposed method in this study has the lowest RMSE (1196.5 m) and MAE (958.5 m), reflecting a modest yet consistent improvement in performance across the observed LCL range (Figure 4.2d). Furthermore, the new method reduces the spread of high-density LCL estimates below the 1:1 line, especially in the 1000–2500 m range, which is critical for cloud formation studies in the lower troposphere. Given its relatively lower error and higher consistency, the new LCL formulation is employed for estimating LCL heights over the Ahmedabad region from August 2022 to December 2024, to study the diurnal and seasonal characteristics of convective cloud formation near and below the LCL.

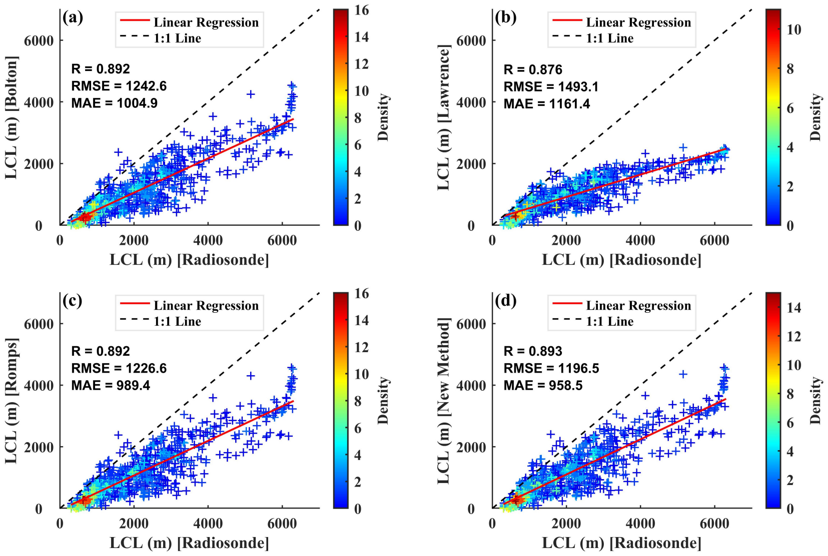

Figure 4.2: Comparison of different methods (a) Bolton, (b) Lawrence, (c) Romps, and (d) New Derived equation for the calculation of LCL with radiosonde observations over the Ahmedabad region.

4.3 Seasonal variation of LCL over the Ahmedabad region

Figure 4.3 presents the monthly mean diurnal variation of LCL over Ahmedabad for the period 2023–2024. Across all months, a clear diurnal cycle in LCL is observed, with values increasing after sunrise, peaking between 0900 and 1100 UTC, and decreasing toward nighttime. This pattern is primarily driven by increased surface heating and associated changes in near-surface temperature and humidity. However, the radiative transfer within the local atmospheric column also plays a crucial role. Daytime solar heating increases the lapse rate, while nighttime longwave radiative cooling near the surface enhances stability and lowers the LCL.

Seasonally, the LCL demonstrates distinct variability. During winter (December–

February), LCL values remain relatively low due to cooler temperatures and higher humidity; however, February shows an anomaly with higher LCLs than December and January, likely driven by transitional warming and drier boundary layer conditions (Figure 4.3a). In contrast, the pre-monsoon season (March–May) exhibits the highest LCL values of the year, with peak heights reaching 3161 ± 547 m in March, 3304 ± 522 m in April, and 3236 ± 677 m in May (Figure 4.3b). These elevated LCLs reflect intense solar heating and a drier atmosphere, indicating that deeper boundary layer processes are required for cloud initiation during this season.

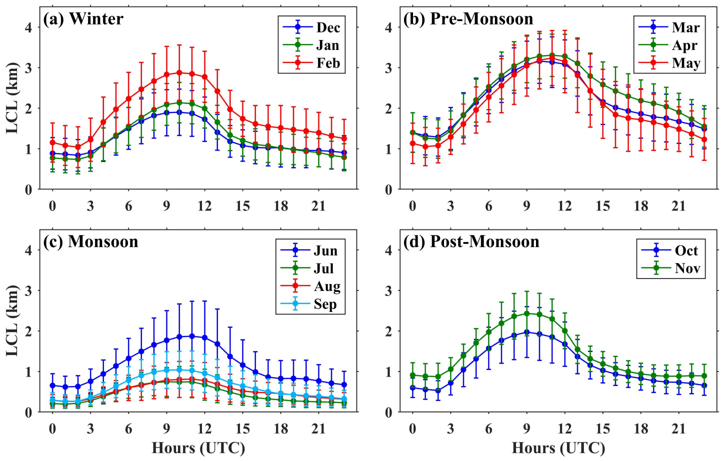

Figure 4.3: Monthly mean diurnal variation of LCL over Ahmedabad from January 2023 to December 2024 during different seasons (a) Winter (December, January, February), (b) Pre-Monsoon (March, April, May), (c) Monsoon (June, July, August, September), and (d) Post-Monsoon (October, November). The error bars represent the standard deviation.

The monsoon season (June–September) is marked by the lowest LCLs, especially in July and August, where values remain below 1000 m (Figure 4.3c). This reduction is due to abundant moisture and stable thermal profiles, fostering favorable conditions for low-level cloud formation and widespread convective activity. Post-monsoon months (October–November) show a gradual increase in LCL values, reaching 1971 ± 625 m in October and 2428 ± 550 m in November, driven by decreasing humidity and increasing temperatures (Figure 4.3d). The mean peak LCL during the winter, pre-monsoon, monsoon, and post-monsoon seasons are 2341 ± 719 m, 3317 ± 590 m, 1234 ± 679 m, and 2244 ± 608 m, respectively.

These findings are consistent with previous studies. Kumar et al. (2010a) reported similar seasonal variations in the LCL over Anand, a city 76 km from Ahmedabad. The study found that the average LCL peak reaches 3328 m in May (pre-monsoon) and drops to 335 m in August (monsoon). These seasonal variations are primarily governed by changes in temperature, humidity, and atmospheric stability and can have an effect on other atmospheric parameters. Additionally, Thayyen and Dimri (2018) demonstrated that the seasonality in LCL affects the seasonal variability in the slope of the environmental lapse rate. Thus, understanding LCL variability across seasons, along with the influence of both surface heating and radiative processes within the atmospheric column, is critical for interpreting cloud height, convective potential, and rainfall patterns in the region.

4.4 Cloud formation near the LCL

This section investigates the cloud formation near the LCL over Ahmedabad. Figure 4.4 shows a typical case of clouds formed near the LCL on 20 July 2024, a representative monsoon day characterized by abundant low-level moisture and convective activity. The Ceilometer backscatter profile reveals the presence of persistent cloud layers throughout the day (Figure 4.4a). These clouds are marked by high backscatter intensities, indicating optically dense and well-developed cloud structures. Intermittent cloud breaks occur between 1300 and 1500 UTC and between 1800 and 1900 UTC. Figure 4.4b confirms that the CBH closely follows the LCL throughout the day. The mean LCL was approximately 590 ± 269 m, while the observed CBHs largely remained within 700–1200 m, consistent with cloud formation near the LCL. Notably, the CBH and LCL start diverging around 0930 UTC, when clouds briefly rise above the LCL, likely due to thermal overshooting and deeper boundary layer growth driven by surface heating. Thermodynamic conditions from radiosonde profiles further validate these cloud signatures. The temperature profiles at 0000 and 1200 UTC exhibit a decreasing trend with height, with subtle differences below 1.5 km indicating an evolving boundary layer (Figure 4.4c). In particular, a steeper lapse rate below 1 km at 1200 UTC suggests enhanced convective mixing as daytime heating intensifies.

The relative humidity profiles show saturation (RH $\approx$ 100%) between 500 m and 1.2 km at 0000 UTC, which decreases modestly by 1200 UTC, aligning with the cloud altitude band seen in backscatter. The water vapor mixing ratio (WVMR) profiles show a drop from $\sim$22 g kg^{-1} near 500–700 m to $\sim$18 g kg^{-1} at 1.2 km at 0000 UTC (Figure 4.4e). This gradient confirms latent heat release during condensation at or near the LCL. The decrease becomes more gradual at 1200 UTC, consistent with partial evaporation and lifting of the cloud base later in the day. The wind speed profiles indicate moderate near-surface winds ($\sim$6–8 m s^{-1} at 200–600 m) at both 0000 and 1200 UTC, increasing with height until $\sim$1.5–2 km (Figure 4.4f). This wind shear facilitates the vertical transport of moisture and momentum, promoting mixing and cloud sustenance in the lower troposphere. The vertical wind structure also implies that the observed clouds may have been influenced by both mechanical and thermal lifting.

Together, these observations illustrate the canonical formation of boundary-layer clouds near the LCL, primarily shallow stratocumulus or cumulus types, triggered by surface-driven thermals reaching the LCL (Stull, 1988; Turner, 1969; Wood, 2012). The alignment of CBH with the LCL throughout much of the day, along with favorable moisture and wind conditions, underscores the strong coupling between surface processes and cloud dynamics. Occasional departures of cloud base above the LCL, especially between 0930 and 1230 UTC, are likely due to thermal overshooting, where buoyant plumes momentarily lift parcels above their condensation level, creating transient supersaturation and small non-buoyant cloud patches (Stull and Eloranta, 1984). Such near-LCL cloud events are common during the monsoon season over Ahmedabad, when high humidity, deep boundary layers, and favorable convective conditions prevail. These shallow clouds are known to significantly influence the surface radiation budget through their high albedo and modulation of incoming solar radiation, which

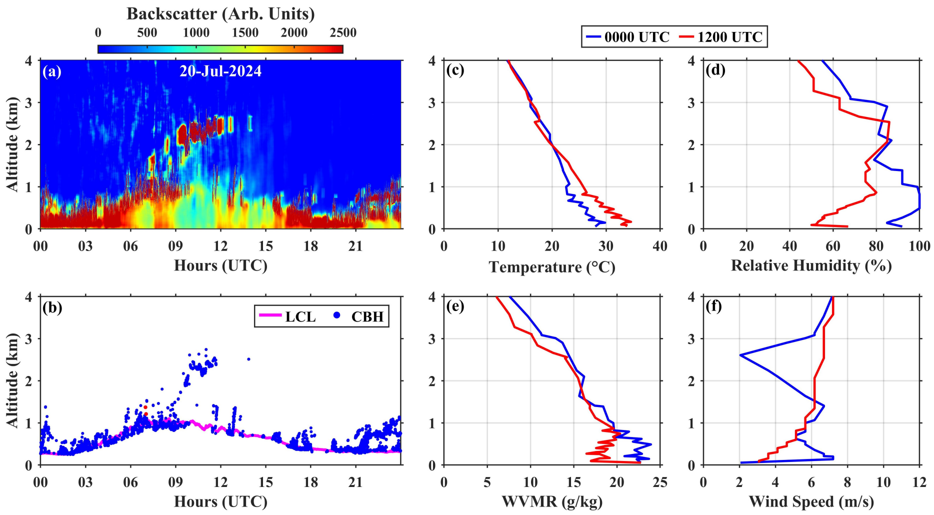

Figure 4.4: A typical case of the formation of clouds near LCL over the Ahmedabad region. (a) Backscatter profile obtained from Ceilometer Lidar on 20 July 2024. (b) Diurnal variation of LCL (pink line) and CBH (blue circle) indicating the formation of clouds near LCL. (c-f) Vertical profile of temperature, relative humidity, WVMR, and wind speed at 0000 and 12000 UTC obtained from the radiosonde.

in turn can influence surface temperatures, stability, and moisture feedbacks (Zhu and Albrecht, 2002).

4.5 Cloud formation below the LCL

Under typical thermodynamic conditions, cloud formation is expected near or above the LCL, where rising air parcels cool adiabatically to saturation. However, the presence of a strong thermal inversion layer below the LCL can inhibit vertical motion, suppress adiabatic lifting, and prevent the air parcel from reaching its theoretical condensation level. As a result, standard LCL-based cloud prediction methods may fail, particularly in stable conditions with low-level inversions. Despite this, observations suggest that clouds can and do form below the estimated LCL under specific atmospheric setups (Hirsch et al., 2017).

Over Ahmedabad, during the observation period from August 2022 to December 2024, clouds forming significantly below the LCL were identified on 19 days. On these days, the mean CBH was 1044 ± 135 m, while the mean LCL and BLH were 2324 ± 450 m and 727 ± 297 m, respectively, clearly showing cloud formation between the BLH and LCL. Figure 4.5 illustrates typical cases of such sub-LCL clouds. These clouds appear primarily between 0600 and 1200 UTC, during which surface heating due to increasing solar radiation drives turbulent mixing and a growing mixed layer. Clouds typically form near the top of this layer and are frequently observed during the post-monsoon and winter months, when stable stratification and shallow boundary layers prevail. Importantly, the Ceilometer differentiates between cloud and haze using backscatter characteristics. Cloud signatures are represented by sharp, well-defined, high-intensity backscatter returns, whereas haze produces weaker and more diffuse backscatter. This separation is crucial, as it confirms that what is detected as a cloud is not a misidentified haze.

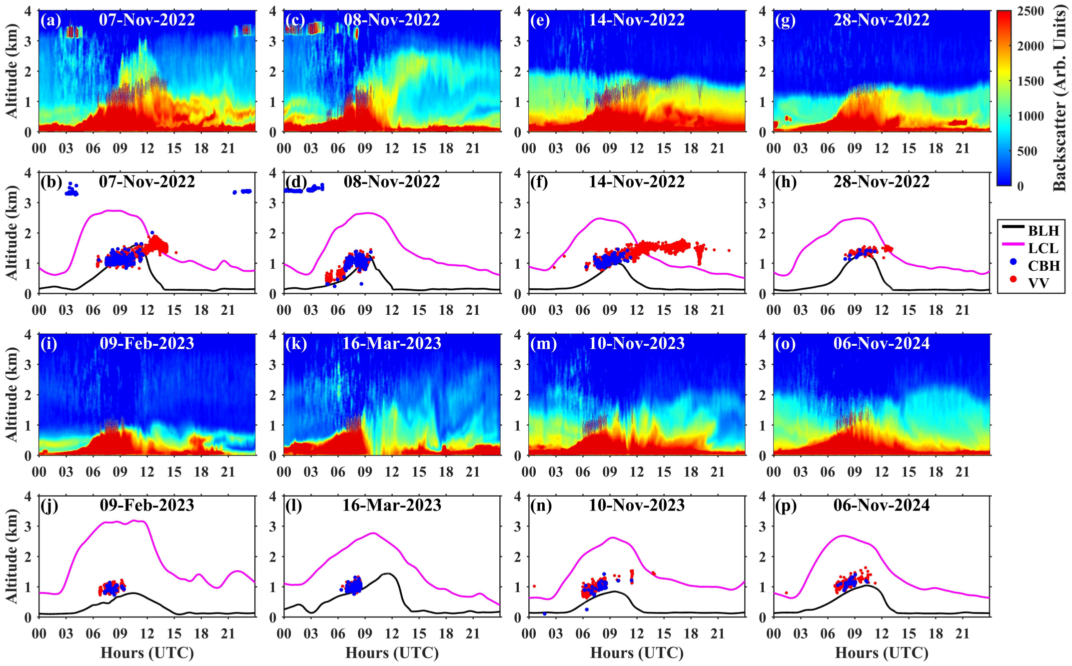

Figure 4.5: Typical cases of the clouds formed below LCL over the Ahmedabad region. These clouds are formed near the boundary layer top between 0600 and 1200 UTC. In all cases, haze is observed either before or after the cloud development. The red circular marker indicates the vertical visibility (VV) during hazy conditions.

The occurrence of haze both before and after the cloud episodes suggests a humid boundary layer that, while not always saturated, supports transient cloud formation. When clouds evaporate, often due to entrainment of drier air or weakened lifting, the water droplets dissipate, but the underlying aerosol particles (acting as CCN) remain. In stable conditions with inversion layers, these particles become trapped near the surface, enhancing haze formation. The formation of sub-LCL clouds is supported by a combination of surface-driven mixing, moisture availability, and capping inversions, conditions that enable localized supersaturation even below the calculated LCL.

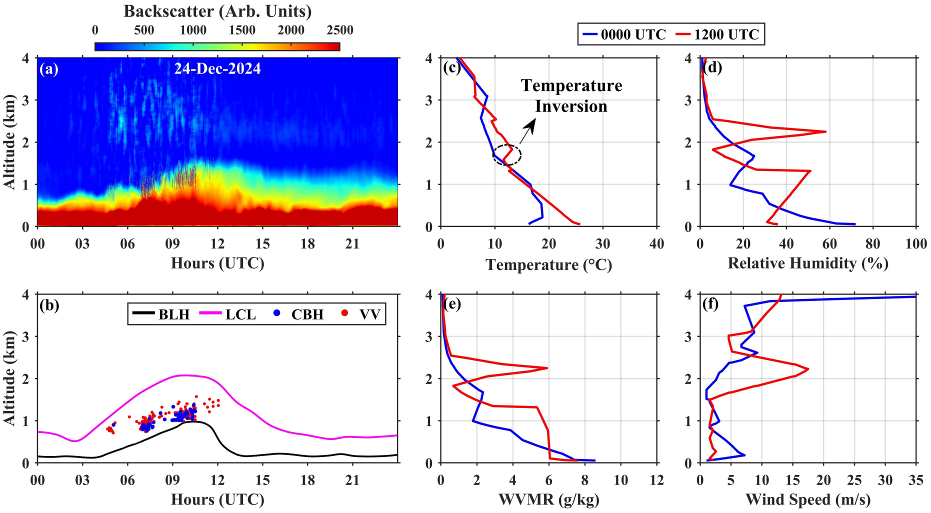

Figure 4.6: Clouds formed below the estimated LCL over the Ahmedabad region. (a) Backscatter profile obtained from the Ceilometer Lidar on 24 December 2024. (b) Diurnal variation of LCL and CBH indicates the formation of clouds below LCL between 0600 and 1200 UTC. (c-f) Vertical profile of temperature, relative humidity, WVMR, and wind speed at 0000 and 12000 UTC obtained from the radiosonde.

Figure 4.6 presents a case study of the formation of clouds below the LCL over Ahmedabad on 24 December 2024. The backscatter profile shows strong backscatter near 1 km between 0600 and 1200 UTC due to cloud presence (Figure 4.6a). As shown in Figure 4.6b, the CBH consistently resides near or just above the BLH, while the LCL remains markedly higher, suggesting that cloud formation occurred under conditions not meeting the classical parcel-lifting theory. The vertical temperature profile at 1200 UTC shows a distinct temperature inversion between approximately 1583 m and 1826 m (Figure 4.6c). This inversion likely suppressed vertical development and acted as a capping mechanism, supporting cloud formation near the BLH rather than at the LCL. The associated RH profile shows only ∼51% RH at the cloud level, a value lower than typical saturation, which is possibly a result of a temporal mismatch between the radiosonde launch and actual cloud occurrence (Figure 4.6d). However, elevated WVMR near the cloud layer indicate the presence of a moist subcloud layer, which may have supported localized supersaturation and cloud droplet activation in confined regions (Figure 4.6e). This behavior is consistent with previous studies suggesting that shallow clouds can form below LCL in the presence of high aerosol loading or humidity perturbations. Moreover, the wind speed profile shows calm conditions below the inversion, conducive to decoupling and trapping moisture, while stronger winds (∼17 m s^{-1}) above the inversion could contribute to stabilizing the upper layer, further anchoring the cloud base below the LCL (Figure 4.6f). Together, these thermodynamic and dynamic structures illustrate how the combination of an elevated LCL, capped boundary layer, and inversion stratification can foster shallow cloud formation below the classical condensation level.

4.6 Conducive surface conditions for the formation of clouds below LCL

Figure 4.7 shows the relationship between the LCL–BLH difference, surface temperature, and relative humidity under different sky conditions. Under clear sky conditions, the LCL is predominantly positioned above the BLH, reflecting suppressed convective development. Surface temperature ranges widely from 10 °C to 37 °C, while relative humidity spans from 7% to 90%, indicating substantial variability in near-surface thermodynamic conditions. Correspondingly, the LCL–BLH difference ranges from −1611 m to 3949 m, further highlighting the heterogeneity in boundary layer dynamics during clear conditions. For cases where clouds form near the LCL, the LCL and BLH are generally in close proximity, with most differences falling within ±1000 m. Surface temperatures for these instances lie between 22 °C and 41 °C, while relative humidity varies from 18% to 97%, suggesting a relatively moist and unstable environment conducive to cloud formation through parcel lifting. In contrast, for clouds forming below the LCL, the LCL consistently remains higher than the BLH, a feature that aligns with earlier observations (Altaratz et al., 2021). In these cases, surface temperatures range from 24 °C to 37 °C, and relative humidity from 17% to 49%. The LCL–BLH difference falls between 750 m and 2985 m, indicating a significant decoupling between the lifting condensation level and the boundary layer top.

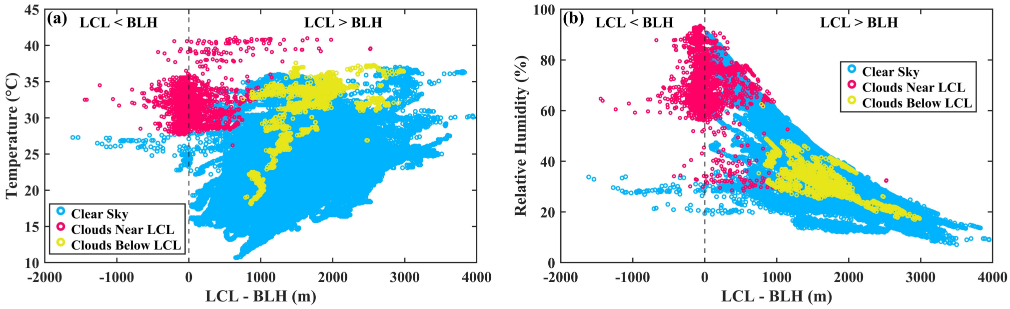

Figure 4.7: Scatter plot illustrating the relationship between (LCL – BLH) and (a) surface temperature and (b) relative humidity for different sky conditions: clear sky (blue), clouds near LCL (red), and clouds below LCL (yellow).

Figure 4.8 depicts the daytime mean surface sensible and latent heat fluxes from ERA5 for the three sky conditions. Across all scenarios, latent heat flux consistently exceeds sensible heat flux, emphasizing its dominant role in regulating boundary layer processes that support convection and cloud formation in semi-arid regions (Alonge et al., 2007). The highest fluxes occur when clouds form near the LCL, with mean values of $152 \pm 115\ \mathrm{W\,m^{-2}}$ for sensible heat and $168 \pm 84\ \mathrm{W\,m^{-2}}$ for latent heat. For clouds below the LCL, latent heat flux increases notably compared to clear skies, reaching an average of $147 \pm 74\ \mathrm{W\,m^{-2}}$, while sensible heat flux remains similar. This suggests that enhanced surface moisture availability, rather than increased thermal instability, plays a more dominant role in supporting cloud formation in these cases. Collectively, these observations indicate that cloud formation below the LCL results from a complex interplay between surface energy fluxes, thermodynamic stratification (as reflected in the LCL–BLH separation), and moisture dynamics.

Further, the interplay between latent heat flux, convection, and cloud formation is fundamental to atmospheric dynamics, particularly in semi-arid regions where surface–atmosphere interactions are highly sensitive to soil moisture availability and radiative forcing. The findings underscore the critical role of latent heat flux in enhancing boundary layer instability and facilitating cloud development. Clouds forming near the LCL exhibit optimal energy exchange conditions, with efficient thermodynamic coupling between the surface and the overlying atmosphere. In contrast, sub-LCL cloud formation reflects more complex feedback mechanisms that modulate local humidity and temperature gradients, often under relatively stable or weakly convective conditions.

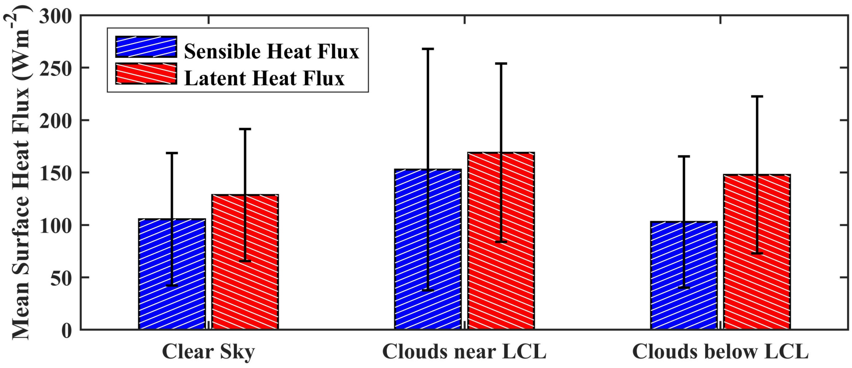

Figure 4.8: Mean surface upward sensible and latent heat flux during daytime over Ahmedabad for clear sky, clouds near LCL, and clouds below LCL derived from ERA5 reanalysis. The error bars represent the standard deviation.

In addition to thermodynamic influences, aerosol–cloud interactions likely contribute to the formation of sub-LCL clouds. Hygroscopic aerosols, prevalent in urban and semi-arid environments like Ahmedabad, can act as CCN and facilitate droplet activation even under sub-saturated conditions, in accordance with Köhler theory (Petters and Kreidenweis, 2007). This mechanism has been observed in polluted atmospheres, where aerosol-driven microphysical processes increase the probability of shallow cloud formation below the LCL (Kawana et al., 2014).

These insights underscore the importance of simultaneously accounting for thermodynamic conditions and aerosol–cloud interactions to accurately capture sub-LCL cloud formation in predictive atmospheric models. The partitioning of surface heat fluxes, governed by both radiative and thermodynamic controls, plays a decisive role in shaping regional weather and climate variability. A deeper understanding of these coupled processes is essential for improving the representation of cloud–aerosol interactions in numerical weather prediction and climate models, particularly in arid and semi-arid environments where small perturbations in surface fluxes and aerosol loading can exert a disproportionate influence on cloud characteristics.

4.7 A case study of boundary layer clouds over Ahmedabad

This section presents a case study of low-level boundary layer clouds observed over Ahmedabad, highlighting their evolution, thermodynamic drivers, and coupling with the ABL. Such in-depth examination complements the earlier statistical analyses by offering a process-level understanding of cloud and ABL interactions. Boundary layer clouds are distinctive low-level cloud formations that typically develop near the top of the boundary layer. Using ground-based Raman Lidar measurements, these clouds were observed during two consecutive days—10 and 11 June 2016—when persistent cloud layers were present over the study site. The results reveal a pronounced sensitivity of these clouds to the diurnal evolution of the ABL, underscoring a strong coupling between cloud properties and boundary layer dynamics.

Figure 4.9 shows the range–time intensity plots of the range-corrected backscattered signal for the two observation days. On 10 June, low-level clouds persisted throughout the day, primarily between 1–2.5 km. A prominent red–yellow patch within $\sim$1 km indicates elevated aerosol–water vapour loading inside the boundary layer. This loading decreased during 08–11 UTC, consistent with the diurnal boundary layer development, when the mixing layer deepened towards midday and facilitated efficient vertical mixing of aerosols. On 11 June, a similar persistent cloud layer was

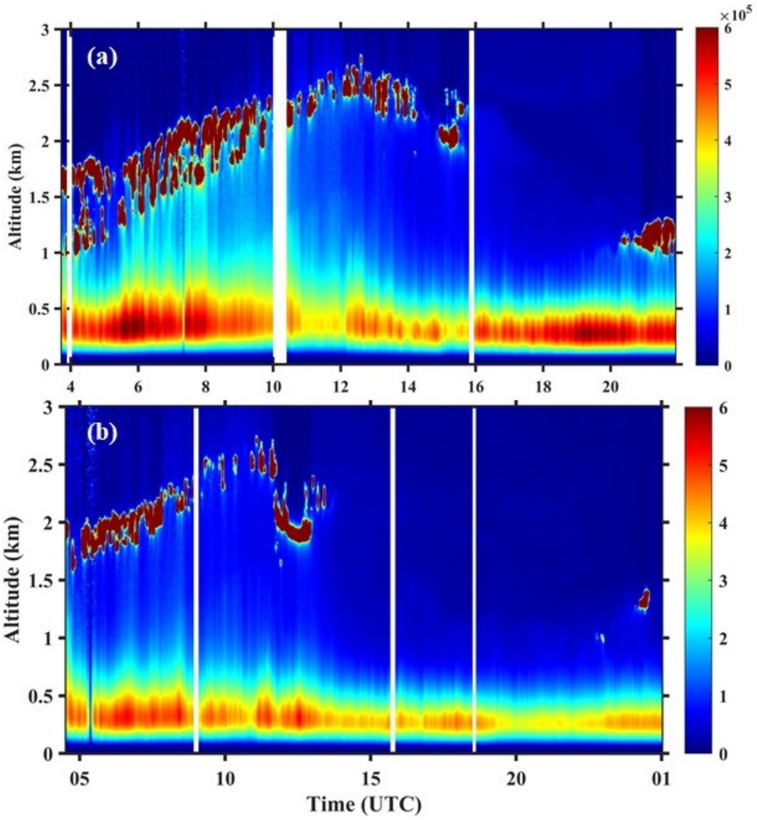

Figure 4.9: Range-time intensity plot of range corrected backscattered signal obtained using Raman Lidar over Ahmedabad on (a) 10 June, (b) 11 June, 2016.

observed, extending between 1.5 km and 2.5–3 km, although aerosol loading within the boundary layer was notably lower compared to the previous day.

Figure 4.10 shows the diurnal variation of the cloud base height (CBH, in red) derived from the Raman Lidar. On 10 June, CBH increased from ∼1 km in the early hours to above 2.5 km during peak solar heating (∼15 LT; UTC+5.5 h), before decreasing later in the day. Between 05–13 UTC, the difference between CBH and boundary layer height (BLH) was minimal, indicating strong coupling. During a midday cloud break, this gap widened to ∼1.36 km by 16 UTC. A similar pattern was noted on 11 June, with CBH and BLH closely coupled for most of the day, the gap reaching ∼1 km at 15 UTC. On both days, CBH remained within the boundary layer during daytime and only ∼0.5 km above the stable nighttime boundary layer, again indicating persistent coupling. Interestingly, on 11 June, CBH peaked earlier, and cloud breakup occurred faster compared to the previous day.

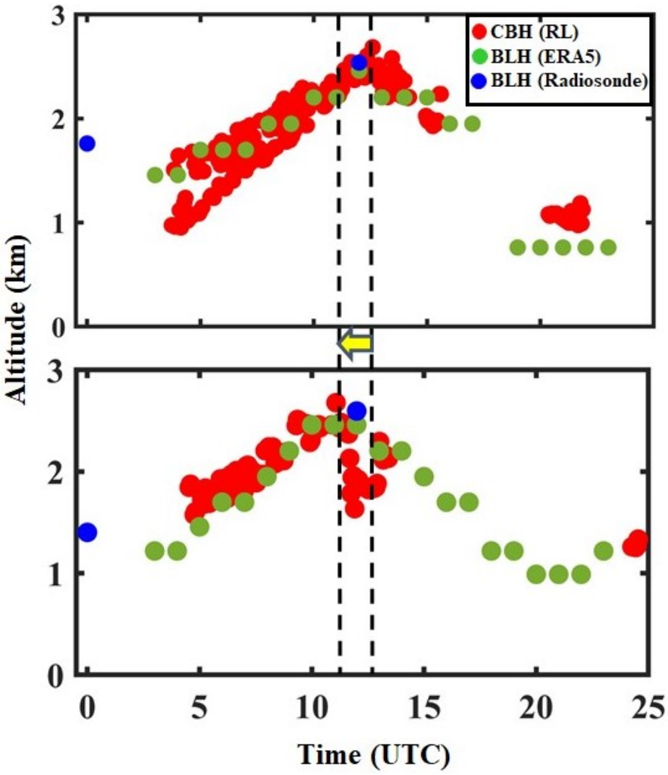

Figure 4.10: Time series of CBH from Raman Lidar, BLH from ERA5 and Radiosonde over Ahmedabad during 10-11 June, 2016.

Surface forcings, particularly sensible and latent heat fluxes, play a pivotal role in modulating boundary layer development, as discussed in the previous section. Since CBH evolution paralleled BLH changes, the same surface-driven processes that control ABL growth also governed the observed cloud variability. The faster breakup on 11 June may be linked to the initial cloud fraction present at the start of the day, suggesting feedback between early cloud cover and subsequent diurnal evolution. This case study demonstrates that the dynamics within the boundary layer directly influence cloud radiative effects, and in turn, clouds modulate ABL thermodynamics. The findings provide valuable ground-based observational evidence over an urban environment, contributing to improved model representation of low-level cloud–boundary layer coupling over land.

4.8 Summary and conclusions

This chapter examined cloud formation below the LCL over the semi-arid region of Ahmedabad using surface observations, radiosonde data, and ground-based remote sensing. An analytical LCL estimate derived from surface temperature and humidity showed good agreement with established formulations and radiosonde-based LCLs. While convective clouds near the LCL occur frequently during the monsoon, clouds forming well below the LCL were detected mainly during the post-monsoon and winter seasons. These sub-LCL clouds typically appeared between 0600 and 1200 UTC within the mixed layer, with mean CBH around 1 km, substantially lower than the corresponding LCL ($\sim$ 2.3 km). Their development occurred under moderate temperatures (24–37°C) and relatively low humidity (17–49%), indicating conditions not usually favorable for classical moist convection.

Surface energy flux analysis showed that events with clouds below the LCL were associated with reduced sensible heat flux and moderate latent heat flux, lower than LCL-near cloud events but higher than clear-sky conditions. This highlights the sensitivity of cloud formation in semi-arid regions to land–atmosphere coupling, soil moisture availability, and diurnal radiative forcing. A case study using Raman Lidar (10–11 June 2016) further demonstrated strong coupling between daytime boundary layer growth and low-level cloud evolution, with CBH closely following BLH throughout the diurnal cycle. Differences in morning boundary layer conditions and surface fluxes modulated the timing of cloud breakup on the two days.

Overall, this chapter shows that sub-LCL cloud formation in Ahmedabad arises from complex interactions among surface fluxes, boundary layer dynamics, and regional thermodynamics. Improved representation of these processes in models is essential for better prediction of low-level clouds in semi-arid environments. Future work should explore high-resolution measurements and modeling to clarify the mechanisms driving these unique cloud–ABL interactions.

****

Chapter 5

Impact of Extreme Events on ABL Dynamics and Cloud Properties

‘

Extreme atmospheric events, such as dust storms and severe air pollution episodes, exert profound impacts on the structure and evolution of the ABL and the associated cloud properties. These events not only influence local meteorology but also have far-reaching implications for air quality, human health, and regional climate. While dust storms predominantly affect arid and semi-arid regions through the entrainment of mineral particles into the atmosphere, severe pollution episodes are often driven by anthropogenic emissions interacting with unfavorable meteorological conditions. These phenomena exert a strong influence on ABL dynamics, where they alter vertical mixing and radiative processes, in turn modifying cloud microphysics and affecting overall atmospheric stability.

Dust storms are characterized by strong winds that lift and transport loose sand and dust particles over vast distances (Goudie, 2009), particularly in regions with sparse vegetation and low soil moisture (Shao and Dong, 2006). These events influence the Earth's radiation budget through scattering and absorption of solar radiation (Fountoukis et al., 2020; Kedia et al., 2018; Slingo et al., 2006) and act as cloud condensation and ice nuclei, thereby altering cloud formation and precipitation patterns (Karydis et al., 2011; Kumar et al., 2009; Möhler et al., 2006). In India, dust storms frequently impact the northern and western regions, including the Indo-Gangetic Plains and the semi-arid landscapes of Western India (Banerjee et al., 2021; Dumka et al., 2019a; Kumar et al., 2015; Singh et al., 2022). The city of Ahmedabad, located near the Thar Desert, experiences such events, especially in the pre-monsoon season, which drastically alter surface meteorology, degrade visibility, elevate particulate matter concentrations, and modify ABL structure (Saha et al., 2022; Santra et al., 2018). This chapter investigates a sudden pre-monsoon dust storm over Ahmedabad using ground-based Ceilometer Lidar, collocated weather sensors, satellite data, radiosonde observations, and reanalysis products to quantify its impact on ABL evolution and cloud dynamics.

In contrast, post-monsoon and winter seasons over Delhi are marked by extreme air pollution episodes, often accompanied by dense fog, that pose severe health risks and disrupt transportation. These events are driven by a combination of intense anthropogenic emissions, vehicular traffic, industrial activities, and biomass burning, and adverse meteorological conditions that suppress vertical mixing (Guttikunda and Goel, 2013; Sharma et al., 2018; Singh et al., 2020). During these seasons, the ABL remains shallow due to weak solar heating and strong nocturnal radiative cooling, trapping pollutants near the surface and leading to frequent exceedances of air quality standards (Murthy et al., 2020). The coexistence of high humidity and elevated particulate matter concentrations favors the formation of low-level clouds or fog, which, when mixed with pollutants, produce smog events that reduce visibility and further degrade air quality (Gautam et al., 2023). Despite numerous studies on air quality and meteorology over Delhi (Kanawade et al., 2020; Nair et al., 2023; Tyagi et al., 2017), high-resolution vertical profiling of the ABL during extreme smog events remains limited. In this chapter, the ABL structure and cloud/fog evolution during severe pollution episodes over Delhi in the 2023–2024 post-monsoon and winter seasons are discussed. Using Ceilometer Lidar observations, along with satellite datasets (INSAT-3D/3DR) and reanalysis products (CAMS, ERA5), the role of meteorology, pollutant loading, and boundary layer processes in shaping fog and smog development is investigated.

By combining analyses of a dust storm over Ahmedabad and severe pollution/fog events over Delhi, this chapter provides a comparative perspective on how distinct extreme events, driven by different sources and seasons, can similarly disrupt ABL structure and cloud processes. Such insights are essential for improving predictive capabilities and for developing targeted mitigation strategies in regions vulnerable to atmospheric extremes.

5.1 Impact of a pre-monsoon dust storm on ABL structure and cloud dynamics over Ahmedabad

This study investigates the characteristics and impacts of a sudden pre-monsoon dust storm over Ahmedabad, a semi-arid region in Western India. Multiple observational platforms were employed, including ground-based Ceilometer Lidar, satellite datasets, surface weather sensors, radiosonde soundings, and reanalysis datasets, to assess the storm's influence on boundary layer dynamics and cloud development. Backscatter profiles from the Ceilometer Lidar were used to characterize the vertical structure of the boundary layer and associated clouds, while collocated weather sensors provided surface meteorological conditions. Satellite observations offered insights into the large-scale dust and cloud evolution, as well as cloud microphysical properties. By integrating these datasets, the study presents a comprehensive analysis of the dust storm's impact on atmospheric structure and cloud processes over the Ahmedabad region.

5.1.1 Observation of dust storm and clouds from satellite

Figure 5.1 presents brightness temperature imagery from the INSAT-3D satellite for 13 May 2024, covering the period from 0630 to 2300 UTC. In satellite imagery, clouds can be identified by their higher reflectance and lower brightness temperatures compared to the underlying surface (Frey et al., 2008). Around Ahmedabad (marked with a circle), two convective systems began forming at approximately 0700 UTC, one toward the southwest and the other toward the northeast. By 1100 UTC, the resulting clouds had expanded to cover the Ahmedabad region and persisted until the following morning. Low brightness temperatures indicate that these clouds extended across much of Rajasthan and Gujarat.

According to the India Meteorological Department (IMD), isolated to scattered light-to-moderate rainfall, accompanied by thunderstorms, lightning, and gusty winds (30–40 km/h), was forecast for the Gujarat region on 13–14 May 2024. Ahmedabad experienced a significant dust storm beginning around 1140 UTC on 13 May, which subsided by 1210 UTC and was followed shortly afterward by rainfall. Such dust storms, often triggered by outflows from moist convection, are common during the pre-monsoon season (Knippertz, 2014). This event represents a similar convection-driven dust storm over western India, with INSAT-3D effectively capturing the evolution of the convective systems leading to cloud formation and subsequent weather events, highlighting the value of geostationary satellite observations for monitoring regional weather patterns.

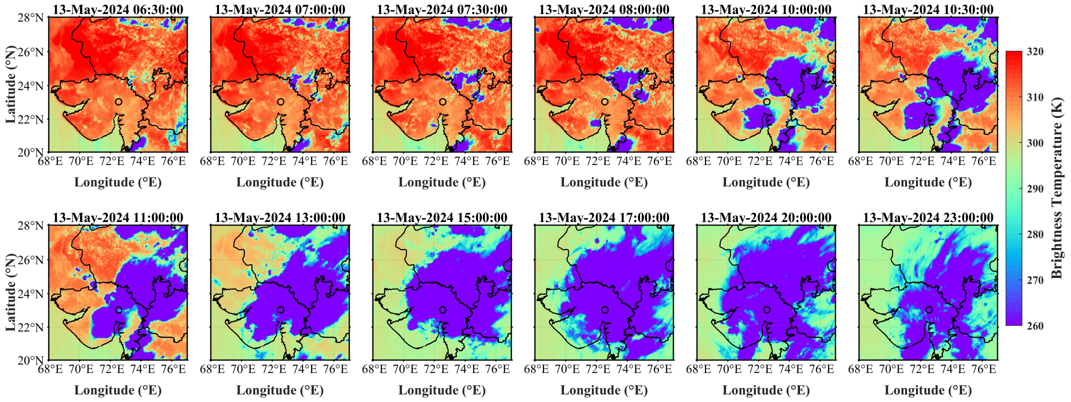

Figure 5.1: Brightness temperature obtained from the INSAT-3D satellite depicting dust and cloud occurrence over the western Indian region on 13 May 2024.

Figure 5.2 shows MODIS reflectance data over western India from 12 to 14 May 2024, with two overpasses each day. On 12 May, low reflectance values were observed over Ahmedabad at 0430 and 0850 UTC. By 0930 UTC on 13 May, significant dust and cloud cover were evident in the vicinity of Ahmedabad, with large patches, several kilometers in size, detected to the southwest and northeast, indicated by high reflectance values. On 14 May, residual high dust concentrations were still apparent over the region.

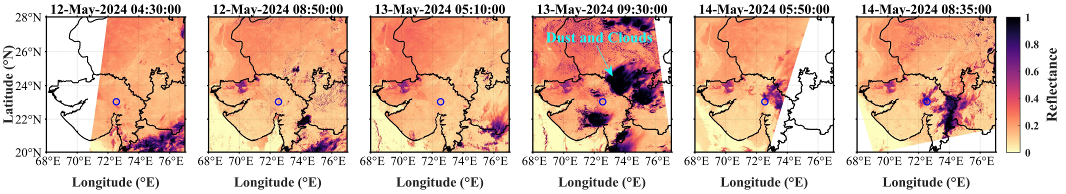

Figure 5.2: Reflectance over the western Indian region from MODIS observations during 12–14 May 2024. High reflectance on 13 May 2024 at 0930 UTC indicates the presence of dust and cloud cover.

These results demonstrate the capability of both INSAT-3D and MODIS to detect dust and cloud features. However, INSAT-3D's geostationary position provides continuous coverage with minimal temporal gaps, making it particularly effective for tracking the rapidly evolving behavior of dust storms and associated cloud systems. Advances in satellite remote sensing have greatly improved dust storm monitoring, leveraging differences in visible and near-infrared reflectance between dust, clouds, and surface features, as well as thermal infrared brightness temperatures (Di et al., 2016; Evan et al., 2006; Sun et al., 2019). Dust typically shows increasing reflectance from 0.4 to 2.5 μm, with a minimum in MODIS band 3 (0.469 μm) and a maximum in band 7 (2.13 μm), whereas clouds have maximum reflectance in band 3 (Qu et al., 2006). This spectral contrast aids dust–cloud discrimination. However, when dust storms are obscured by thick cloud cover, as in this case, satellite detection becomes challenging. To address these limitations, ground-based instruments offer essential complementary measurements.

5.1.2 Clouds and boundary layer dynamics

Figure 5.3 presents the impact of a dust storm on atmospheric clouds and the ABL using Ceilometer Lidar backscatter over Ahmedabad from 12 to 14 May 2024. The normalized backscatter signal, used to distinguish the mixed layer from the free troposphere, shows prominent returns from the lower troposphere, characteristic of the ABL. The BLH, indicated by the black line in Figure 5.3a–c, was derived through gradient analysis, followed by outlier removal, interpolation for missing values, and smoothing of the raw backscatter profiles. On 12 May 2024, a well-defined daytime ABL was observed, with the BLH reaching $\sim$ 2 km before transitioning into a stable nocturnal boundary layer. The next day, the ABL exhibited rapid growth, with BLH peaking near 2.5 km by 1000 UTC. However, around 1140 UTC, the onset of a severe dust storm (Figure 5.3b) caused a rapid collapse of the boundary layer, which was followed by rainfall. After the rain, a thick nocturnal boundary layer began forming around 0600 UTC. By 14 May 2024, the ABL started to recover but remained shallower, with the daytime BLH peaking at only $\sim$ 800 m and a reduced nocturnal BLH, likely due to lower surface temperatures.

ABL evolution is strongly modulated by temperature and relative humidity, with surface heating directly influencing BLH growth (Garratt, 1994). The post-storm rainfall on 13 May cooled surface temperatures, contributing to the suppressed BLH on 14 May. Figure 5.3d–f presents the CBH and vertical visibility during the study period. On 12 May, only sparse clouds were detected at varying altitudes. Following the dust storm on 13 May, widespread cloud cover developed over Ahmedabad, accompanied by rain. Notably, clouds with CBH near 2.7 km at 1210 UTC rose to $\sim$ 7.6 km by 2300 UTC. During the dust storm, vertical visibility decreased to 340–660 m. The rapid collapse of the ABL during such events has been similarly reported by Saha et al. (2022).

Figure 5.4 depicts the influence of the dust storm and subsequent rainfall on the ABL. The dust storm period is highlighted between two white dashed lines. An abrupt

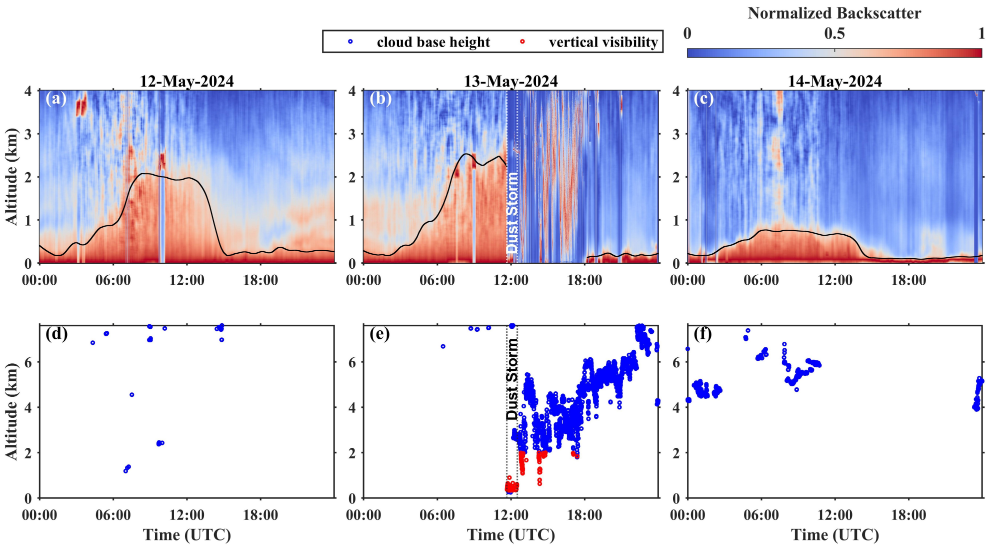

Figure 5.3: (a-c) Boundary layer profile derived from the backscatter signal received from the Ceilometer Lidar at Ahmedabad, during 12-14 May 2024. (d-f) shows the cloud base height (blue circle) and vertical visibility (red circle). The dust storm event is marked between the two white dotted lines in (e) and (f).

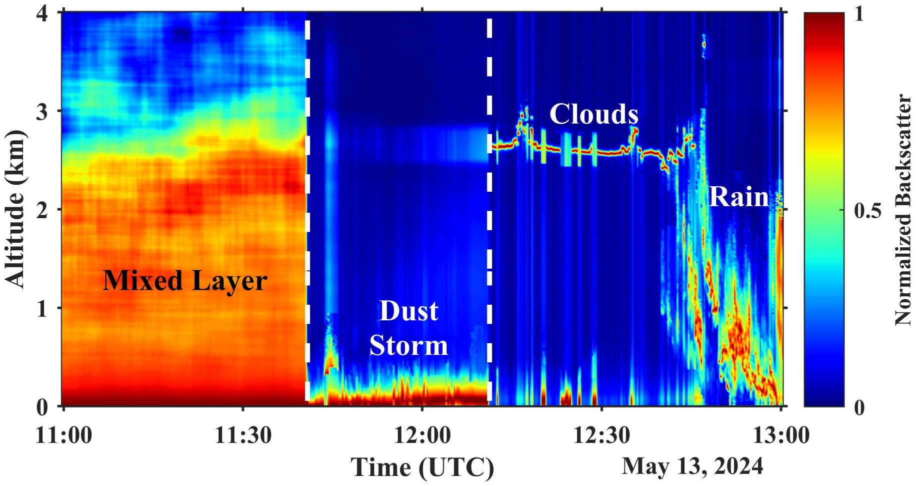

Figure 5.4: Ceilometer Lidar backscatter over Ahmedabad from 1100 to 1300 UTC on 13 May 2024, depicting a well-developed mixed layer before the dust storm, followed by cloud formation and rainfall after the event.

and pronounced disruption in the ABL occurred at 1140 UTC, coinciding with the onset of the storm. Before this, the ABL had evolved into a well-defined mixed layer, with the BLH reaching about 2.5 km. Strong backscatter signals, characteristic of the mixed layer, extended from the surface up to this height. At 1140 UTC, with the arrival of the dust storm, the strong backscatter became confined to only the lowest ~ 250 m, indicating heavy dust loading in the near-surface ABL. The dust appeared concentrated near the ground, behaving like a density current in the lowest troposphere, suggesting a local origin rather than long-range transport. The accompanying cold front compressed the boundary layer, making it shallower (Choi et al., 2008). Around 1210 UTC, clouds formed with a CBH of ~ 2.7 km, persisting into the next morning. Rainfall, starting at 1218 UTC and lasting until 1754 UTC, dissipated the mixed layer and promoted dust settling, leaving behind a much weaker residual layer compared to the previous day. The genesis and cause of this dust storm are discussed in the following section.

5.1.3 Synoptic meteorological conditions

The synoptic meteorological conditions during the dust storm were examined using mean sea level pressure (MSLP) and wind fields from the ERA5 reanalysis. Figure 5.5 shows the MSLP variation over the western Indian region on 13 May 2024 from 0900 to 1300 UTC. A pronounced deepening of the thermal low (formed by intense surface heating) is evident over Ahmedabad between 1000 and 1200 UTC, followed by dissipation thereafter. This deepening was a key driver of strong near-surface winds that initiated the dust storm in the study area. Such pre-monsoon dust storm events are often linked to similar synoptic patterns, with low-pressure systems centered over the Thar Desert and western Indo-Gangetic Plain (Dumka et al., 2019a; Kumar et al., 2014, 2015; Sharma et al., 2012). For instance, Dumka et al. (2019) documented a comparable event over northern India during 12–16 June 2018, where strong near-surface southwesterlies (~ 15–20 m/s) developed in association with monsoon flow responding to thermal low deepening over the Thar Desert. Intense daytime heating over arid and semi-arid regions such as Ahmedabad intensifies the thermal low, promoting convective turbulence and vertical mixing that distributes dust uniformly within the boundary layer, reaching up to ~ 4 km (Kumar et al., 2014).

Additionally, ERA5-derived winds at 1000 hPa and 925 hPa on 13 May 2024, from 1000 UTC to 1200 UTC, are shown in Figure 5.6. The winds at 1000 hPa reveal

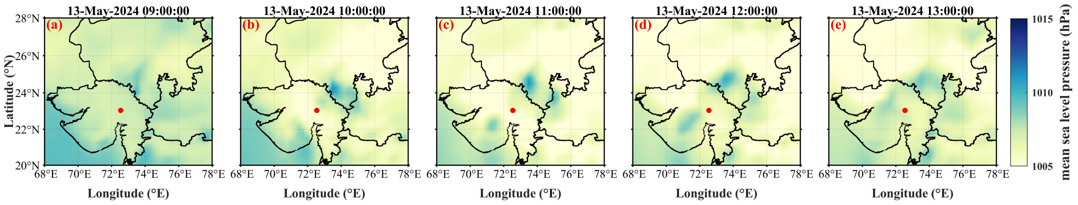

Figure 5.5: Variation in mean sea level pressure (MSLP) over the western-Indian region during 13 May 2024, from 0900 UTC to 1300 UTC.

westerlies of $\sim$ 4–6 $\mathrm{m\,s^{-1}}$ over the Arabian Sea, associated with the summer monsoon flow. A core of stronger winds ($> 10\,\mathrm{m\,s^{-1}}$) is observed advancing progressively inland from the Arabian Sea toward southwest Gujarat, in response to the deepening of the heat low over the Ahmedabad region (Figure 5.6a–c). These near-surface winds played a pivotal role in triggering the sudden onset of the dust storm. When such strong monsoon winds move northward into the semi-arid and arid regions of Gujarat and Rajasthan, they can initiate dust emissions. This process occurs because the monsoon flow behaves like a density current, driven by the density contrast between the cooler, moisture-laden monsoon air and the warm, dry air over these regions (Bou Karam et al., 2008). At 925 hPa, strong winds are also evident over southeastern Rajasthan during the same period (Figure 5.6d–f).

The radiosonde launch site at Ahmedabad Airport is located approximately 13 km from the Physical Research Laboratory, where the Ceilometer Lidar and weather stations operate. Radiosondes are released twice daily at 0000 UTC and 1200 UTC. Figure 5.7 presents vertical profiles of key meteorological parameters from 12–14 May 2024 at 1200 UTC. A dust storm impacted the study site on 13 May 2024 between 1140 and 1210 UTC, so the profiles for this date capture conditions during the event. The temperature profile remained broadly consistent across the three days, peaking on the day of the dust storm and reaching its lowest values the following day (Figure 5.7a). During the storm, relative humidity rose from 7% at the surface to 82% near 2.6 km altitude (Figure 5.7b). As discussed in Section 3.2, the Ceilometer detected clouds at ~ 2.7 km after the storm, and this peak in humidity supports the likelihood of cloud formation. The water vapor mixing ratio (WVMR) followed a

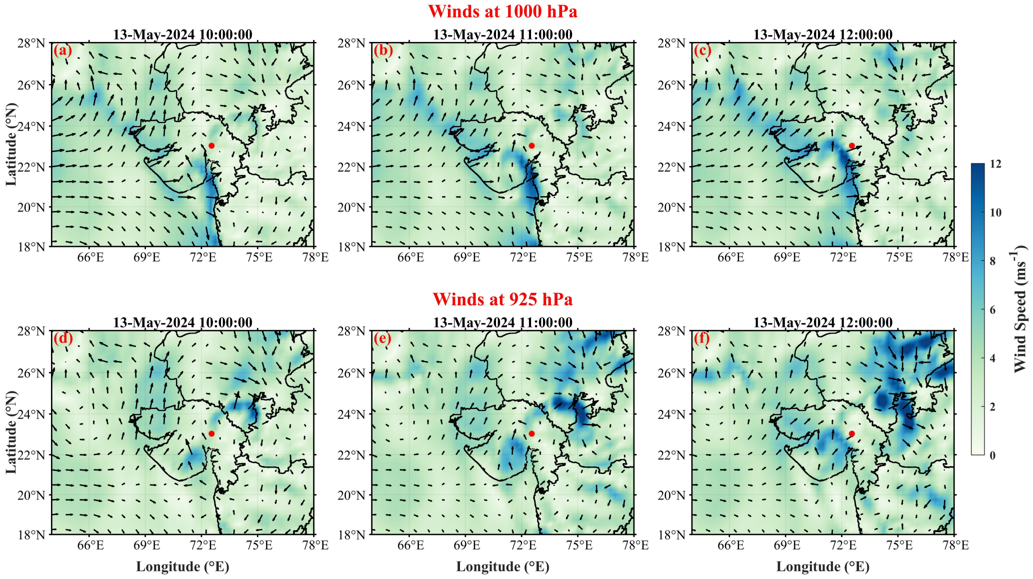

Figure 5.6: ERA5-derived wind fields over the western Indian region on 13 May 2024 between 1000 and 1200 UTC at 1000 hPa (top panel) and 925 hPa (bottom panel).

similar pattern, increasing from the surface to $\sim$ 2.6 km and reaching 12.62 g/kg. WVMR values were higher on 12 May and lower on 14 May, likely influenced by rainfall on 13 May (Figure 5.7c). Near-surface wind speeds were lowest on 12 May ($\sim$ 2 m/s) but increased to $\sim$ 6 m/s at 100 m height during the storm (Figure 5.7d).

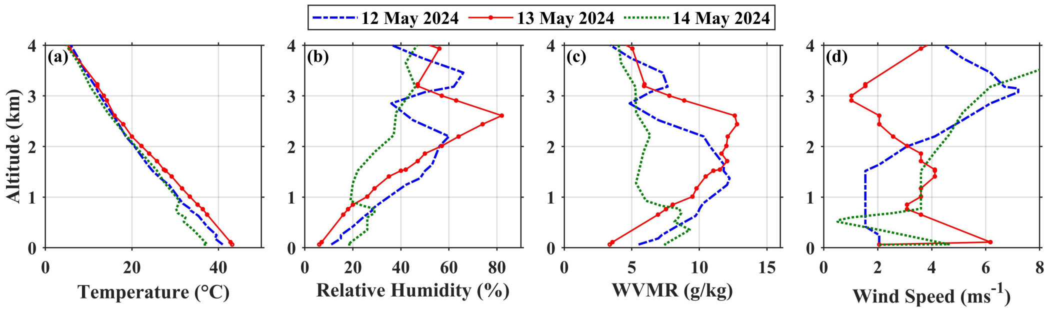

Figure 5.7: Vertical profiles of temperature, relative humidity, water vapor mixing ratio (WVMR), and wind speed over Ahmedabad on 12, 13, and 14 May 2024 at 1200 UTC, derived from radiosonde observations.

5.1.4 Dust and cloud interaction

The dust storm, triggered by two moist convection systems over the Western Indian region, led to widespread cloud formation across large areas of Rajasthan and Gujarat, ultimately producing precipitation. Table 5.1 summarizes the cloud properties during this event as observed by the MODIS and VIIRS instruments. Deep convective clouds with top heights between 13 and 16 km were seen advancing toward Ahmedabad from the southwest. These clouds exhibited a cloud water path (CWP) of approximately 1530 g/m^2 and cloud optical thickness (COT) near 150. Similarly, strong convection over southeastern Rajasthan generated clouds with vertical extents around 11 km, COT of 150, and a CWP close to 1209 g/m^2, consistent with MODIS observations. These findings were corroborated by VIIRS data onboard the Suomi National Polar-orbiting Partnership (SNPP) satellite.

Table 5.1: Cloud properties derived from the MODIS, VIIRS/NOAA-20, and VIIRS/SNPP on 13 May 2024 over the Western Indian region.

Time	(Latitude, Longitude)	Instrument/Satellite	CER (μm)	COT	CWP (g m^{-2})	CTH (m)
2024-05-13 08:35	(22.00°N, 72.40°E)	MODIS	17.92	137	1497	14337
2024-05-13 08:48	(22.00°N, 72.00°E)	VIIRS SNPP	13.12	150	1187	13161
2024-05-13 09:12	(22.00°N, 72.00°E)	VIIRS NOAA-20	16.82	150	1529	15972
2024-05-13 07:36	(24.61°N, 73.67°E)	VIIRS NOAA-20	14.43	8	70	12904
2024-05-13 08:48	(24.61°N, 73.67°E)	VIIRS SNPP	16.65	127	1284	13132
2024-05-13 09:30	(24.61°N, 73.67°E)	MODIS	13.35	150	1209	13846

The deep convective clouds associated with the dust storm resulted in intense precipitation over Ahmedabad. Dust particles interact with clouds, altering their microphysical characteristics and influencing precipitation processes (Bangert et al., 2012; Feng et al., 2023; Huang et al., 2018; Weger et al., 2018; Yin et al., 2002). Insoluble dust becomes a more effective cloud condensation nucleus (CCN) after acquiring a sulfate coating within convective clouds, thereby enhancing droplet activation and precipitation formation in subsequent cloud development (Yin et al., 2002). Moreover, dust particles can intensify extreme precipitation by promoting ice cloud formation and strengthening convection. Acting as ice nuclei in the upper troposphere, they facilitate ice cloud growth and amplify convection through latent heat release (Feng et al., 2023). These observations underscore the significant influence of the dust storm on cloud development and microphysical properties in the region. Satellite data from MODIS and VIIRS offer valuable insights into the complex interactions between dust aerosols and cloud dynamics during such atmospheric events.

5.2 ABL and low-level cloud/fog evolution during severe pollution episodes over Delhi

This study addresses the critical need to understand how meteorological conditions and ABL dynamics influence pollution buildup and fog formation in Delhi, with a particular focus on dense smog episodes. Delhi, the National Capital Territory of India, is a densely populated metropolitan area situated in the Indo-Gangetic Plain (IGP). The city, encompassing approximately 1483 km^2, lies between 28.39°N and 28.88°N latitude and 76.84°E and 77.33°E longitude, spanning three main geographical zones: the low-lying Yamuna floodplains, the Aravalli Ridge, and the broader Indo-Gangetic Plain (Figure 5.8). The Yamuna River flows through the city, with most urban areas located to its west. Delhi's elevation ranges from 180 to 316 meters above mean sea level.

The city's unique topography and geography heavily influence its air quality, fog formation, and boundary layer processes. Delhi is vulnerable to regional pollution transport, especially from agricultural residue burning in Punjab and Haryana during the post-monsoon season, while the Himalayas to the north limit pollutant dispersion (Govardhan et al., 2023). The Aravalli Ridge on Delhi's western and southern borders disrupts wind flow, reducing ventilation and promoting pollutant accumulation. These features create a natural bowl-like basin that inhibits pollution dispersion. The Yamuna floodplains contribute to higher humidity, enhancing fog formation that often mixes with pollutants to form dense smog (Sathiyamoorthy et al., 2016). During winter, temperature inversions trap pollutants near the surface, intensified by Delhi's urban

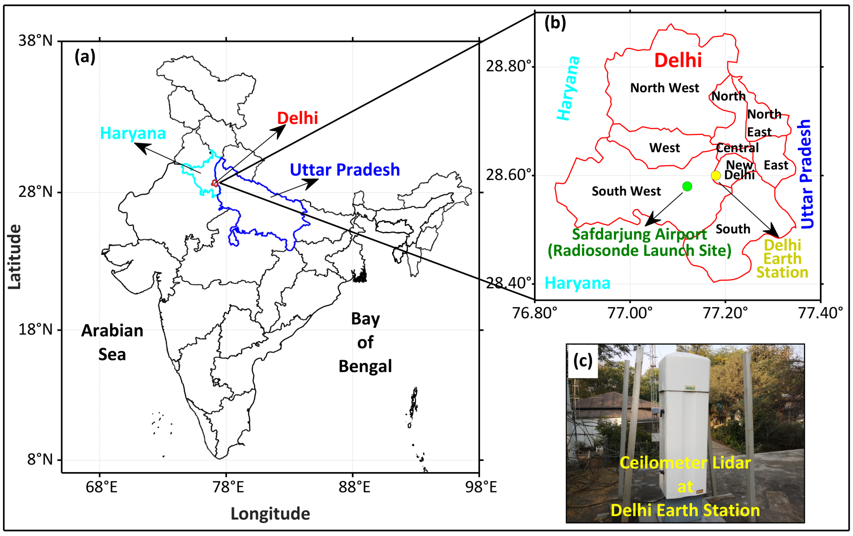

Figure 5.8: (a) Geographic location of Delhi in India. (b) Map of Delhi showing locations of the Delhi Earth Station, where the Ceilometer Lidar is operational, and Safdarjung Airport, the site of radiosonde launches. (c) The Ceilometer Lidar operational at the Delhi Earth Station (DES), New Delhi.

heat island effect, which inhibits vertical mixing (Pandey et al., 2012). Together, these factors create a complex microclimate driving severe pollution and fog episodes in Delhi's post-monsoon and winter seasons.

5.2.1 $PM_{2.5}$, PM_{10}, and AOD over Delhi and the IGP region during post-monsoon and winter

The IGP has experienced severe air pollution in recent decades, particularly during the post-monsoon (October and November) and winter months (December, January, and February). This is attributed to increased transportation, industrial activities, residential energy use, and biomass burning, combined with the influence of local and large-scale meteorological conditions (Awasthi et al., 2024; Garsa et al., 2023; Singh et al., 2020). Figure 5.9 shows the monthly mean surface concentrations of $PM_{2.5}$ (a–e), PM_{10} (f–j), and total aerosol optical depth (AOD) (k–o) over the IGP region from October 2023 to February 2024 obtained from CAMS reanalysis. Clearly, the pollution hotspots include Delhi and parts of the eastern IGP.

Over Delhi and the IGP region, the concentrations of $PM_{2.5}$ and PM_{10} begin rising in October, peak in November and December, and then decline in January and February. Delhi exhibits the highest levels of $PM_{2.5}$ and PM_{10} within the IGP region. The monthly mean $PM_{2.5}$ concentrations in Delhi from October 2023 to February 2024 were found to be 248 μgm^{-3}, 398 μgm^{-3}, 358 μgm^{-3}, 344 μgm^{-3}, and 268 μgm^{-3}, respectively, as per CAMS reanalysis data (Fig. 5.9a–e). Similarly, the monthly mean PM_{10} concentrations were 349 μgm^{-3}, 561 μgm^{-3}, 506 μgm^{-3}, 487 μgm^{-3}, and 379 μgm^{-3}, respectively (Figure 5.9f–j). Vehicular emissions and biomass burning are among the primary sources of these high levels of $PM_{2.5}$ and PM_{10} in Delhi during the post-monsoon and winter seasons (Singh et al., 2020). The surge in $PM_{2.5}$ and PM_{10} concentrations is also driven by stable meteorological conditions, pollution transport from agricultural burning in Punjab and Haryana, and greater domestic heating during colder months (Jain et al., 2020).

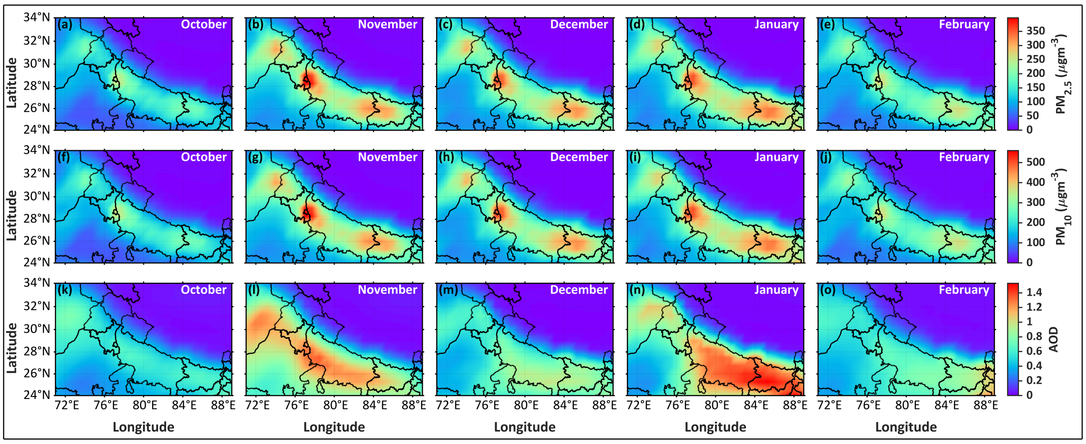

Figure 5.9: Monthly mean values of surface $PM_{2.5}$ (a-e), PM_{10} (f-j), and total AOD (k-o) over the IGP during post-monsoon (October and November) and winter (December, January, and February), based on CAMS reanalysis data from 2023 to 2024.

In contrast to $PM_{2.5}$ and PM_{10}, the AOD does not follow the same spatiotemporal trend during October 2023 to February 2024. AOD over the Indo-Gangetic Plain is higher during November and January than in October, December, and February due to a combination of agricultural and meteorological factors (Jethva et al., 2005). In November, widespread crop residue burning in Punjab and Haryana releases large quantities of aerosols transported across the region by prevailing winds. While burning activity subsides by January, winter meteorological conditions, such as low BLH, temperature inversions, and calm winds, trap pollutants near the surface, maintaining high aerosol concentrations. In contrast, October marks the start of post-monsoon burning with lower initial AOD, while December and February experience slightly better atmospheric dispersion, leading to comparatively lower AOD levels.

While $PM_{2.5}$ and PM_{10} concentrations are highest over Delhi from October to February due to local emissions and strong wintertime surface inversions, AOD is higher over the central and eastern IGP. This discrepancy arises because AOD measures the total columnar aerosol load, not just surface-level particles. In eastern IGP, aerosols transported from upwind regions like Punjab and Delhi accumulate aloft, and higher humidity supports secondary aerosol formation, enhancing AOD. Thus, while surface PM peaks in Delhi, regional transport and vertical distribution cause higher AOD further east. Over Delhi, the monthly mean AOD values during October 2023 to February 2024 were 0.62, 1.28, 0.73, 0.98, and 0.67, respectively.

While CAMS reanalysis data provided valuable insights into the regional spatiotemporal patterns of $PM_{2.5}$, PM_{10}, and AOD across the IGP region, due to their broad spatial coverage and consistent data availability, a comparison with ground-based measurements over Delhi reveals a notable overestimation of $PM_{2.5}$ concentrations. The overestimation is likely due to limitations in the vertical resolution and surface-level calibration of reanalysis products, particularly in complex urban environments like Delhi, where local emission sources and boundary layer dynamics play a critical role in pollutant accumulation.

5.2.2 Diurnal variation of BLH and $PM_{2.5}$ over the Delhi region during post-monsoon and winter

The ABL is essential in governing the dispersion of pollutants, which directly impact air quality. One of the key factors influencing pollutant concentrations is the BLH, which, along with emission and deposition rates, determines how pollutants spread and accumulate in the atmosphere (Murthy et al., 2020). Figure 5.10a–e shows the monthly mean diurnal variation of the BLH over the Delhi region from October 2023 to February 2024, derived using Ceilometer Lidar observations and ERA5 reanalysis data. The Ceilometer-derived BLH (represented by the black line) reveals a very shallow boundary layer in November and January, with peak BLH values reaching only 312 ± 265 m and 184 m, respectively. The BLH increases slightly in December, with a peak value of 551 ± 244 m. However, the BLH is notably deeper in October and February, with peak values of 1093 ± 469 m and 1119 ± 1048 m, respectively.

These monthly variations in BLH over the Delhi region are primarily driven by changes in surface temperature, solar radiation, and atmospheric stability. In October and February, relatively higher solar insolation and warmer surface temperatures enhance convective turbulence, leading to deeper boundary layers. In contrast, during the winter months of November to January, the region experiences reduced solar heating, lower temperatures, and frequent temperature inversions that stabilize the atmosphere and suppress vertical mixing. The nighttime values of BLH are very low. At night, a strong radiative thermal inversion results in the region being covered by a shallow ABL (Murthy et al., 2020; Raj et al., 2021). The ERA5-derived BLH shows a gradual decrease from October to January and then an increase in February, with corresponding peak values of 1759 ± 428 m, 1439 ± 353 m, 1015 ± 287 m, 827 ± 282 m, and 1142 ± 442 m, respectively. Notably, the ERA5 reanalysis tends to overestimate BLH compared to ground-based Ceilometer Lidar observations during the day, while underestimating it at night.

Figure 5.10f–j shows the monthly mean diurnal variation of $PM_{2.5}$ concentration over the Delhi region from October 2023 to February 2024 obtained from the air quality monitoring system at the US Embassy in Delhi. The maximum hourly mean $PM_{2.5}$ values during October, November, December, January, and February are 125 ± 73 μgm^{-3}, 301 ± 110 μgm^{-3}, 253 ± 83 μgm^{-3}, 280 ± 90 μgm^{-3}, and 135 ± 60 μgm^{-3}, respectively. Earlier studies reported similar and higher hourly mean val-

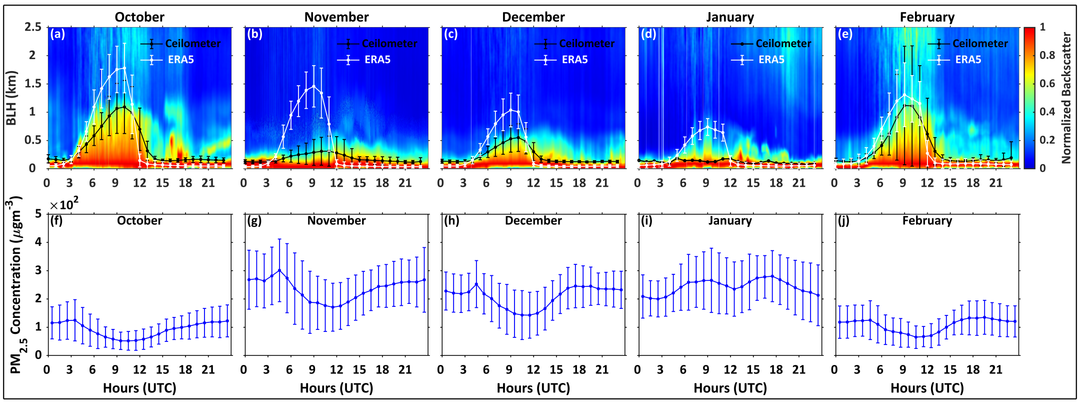

Figure 5.10: (a-e) Monthly mean diurnal variation of the BLH over Delhi derived using backscatter signal from Ceilometer Lidar from October 2023 to February 2024. The background illustrates a typical boundary layer profile for each month, representing the average boundary layer characteristics for that month. The black and white markers represent the hourly mean (with standard deviation) of BLH derived from Ceilometer Lidar and ERA5 reanalysis, respectively. (f-j) Variation of $PM_{2.5}$ concentration derived from the air quality monitoring system at the US Embassy in Delhi.

ues of $PM_{2.5}$ concentration over the Delhi region (Dumka et al., 2019b; Tiwari et al., 2018; Tyagi et al., 2017). The minimum mean concentration of $PM_{2.5}$ occurs between 09:00 to 12:00 UTC in October, November, December, and February when the BLH is maximum. This is in agreement with the inverse relationship between the $PM_{2.5}$ concentrations and BLH. It is found that a negative relationship exists between $PM_{2.5}$ concentrations and BLH, which can be approximated as a power function. A similar relationship between the $PM_{2.5}$ concentrations and BLH is reported in a study of haze episodes in winter in the North China Plain (Li et al., 2020).

5.2.3 Meteorological conditions over the Delhi region during post-monsoon and winter

The local and large-scale meteorological conditions play a critical role in shaping heavy air pollution and fog formation in the Delhi region. Figure 5.11 shows the monthly mean diurnal variation of temperature, dew point, relative humidity, wind speed, wind direction, and the ventilation coefficient (VC) over the Delhi region from October 2023 to February 2024. The VC is a parameter that indicates the atmosphere's capacity to disperse pollutants and is considered a measure of air quality (Iyer and Raj, 2013). It is calculated as the product of the BLH and wind speed. The VC is calculated using wind speed data obtained from AWS and BLH data from the Ceilometer Lidar measurements.

During the observation period, maximum and minimum temperatures were recorded in October and January, respectively (Figure 5.11a). The monthly mean temperatures during October 2023 – February 2024 were approximately 26±5 °C (October), 20±5°C (November), 15±5°C (December), 12±4°C (January), and 18±6°C (February). The dew point followed a similar monthly trend. However, its diurnal variation remained weak (Figure 5.11b). This weak diurnal variation in dew point, combined with consistently high nighttime relative humidity, approaching 100% on several occasions in December and January (Figure 5.11c), indicates favorable conditions for persistent fog formation. These fog events can significantly hinder pollutant dispersion, promote secondary aerosol formation via aqueous-phase reactions, and contribute to poor visibility and elevated particulate matter levels (Acharja et al., 2022; Jia et al., 2023; Mishra et al., 2023). Relative humidity was highest during December and January, with monthly mean values of 81±21% and 83±17%, respectively, compared to 70%±20% (October), 80%±18% (November), and 70%±22% (February). Wind speed showed a contrasting trend, with the highest values observed in February and the lowest in November and December (Figure 5.11d). The monthly mean wind speeds were $0.83\pm1.19\text{ms}^{-1}$ (October), $0.44\pm0.87\text{ms}^{-1}$ (November), $0.59\pm1.01\text{ms}^{-1}$ (December), $1.01\pm1.14\text{ms}^{-1}$ (January), and $1.44\pm1.54\text{ms}^{-1}$ (February). These low wind speeds during post-monsoon and winter further exacerbate pollution accumulation by reducing horizontal ventilation and pollutant dispersion (Garsa et al., 2023).

Figure 5.11e shows the diurnal variation of the VC in the Delhi region from October 2023 to February 2024, showing a midday peak pattern similar to that of BLH. VC values remained below $1000\text{m}^2\text{s}^{-1}$ during November, December, and January, indica-

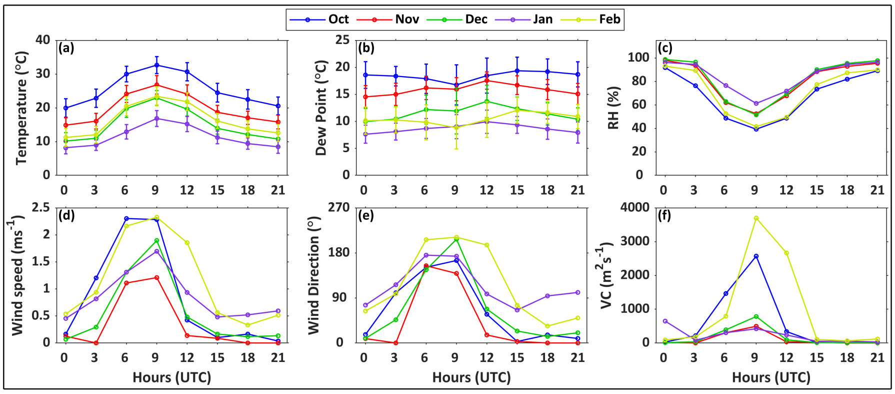

Figure 5.11: Monthly mean diurnal variation of (a) temperature, (b) dew point, (c) relative humidity, (d) wind speed, (e) wind direction, and (f) ventilation coefficient over Delhi from October 2023 to February 2024.

tive of limited vertical mixing. The average monthly VC values were approximately $592\pm1171\mathrm{m}^2\mathrm{s}^{-1}$ (October), $112\pm367\mathrm{m}^2\mathrm{s}^{-1}$ (November), $182\pm423\mathrm{m}^2\mathrm{s}^{-1}$ (December), $223\pm547\mathrm{m}^2\mathrm{s}^{-1}$ (January), and $994\pm2257\mathrm{m}^2\mathrm{s}^{-1}$ (February). These low VC values during the winter months significantly restrict the atmospheric dispersion potential, thereby facilitating the buildup of pollutants near the surface and aggravating air quality degradation. Saha et al. (2019) reported a long-term average VC of $1249\pm236\mathrm{m}^2\mathrm{s}^{-1}$ in Delhi during 2006–2014. Another study by Iyer and Raj (2013) reported a decreasing trend in VC over four metropolitan cities, Mumbai, Delhi, Kolkata, and Chennai, between 1970 and 2000. This decline suggests an increasing pollution potential and deteriorating air quality in these urban centers. Compared to Delhi, other metros exhibited lower pollution potential due to the mitigating effects of sea breezes, which facilitated pollutant dispersion and reduced ground-level concentrations. Delhi's landlocked geography and winter meteorological conditions contribute to poorer dispersion capacity and higher pollution levels.

5.2.4 Fog occurrence frequency over Delhi and the IGP region during winter

Fog is a low-lying cloud that touches the ground, significantly reducing horizontal visibility to less than 1 km. In Delhi, dense fog typically forms during winter due to stable atmospheric conditions, lower surface temperatures, high relative humidity, and a strong low-level inversion that sometimes persists throughout the night (Kulkarni et al., 2019). These conditions are further exacerbated by local emissions from vehicular traffic and industrial sources, which contribute to the availability of condensation nuclei and can enhance fog formation and persistence. Furthermore, the role of synoptic systems such as western disturbances has been emphasized in multiple studies (Parde et al., 2024; Smith et al., 2023). These systems contribute to fog formation by increasing low-level moisture and enhancing radiative cooling during winter nights. The fog episodes over Delhi and adjoining areas often coincide with the passage or influence of western disturbances, which reinforces the importance of integrating synoptic-scale analysis in future fog prediction models.

Figure 5.12 presents the spatial distribution of fog occurrence frequency over the IGP during December 2023 and January 2024, derived from INSAT-3D and INSAT-3DR satellite observations. The monthly mean fog occurrence exceeds 75% in certain regions, highlighting the intensity and spatial extent of fog episodes during the core winter months. A clear seasonal progression is evident, with higher fog occurrence frequencies in January compared to December. This increase can be attributed to more prolonged and intense radiative cooling events in January, often coinciding with calm wind conditions and higher moisture availability. Notably, INSAT-3D exhibits higher fog detection frequencies than INSAT-3DR. This discrepancy may result from differences in their observation geometry, channel sensitivity, and temporal sampling, as the satellites operate in a staggered manner. Moreover, both satellites reveal a consistent west-to-east decrease in fog frequency across the IGP, likely influenced by regional variations in surface characteristics, aerosol loading, and moisture gradients (Bharali et al., 2024).

Figure 5.11e shows the diurnal variability of fog frequency over Delhi. According to INSAT-3D, the fog frequency remains below 20% throughout the day in December, suggesting limited fog persistence beyond early morning hours. In contrast, INSAT-3DR shows a similar frequency to INSAT-3D between 03:15 and 10:45 UTC,

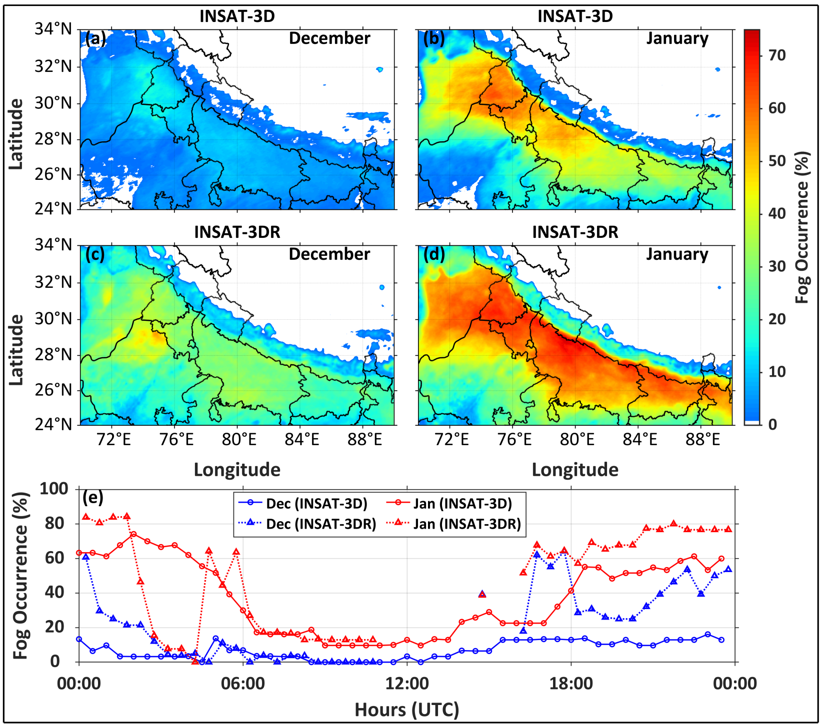

Figure 5.12: (a-d) Fog occurrence frequency over the IGP region in December and January during 2023-2024 derived from INSAT-3D and 3DR satellites. (e) Diurnal variation of fog occurrence frequency over the Delhi region.

indicating a similar daytime fog detection performance of the two satellites. However, during the nighttime, the fog occurrence frequency values from INSAT-3DR reach up to 40%. The discrepancies between the two satellites are observed in the detection of nighttime and early morning fog. In January, a substantial increase in diurnal fog frequency is observed over Delhi and the IGP region. INSAT-3D data indicate a range between 10% and 74%, with maxima occurring during the nighttime (18:00–00:00 UTC) and morning hours (00:00–06:00 UTC), corresponding to typical radiative fog formation times under clear skies and calm conditions. INSAT-3DR shows a comparable pattern, reinforcing the diurnal dependence of fog formation on surface cooling rates and nocturnal boundary layer dynamics.

Several studies attempted to study the trend in fog occurrence frequency over Delhi and the IGP region. Kutty et al. (2020) investigated a 37-year dataset (1977/78 to 2013/14) and identified a statistically significant increasing trend in wintertime fog frequency. This increase was attributed to changes in associated meteorological parameters such as surface cooling, moisture content, and synoptic-scale influences. Interestingly, the study also identified a shift in fog visibility patterns before and after 1998, possibly linked to the rise in aerosol loading and land-use changes. Smith et al. (2023) corroborated these findings using ground-based observations, noting significantly positive trends in the frequency of fog events at key IGP locations, Delhi, Lucknow, and Patna, between 1997/1998 and 2018/2019. Their analysis revealed that this increase was primarily driven by radiation fog, a type that forms under clear, stable, and humid conditions typically found in the region during winter. These long-term trends affirm the continued relevance of studying fog using both ground-based and satellite platforms.

5.2.5 Severe air pollution and fog episodes over Delhi during October 2023 – February 2024

Figure 5.13 presents the temporal variation of BLH, vertical visibility (VV), cloud base heights (CBH1 and CBH2), $PM_{2.5}$ concentration, and relative humidity over the Delhi region from October 2023 to February 2024. With the onset of the post-monsoon season in October, the region begins to experience a buildup of haze and pollution, along with a gradual decline in BLH. A prolonged episode of heavy haze and pollution is evident between 20 October and 25 November 2023, characterized by consistently low BLH, poor visibility (VV < 2 km), and high surface-level $PM_{2.5}$ concentrations exceeding 500 μgm^{-3}. Concurrently, an increase in daily maximum relative humidity is observed, which further contributes to the trapping of pollutants near the surface. Following this period, from 4 December to 19 December 2023, a temporary improvement in air quality is observed, as $PM_{2.5}$ concentrations slightly decline and haze conditions subside.

However, starting 20 December, $PM_{2.5}$ levels spike once again, initiating another phase of severe pollution. From 25 December, early morning fog events begin to appear, persisting until 28 December, followed by the formation of persistent low-level

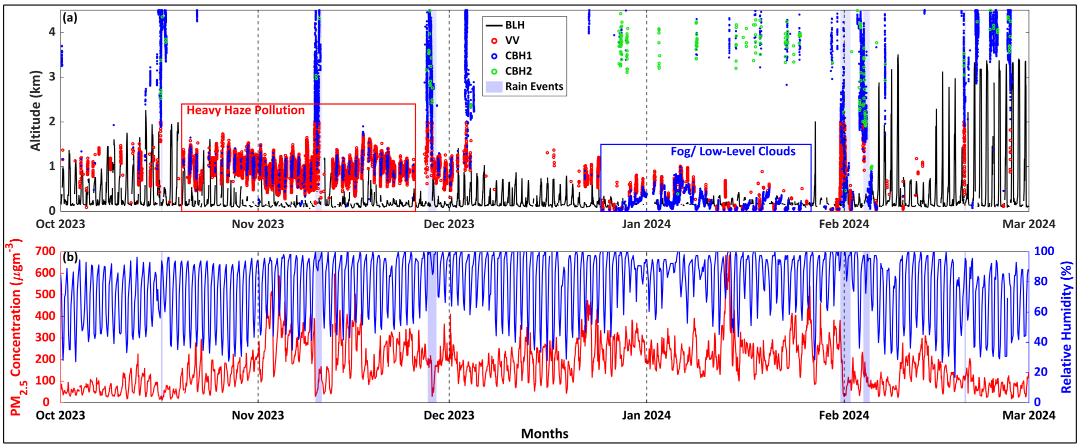

Figure 5.13: (a) Temporal variation of BLH, VV, CBH1, and CBH2 over the Delhi region derived from Ceilometer Lidar during October 2023 to February 2024. Periods of heavy haze pollution (red box) and fog/low-level clouds (blue box) are highlighted. (b) Variation of $PM_{2.5}$ and relative humidity during the same period. The blue shaded regions represent the rain events.

clouds (Figure 5.13a). This fog episode, lasting from 25 December 2023 to 26 January 2024, is marked by shallow BLH, high relative humidity reaching 100% during nighttime and early mornings, and the presence of a second cloud layer between 3 to 5 km, indicating complex vertical stratification. The combination of fog, low-level clouds, and elevated humidity during this period further suppresses vertical mixing, allowing pollutants to accumulate near the surface. A noticeable decline in $PM_{2.5}$ concentrations is observed from 13 February 2024 onwards, coinciding with a rise in BLH, indicating improved atmospheric dispersion conditions. Several short-duration rain events occurred throughout the study period, and each is associated with a distinct and immediate drop in $PM_{2.5}$ concentrations (Figure 5.13b), highlighting the role of wet deposition in temporarily improving air quality.

Table 5.2 compares the meteorological conditions during the two events: a heavy haze pollution episode from 12–18 November 2023 and a fog event from 25–31 December 2023.

Between October 2023 and February 2024, the combined frequency of haze pollution, fog, and low-level clouds was approximately 22.46%, as observed using the

Table 5.2: Summary of key meteorological and air quality parameters over Delhi during 12-18 November and 25-31 December 2023.

Parameter	**12–18 Nov 2023**	**25–31 Dec 2023**
Surface Temperature (°C)	$\sim$19 ± 5	$\sim$14 ± 4
Relative Humidity (%)	80 ± 19	87 ± 14
Wind Speed (m s^{-1})	mostly stagnant; Mean: $\sim$0.33 ± 0.76	light; Mean: $\sim$0.7 ± 0.9
Dominant Wind Direction	Calm, NW	NW, W
Boundary Layer Height (m)	247 ± 263	163 ± 90
$PM_{2.5}$ (µg m^{-3})	Peak: $\sim$599; Mean: $\sim$236 ± 117	Peak: $\sim$385; Mean: $\sim$258 ± 56
Fog/Smog Presence	Haze	Persistent fog & dense smog

Ceilometer Lidar. For haze and fog events, the Ceilometer provides vertical visibility. The strength of the backscatter signal follows the order: haze $<$ fog $<$ cloud. In foggy conditions, most of the backscatter signal is concentrated below 500 m. In contrast, during haze events, the signal is not completely attenuated near the surface and extends throughout the 0–2 km range. During the observation period, the highest frequency of these phenomena occurred in November (45.10%) and January (39.55%). In November, haze pollution was the dominant contributor, whereas fog and low-level clouds were more prevalent in January. Relatively lower frequencies were observed in October (10.92%), December (14.26%), and February (2.42%).

5.3 Summary and conclusions

This chapter presented two distinct case studies highlighting the interplay between ABL dynamics, meteorological conditions, and extreme atmospheric events over different regions of India. The first study examined a sudden dust storm over Ahmedabad on 13 May 2024, triggered by the outflow of two convective systems from southwest

Gujarat and southeast Rajasthan. Satellite observations from INSAT-3D, MODIS, and VIIRS, along with ground-based Ceilometer Lidar data, revealed an abrupt collapse of the mixed layer from ~ 2.5 km to ~ 250 m, accompanied by reduced vertical visibility (340–660 m) and significant increases in near-surface humidity. The event led to the formation of deep convective clouds with vertical extents up to 11 km and heavy rainfall (~ 19 mm). Surface temperatures initially rose to 42°C but dropped sharply the following day, indicating a dust-induced cooling effect. These results underscore the strong coupling between moist convection, dust transport, and ABL structure, and demonstrate the value of integrated satellite, lidar, and meteorological observations for real-time monitoring.

The second study investigated ABL behavior during severe air pollution and fog episodes over Delhi between October 2023 and February 2024. Continuous Ceilometer Lidar observations revealed pronounced seasonal and diurnal variability, with shallow daytime BLH during peak pollution months (November–January) and persistently low nocturnal BLH due to temperature inversions. An inverse relationship between $PM_{2.5}$ concentration and BLH was identified, with ventilation coefficients below 800 $m^2\ s^{-1}$ corresponding to the most severe events. Satellite-based fog detection showed peak occurrence in December–January (up to 75%), with ground-based data confirming high frequencies of haze, fog, and low clouds, particularly in November and January. The findings highlight the limitations of model and reanalysis products in representing shallow inversions and underscore the importance of high-resolution ground-based monitoring for accurate urban air quality forecasting.

Together, these case studies demonstrate how extreme atmospheric events—whether dust storms in arid regions or pollution–fog episodes in megacities—are intricately linked to ABL processes. They reinforce the critical role of localized meteorological conditions, topographic influences, and synoptic-scale forcing in driving event intensity and persistence. Furthermore, they illustrate that combining ground-based remote sensing, satellite observations, and reanalysis products provides a powerful framework for diagnosing and forecasting atmospheric hazards. Such integrated approaches are essential for improving early warning systems, mitigating public health risks, and guiding long-term environmental management strategies in climate-sensitive and densely populated regions.

****

Chapter 6

Evaluating and Improving ABL Forecasts from WRF using Machine Learning and Lidar Observations

‘

The ABL is the lowest part of the troposphere directly influenced by interactions with the Earth’s surface, where turbulent motions govern the exchange of heat, momentum, and moisture (Stull, 1988). It responds rapidly to surface forcings such as heating, cooling, and friction, and plays a central role in processes like energy balance, moisture transport, pollutant dispersion, and cloud formation (Garratt, 1994). As a transitional zone between the surface and the free troposphere, the ABL exhibits pronounced spatial and temporal variability shaped by land surface characteristics, atmospheric stability, and synoptic-scale conditions (Mahrt, 1999). Its depth, commonly referred to as the BLH, varies significantly in response to the diurnal cycle of solar radiation and surface heterogeneities such as vegetation, soil moisture, and terrain roughness. Given its central role in weather patterns, air quality, and the hydrological cycle, the ABL is crucial across multiple disciplines, including meteorology, hydrology, agriculture, aeronautics, and climate science (Garratt, 1994).

Accurate forecasting of the ABL is essential for improving weather prediction, air quality assessments, and climate modeling. The ABL strongly influences near-surface meteorological conditions such as temperature, wind speed, humidity, and cloud cover, all of which are critical inputs for NWP models (Holtslag et al., 2013). Errors in estimating the BLH can lead to significant biases in simulated surface temperature and pollutant concentrations, particularly under stable and convective conditions (Banks et al., 2016; Seidel et al., 2012). In air quality forecasting, underestimation of the BLH often results in overprediction of pollutant concentrations near the surface, while overestimation can dilute emissions unrealistically (Cheng et al., 2012; Davies et al., 2007; von Engeln and Teixeira, 2013; Yang et al., 2017). Furthermore, ABL processes regulate vertical mixing and cloud development, thereby affecting convective initiation, precipitation forecasts, and radiative forcing estimates (Davy and Esau, 2016). Thus, reliable representation and prediction of ABL dynamics are vital for a wide range of atmospheric applications, from local-scale dispersion modeling to global climate projections.

Despite advancements in modeling capabilities, capturing the ABL's evolution remains a significant challenge for NWP and regional climate models. A large part of this uncertainty arises from the simplifications inherent in boundary layer parameterization schemes, particularly in complex terrain, coastal regions, and under weakly forced conditions. Existing schemes often struggle to accurately simulate BLH, especially during nocturnal and transition periods when turbulence is suppressed or intermittently generated (Maroneze et al., 2023). Additionally, observational constraints have historically limited the evaluation and improvement of ABL representations in models, although recent advancements in remote sensing platforms, such as ground-based Lidars, have enabled continuous, high-resolution BLH observations over extended periods.

To address these gaps, blending physical modeling with data-driven techniques has emerged as a promising avenue. Machine learning (ML) methods, which can identify complex nonlinear relationships in data, offer potential to correct systematic model biases, enhance forecasts, and improve model-observation agreement (Gupta et al., 2021; McGovern et al., 2019). In particular, the integration of ML post-processing frameworks with high-frequency observational datasets allows for model output correction in a computationally efficient manner, without the need to modify the model's internal dynamics. Such hybrid modeling approaches have gained momentum across a range of meteorological variables (Kaushik et al., 2025).

In this study, the performance of a state-of-the-art mesoscale model in simulating BLH over a complex urban environment, Ahmedabad, is evaluated, using an extensive Lidar observation dataset spanning two years (2022–2023). The study further demonstrates the application of ML-based bias correction techniques to improve the representation of BLH in the model output. By conducting a systematic evaluation using both continuous and categorical verification metrics, we assess the skill of the original and corrected forecasts across various temporal and seasonal regimes. The results provide new insights into the limitations of current physical parameterizations and the potential of data-driven corrections in enhancing boundary layer predictions for both weather and air quality applications.

6.1 Machine learning based hybrid model

Despite the widespread use of the WRF model in simulating atmospheric processes, it often struggles to accurately represent the BLH, especially under stable or weakly convective conditions. These inaccuracies stem from several factors: (i) the choice of PBL schemes, which differ significantly in their treatment of turbulence, entrainment, and surface-layer coupling (Hu et al., 2010); (ii) simplified assumptions in vertical mixing and surface flux parameterizations; and (iii) inadequate representation of local-scale processes like urban effects, vegetation heterogeneity, and land-atmosphere feedbacks (Shin and Hong, 2011). These issues lead to systematic biases, particularly under nighttime stable conditions or during transition periods (morning/evening), where BLH is often under- or overestimated.

To address these deficiencies, hybrid model approaches that incorporate ML techniques into physical model outputs have shown promising results in recent studies (Chattopadhyay et al., 2020; Han et al., 2022; Peng et al., 2023). ML models can learn non-linear relationships between input meteorological variables and observed BLH values, effectively compensating for the limitations of physical parameterizations. By integrating Ceilometer-based observational data with WRF model output, ML algorithms can correct systematic biases and improve the fidelity of BLH forecasts without altering the underlying physics of the numerical model. This hybrid methodology leverages both the process-based strengths of WRF and the data-driven flexibility of ML.

The schematic of the proposed hybrid model framework is shown in Figure 6.1. The process begins with quality-controlled (QC) outputs from WRF forecasts and ground-based Ceilometer observations of BLH. These datasets are temporally collocated to ensure alignment between model output and observed data. A suite of machine learning regression models is trained to map WRF-predicted features to the observed BLH.

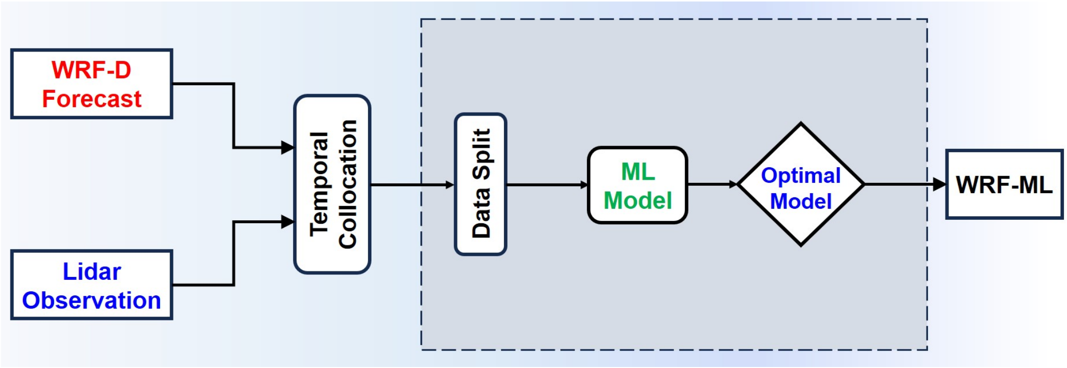

Figure 6.1: Flowchart depicting the machine learning-based hybrid model designed to enhance boundary layer height (BLH) predictions from WRF.

A suite of machine learning regression models is trained to map WRF-predicted features to the observed BLH. The ML models considered include:

- CatBoost,
- XGBoost,

- Random Forest Regressor,
- Linear Regressor,
- Support Vector Machine (SVM) Regressor,
- AdaBoost Regressor,
- Bagging Regressor, and
- K-Nearest Neighbors (KNN) Regressor.

Each model is evaluated using standard statistical metrics (e.g., RMSE, MAE, R^2), and the best-performing model is selected as the optimal model. If the model does not meet the predefined accuracy thresholds, the process is iterated with adjusted hyperparameters or feature selections. Once an optimal model is identified, it is integrated with WRF output to generate an improved forecast, denoted as WRF-ML.

6.2 Comparison of BLH obtained from Ceilometer Lidar, WRF, and WRF improved using ML

Figure 6.2 presents a comparison of the BLH derived from Ceilometer Lidar observations, the direct WRF model output (WRF-D), and the machine learning-corrected WRF output (WRF-ML) during 2022–2023. The WRF-D consistently overestimates the BLH compared to Ceilometer Lidar observations, particularly during the pre-monsoon and monsoon months (March–August), when convective boundary layers are typically deeper (Figure 6.2a). This positive bias is indicative of the model's difficulty in capturing the fine-scale processes that govern turbulent mixing, entrainment, and surface flux variability. The WRF-ML shows significantly improved alignment with the observed values throughout the observation period. Notably, during pre-monsoon and monsoon, when the deviation between WRF-D and Ceilometer Lidar observations is most pronounced, WRF-ML demonstrates substantial bias reduction and variability closer to the observations. This reflects the ability of the machine learning model to learn and correct for systematic seasonal errors in the WRF outputs by leveraging observational data patterns.

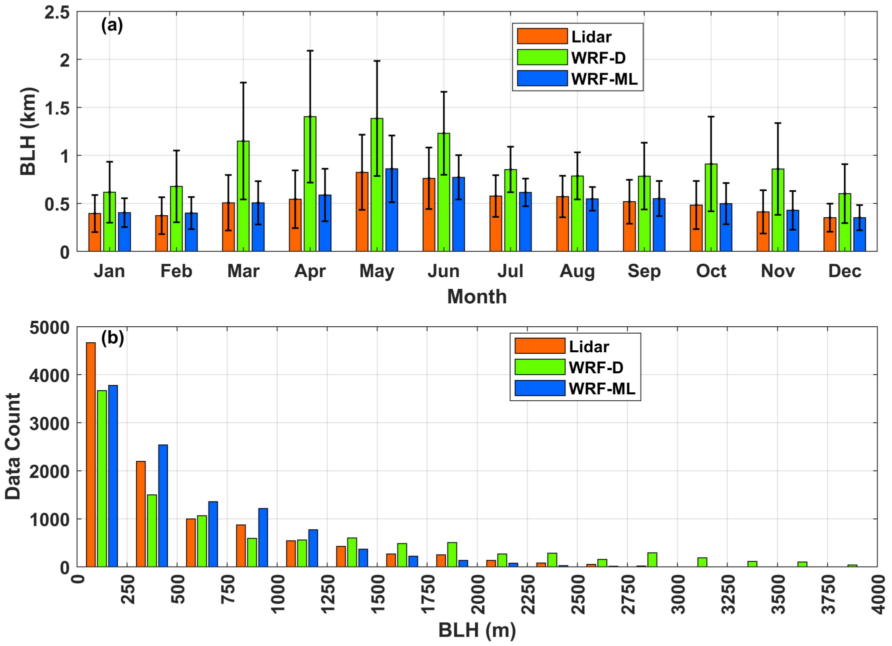

Figure 6.2: (a) Monthly mean boundary layer height (BLH) over Ahmedabad during 2022-2023 obtained from Ceilometer Lidar, WRF-D, and WRF-ML. Error bars represent ± half the standard deviation to avoid negative BLH values (b) Frequency distribution of BLH values derived from Ceilometer Lidar observations, WRF-D, and WRF-ML during 2022–2023, binned at 250-meter intervals.

Figure 6.2b shows the frequency distribution of BLH values categorized in 250-meter bins derived from Lidar, WRF-D, and WRF-ML. The Ceilometer Lidar observations exhibit a sharp peak in the 0–250 m range, with a steep decline in frequency for higher BLH values, indicating that shallow boundary layers are dominant throughout the year. In contrast, WRF-D shows a broader and slightly flatter distribution, with a considerable number of cases extending into the 1000–3000 m range. This highlights the model's tendency to overpredict deeper boundary layers, which aligns with the positive seasonal biases discussed in Figure 6.2a. The overrepresentation of high BLH values in WRF-D underscores its mischaracterization of convective mixing, particularly in regimes where shallow or stable boundary layers are more likely. The WRF-ML model, however, brings the distribution much closer to that of the observations. It captures the peak in the lower BLH bins (0–500 m) more accurately and substantially reduces the exaggerated frequency of high BLH values (>1500 m) seen in WRF-D. This improved match across the entire distribution supports the conclusion that the ML correction effectively suppresses unrealistic growth of the BLH while preserving natural variability.

Overall, the frequency distribution further confirms the WRF-ML model's superior performance not only in mean seasonal representation but also in accurately replicating the statistical structure of BLH, making it more suitable for operational and research applications where fidelity to observed variability is crucial.

Figure 6.3a compares the monthly averaged BLH across different forecast lead times, ranging from 3 to 72 hours. The Ceilometer-derived BLH shows characteristic seasonal and diurnal patterns, with elevated BLH values during pre-monsoon and monsoon months (April–July), particularly at forecast lead times corresponding to late afternoon hours. These features are consistent with enhanced convective activity and solar heating during this time of year. In contrast, the WRF-D forecasts substantially overestimate BLH during the same periods and forecast hours, with values exceeding 2.5–3.0 km, particularly in April through June (Figure 6.3b). These exaggerated peaks are likely due to WRF's misrepresentation of turbulent entrainment and overactive convective mixing within the ABL, especially when using default PBL parameterizations. This leads to a strong positive bias in convective boundary layer growth that is not supported by observations.

The WRF-ML output, on the other hand, shows markedly improved fidelity in reproducing the observed seasonal and diurnal variations (Figure 6.3c). The overestimated peaks present in WRF-D are effectively suppressed, and the resulting patterns closely resemble those seen in the Ceilometer Lidar observation. The ML correction performs particularly well in reducing the BLH overprediction during mid-day and early evening hours, key times for boundary layer evolution. These results further highlight the effectiveness of the hybrid WRF–ML approach in not only improving seasonal and statistical performance but also in capturing the temporal evolution of the boundary layer across different forecast lead times. By integrating observational constraints, the ML correction dynamically adjusts model biases and enhances the spatiotemporal realism of BLH forecasts, an improvement particularly relevant for applications in air quality forecasting, plume dispersion, and weather prediction.

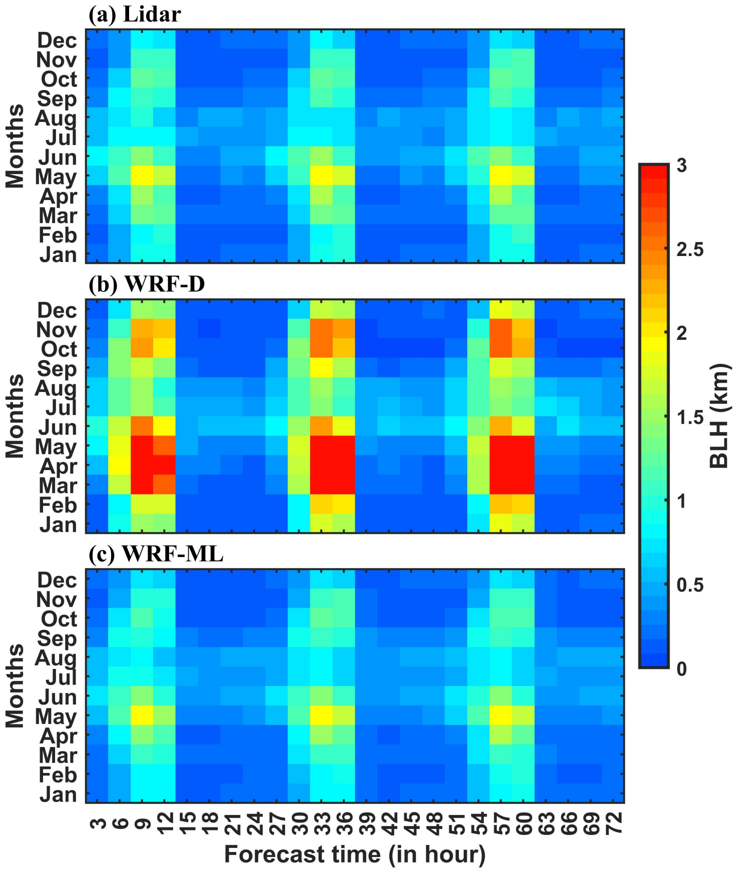

Figure 6.3: Comparison of monthly averaged BLH forecast from WRF-D and WRF-ML with the Ceilometer Lidar observations over Ahmedabad during 2022-2023.

6.3 Statistical performance of the WRF-D and WRF-ML

This section evaluates the performance of the WRF-D and WRF-ML against Ceilometer-derived BLH. Figure 6.4 illustrates the spatiotemporal performance of both WRF-D and WRF-ML using three standard statistical metrics, bias and root mean square error (RMSE), across varying forecast lead times (3–72 hours) and months. The WRF-D exhibits a persistent positive bias in BLH, especially during the pre-monsoon and monsoon months (April to September). This overestimation, which frequently exceeds 2 km, reflects the model's tendency to generate overly deep mixed layers due to the parameterized surface heat fluxes and convective schemes. The bias becomes more prominent at longer forecast lead times, suggesting the accumulation of systematic errors as synoptic information degrades.

In contrast, the WRF-ML forecasts demonstrate substantial improvement, with biases significantly reduced across all months and lead times. The machine learning correction effectively compensates for the seasonal dependence of model errors, particularly under conditions of intense surface heating and active convection. During winter and post-monsoon periods (November to February), the corrections bring the model closer to observations, though a slight underestimation is occasionally noted. This may be attributed to the difficulty in capturing shallow stable layers and low-level inversions, which are often poorly represented in deterministic setups due to coarse vertical resolution and simplified turbulence closure.

The RMSE values further substantiate the improved performance of WRF-ML. While WRF-D shows RMSE values exceeding 2 km during periods of strong diurnal ABL variability (e.g., March to June), the corrected forecasts exhibit consistently lower RMSE, particularly for forecast hours between 12 and 48. These improvements are pronounced during spring and early winter when the ABL transitions rapidly between stable and unstable states. The ability of WRF-ML to learn from historical deviations enables it to constrain overpredictions and smooth spurious variability inherent to the physical parameterizations.

Table 6.1 shows the statistical performance of both models seasonally using three standard metrics: mean absolute error (MAE), RMSE, and mean absolute percentage error (MAPE). Across all seasons, the WRF-ML shows substantial improvements. These seasonal metrics underscore the limitations of the standalone WRF model

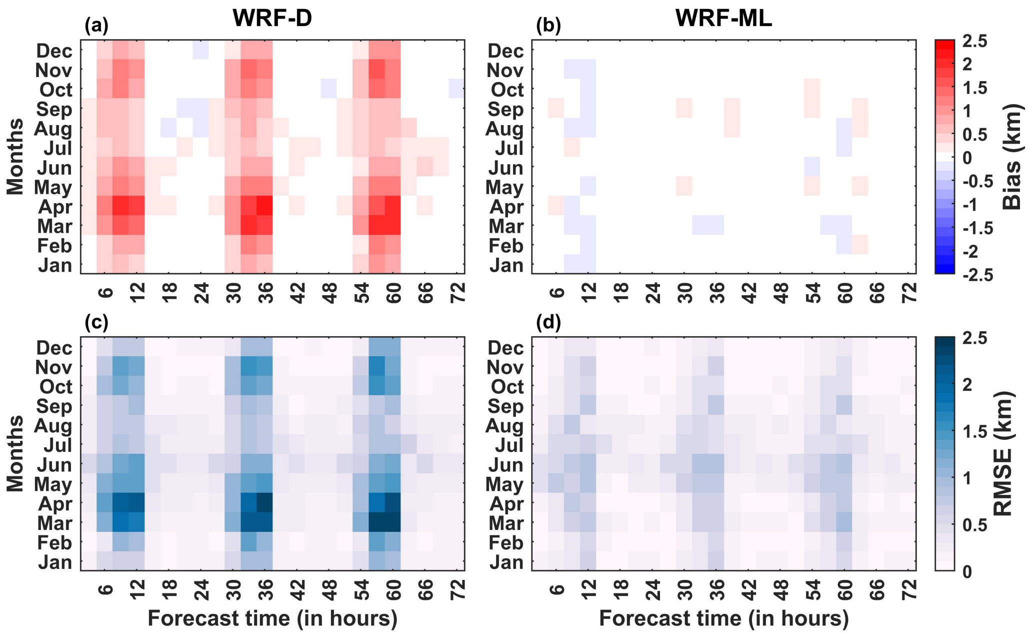

Figure 6.4: Spatiotemporal evaluation of WRF-D (left column) and WRF-ML (right column) BLH forecasts against Ceilometer Lidar observations during 2022–2023. Panels show monthly mean (a–b) bias (WRF Lidar) and (c–d) root mean square error (RMSE) at various forecast lead times.

in capturing BLH dynamics and highlight the capacity of ML-based correction to enhance both accuracy and reliability across contrasting meteorological regimes.

The relative improvement in forecast accuracy achieved by WRF-ML is quantified in Figure 6.5, which shows the percentage reduction in RMSE compared to WRF-D across all forecast lead times and months. The improvements are widespread and robust, with the most significant gains (exceeding 100%) occurring during summer and post-monsoon months. These periods are characterized by strong diurnal cycles and large variability in cloud cover and surface heating, conditions under which deterministic models typically struggle.

Notably, medium-range forecasts (12–60 hours) benefit the most from ML corrections, suggesting that the ML layer effectively captures residual errors after the primary synoptic signals have decayed. However, there is also occasional degradation in performance (blue regions), particularly at the extreme short (3–6 hours) and long

Table 6.1: Seasonal performance of WRF-D and WRF-ML in BLH estimation over Ahmedabad during 2022-2023.

Season	Model	MAE (m)	RMSE (m)	MAPE (%)
Winter	WRF-D	312.31	518.91	93.61
	WRF-ML	130.53	242.26	44.87
Pre-monsoon	WRF-D	640.35	1037.88	211.83
	WRF-ML	243.93	409.90	78.04
Monsoon	WRF-D	433.61	618.36	167.99
	WRF-ML	282.90	427.13	97.40
Post-monsoon	WRF-D	430.99	728.29	92.94
	WRF-ML	141.16	253.34	37.91

(66–72 hours) forecast ranges. These cases may reflect instances where the original model already performed adequately or where the training data were insufficient to resolve subtle error structures. Such limitations underscore the importance of model interpretability and data representativeness in ML-based forecast systems.

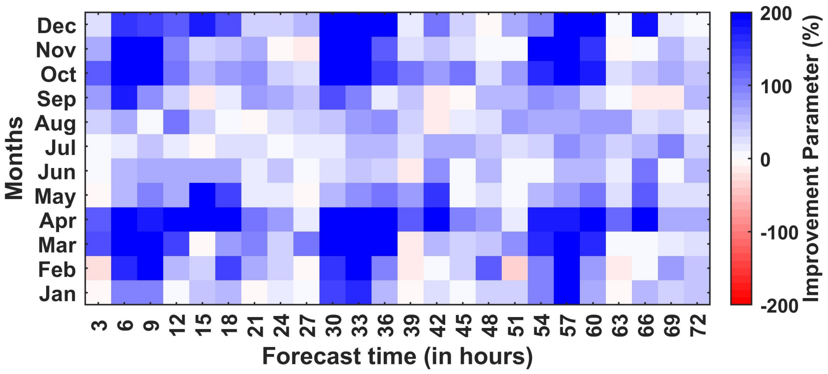

Figure 6.5: Monthly and forecast hour-wise distribution of the Improvement Parameter (%), quantifying the relative enhancement in BLH estimation by the WRF-ML over the WRF-D during 2022-2023. The improvement parameter is computed based on the reduction in RMSE relative to Ceilometer Lidar observations.

The machine learning correction significantly enhances the performance of BLH forecasts in both amplitude and structure, especially during dynamically active periods and at operationally relevant forecast horizons. These results demonstrate the promise of hybrid dynamical–statistical approaches in improving ABL characterization, with potential implications for urban meteorology, air quality forecasting, and coupled Earth system modeling.

To further examine the model performance in terms of the distribution of errors, Figure 6.6 presents the frequency distribution of BLH differences (ΔBLH $=$ Lidar $-$ WRF) for both the WRF-D and WRF-ML configurations. The distribution for WRF-D (blue curve) is noticeably broader, with a pronounced negative bias (-0.36 km) and a root mean square deviation (RMSD) of 0.68 km, reflecting systematic overestimation of the boundary layer depth. In contrast, the WRF-ML output (red curve) exhibits a sharply peaked and symmetrically centered distribution, with near-zero bias (0.00093 km) and a significantly reduced RMSD of 0.36 km.

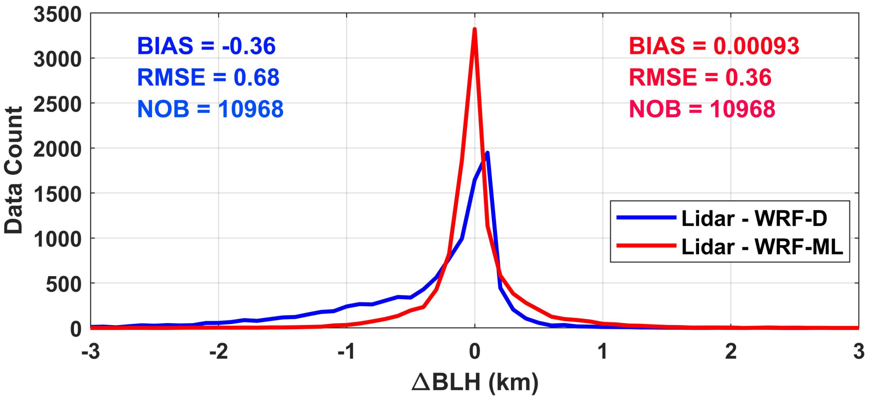

Figure 6.6: Frequency distribution of BLH differences (ΔBLH = Lidar $-$ WRF) for WRF-D (blue) and WRF-ML (red), along with statistical metrics: bias and root mean square deviation (RMSD). The ML-corrected output shows significantly reduced bias and RMSD, highlighting improved agreement with observed BLH.

This improvement demonstrates that the machine learning correction not only narrows the spread of forecast errors but also effectively eliminates systematic bias. The sharper peak at ΔBLH $= 0$ in the WRF-ML distribution indicates a high concentration of predictions closely matching observed values, which is particularly important for applications sensitive to accurate ABL depth (e.g., pollutant dispersion, cloud initiation, and convective triggering). Both datasets include an equal number of valid samples ($N = 10,968$), ensuring a fair comparison and reinforcing the robustness of these improvements.

6.4 Categorical verification of forecast skill

To provide an event-based perspective on model skill, categorical verification metrics were computed for varying BLH thresholds using observed and forecast values. Figure 6.7 presents four key skill scores, Probability of Detection (POD), False Alarm Ratio (FAR), True Skill Statistic (TSS), and Equitable Threat Score (ETS), for both the WRF-D and WRF-ML, evaluated over the 2022–2023 period. Across all four metrics, the WRF-ML demonstrates notable improvement over WRF-D, particularly for lower to moderate BLH thresholds (< 1500 m). The POD values are consistently higher in WRF-ML, indicating improved detection of shallow boundary layers that often govern near-surface pollutant dynamics and cloud initiation. Simultaneously, the reduction in FAR highlights fewer false detections, which is critical for operational reliability.

The composite metrics, TSS and ETS, also favor WRF-ML, especially in the low-to-mid BLH range. The TSS, which accounts for both hits and false alarms while being unbiased to event frequency, and the ETS, which adjusts for random chance agreement, both exhibit higher values under the ML-enhanced system. These improvements suggest that the machine learning correction not only enhances deterministic accuracy but also improves the model's ability to probabilistically discriminate between the occurrence and non-occurrence of specific BLH thresholds. However, at higher BLH thresholds (> 1500 m), both configurations show deteriorated performance across all metrics. This may reflect increased uncertainty in Lidar retrievals at elevated altitudes, limitations of model physics in capturing deep convective boundary layers, or reduced observational sampling in such conditions. Nonetheless, WRF-ML maintains relatively better skill even in this degraded regime, indicating its robustness across a range of ABL depths.

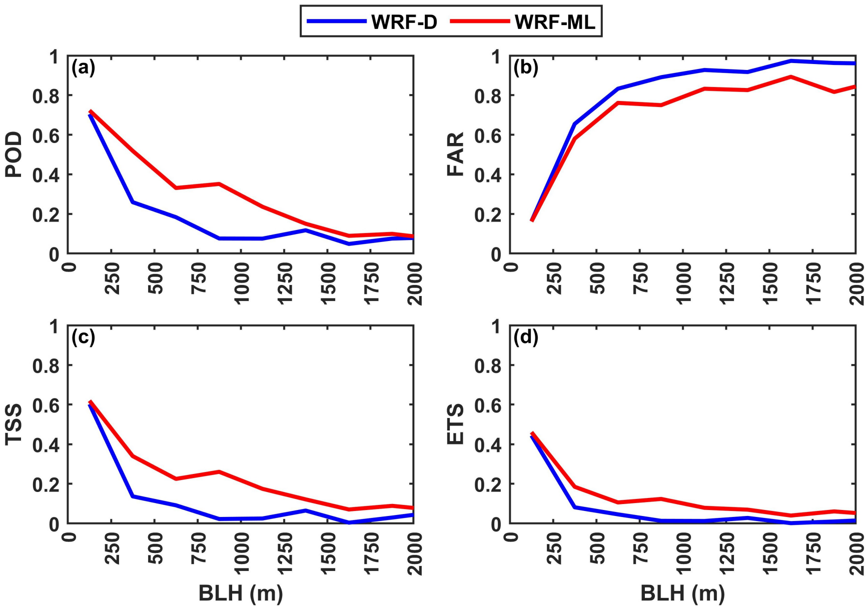

Figure 6.7: Evaluation of categorical verification metrics across BLH thresholds using WRF-D (blue) and WRF-ML (red) during 2022-2023. The panels show: (a) POD, (b) FAR, (c) TSS, and (d) ETS. WRF-ML consistently outperforms WRF-D for lower BLH thresholds (< 1500 m), exhibiting higher POD, TSS, and ETS, along with reduced FAR, reflecting enhanced capability in detecting shallow to moderate boundary layers. Both models show degraded performance at higher BLH thresholds (> 1500 m), though WRF-ML retains relatively more skill.

6.5 Summary and conclusions

This chapter presents a comprehensive assessment of the BLH forecasting capabilities of the WRF model over Ahmedabad, a semi-arid urban city in Western India, and demonstrates how ML techniques can be effectively integrated with physics-based models to enhance BLH prediction accuracy. The ABL is a critical component of the lower atmosphere, modulating energy, momentum, and mass exchanges between the Earth's surface and the free troposphere. Accurate prediction of BLH is essential for a wide range of applications, including weather forecasting, air quality modeling, and climate research. However, traditional numerical weather prediction models such as WRF often suffer from systematic errors in representing BLH, especially under stable or transition regimes. To address these limitations, the study combines

WRF model outputs with a data-driven machine learning correction scheme, referred to as WRF-ML. The evaluation spans a two-year period (2022–2023), leveraging high-resolution BLH observations from a ground-based Ceilometer Lidar deployed in Ahmedabad.

The performance of the WRF-D and WRF-ML is assessed through multiple approaches:

1. Spatiotemporal error analysis reveals that WRF-ML substantially reduces both the mean bias and RMSE in monthly forecasts compared to WRF-D, especially during convective months and at shorter forecast lead times.

2. Frequency distribution analysis demonstrates that WRF-ML better captures the distribution of BLH differences (ΔBLH = Lidar – WRF), with narrower spread and reduced bias, suggesting improved alignment with observed conditions.

3. Categorical verification metrics, including POD, FAR, TSS, and ETS, show that WRF-ML consistently outperforms WRF-D across low to moderate BLH thresholds ($<$ 1500 m), where accurate detection is often more challenging. Performance for both models declines at higher thresholds, but WRF-ML still retains relatively better skill.

Through this analysis, the study highlights the strengths and limitations of WRF in representing ABL dynamics over a rapidly urbanizing region and demonstrates the potential of machine learning corrections to mitigate systematic biases inherent in physical models.

Overall, this hybrid modeling framework, combining the dynamical consistency of WRF with the adaptability of ML, offers a promising avenue for improving high-resolution BLH forecasts in complex urban and transitional boundary layer environments. The results support broader adoption of physics–ML fusion techniques in operational forecasting systems and environmental applications.

****

Chapter 7

Summary and Scope for Future Work

7.1 Summary

‘

This thesis aimed to enhance the understanding of the dynamics of the ABL and cloud processes over three climatically diverse semi-arid locations in Western India, Ahmedabad, Mt. Abu, and Udaipur, using an integrated observational and modeling framework. The overarching goal was to improve the understanding of ABL, clouds, and their interactions in this complex and understudied environment, where heterogeneous land cover, rugged terrain, and strong diurnal variability in surface energy balance make the region highly sensitive to land–atmosphere coupling, particularly under monsoonal and pre-monsoonal conditions. Despite their climatic and socio-economic importance, the study of ABL and clouds in these regions is scarce, limiting the accuracy with which weather and climate models represent key processes such as convective initiation, fog and low cloud formation, and pollution dispersion.

This thesis addresses these gaps by integrating ground-based Lidar observations, satellite products, reanalysis datasets, and numerical modeling to investigate the spatiotemporal variability of ABL and cloud characteristics over these regions. These sites were deliberately chosen to represent a range of surface and topographic conditions: an urbanized heat island with high pollution levels (Ahmedabad), a high-altitude forested terrain influenced by orographic lifting (Mt. Abu), and a lake-dominated semi-arid valley near the Thar Desert (Udaipur).

The observational analyses reveal pronounced seasonal and diurnal cycles in both CBH and BLH, modulated by local meteorology, topography, and synoptic forcing. The monsoon season is characterized by substantially lower CBHs ($\sim$1.5–2 km) and BLHs ($\sim$1.0–1.5 km) due to persistent cloud cover and elevated humidity, conditions favorable for moist convection and rainfall generation. In contrast, the pre-monsoon months exhibit the highest BLHs ($>$2.5–3 km) and CBHs (up to 6.5 km), driven by intense surface heating and vigorous convective mixing. Udaipur records the highest frequency of cloud occurrence, while Mt. Abu experiences more frequent full-sky obscuration events due to mist and orographically induced cloud formation.

Furthermore, long-term trends indicate notable shifts in the seasonal distribution of rainfall and cloud occurrence, particularly over Ahmedabad, where September has seen a significant increase in both rainfall and low-level cloud frequency over the past two decades. These changes are likely linked to aerosol-cloud-radiation interactions, which alter cloud microphysics and precipitation efficiency. Such shifts have important implications for regional hydrology, agriculture, and urban water management.

In addition to seasonal climatology, this thesis investigated and characterized clouds forming near and below the LCL. The anomalous low clouds forming below the estimated LCL were primarily observed in post-monsoon and winter, forming within the mixed layer under conditions of moderate humidity, elevated latent heat flux, and relatively suppressed sensible heat flux. Their occurrence highlights the sensitivity of cloud processes to subtle changes in surface energy partitioning and boundary layer thermodynamics.

Furthermore, this thesis also underscores the critical role of ABL and cloud processes during extreme atmospheric events. A pre-monsoon dust storm over Ahmedabad demonstrated how convective outflows and dust transport can rapidly collapse the mixed layer, trigger deep convection, and generate heavy rainfall. Conversely, severe winter pollution and fog episodes over Delhi revealed how shallow, inversion-trapped boundary layers exacerbate air quality degradation and limit vertical dispersion. These findings emphasize that both dust-induced convective storms and pollution–fog events are fundamentally rooted in boundary layer dynamics, and that their intensity and persistence are shaped by the interplay of local and large-scale drivers.

From a modeling perspective, the thesis evaluates the skill of the WRF model in simulating BLH over the semi-arid region of Western India and demonstrates the benefits of coupling physical models with ML corrections. The hybrid WRF–ML framework markedly improves BLH forecasts by reducing systematic biases, better capturing diurnal cycles, and enhancing detection of low-to-moderate BLH regimes where traditional model skill is weakest. This approach showcases the potential of physics–data fusion for operational forecasting in complex environments.

Overall, the thesis established a robust observational and modeling baseline for understanding ABL and cloud processes over the semi-arid Western Indian region. The findings underscore the significant influence of local meteorology, surface characteristics, and synoptic forcing on both BLH and CBH variability; reveal the occurrence of unique low-cloud formations below the LCL; demonstrate the sensitivity of ABL dynamics to extreme dust, fog, and pollution events; and show how advanced modeling techniques can enhance predictive capability. These insights address critical knowledge gaps and provide a foundation for improving weather and climate model representations of ABL–cloud interactions in complex semi-arid environments.

7.2 Scope for future work

While this thesis has significantly advanced the understanding of ABL and cloud processes over semi-arid Western India, it also opens several avenues for future research.

- There is a need to explore dynamically driven processes, particularly the role of mesoscale and synoptic-scale atmospheric waves, such as gravity waves, Kelvin waves, and Rossby wave trains, in modulating cloud occurrence, structure, and variability over the region. Such phenomena can strongly influence convective initiation, vertical mixing, and precipitation patterns, yet remain poorly characterized in the context of semi-arid environments.

- The observational approach demonstrated here should be expanded to other geographic regions across India. Applying the same integrated ground-based Lidar, satellite, and reanalysis framework to coastal, Himalayan, and IGP regions would enable a broader comparative understanding of ABL and cloud interactions under diverse climatic and surface conditions. This would also help identify region-specific sensitivities and improve the representation of local processes in regional and global models.

- Long-term continuous observations of clouds and boundary layer characteristics are essential. Extending the temporal coverage of such datasets would enable the detection of multi-decadal trends, climate change signals, and the influence of slowly evolving drivers such as urbanization, land-use change, and aerosol loading. Such datasets are invaluable for identifying shifts in the seasonal cycle, extreme event frequency, and cloud–precipitation relationships.

- Systematic observational records of the type used in this thesis can play a crucial role in the calibration and validation of satellite retrievals. Ground-based Lidar profiles, when combined with high-temporal-resolution meteorological measurements, provide an independent reference against which satellite-based cloud products (e.g., from INSAT, MODIS, and future missions) can be evaluated. Such validation efforts would improve the accuracy and reliability of satellite-based monitoring systems, benefiting operational forecasting and climate research.

- The model evaluation and improvement framework demonstrated here, where observational datasets are used to assess model performance and machine learning techniques are applied to reduce systematic biases, can be applied to other regions of India. This approach could enhance regional-scale weather prediction, especially for parameters such as BLH, CBH, and low-cloud occurrence that are critical for forecasting precipitation, fog, dust storms, and air quality episodes. Implementing such frameworks in operational centers would support more accurate hazard warnings and resource management strategies.

In summary, the methodologies and findings of this thesis provide a foundation for both wider spatial application and deeper process-focused studies. Expanding the observational footprint, extending the temporal baseline, and integrating improved modeling strategies across multiple regions will be essential for building a comprehensive, high-fidelity understanding of ABL and cloud interactions across India's diverse climatic zones.

****

Bibliography

Acharja, P., Ali, K., Ghude, S. D., Sinha, V., Sinha, B., Kulkarni, R., Gultepe, I., and Rajeevan, M. N.: Enhanced secondary aerosol formation driven by excess ammonia during fog episodes in Delhi, India, Chemosphere, 289, 133 155, `10.1016/j.chemosphere.2021.133155`, 2022.

Albrecht, B. A.: Aerosols, Cloud Microphysics, and Fractional Cloudiness, Science, 245, 1227–1230, `10.1126/science.245.4923.1227`, 1989.

Alonge, C. J., Mohr, K. I., and Tao, W.-K.: Numerical Studies of Wet versus Dry Soil Regimes in the West African Sahel, Journal of Hydrometeorology, `10.1175/JHM559.1`, 2007.

Altaratz, O., Koren, I., Agassi, E., Hirsch, E., Levi, Y., and Stav, N.: The Environmental Conditions Behind the Formation of Small (subLCL) Clouds, Geophysical Research Letters, 48, e2021GL096 242, `10.1029/2021GL096242`, 2021.

Andrews, D. G.: An Introduction to Atmospheric Physics, Cambridge University Press, Cambridge, 2nd edn., `10.1017/CBO9780511800788`, 2010.

Ansari, M. I., Madan, R., and Bhatia, S.: Verification of quality of GPS based radiosonde data, MAUSAM, 66, 367–374, `10.54302/mausam.v66i3.547`, 2015.

Arakawa, A.: The Cumulus Parameterization Problem: Past, Present, and Future, Journal of Climate, 17, 2493–2525, `10.1175/1520-0442(2004)017<2493:RATCPP>2.0.CO;2`, 2004.

Arking, A.: The Radiative Effects of Clouds and their Impact on Climate, Bulletin of the American Meteorological Society, 72, 795–813, `10.1175/1520-0477(1991)072<0795:TREOCA>2.0.CO;2`, 1991.

Arya, S. P.: Introduction to Micrometeorology, vol. 79 of *International Geophysics*, Academic Press, San Diego, 2nd edn., URL `https://books.google.com/books/about/Introduction_to_Micrometeorology.html?id=riWkURgS_I8C`, 2001.

Awasthi, A., Sinha, B., Hakkim, H., Mishra, S., Mummidivarapu, V., Singh, G., Ghude, S. D., Soni, V. K., Nigam, N., Sinha, V., and Rajeevan, M. N.: Biomass-burning sources control ambient particulate matter, but traffic and industrial sources control volatile organic compound (VOC) emissions and secondary-pollutant formation during extreme pollution events in Delhi, Atmospheric Chemistry and Physics, 24, 10 279–10 304, `10.5194/acp-24-10279-2024`, 2024.

Ball, F. K.: Control of Inversion Height by Surface Heating, Quarterly Journal of the Royal Meteorological Society, 86, 483–494, `10.1002/qj.49708637005`, 1960.

Banerjee, P., Satheesh, S. K., and Moorthy, K. K.: The Unusual Severe Dust Storm of May 2018 Over Northern India: Genesis, Propagation, and Associated Conditions, Journal of Geophysical Research: Atmospheres, 126, e2020JD032 369, `10.1029/2020JD032369`, 2021.

Bangert, M., Nenes, A., Vogel, B., Vogel, H., Barahona, D., Karydis, V. A., Kumar, P., Kottmeier, C., and Blahak, U.: Saharan dust event impacts on cloud formation and radiation over Western Europe, Atmospheric Chemistry and Physics, 12, 4045–4063, `10.5194/acp-12-4045-2012`, 2012.

Banks, R. F., Tiana-Alsina, J., Baldasano, J. M., Rocadenbosch, F., Papayannis, A., Solomos, S., and Tzanis, C. G.: Sensitivity of boundary-layer variables to PBL schemes in the WRF model based on surface meteorological observations, lidar, and radiosondes during the HygrA-CD campaign, Atmospheric Research, 176-177, 185–201, `10.1016/j.atmosres.2016.02.024`, 2016.

Banta, R. M., Newsom, R. K., Lundquist, J. K., Pichugina, Y. L., Coulter, R. L., and Mahrt, L.: Nocturnal Low-Level Jet Characteristics Over Kansas During CASES-99, Boundary-Layer Meteorology, 105, 221–252, 10.1023/A:1019992330866, 2002.

Barry, R. G. and Chorley, R. J.: Atmosphere, Weather and Climate, Routledge, London, URL https://doi.org/10.4324/9780203871027, 2009.

Benner, T. C. and Curry, J. A.: Characteristics of small tropical cumulus clouds and their impact on the environment, Journal of Geophysical Research: Atmospheres, 103, 28 753–28 767, 10.1029/98JD02579, 1998.

Bharali, C., Barth, M., Kumar, R., Ghude, S. D., Sinha, V., and Sinha, B.: Role of atmospheric aerosols in severe winter fog over the Indo-Gangetic Plain of India: a case study, Atmospheric Chemistry and Physics, 24, 6635–6662, 10.5194/acp-24-6635-2024, 2024.

Bolton, D.: The Computation of Equivalent Potential Temperature, Monthly Weather Review, 108, 1046–1053, 10.1175/1520-0493(1980)108, 1980.

Bony, S. and Dufresne, J.-L.: Marine boundary layer clouds at the heart of tropical cloud feedback uncertainties in climate models, Geophysical Research Letters, 32, 10.1029/2005GL023851, 2005.

Bony, S., Stevens, B., Frierson, D. M. W., Jakob, C., Kageyama, M., Pincus, R., Shepherd, T. G., Sherwood, S. C., Siebesma, A. P., Sobel, A. H., Watanabe, M., and Webb, M. J.: Clouds, circulation and climate sensitivity, Nature Geoscience, 8, 261–268, 10.1038/ngeo2398, 2015.

Bou Karam, D., Flamant, C., Knippertz, P., Reitebuch, O., Pelon, J., Chong, M., and Dabas, A.: Dust emissions over the Sahel associated with the West African monsoon intertropical discontinuity region: A representative case-study, Quarterly Journal of the Royal Meteorological Society, 134, 621–634, 10.1002/qj.244, 2008.

Brunt, D.: The adiabatic lapse-rate for dry and saturated air, Quarterly Journal of the Royal Meteorological Society, 59, 351–360, 10.1002/qj.49705925204, 1933.

Caballero, R.: Physics of the Atmosphere and Climate, Cambridge University Press, Cambridge, 2nd edn., URL https://books.google.com/books/about/Physics_of_the_Atmosphere.html?id=8XjZoQEACAAJ, 2014.

Caicedo, V., Rappenglück, B., Lefer, B., Morris, G., Toledo, D., and Delgado, R.: Comparison of aerosol lidar retrieval methods for boundary layer height detection using ceilometer aerosol backscatter data, Atmospheric Measurement Techniques, 10, 1609–1622, 10.5194/amt-10-1609-2017, 2017.

Cao, C., Blonski, S., Wang, W., Uprety, S., Shao, X., Choi, J., Lynch, E., and Kalluri, S.: NOAA-20 VIIRS on-orbit performance, data quality, and operational Cal/Val support, in: Earth Observing Missions and Sensors: Development, Implementation, and Characterization V, pp. 63–71, SPIE, 10.1117/12.2324329, 2018.

Cess, R. D., Potter, G. L., Blanchet, J.-P., Boer, G. J., Ghan, S. J., Kiehl, J. T., Le Treut, H., Li, Z.-X., Liang, X.-Z., Mitchell, J. F. B., Morcrette, J.-J., Randall, D. A., Riches, M. R., Roeckner, E., Schlese, U., Slingo, A., Taylor, K. E., Washington, W. M., Wetherald, R. T., and Yagai, I.: Interpretation of Cloud-Climate Feedback as Produced by 14 Atmospheric General Circulation Models, Science, 245, 513–516, 10.1126/science.245.4917.513, 1989.

Chattopadhyay, A., Nabizadeh, E., and Hassanzadeh, P.: Analog Forecasting of Extreme-Causing Weather Patterns Using Deep Learning, Journal of Advances in Modeling Earth Systems, 12, e2019MS001 958, 10.1029/2019MS001958, 2020.

Chen, H., Sun, C., Xiong, X., Sarid, G., and Sun, J.: SNPP VIIRS Day Night Band: Ten Years of On-Orbit Calibration and Performance, Remote Sensing, 13, 4179, 10.3390/rs13204179, 2021.

Cheng, F.-Y., Chin, S.-C., and Liu, T.-H.: The role of boundary layer schemes in meteorological and air quality simulations of the Taiwan area, Atmospheric Environment, 54, 714–727, 10.1016/j.atmosenv.2012.01.029, 2012.

Choi, H., Zhang, Y. H., and Kim, K. H.: Sudden high concentration of TSP affected by atmospheric boundary layer in Seoul metropolitan area during duststorm period, Environment International, Assessment of Urban and Regional Air Quality and its Impacts, 34, 635–647, `10.1016/j.envint.2007.12.023`, 2008.

Craven, J., Jewell, R., and Brooks, H.: Comparison between observed convective cloud-base heights and lifting condensation level for two different lifted parcels, Bulletin of the American Meteorological Society, URL `https://journals.ametsoc.org`, 2002.

Daidzic, N. E.: On Atmospheric Lapse Rates, International Journal of Aviation, Aeronautics, and Aerospace, 6, `10.15394/ijaaa.2019.1374`, 2019.

Dang, R., Yang, Y., Hu, X.-M., Wang, Z., and Zhang, S.: A Review of Techniques for Diagnosing the Atmospheric Boundary Layer Height (ABLH) Using Aerosol Lidar Data, Remote Sensing, 11, 1590, `10.3390/rs11131590`, 2019.

Davies, F., Middleton, D. R., and Bozier, K. E.: Urban air pollution modelling and measurements of boundary layer height, Atmospheric Environment, 41, 4040–4049, `10.1016/j.atmosenv.2007.01.015`, 2007.

Davy, R. and Esau, I.: Differences in the efficacy of climate forcings explained by variations in atmospheric boundary layer depth, Nature Communications, 7, 11 690, `10.1038/ncomms11690`, 2016.

Deardorff, J. W.: Numerical Investigation of Neutral and Unstable Planetary Boundary Layers, Journal of the Atmospheric Sciences, 29, 91–115, `10.1175/1520-0469(1972)029<0091:NIONAU>2.0.CO;2`, 1972.

Deardorff, J. W.: Three-Dimensional Numerical Study of the Height and Mean Structure of a Heated Planetary Boundary Layer, Boundary-Layer Meteorology, 7, 81–106, `10.1007/BF00224974`, 1974.

Deardorff, J. W.: Prediction of Convective Mixed-Layer Entrainment for Realistic Capping Inversion Structure, Journal of the Atmospheric Sciences, 36, 424–436, `10.1175/1520-0469(1979)036<0424:POCMLE>2.0.CO;2`, 1979.

Deardorff, J. W. and Willis, G. E.: Further results from a laboratory model of the convective planetary boundary layer, Boundary-Layer Meteorology, 32, 205–236, 10.1007/BF00121880, 1985.

Di, A., Xue, Y., Yang, X., Leys, J., Guang, J., Mei, L., Wang, J., She, L., Hu, Y., He, X., Che, Y., and Fan, C.: Dust Aerosol Optical Depth Retrieval and Dust Storm Detection for Xinjiang Region Using Indian National Satellite Observations, Remote Sensing, 8, 702, 10.3390/rs8090702, 2016.

Dumka, U. C., Kaskaoutis, D. G., Francis, D., Chaboureau, J.-P., Rashki, A., Tiwari, S., Singh, S., Liakakou, E., and Mihalopoulos, N.: The Role of the Intertropical Discontinuity Region and the Heat Low in Dust Emission and Transport Over the Thar Desert, India: A Premonsoon Case Study, Journal of Geophysical Research: Atmospheres, 124, 13 197–13 219, 10.1029/2019JD030836, 2019a.

Dumka, U. C., Tiwari, S., Kaskaoutis, D. G., Soni, V. K., Safai, P. D., and Attri, S. D.: Aerosol and pollutant characteristics in Delhi during a winter research campaign, Environmental Science and Pollution Research, 26, 3771–3794, 10.1007/s11356-018-3885-y, 2019b.

d'Entremont, R. P. and Gustafson, G. B.: Analysis of Geostationary Satellite Imagery Using a Temporal-Differencing Technique, Earth Interactions, 7, 1–10, URL https://journals.ametsoc.org/view/journals/eint/7/1/1087-3562_2003_007_0001_aogsiu_2.0.co_2.xml, 2003.

Eastman, R., Warren, S. G., and Hahn, C. J.: Variations in Cloud Cover and Cloud Types over the Ocean from Surface Observations, 1954–2008, Journal of Climate, 24, 5914–5934, 10.1175/2011JCLI3972.1, 2011.

Emanuel, K. A.: Atmospheric Convection, Oxford University Press, New York, NY, URL https://global.oup.com/academic/product/atmospheric-convection-9780195066302, 1994.

Emanuel, K. A. and Živković-Rothman, M.: Development and Evaluation of a Convection Scheme for Use in Climate Models, Journal of the Atmospheric Sciences, 56, 1766–1782, 10.1175/1520-0469(1999)056<1766:DAEOAC>2.0.CO;2, 1999.

Emeis, S.: Surface-Based Remote Sensing of the Atmospheric Boundary Layer, Springer Science & Business Media, URL https://link.springer.com/book/10.1007/978-90-481-3212-5, 2010.

Eresmaa, N., Karppinen, A., Joffre, S. M., Räsänen, J., and Talvitie, H.: Mixing height determination by ceilometer, Atmospheric Chemistry and Physics, 6, 1485–1493, 10.5194/acp-6-1485-2006, 2006.

Evan, A. T., Heidinger, A. K., and Pavolonis, M. J.: Development of a new over-water Advanced Very High Resolution Radiometer dust detection algorithm, International Journal of Remote Sensing, 27, 3903–3924, 10.1080/01431160600646359, 2006.

Fan, J., Wang, Y., Rosenfeld, D., and Liu, X.: Review of Aerosol–Cloud Interactions: Mechanisms, Significance, and Challenges, Journal of the Atmospheric Sciences, 73, 4221–4252, 10.1175/JAS-D-16-0037.1, 2016.

Feng, T., Yuan, T., Cao, J., Wang, Z., Zhi, R., Hu, Z., and Huang, J.: The influence of dust on extreme precipitation at a large city in North China, Science of The Total Environment, 901, 165 890, 10.1016/j.scitotenv.2023.165890, 2023.

Fernando, H. J. S. and Weil, J. C.: Whither the Stable Boundary Layer? A Shift in the Research Agenda, Bulletin of the American Meteorological Society, 91, 1475–1484, 10.1175/2010BAMS2770.1, 2010.

Fernando, H. J. S., Lee, S. M., Anderson, J., Princevac, M., Pardyjak, E., and Grossman-Clarke, S.: Urban Fluid Mechanics: Air Circulation and Contaminant Dispersion in Cities, Environmental Fluid Mechanics, 1, 107–164, 10.1023/A:1011504001479, 2001.

Fiocco, G. and Smullin, L. D.: Detection of Scattering Layers in the Upper Atmosphere (60–140 km) by Optical Radar, Nature, 199, 1275–1276, 10.1038/1991275a0, 1963.

Flohn, H. and Penndorf, R.: The Stratification of the Atmosphere (I), Bulletin of the American Meteorological Society, 31, 71–79, 10.1175/1520-0477-31.3.71, 1950.

Forster, P., Storelvmo, T., Armour, K., Collins, W., Dufresne, J.-L., Frame, D., Lunt, D., Mauritsen, T., Palmer, M., Watanabe, M., Wild, M., and Zhang, H.: The Earth's Energy Budget, Climate Feedbacks, and Climate Sensitivity, pp. 923–1054, Cambridge University Press, Cambridge, United Kingdom and New York, NY, USA, 10.1017/9781009157896.009, figure 7.6, 2021.

Fountoukis, C., Harshvardhan, H., Gladich, I., Ackermann, L., and Ayoub, M. A.: Anatomy of a Severe Dust Storm in the Middle East: Impacts on Aerosol Optical Properties and Radiation Budget, Aerosol and Air Quality Research, 20, 155–165, 10.4209/aaqr.2019.04.0165, 2020.

Frey, R. A., Ackerman, S. A., Liu, Y., Strabala, K. I., Zhang, H., Key, J. R., and Wang, X.: Cloud Detection with MODIS. Part I: Improvements in the MODIS Cloud Mask for Collection 5, 10.1175/2008JTECHA1052.1, 2008.

Fukushima, A., Kanamori, H., and Matsumoto, J.: Regionality of Long-Term Trends and Interannual Variation of Seasonal Precipitation over India, Progress in Earth and Planetary Science, 6, 1–14, 10.1186/s40645-019-0255-4, 2019.

Gal-Chen, T., Xu, M., and Eberhard, W. L.: Estimations of atmospheric boundary layer fluxes and other turbulence parameters from Doppler lidar data, Journal of Geophysical Research: Atmospheres, 97, 18 409–18 423, 10.1029/91JD03174, 1992.

Garcia, R.: Dynamics, Radiation, and Photochemistry in the Mesosphere: Implications for the Formation of Noctilucent Clouds, Journal of Geophysical Research: Atmospheres, 94, 14 605–14 615, 10.1029/JD094iD12p14605, 1989.

Garratt, J.: Review: The atmospheric boundary layer, Earth-Science Reviews, 37, 89–134, 10.1016/0012-8252(94)90026-4, 1994.

Garsa, K., Khan, A. A., Jindal, P., Middey, A., Luqman, N., Mohanty, H., and Tiwari, S.: Assessment of meteorological parameters on air pollution variability over Delhi, Environmental Monitoring and Assessment, 195, 1315, 10.1007/s10661-023-11922-2, 2023.

Gautam, R., Patel, P. N., Singh, M. K., Liu, T., Mickley, L. J., Jethva, H., and DeFries, R. S.: Extreme Smog Challenge of India Intensified by Increasing Lower Tropospheric Stability, Geophysical Research Letters, 50, e2023GL103 105, 10.1029/2023GL103105, 2023.

Georgakakos, K. P. and Bras, R. L.: A hydrologically useful station precipitation model: 1. Formulation, Water Resources Research, 20, 1585–1596, 10.1029/WR020i011p01585, 1984.

Gopikrishnan, G. S., Kuttippurath, J., Thapliyal, P. K., and Shukla, M. V.: Validation of INSAT-3D and INSAT-3DR Temperature Profile Retrievals Using Ground-Based, Satellite, and Reanalysis Data, Journal of Geophysical Research: Atmospheres, 128, e2023JD038 912, 10.1029/2023JD038912, 2023.

Goudie, A. S.: Dust storms: Recent developments, Journal of Environmental Management, 90, 89–94, 10.1016/j.jenvman.2008.07.007, 2009.

Govardhan, G., Ambulkar, R., Kulkarni, S., Vishnoi, A., Yadav, P., Choudhury, B. A., Khare, M., and Ghude, S. D.: Stubble-burning activities in north-western India in 2021: Contribution to air pollution in Delhi, Heliyon, 9, e16 939, 10.1016/j.heliyon.2023.e16939, 2023.

Gueymard, C. A. and Yang, D.: Worldwide validation of CAMS and MERRA-2 reanalysis aerosol optical depth products using 15 years of AERONET observations, Atmospheric Environment, 225, 117 216, 10.1016/j.atmosenv.2019.117216, 2020.

Guhathakurta, P. and Revadekar, J.: Observed Variability and Long-Term Trends of Rainfall Over India, in: Observed Climate Variability and Change over the Indian Region, edited by Rajeevan, M. N. and Nayak, S., pp. 1–15, Springer, Singapore, 10.1007/978-981-10-2531-0_1, 2017.

Gupta, P. K., Saxena, A., Dattaprakash, B., Sheriff, R. S., Chaudhari, S. H., Ullanat, V., and Chayapathy, V.: Applications of Artificial Intelligence in Environmental Science, in: Artificial Intelligence (AI), CRC Press, 2021.

Guttikunda, S. K. and Goel, R.: Health impacts of particulate pollution in a megacity—Delhi, India, Environmental Development, 6, 8–20, 10.1016/j.envdev.2012.12.002, 2013.

Haeffelin, M., Angelini, F., Morille, Y., Martucci, G., Frey, S., Gobbi, G. P., Lolli, S., O'Dowd, C. D., Sauvage, L., Xueref-Rémy, I., Wastine, B., and Feist, D. G.: Evaluation of Mixing-Height Retrievals from Automatic Profiling Lidars and Ceilometers in View of Future Integrated Networks in Europe, Boundary-Layer Meteorology, 143, 49–75, 10.1007/s10546-011-9643-z, 2012.

Hamblyn, R.: Luke Howard, namer of clouds, Weather, 77, 376–379, 10.1002/wea.4304, 2022.

Han, Y., Mi, L., Shen, L., Cai, C. S., Liu, Y., Li, K., and Xu, G.: A short-term wind speed prediction method utilizing novel hybrid deep learning algorithms to correct numerical weather forecasting, Applied Energy, 312, 118 777, 10.1016/j.apenergy.2022.118777, 2022.

Hartmann, D. L., Ockert-Bell, M. E., and Michelsen, M. L.: The Effect of Cloud Type on Earth's Energy Balance: Global Analysis, Journal of Climate, 5, 1281–1304, 10.1175/1520-0442(1992)005<1281:TEOCTO>2.0.CO;2, 1992.

Hersbach, H., Bell, B., Berrisford, P., Hirahara, S., Horányi, A., Muñoz-Sabater, J., Nicolas, J., Peubey, C., Radu, R., Schepers, D., Simmons, A., Soci, C., Abdalla, S., Abellan, X., Balsamo, G., Bechtold, P., Biavati, G., Bidlot, J., Bonavita, M., De Chiara, G., Dahlgren, P., Dee, D., Diamantakis, M., Dragani, R., Flemming, J., Forbes, R., Fuentes, M., Geer, A., Haimberger, L., Healy, S., Hogan, R. J., Hólm, E., Janisková, M., Keeley, S., Laloyaux, P., Lopez, P., Lupu, C., Radnoti, G., de Rosnay, P., Rozum, I., Vamborg, F., Villaume, S., and Thépaut, J.-N.: The ERA5 global reanalysis, Quarterly Journal of the Royal Meteorological Society, 146, 1999–2049, 10.1002/qj.3803, 2020.

Hibberd, M. F. and Sawford, B. L.: A saline laboratory model of the planetary convective boundary layer, Boundary-Layer Meteorology, 67, 229–250, 10.1007/BF00713143, 1994.

Hirsch, E., Koren, I., Levin, Z., Altaratz, O., and Agassi, E.: On Transition-Zone Water Clouds, Atmospheric Chemistry and Physics, 14, 9001–9012, 10.5194/acp-14-9001-2014, 2014.

Hirsch, E., Koren, I., Altaratz, O., Levin, Z., and Agassi, E.: Enhanced humidity pockets originating in the mid boundary layer as a mechanism of cloud formation below the lifting condensation level, Environmental Research Letters, 12, 024 020, 10.1088/1748-9326/AA5BA4, 2017.

Holtslag, A. and Nieuwstadt, F.: Scaling the atmospheric boundary layer, Boundary-Layer Meteorology, 36, 201–209, 10.1007/BF00117468, 1986.

Holtslag, A. A. M. and Boville, B. A.: Local Versus Nonlocal Boundary-Layer Diffusion in a Global Climate Model, Journal of Climate, 6, 1825–1842, 10.1175/1520-0442(1993)006<1825:LVNBLD>2.0.CO;2, 1993.

Holtslag, A. A. M., Svensson, G., Baas, P., Basu, S., Beare, B., Beljaars, A. C. M., Bosveld, F. C., Cuxart, J., Lindvall, J., Steeneveld, G. J., Tjernström, M., and van der Wiel, B. J. H.: Stable Atmospheric Boundary Layers and Diurnal Cycles: Challenges for Weather and Climate Models, Bulletin of the American Meteorological Society, 10.1175/BAMS-D-11-00187.1, 2013.

Houze, R. A. J.: Cloud Dynamics, International Geophysics, Volume 104, Academic Press, Oxford, UK, 2nd edn., URL https://shop.elsevier.com/books/cloud-dynamics/houze-jr/978-0-12-374266-7, 2014.

Houze Jr., R.: Orographic effects on precipitating clouds, Reviews of Geophysics, 50, 10.1029/2011RG000365, 2012.

Hu, X.-M., Nielsen-Gammon, J. W., and Zhang, F.: Evaluation of Three Planetary Boundary Layer Schemes in the WRF Model, Journal of Applied Meteorology and Climatology, 10.1175/2010JAMC2432.1, 2010.

Huang, Z., Nee, J.-B., Chiang, C.-W., Zhang, S., Jin, H., Wang, W., and Zhou, T.: Real-Time Observations of Dust–Cloud Interactions Based on Polarization and Raman Lidar Measurements, Remote Sensing, 10, 1017, 10.3390/rs10071017, 2018.

Hunt, G. E.: Radiative properties of terrestrial clouds at visible and infra-red thermal window wavelengths, Quarterly Journal of the Royal Meteorological Society, 99, 346–369, 10.1002/qj.49709942013, 1973.

Hutchison, K. D.: The retrieval of cloud base heights from MODIS and three-dimensional cloud fields from NASA's EOS Aqua mission, International Journal of Remote Sensing, 23, 5249–5265, 10.1080/01431160110117391, 2002.

Inness, A., Ades, M., Agustí-Panareda, A., Barré, J., Benedictow, A., Blechschmidt, A.-M., Dominguez, J. J., Engelen, R., Eskes, H., Flemming, J., Huijnen, V., Jones, L., Kipling, Z., Massart, S., Parrington, M., Peuch, V.-H., Razinger, M., Remy, S., Schulz, M., and Suttie, M.: The CAMS reanalysis of atmospheric composition, Atmospheric Chemistry and Physics, 19, 3515–3556, 10.5194/acp-19-3515-2019, 2019.

Iyer, U. S. and Raj, P. E.: Ventilation coefficient trends in the recent decades over four major Indian metropolitan cities, Journal of Earth System Science, 122, 537–549, 10.1007/s12040-013-0270-6, 2013.

Jain, S., Sharma, S. K., Vijayan, N., and Mandal, T. K.: Seasonal characteristics of aerosols (PM2.5 and PM10) and their source apportionment using PMF: A four year study over Delhi, India, Environmental Pollution, 262, 114 337, 10.1016/j.envpol.2020.114337, 2020.

Jaswal, A. K., Kore, P. A., and Singh, V.: Variability and Trends in Low Cloud Cover over India during 1961–2010, MAUSAM, 68, 235–252, 10.54302/mausam.v68i2.627, 2017.

Jethva, H., Satheesh, S. K., and Srinivasan, J.: Seasonal variability of aerosols over the Indo-Gangetic basin, Journal of Geophysical Research: Atmospheres, 110, 10.1029/2005JD005938, 2005.

Jia, L., Xu, Y., and Duan, M.: Explosive formation of secondary organic aerosol due to aerosol-fog interactions, Science of The Total Environment, 866, 161 338, 10.1016/j.scitotenv.2022.161338, 2023.

John, J., Dey, I., Pushpakar, A., Sathiyamoorthy, V., and Shukla, B. P.: INSAT-3D cloud microphysical product: retrieval and validation, International Journal of Remote Sensing, 40, 1481–1494, 10.1080/01431161.2018.1524606, 2019.

Kanawade, V. P., Srivastava, A. K., Ram, K., Asmi, E., Vakkari, V., Soni, V. K., Varaprasad, V., and Sarangi, C.: What caused severe air pollution episode of November 2016 in New Delhi?, Atmospheric Environment, 222, 117 125, 10.1016/j.atmosenv.2019.117125, 2020.

Karydis, V. A., Kumar, P., Barahona, D., Sokolik, I. N., and Nenes, A.: On the Effect of Dust Particles on Global Cloud Condensation Nuclei and Cloud Droplet Number, Journal of Geophysical Research - Atmospheres, 116, 10.1029/2011JD016283, 2011.

Kaufman, Y. J., Tanré, D., and Boucher, O.: A satellite view of aerosols in the climate system, Nature, 419, 215–223, 10.1038/nature01091, 2002.

Kaushik, N. K., Singh, K. P., Ojha, M., Srivastava, S. S., Mahida, D., Kumar, P., Mishra, A., and Prabhu, C. N.: Development of hybrid dynamical and machine learning based weather forecasting using a network of dense weather stations, Atmospheric Research, 326, 108 342, 10.1016/j.atmosres.2025.108342, 2025.

Kawana, K., Kuba, N., and Mochida, M.: Assessment of cloud condensation nucleus activation of urban aerosol particles with different hygroscopicity and the application to the cloud parcel model, Journal of Geophysical Research: Atmospheres, 119, 3352–3371, 10.1002/2013JD020827, 2014.

Kedia, S., Kumar, R., Islam, S., Sathe, Y., and Kaginalkar, A.: Radiative impact of a heavy dust storm over India and surrounding oceanic regions, Atmospheric Environment, 185, 109–120, 10.1016/j.atmosenv.2018.05.005, 2018.

Khatri, P., Yoshida, K., and Hayasaka, T.: Aerosol Effects on Water Cloud Properties in Different Atmospheric Regimes, Journal of Geophysical Research: Atmospheres, 128, e2023JD039 729, 10.1029/2023JD039729, 2023.

King, M. D., Menzel, W. P., Kaufman, Y. J., Tanre, D., Gao, B.-C., Platnick, S., Ackerman, S. A., Remer, L. A., Pincus, R., and Hubanks, P. A.: Cloud and aerosol properties, precipitable water, and profiles of temperature and water vapor from MODIS, IEEE Transactions on Geoscience and Remote Sensing, 41, 442–458, 10.1109/TGRS.2002.808226, 2003.

King, M. D., Platnick, S., Menzel, W. P., Ackerman, S. A., and Hubanks, P. A.: Spatial and Temporal Distribution of Clouds Observed by MODIS Onboard the Terra and Aqua Satellites, IEEE Transactions on Geoscience and Remote Sensing, 51, 3826–3852, 10.1109/TGRS.2012.2227333, 2013.

Kishore, P., Jyothi, S., Basha, G., Rao, S. V. B., Rajeevan, M., Velicogna, I., and Sutterley, T. C.: Precipitation climatology over India: validation with observations and reanalysis datasets and spatial trends, Climate Dynamics, 46, 541–556, 10.1007/s00382-015-2597-y, 2016.

Klett, J. D.: Stable analytical inversion solution for processing lidar returns, Applied Optics, 20, 211–220, 10.1364/AO.20.000211, 1981.

Knippertz, P.: Meteorological Aspects of Dust Storms, in: Mineral Dust: A Key Player in the Earth System, edited by Knippertz, P. and Stuut, J.-B. W., pp. 121–147, Springer Netherlands, Dordrecht, 10.1007/978-94-017-8978-3_6, 2014.

Konwar, M., Das, S., Deshpande, S., Chakravarty, K., and Goswami, B.: Microphysics of clouds and rain over the Western Ghat, Journal of Geophysical Research: Atmospheres, 119, 6140–6159, 10.1002/2014JD021606, 2014.

Kotthaus, S., Bravo-Aranda, J. A., Collaud Coen, M., Guerrero-Rascado, J. L., Costa, M. J., Cimini, D., O'Connor, E. J., Hervo, M., Alados-Arboledas, L., Jiménez-Portaz, M., Mona, L., Ruffieux, D., Illingworth, A., and Haeffelin, M.:

Atmospheric boundary layer height from ground-based remote sensing: a review of capabilities and limitations, Atmospheric Measurement Techniques, 16, 433–479, 10.5194/amt-16-433-2023, 2023.

Kulkarni, R., Jenamani, R. K., Pithani, P., Konwar, M., Nigam, N., and Ghude, S. D.: Loss to Aviation Economy Due to Winter Fog in New Delhi during the Winter of 2011–2016, Atmosphere, 10, 198, 10.3390/atmos10040198, 2019.

Kumar, M., Mallik, C., Kumar, A., Mahanti, N. C., and Shekh, A. M.: Evaluation of the boundary layer depth in semi-arid region of India, Dynamics of Atmospheres and Oceans, 49, 96–107, 10.1016/J.DYNATMOCE.2009.01.002, 2010a.

Kumar, P., Nenes, A., and Sokolik, I. N.: Importance of adsorption for CCN activity and hygroscopic properties of mineral dust aerosol, Geophysical Research Letters, 36, 10.1029/2009GL040827, 2009.

Kumar, P., Shukla, M. V., and Varma, A. K.: Impact of all-sky water vapour channel radiance from INSAT-3D/3DR satellite over South Asia region using WRF model, Quarterly Journal of the Royal Meteorological Society, 148, 2532–2545, 10.1002/qj.4323, 2022.

Kumar, S. and Bhat, G.: Vertical structure of orographic precipitating clouds observed over south Asia during summer monsoon season, Journal of Earth System Science, 126, 114, 10.1007/s12040-017-0897-9, 2017.

Kumar, S., Hazra, A., and Goswami, B.: Role of interaction between dynamics, thermodynamics and cloud microphysics on summer monsoon precipitating clouds over the Myanmar Coast and the Western Ghats, Climate Dynamics, 43, 911–924, 10.1007/s00382-013-1909-3, 2014.

Kumar, S., Kumar, S., Kaskaoutis, D. G., Singh, R. P., Singh, R. K., Mishra, A. K., Srivastava, M. K., and Singh, A. K.: Meteorological, atmospheric and climatic perturbations during major dust storms over Indo-Gangetic Basin, Aeolian Research, 17, 15–31, 10.1016/j.aeolia.2015.01.006, 2015.

Kumar, V., Jain, S. K., and Singh, Y.: Analysis of long-term rainfall trends in India, Hydrological Sciences Journal, 55, 484–496, 10.1080/02626667.2010.481373, 2010b.

Kundu, A., Kundu, S. S., Sharma, S. K., Gogoi, M., Banik, T., Borgohain, A., Mahanta, R., and Debnath, A.: The behavior of cloud base height over a hilly remote station of North-East India using ground-based remote sensing technique, Atmospheric Research, 282, 106 512, 10.1016/j.atmosres.2022.106512, 2023.

Kutty, S. G., Dimri, A. P., and Gultepe, I.: Climatic trends in fog occurrence over the Indo-Gangetic plains, International Journal of Climatology, 40, 2048–2061, 10.1002/joc.6317, 2020.

Lammert, A. and Bösenberg, J.: Determination of the convective boundary-layer height with laser remote sensing, Boundary-Layer Meteorology, 119, 159–170, 10.1007/s10546-005-9020-x, 2006.

Lawrence, M. G.: The Relationship between Relative Humidity and the Dewpoint Temperature in Moist Air: A Simple Conversion and Applications, Bulletin of the American Meteorological Society, 86, 225–234, 10.1175/BAMS-86-2-225, 2005.

Lee, M.-I., Kang, I.-S., Kim, J.-K., and Mapes, B.: Influence of cloud-radiation interaction on simulating tropical intraseasonal oscillation with an atmospheric general circulation model, Journal of Geophysical Research: Atmospheres, 106, 14 219–14 233, 10.1029/2001JD900143, 2001.

Lente, G. and Ősz, K.: Barometric formulas: various derivations and comparisons to environmentally relevant observations, ChemTexts, 6, 13, 10.1007/s40828-020-0111-6, 2020.

Li, Q., Wu, B., Liu, J., Zhang, H., Cai, X., and Song, Y.: Characteristics of the atmospheric boundary layer and its relation with PM2.5 during haze episodes in winter in the North China Plain, Atmospheric Environment, 223, 117 265, 10.1016/j.atmosenv.2020.117265, 2020.

Li, Z., Guo, J., Ding, A., Liao, H., Liu, J., Sun, Y., Wang, T., Xue, H., Zhang, H., and Zhu, B.: Aerosol and boundary-layer interactions and impact on air quality, National Science Review, 4, 810–833, 10.1093/nsr/nwx117, 2017.

Liang, S., Fang, H., Chen, M., Shuey, C. J., Walthall, C., Daughtry, C., Morisette, J., Schaaf, C., and Strahler, A.: Validating MODIS land surface reflectance and albedo products: methods and preliminary results, Remote Sensing of Environment, 83, 149–162, 10.1016/S0034-4257(02)00092-5, 2002.

Lin, J., Qian, T., Bechtold, P., Grell, G., Zhang, G. J., Zhu, P., Freitas, S. R., Barnes, H., and Han, J.: Atmospheric Convection, Atmosphere-Ocean, 60, 422–476, 10.1080/07055900.2022.2082915, 2022.

Liou, K.-N.: Radiation and Cloud Processes in the Atmosphere: Theory, Observation and Modeling, vol. 20 of *Oxford Monographs in Geology and Geophysics*, Oxford University Press, Oxford, URL https://books.google.com/books?id=7IGYj-kiUu4C, 1992.

Lo Feudo, T., Calidonna, C. R., Avolio, E., and Sempreviva, A. M.: Study of the Vertical Structure of the Coastal Boundary Layer Integrating Surface Measurements and Ground-Based Remote Sensing, Sensors, 20, 6516, 10.3390/s20226516, 2020.

Lü, Q., Li, J., Wang, T., and Huang, J.: Cloud Radiative Forcing Induced by Layered Clouds and Associated Impact on the Atmospheric Heating Rate, Journal of Meteorological Research, 29, 779–792, 10.1007/s13351-015-5078-7, 2015.

Luebke, A. E., Ehrlich, A., Schäfer, M., Wolf, K., and Wendisch, M.: An assessment of macrophysical and microphysical cloud properties driving radiative forcing of shallow trade-wind clouds, Atmospheric Chemistry and Physics, 22, 2727–2744, 10.5194/acp-22-2727-2022, 2022.

Mahajan, P. N. and Fataniya, A. B.: Study of convective boundary layer dynamics and its impact on air pollution during COVID-19 lockdown over India using satellite observations and reanalysis data, Meteorology and Atmospheric Physics, 132, 711–726, 10.1007/s00703-020-00768-0, 2020.

Mahrt, L.: Boundary-layer moisture regimes, Quarterly Journal of the Royal Meteorological Society, 117, 151–176, 10.1002/qj.49711749708, 1991.

Mahrt, L.: Stratified Atmospheric Boundary Layers, Boundary-Layer Meteorology, 90, 375–396, 10.1023/A:1001765727956, 1999.

Mahrt, L.: Common microfronts and other solitary events in the nocturnal boundary layer, Quarterly Journal of the Royal Meteorological Society, 136, 1712–1722, 10.1002/qj.694, 2010.

Maiman, T. H.: Stimulated Optical Radiation in Ruby, Nature, 187, 493–494, 10.1038/187493a0, 1960.

Maroneze, R., Costa, F. D., Acevedo, O. C., Medeiros, L. E., Puhales, F. S., Anabor, V., and Mortarini, L.: A New Stable Boundary Layer Parameterization for Numerical Weather Prediction Models: A Heat Flux Budget Approach, Boundary-Layer Meteorology, 188, 209–228, 10.1007/s10546-023-00810-4, 2023.

Martucci, G., Milroy, C., and O'Dowd, C. D.: Detection of Cloud-Base Height Using Jenoptik CHM15K and Vaisala CL31 Ceilometers, Journal of Atmospheric and Oceanic Technology, 27, 861–875, 10.1175/2009JTECHA1326.1, 2010.

Masson-Delmotte, V., Zhai, P., Pirani, A., Connors, S. L., Péan, C., Berger, S., Caud, N., Chen, Y., Goldfarb, L., Gomis, M. I., Huang, M., Leitzell, K., Lonnoy, E., Matthews, J. B. R., Maycock, T. K., Waterfield, T., Yelekçi, O., Yu, R., and Zhou, B., eds.: Climate Change 2021: The Physical Science Basis. Contribution of Working Group I to the Sixth Assessment Report of the Intergovernmental Panel on Climate Change, Cambridge University Press, Cambridge, United Kingdom and New York, NY, USA, 10.1017/9781009157896, 2021.

McGovern, A., Lagerquist, R., Gagne, D. J., Jergensen, G. E., Elmore, K. L., Homeyer, C. R., and Smith, T.: Making the Black Box More Transparent: Understanding the Physical Implications of Machine Learning, Bulletin of the American Meteorological Society, 10.1175/BAMS-D-18-0195.1, 2019.

Menut, L., Flamant, C., Pelon, J., and Flamant, P. H.: Urban boundary-layer height determination from lidar measurements over the Paris area, Applied Optics, 38, 945–954, 10.1364/AO.38.000945, 1999.

Mishra, M., Gulia, S., Shukla, N., Goyal, S. K., and Kulshrestha, U. C.: Review of Secondary Aerosol Formation and Its Contribution in Air Pollution Load of Delhi NCR, Water Air Soil Pollut, 234, 47, 10.1007/s11270-022-06047-0, 2023.

Moeng, C.-H. and Sullivan, P.: A Comparison of Shear- and Buoyancy-Driven Planetary Boundary Layer Flows, Journal of the Atmospheric Sciences, 51, 999–1022, 10.1175/1520-0469(1994)051<0999:ACOSAB>2.0.CO;2, 1994.

Moeng, C.-H., Cotton, W. R., Bretherton, C., Chlond, A., Khairoutdinov, M., Krueger, S., Lewellen, W. S., MacVean, M. K., Pasquier, J. R. M., Rand, H. A., Siebesma, A. P., Stevens, B., and Sykes, R. I.: Simulation of a Stratocumulus-Topped Planetary Boundary Layer: Intercomparison among Different Numerical Codes, Bulletin of the American Meteorological Society, 77, 261–278, 10.1175/1520-0477(1996)077<0261:SOASTP>2.0.CO;2, 1996.

Murray, B. J. and Liu, X.: Chapter 15 - Ice-nucleating particles and their effects on clouds and radiation, in: Aerosols and Climate, edited by Carslaw, K. S., pp. 619–649, Elsevier, 10.1016/B978-0-12-819766-0.00014-6, 2022.

Murthy, B. S., Latha, R., Tiwari, A., Rathod, A., Singh, S., and Beig, G.: Impact of mixing layer height on air quality in winter, Journal of Atmospheric and Solar-Terrestrial Physics, 197, 105 157, 10.1016/j.jastp.2019.105157, 2020.

Möhler, O., Field, P. R., Connolly, P., Benz, S., Saathoff, H., Schnaiter, M., Wagner, R., Cotton, R., Krämer, M., Mangold, A., and Heymsfield, A. J.: Efficiency of the deposition mode ice nucleation on mineral dust particles, Atmospheric Chemistry and Physics, 6, 3007–3021, 10.5194/acp-6-3007-2006, 2006.

Münkel, C., Eresmaa, N., Räsänen, J., and Karppinen, A.: Retrieval of Mixing Height and Dust Concentration with Lidar Ceilometer, Boundary-Layer Meteorology, 124, 117–128, 10.1007/s10546-006-9103-3, 2007.

Nair, A. S., Singh, P., Soni, K., Meena, K., and Sharma, R.: Sway of aerosol on Atmospheric Boundary Layer influencing air pollution of Delhi, Urban Climate, 49, 101 478, 10.1016/j.uclim.2023.101478, 2023.

Narendra Reddy, N., Venkat Ratnam, M., Basha, G., and Ravikiran, V.: Cloud vertical structure over a tropical station obtained using long-term high-resolution radiosonde measurements, Atmospheric Chemistry and Physics, 18, 11 709–11 727, 10.5194/acp-18-11709-2018, 2018.

Nowak, J. L., Siebert, H., Szodry, K.-E., and Malinowski, S. P.: Coupled and decoupled stratocumulus-topped boundary layers: turbulence properties, Atmospheric Chemistry and Physics, 21, 10 965–10 991, 10.5194/acp-21-10965-2021, 2021.

Pandey, P., Kumar, D., Prakash, A., Masih, J., Singh, M., Kumar, S., Jain, V. K., and Kumar, K.: A study of urban heat island and its association with particulate matter during winter months over Delhi, Science of The Total Environment, 414, 494–507, 10.1016/j.scitotenv.2011.10.043, 2012.

Parde, A. N., Ghude, S. D., Dhangar, N. G., Bhautmage, U. P., Wagh, S., Lonkar, P., Govardhan, G., Kumar, R., Biswas, M., and Chen, F.: Challenges in Simulating Prevailing Fog Types Over Urban Region of Delhi, Journal of Geophysical Research: Atmospheres, 129, e2023JD039 772, 10.1029/2023JD039772, 2024.

Parthasarathy, B.: Interannual and long-term variability of Indian summer monsoon rainfall, Proceedings of the Indian Academy of Sciences - Earth and Planetary Sciences, 93, 371–385, 10.1007/BF02843255, 1984.

Peng, K., Xin, J., Zhu, X., Wang, X., Cao, X., Ma, Y., Ren, X., Zhao, D., Cao, J., and Wang, Z.: Machine learning model to accurately estimate the planetary boundary layer height of Beijing urban area with ERA5 data, Atmospheric Research, 293, 106 925, 10.1016/j.atmosres.2023.106925, 2023.

Petters, M. D. and Kreidenweis, S. M.: A Single Parameter Representation of Hygroscopic Growth and Cloud Condensation Nucleus Activity, Atmospheric Chemistry and Physics, 7, 1961–1971, 10.5194/acp-7-1961-2007, 2007.

Pino, D., Jonker, H. J. J., de Arellano, J. V.-G., and Dosio, A.: Role of Shear and the Inversion Strength During Sunset Turbulence Over Land: Characteristic Length Scales, Boundary-Layer Meteorology, 121, 537–556, 10.1007/s10546-006-9080-6, 2006.

Platnick, S., King, M. D., Ackerman, S. A., Menzel, W. P., Baum, B. A., Riedi, J. C., and Frey, R. A.: The MODIS cloud products: Algorithms and examples from Terra, IEEE Transactions on Geoscience and Remote Sensing, 41, 459–473, 10.1109/TGRS.2002.808301, 2003.

Poulos, G. S. and Burns, S. P.: An Evaluation of Bulk Ri-Based Surface Layer Flux Formulas for Stable and Very Stable Conditions with Intermittent Turbulence, Journal of the Atmospheric Sciences, 60, 2523–2537, 10.1175/1520-0469(2003)060<2523:AEOBRS>2.0.CO;2, 2003.

Pruppacher, H. R. and Klett, J. D.: Microphysics of Clouds and Precipitation, Springer Science & Business Media, URL https://link.springer.com/book/10.1007/978-1-935704-13-3, reprinted 1980, 2012.

Qu, J. J., Hao, X., Kafatos, M., and Wang, L.: Asian Dust Storm Monitoring Combining Terra and Aqua MODIS SRB Measurements, IEEE Geoscience and Remote Sensing Letters, 3, 484–486, 10.1109/LGRS.2006.877752, 2006.

Rai, D. and Pattnaik, S.: Evaluation of WRF planetary boundary layer parameterization schemes for simulation of monsoon depressions over India, Meteorology and Atmospheric Physics, 131, 1529–1548, 10.1007/s00703-019-0656-3, 2019.

Raj, S. S., Krüger, O. O., Sharma, A., Panda, U., Pöhlker, C., Walter, D., Förster, J.-D., Singh, R. P., S., S., Klimach, T., Darbyshire, E., Martin, S. T., McFiggans, G., Coe, H., Allan, J. R., R., R., Soni, V. K., Su, H., Andreae, M. O., Pöschl, U., Pöhlker, M. L., and Gunthe, S. S.: Planetary Boundary Layer Height Modulates Aerosol—Water Vapor Interactions During Winter in the Megacity of Delhi, Journal of Geophysical Research: Atmospheres, 126, e2021JD035 681, 10.1029/2021JD035681, 2021.

Raja, P., Srinivas, C. V., Hari Prasad, K. B. R. R., and Singh, N.: Land Surface Processes Simulation Over Thar Desert in Northwest India, Pure and Applied Geophysics, 173, 2195–2214, 10.1007/s00024-016-1246-7, 2016.

Ramanathan, V., Cess, R. D., Harrison, E. F., Minnis, P., Barkstrom, B. R., Ahmad, E., and Hartmann, D.: Cloud-Radiative Forcing and Climate: Results from the Earth Radiation Budget Experiment, Science, 243, 57–63, 10.1126/science.243.4887.57, 1989.

Ramaswamy, V., Boucher, O., Haigh, J., Hauglustaine, D., Haywood, J., Myhre, G., Nakajima, T., Shi, G., and Solomon, S.: Radiative Forcing of Climate Change, in: Climate Change 2001: The Scientific Basis, edited by Houghton, J., Ding, Y., Griggs, D., Noguer, M., van der Linden, P., Dai, X., Maskell, K., and Johnson, C., pp. 349–416, Cambridge University Press, 2001.

Randall, D., Khairoutdinov, M., Arakawa, A., and Grabowski, W.: Breaking the Cloud Parameterization Deadlock, Bulletin of the American Meteorological Society, 84, 1547–1564, 10.1175/BAMS-84-11-1547, 2003.

Randall, D. A. and Tjemkes, S.: Clouds, the Earth's Radiation Budget, and the Hydrologic Cycle, Global and Planetary Change, 4, 3–9, 10.1016/0921-8181(91)90063-3, operational satellites: Sentinels for the monitoring of climate and global change, 1991.

Rogers, R. R. and Yau, M. K.: A Short Course in Cloud Physics, Elsevier Science & Technology Books, Oxford, 3rd edn., URL https://www.elsevier.com/books/a-short-course-in-cloud-physics/rogers/978-0-08-057094-5, 1989.

Romps, D. M.: Exact Expression for the Lifting Condensation Level, Journal of the Atmospheric Sciences, 74, 3891–3900, 10.1175/JAS-D-17-0102.1, 2017.

Roy, S. S. and Balling, R. C.: Analysis of Trends in Maximum and Minimum Temperature, Diurnal Temperature Range, and Cloud Cover over India, Geophysical Research Letters, 32, L12 702, 10.1029/2004GL022201, 2005.

Saha, D., Soni, K., Mohanan, M. N., and Singh, M.: Long-term trend of ventilation coefficient over Delhi and its potential impacts on air quality, Remote Sensing Applications: Society and Environment, 15, 100 234, 10.1016/j.rsase.2019.05.003, 2019.

Saha, S., Niranjan Kumar, K., Sharma, S., Kumar, P., and Joshi, V.: Can Quasi-Periodic Gravity Waves Influence the Shape of Ice Crystals in Cirrus Clouds?, Geophysical Research Letters, 47, e2020GL087 909, 10.1029/2020GL087909, 2020.

Saha, S., Sharma, S., Kumar, K. N., Kumar, P., Joshi, V., Georgoussis, G., and Lal, S.: A case study on the vertical distribution and characteristics of aerosols using ground-based Raman lidar, satellite and model over Western India, International Journal of Remote Sensing, 42, 6417–6432, 10.1080/01431161.2021.1938737, 2021.

Saha, S., Sharma, S., Chhabra, A., Kumar, K. N., Kumar, P., Kamat, D., and Lal, S.: Impact of dust storm on the atmospheric boundary layer: a case study from western India, Natural Hazards, 113, 143–155, 10.1007/s11069-022-05293-z, 2022.

Salamalikis, V., Vamvakas, I., Blanc, P., and Kazantzidis, A.: Ground-based validation of aerosol optical depth from CAMS reanalysis project: An uncertainty input on direct normal irradiance under cloud-free conditions, Renewable Energy, 170, 847–857, 10.1016/j.renene.2021.02.025, 2021.

Salby, M. L.: Fundamentals of Atmospheric Physics, vol. 61 of *International Geophysics Series*, Academic Press, San Diego, URL https://www.sciencedirect.com/bookseries/international-geophysics/vol/61/suppl/C, 1996.

Samanta, S., Tyagi, B., Vissa, N. K., and Sahu, R. K.: A New Thermodynamic Index for Thunderstorm Detection Based on Cloud Base Height and Equivalent Potential Temperature, Journal of Atmospheric and Solar-Terrestrial Physics, 207, 105 367, 10.1016/j.jastp.2020.105367, 2020.

Sanchez-Mejia, Z. M. and Papuga, S. A.: Empirical Modeling of Planetary Boundary Layer Dynamics Under Multiple Precipitation Scenarios Using a Two-Layer Soil Moisture Approach: An Example From a Semiarid Shrubland, Water Resources Research, 53, 8807–8824, 10.1002/2016WR020275, 2017.

Santanello, J. A., Peters-Lidard, C. D., Kumar, S. V., Alonge, C., and Tao, W.-K.: A Modeling and Observational Framework for Diagnosing Local Land–Atmosphere Coupling on Diurnal Time Scales, Journal of Hydrometeorology, 10, 577–599, 10.1175/2009JHM1066.1, 2009.

Santra, P., Kumar, S., and Roy, M. M.: Thar Desert: Source for Dust Storm, in: Natural Hazards, CRC Press, 2018.

Sathiyamoorthy, V., Arya, R., and Kishtawal, C. M.: Radiative characteristics of fog over the Indo-Gangetic Plains during northern winter, Climate Dynamics, 47, 1793–1806, 10.1007/s00382-015-2933-2, 2016.

Satyanarayana, A. N. V., Lykossov, V. N., Mohanty, U. C., and Machul'skaya, E. E.: Parameterization of Land Surface Processes to Study Boundary Layer Characteristics over a Semiarid Region in Northwest India, Journal of Applied Meteorology, 42, 528–540, 10.1175/1520-0450(2003)042<0528:POLSPT>2.0.CO;2, 2003.

Schmidt, J., Wandinger, U., and Malinka, A.: Dual-field-of-view Raman lidar measurements for the retrieval of cloud microphysical properties, Applied Optics, 52, 2235–2247, 10.1364/AO.52.002235, 2013.

Schrieber, K., Stull, R. B., and Zhang, Q.: Distributions of surface-layer buoyancy versus lifting condensation level over a heterogeneous land surface, Journal of the Atmospheric Sciences, 53, 1086–1107, 10.1175/1520-0469(1996)053<1086:DOSLBV>2.0.CO;2, 1996.

Seaman, C. J., Noh, Y.-J., Miller, S. D., Heidinger, A. K., and Lindsey, D. T.: Cloud-Base Height Estimation from VIIRS. Part I: Operational Algorithm Validation against CloudSat, Journal of Atmospheric and Oceanic Technology, 34, 567–583, 10.1175/JTECH-D-16-0109.1, 2017.

Seibert, P., Beyrich, F., Gryning, S.-E., Joffre, S., Rasmussen, A., and Tercier, P.: Review and intercomparison of operational methods for the determination of the mixing height, Atmospheric Environment, 34, 1001–1027, `10.1016/S1352-2310(99)00349-0`, 2000.

Seidel, D. J., Ao, C. O., and Li, K.: Estimating climatological planetary boundary layer heights from radiosonde observations: Comparison of methods and uncertainty analysis, Journal of Geophysical Research: Atmospheres, 115, D16 113, `10.1029/2009JD013680`, 2010.

Seidel, D. J., Zhang, Y., Beljaars, A., Golaz, J.-C., Jacobson, A. R., and Medeiros, B.: Climatology of the planetary boundary layer over the continental United States and Europe, Journal of Geophysical Research: Atmospheres, 117, `10.1029/2012JD018143`, 2012.

Seinfeld, J. H. and Pandis, S. N.: Atmospheric Chemistry and Physics: From Air Pollution to Climate Change, John Wiley & Sons, Hoboken, NJ, 3rd edn., URL `https://www.wiley.com/en-us/Atmospheric+Chemistry+and+Physics%3A+From+Air+Pollution+to+Climate+Change%2C+3rd+Edition-p-9781118947401`, 2016.

Shao, Y. and Dong, C. H.: A review on East Asian dust storm climate, modelling and monitoring, Global and Planetary Change, 52, 1–22, `10.1016/j.gloplacha.2006.02.011`, 2006.

Sharma, A. K., Baliyan, P., and Kumar, P.: Air pollution and public health: the challenges for Delhi, India, Reviews on Environmental Health, 33, 77–86, `10.1515/reveh-2017-0032`, 2018.

Sharma, D., Singh, D., and Kaskaoutis, D. G.: Impact of Two Intense Dust Storms on Aerosol Characteristics and Radiative Forcing over Patiala, Northwestern India, Advances in Meteorology, 2012, 956 814, `10.1155/2012/956814`, 2012.

She, C.-Y. and Friedman, J. S.: Atmospheric Lidar Fundamentals, Cambridge University Press, URL `https://www.cambridge.`

org / core / books / atmospheric - lidar - fundamentals / 8E3087407C9A1C456C0E3FDC50C539E0, 2022.

Shin, H. H. and Hong, S.-Y.: Intercomparison of Planetary Boundary-Layer Parametrizations in the WRF Model for a Single Day from CASES-99, Boundary-Layer Meteorology, 139, 261–281, 10.1007/s10546-010-9583-z, 2011.

Singh, J., Singh, N., Ojha, N., Srivastava, A. K., Bisht, D. S., Rajeev, K., Kumar, K. N. V. P., Singh, R. S., Panwar, V., Dhaka, S. K., Kumar, V., Nakayama, T., Matsumi, Y., Hayashida, S., and Dimri, A. P.: Genesis of a Severe Dust Storm Over the Indian Subcontinent: Dynamics and Impacts, Earth and Space Science, 9, e2021EA001 702, 10.1029/2021EA001702, 2022.

Singh, V., Biswal, A., Kesarkar, A. P., Mor, S., and Ravindra, K.: High resolution vehicular PM10 emissions over megacity Delhi: Relative contributions of exhaust and non-exhaust sources, Science of The Total Environment, 699, 134 273, 10.1016/j.scitotenv.2019.134273, 2020.

Skamarock, W. C., Klemp, J. B., Dudhia, J., Gill, D. O., Liu, Z., Berner, J., Wang, W., Powers, J. G., Duda, M. G., Barker, D. M., and Huang, X.-Y.: A Description of the Advanced Research WRF Model Version 4, NCAR Technical Note NCAR/TN-556+STR, National Center for Atmospheric Research, 10.5065/1dfh-6p97, 2019.

Slingo, A.: Sensitivity of the Earth's Radiation Budget to Changes in Low Clouds, Nature, 343, 49–51, 10.1038/343049a0, 1990.

Slingo, A. and Slingo, J. M.: The response of a general circulation model to cloud longwave radiative forcing. I: Introduction and initial experiments, Quarterly Journal of the Royal Meteorological Society, 114, 1027–1062, 10.1002/qj.49711448209, 1988.

Slingo, A., Ackerman, T. P., Allan, R. P., Kassianov, E. I., McFarlane, S. A., Robinson, G. J., Barnard, J. C., Miller, M. A., Harries, J. E., Russell, J. E., and Dewitte, S.: Observations of the impact of a major Saharan dust storm on the atmospheric radiation balance, Geophysical Research Letters, 33, 10.1029/2006GL027869, 2006.

Smith, D. K. E., Dorling, S. R., Renfrew, I. A., Ross, A. N., and Poku, C.: Fog trends in India: Relationships to fog type and western disturbances, International Journal of Climatology, 43, 818–836, 10.1002/joc.7832, 2023.

Smith, N., Bange, J., Beyrich, F., Lothon, M., and Lohou, F.: Progress in observing and understanding the atmospheric boundary layer with ground-based and airborne instrumentation, Atmospheric Measurement Techniques, 14, 4261–4293, 10.5194/amt-14-4261-2021, 2021.

Spänkuch, D., Hellmuth, O., and Görsdorf, U.: What Is a Cloud? Toward a More Precise Definition, Bulletin of the American Meteorological Society, 10.1175/BAMS-D-21-0032.1, 2022.

Stackpole, J.: Numerical Analysis of Atmospheric Soundings, JSTOR, URL https://www.jstor.org/stable/26252131, 1967.

Stephens, G. L.: Cloud Feedbacks in the Climate System: A Critical Review, Journal of Climate, 18, 237–273, 10.1175/JCLI-3243.1, 2005.

Stephens, G. L. and Greenwald, T. J.: The Earth's Radiation Budget and Its Relation to Atmospheric Hydrology: 2. Observations of Cloud Effects, Journal of Geophysical Research: Atmospheres, 96, 15 325–15 340, 10.1029/91JD00972, 1991.

Stephens, G. L. and Kummerow, C. D.: The remote sensing of clouds and precipitation from space: A review, Journal of the Atmospheric Sciences, 64, 3742–3765, 10.1175/2006JAS2375.1, 2007.

Stephens, G. L. and Webster, P. J.: Clouds and Climate: Sensitivity of Simple Systems, Journal of the Atmospheric Sciences, 38, 235–247, 10.1175/1520-0469(1981)038<0235:CACSOS>2.0.CO;2, 1981.

Stephens, G. L., Li, J., Wild, M., Clayson, C. A., Loeb, N., Kato, S., L'Ecuyer, T., Stackhouse, P. W., Lebsock, M., and Andrews, T.: An update on Earth's energy balance in light of the latest global observations, Nature Geoscience, 5, 691–696, 10.1038/ngeo1580, 2012.

Stjern, C., Samset, B., Myhre, G., Forster, P., Hodnebrog, Ø., Andrews, T., Boucher, O., Faluvegi, G., Iversen, T., Kasoar, M., Kharin, V., Kirkevåg, A., Lamarque, J.-F., Olivié, D., Richardson, T., Shawki, D., Shindell, D., Smith, C., Takemura, T., and Voulgarakis, A.: Rapid Adjustments Cause Weak Surface Temperature Response to Increased Black Carbon Concentrations, Journal of Geophysical Research: Atmospheres, 122, 11 462–11 481, 10.1002/2017JD027326, 2017.

Stocker, T. F., Qin, D., Plattner, G.-K., Tignor, M., Allen, S. K., Boschung, J., Nauels, A., Xia, Y., Bex, V., and Midgley, P. M., eds.: Climate Change 2013: The Physical Science Basis. Contribution of Working Group I to the Fifth Assessment Report of the Intergovernmental Panel on Climate Change, Cambridge University Press, Cambridge, United Kingdom and New York, NY, USA, URL https://www.ipcc.ch/report/ar5/wg1/, 2013.

Stohl, A., Forster, C., Frank, A., Seibert, P., and Wotawa, G.: Technical note: The Lagrangian particle dispersion model FLEXPART version 6.2, Atmospheric Chemistry and Physics, 5, 2461–2474, 10.5194/acp-5-2461-2005, 2005.

Stubenrauch, C. J., Rossow, W. B., Kinne, S., Ackerman, S., Cesana, G., Chepfer, H., Di Girolamo, L., Getzewich, B., Guignard, A., Heidinger, A., Maddux, B., Menzel, W. P., Minnis, P., Pearl, C., Platnick, S., Walther, A., Winker, D., and Zeng, S.: Assessment of global cloud datasets from satellites: Project and database initiated by the GEWEX Radiation Panel, Bulletin of the American Meteorological Society, 94, 1031–1049, 10.1175/BAMS-D-12-00117.1, 2013.

Stull, R. and Eloranta, E.: A Case Study of the Accuracy of Routine, Fair-Weather Cloud-Base Reports, Bulletin of the American Meteorological Society, 10, URL https://www.ametsoc.org/, 1984.

Stull, R. B.: Boundary Layer Clouds, in: An Introduction to Boundary Layer Meteorology, edited by Stull, R. B., pp. 545–585, Springer Netherlands, Dordrecht, 10.1007/978-94-009-3027-8_13, 1988.

Stull, R. B.: An Introduction to Boundary Layer Meteorology, vol. 13 of *Atmospheric and Oceanographic Sciences Library*, Springer Science & Business Media, 10.1007/978-94-009-3027-8, 2012.

Stull, R. B.: Practical Meteorology: An Algebra-based Survey of Atmospheric Science, University of British Columbia, version 1.02b edn., URL https://www.eoas.ubc.ca/books/Practical_Meteorology/, 2017.

Su, T., Li, Z., and Zheng, Y.: Cloud-Surface Coupling Alters the Morning Transition From Stable to Unstable Boundary Layer, Geophysical Research Letters, 50, e2022GL102 256, 10.1029/2022GL102256, 2023.

Sullivan, P. P., Moeng, C.-H., Stevens, B., Lenschow, D. H., and Mayor, S. D.: Structure of the Entrainment Zone Capping the Convective Atmospheric Boundary Layer, Journal of the Atmospheric Sciences, 55, 3042–3064, 10.1175/1520-0469(1998)055<3042:SOTEZC>2.0.CO;2, 1998.

Summa, D., Madonna, F., Rosoldi, M., Pandolfi, M., Perrone, M. R., Stelitano, D., Wang, Y., and Wang, X.: Synergistic use of Raman lidar and sun-photometer measurements to derive aerosol optical properties at different boundary layer heights, Atmospheric Measurement Techniques, 16, 1273–1290, 10.5194/amt-16-1273-2023, 2023.

Sun, K., Su, Q., and Ming, Y.: Dust Storm Remote Sensing Monitoring Supported by MODIS Land Surface Reflectance Database, Remote Sensing, 11, 1772, 10.3390/rs11151772, 2019.

Thayyen, R. J. and Dimri, A. P.: Slope Environmental Lapse Rate (SELR) of Temperature in the Monsoon Regime of the Western Himalaya, Frontiers in Environmental Science, 6, 10.3389/fenvs.2018.00042, 2018.

Thomas, G. E. and Olivero, J.: Noctilucent Clouds as Possible Indicators of Global Change in the Mesosphere, Advances in Space Research, 28, 937–946, 10.1016/S0273-1177(01)80021-1, 2001.

Tiwari, S., Thomas, A., Rao, P., Chate, D. M., Soni, V. K., Singh, S., Ghude, S. D., Singh, D., and Hopke, P. K.: Pollution concentrations in Delhi India during winter 2015–16: A case study of an odd-even vehicle strategy, Atmospheric Pollution Research, 9, 1137–1145, 10.1016/j.apr.2018.04.008, 2018.

Tolbert, M. A.: Sulfate Aerosols and Polar Stratospheric Cloud Formation, Science, 264, 527–528, 10.1126/science.264.5158.527, 1994.

Tritscher, I., Pitts, M. C., Poole, L. R., Alexander, S. P., Cairo, F., Chipperfield, M. P., Grooß, J.-U., Höpfner, M., Lambert, A., Luo, B., Molleker, S., Orr, A., Salawitch, R., Snels, M., Spang, R., Woiwode, W., and Peter, T.: Polar Stratospheric Clouds: Satellite Observations, Processes, and Role in Ozone Depletion, Reviews of Geophysics, 59, e2020RG000 702, 10.1029/2020RG000702, 2021.

Turner, D. D., Löhnert, U., Vogelmann, A. M., Wulfmeyer, V., Crewell, S., Cadeddu, M. P., Castellanos, P., Feltz, W. F., and Mather, J. H.: Synergistic use of ground-based remote sensing instruments to observe diurnal variability of the planetary boundary layer and lower troposphere, Bulletin of the American Meteorological Society, 101, E995–E1014, 10.1175/BAMS-D-19-0181.1, 2020.

Turner, J. S.: Buoyant Plumes and Thermals, Annual Review of Fluid Mechanics, 1, 29–44, 10.1146/annurev.fl.01.010169.000333, 1969.

Twomey, S.: The Influence of Pollution on the Shortwave Albedo of Clouds, Journal of the Atmospheric Sciences, 34, 1149–1152, 10.1175/1520-0469(1977)034<1149:TIOPOT>2.0.CO;2, 1977.

Tyagi, S., Tiwari, S., Mishra, A., Singh, S., Hopke, P. K., Singh, S., and Attri, S. D.: Characteristics of absorbing aerosols during winter foggy period over the National Capital Region of Delhi: Impact of planetary boundary layer dynamics and solar radiation flux, Atmospheric Research, 188, 1–10, 10.1016/j.atmosres.2017.01.001, 2017.

Vaisala Oyj: CL31 Technical Description M212734EN-A, Technical report, Vaisala Oyj, URL https://docs.vaisala.com/r/M212734EN-A/en-US, 2024.

Vaishnav, R., Sharma, S., Shukla, K. K., Kumar, P., and Lal, S.: A Comprehensive Statistical Study of Cloud Base Height Using Ceilometer Over Western India, Advances in Space Research, 63, 1708–1718, 10.1016/j.asr.2018.11.006, 2019.

Varghese, M., Jose, J., Anu, A., Murugavel, P., Resmi, E., Bera, S., Thomas, S., Konwar, M., Kalarikkal, N., and Prabha, T.: Cloud and aerosol characteristics during dry and wet days of southwest monsoon over the rain shadow region of Western Ghats, India, Meteorology and Atmospheric Physics, 133, 1299–1316, 10.1007/s00703-021-00811-3, 2021.

Vautard, R., Yiou, P., and van Oldenborgh, G.: Decline of fog, mist and haze in Europe over the past 30 years, Nature Geoscience, 2, 115–119, 10.1038/ngeo414, 2009.

von Engeln, A. and Teixeira, J.: A Planetary Boundary Layer Height Climatology Derived from ECMWF Reanalysis Data, Journal of Climate, 10.1175/JCLI-D-12-00385.1, 2013.

Wallace, J. M. and Hobbs, P. V.: Atmospheric Science: An Introductory Survey, Academic Press / Elsevier, Amsterdam, 2nd edn., URL https://booksite.elsevier.com/9780127329512/, 2006.

Wang, R., Zhou, R., Yang, S., Li, R., Pu, J., Liu, K., and Deng, Y.: A New Algorithm for Estimating Low Cloud-Base Height in Southwest China, doi:10.1175/JAMC-D-21-0221.1, 2022.

Weger, M., Heinold, B., Engler, C., Schumann, U., Seifert, A., Fößig, R., Voigt, C., Baars, H., Blahak, U., Borrmann, S., Hoose, C., Kaufmann, S., Krämer, M., Seifert, P., Senf, F., Schneider, J., and Tegen, I.: The impact of mineral dust on cloud formation during the Saharan dust event in April 2014 over Europe, Atmospheric Chemistry and Physics, 18, 17 545–17 572, 10.5194/acp-18-17545-2018, 2018.

Wei, J., Zhao, J., Chen, H., and Liang, X. Z.: Coupling Between Land Surface Fluxes and Lifting Condensation Level: Mechanisms and Sensitivity to Model

Physics Parameterizations, Journal of Geophysical Research: Atmospheres, 126, e2020JD034 313, 10.1029/2020JD034313, 2021.

Weitkamp, C.: Lidar: Range-Resolved Optical Remote Sensing of the Atmosphere, Springer Science & Business Media, New York, URL https://link.springer.com/book/10.1007/0-387-25101-4, 2005.

Wiegner, M., Geiß, A., Mattis, I., Freudenthaler, V., and Münkel, C.: Profiles of the mixing layer height over an urban area from automatic lidars and ceilometers: Comparison with radiosonde and air quality data, Atmospheric Measurement Techniques, 7, 2071–2084, 10.5194/amt-7-2071-2014, 2014.

Wilde, N. P., Stull, R. B., and Eloranta, E. W.: The LCL Zone and Cumulus Onset, Journal of Applied Meteorology and Climatology, 24, 640–657, 10.1175/1520-0450(1985)024<0640:TLZACO>2.0.CO;2, 1985.

Williams, A. G. and Hacker, J. M.: The composite shape and structure of coherent eddies in the convective boundary layer, Boundary-Layer Meteorology, 61, 213–245, 10.1007/BF02042933, 1992.

Wood, R.: Stratocumulus Clouds, Monthly Weather Review, 140, 2373–2423, 10.1175/MWR-D-11-00121.1, 2012.

Wu, Y., Gao, J., and Zhao, A.: Cloud properties and dynamics over the Tibetan Plateau – A review, Earth-Science Reviews, 248, 104 633, 10.1016/j.earscirev.2023.104633, 2024.

Wyngaard, J. C.: Turbulence in the Atmosphere, Cambridge University Press, Cambridge, UK, URL https://doi.org/10.1017/CBO9780511840524, 2010.

Yang, T., Wang, Z., Zhang, W., Gbaguidi, A., Sugimoto, N., Wang, X., Matsui, I., and Sun, Y.: Technical note: Boundary layer height determination from lidar for improving air pollution episode modeling: development of new algorithm and evaluation, Atmospheric Chemistry and Physics, 17, 6215–6225, 10.5194/acp-17-6215-2017, 2017.

Yao, B., Liu, C., Yin, Y., Liu, Z., Shi, C., Iwabuchi, H., and Weng, F.: Evaluation of cloud properties from reanalyses over East Asia with a radiance-based approach, Atmospheric Measurement Techniques, 13, 1033–1049, 10.5194/amt-13-1033-2020, 2020a.

Yao, B., Teng, S., Lai, R., Xu, X., Yin, Y., Shi, C., and Liu, C.: Can atmospheric reanalyses (CRA and ERA5) represent cloud spatiotemporal characteristics?, Atmospheric Research, 244, 105 091, 10.1016/j.atmosres.2020.105091, 2020b.

Yin, Y., Wurzler, S., Levin, Z., and Reisin, T. G.: Interactions of mineral dust particles and clouds: Effects on precipitation and cloud optical properties, Journal of Geophysical Research: Atmospheres, 107, AAC 19–1–AAC 19–14, 10.1029/2001JD001544, 2002.

Yuval, L. Y., Dayan, U., Levy, I., and Broday, D. M.: On the association between characteristics of the atmospheric boundary layer and air pollution concentrations, Atmospheric Research, 231, 104 675, 10.1016/j.atmosres.2019.104675, 2020.

Zhang, D., Comstock, J., and Morris, V.: Comparison of planetary boundary layer height from ceilometer with ARM radiosonde data, Atmospheric Measurement Techniques, 15, 4735–4749, 10.5194/amt-15-4735-2022, 2022.

Zhu, P. and Albrecht, B.: A Theoretical and Observational Analysis on the Formation of Fair-Weather Cumuli, Journal of the Atmospheric Sciences, 59, 1983–2005, 10.1175/1520-0469(2002)059<1983:ATAOAO>2.0.CO;2, 2002.

List of Publications

Included in the thesis

1. **Kamat, D. K.**, Sharma, S. K., Kumar, P., Kumar, K. N., Saha, S., Patel, A. (2025). Investigation of cloud characteristics over a high-altitude region, Mt. Abu, using ground-based Lidar and satellite observations. *Theoretical and Applied Climatology*, 157, 34. `https://doi.org/10.1007/s00704-025-05985-z`

2. **Kamat, D. K.**, Sharma, S. K., Kumar, P., Kumar, K. N., Saha, S., Patel, A., Kaur, S., Jangra, A. (2025). Atmospheric boundary layer characteristics during severe air pollution and fog events over Delhi: Insights from ground-based Lidar, satellites, and models. *Atmospheric Environment*. p.121684. `https://doi.org/10.1016/j.atmosenv.2025.121684`

3. **Kamat, D. K.**, Sharma, S. K., Kumar, K. N., Kumar, P., Saha, S., Bencherif, H. (2025). Dynamics of convective clouds near and below the lifting condensation level over a semi-arid Western Indian region. *Atmospheric Research*. p.108542. `https://doi.org/10.1016/j.atmosres.2025.108542`

4. **Kamat, D. K.**, Sharma, S. K., Kumar, P., Kumar, K. N., Patel, A., Saha, S., Bencherif, H., Vaishya, A., Shah, R. (2025). Dynamics of mid-level stratiform clouds over the semi-arid regions of Western India: a post-monsoon case study. *Modeling Earth Systems and Environment*, 11(4), 1-12. `https://doi.org/10.1007/s40808-025-02449-1`

5. **Kamat, D. K.**, Sharma, S. K., Kumar, P., Saha, S., Kumar, K. N., Shah, R.

(2025). Long-Term trend in clouds and precipitation over an urban City Ahmedabad in the Western-Indian region. *Journal of the Indian Society of Remote Sensing*, 1-11. https://doi.org/10.1007/s12524-025-02174-3

6. **Kamat, D. K.**, Sharma, S. K., Kumar, P., Kumar, K. N., Aniket, Saha, S., Bencherif, H. (2025). Investigation of atmospheric clouds and boundary layer dynamics during a dust storm in the Western-Indian region. *Remote Sensing Applications: Society and Environment*, 37, 101442. https://doi.org/10.1016/j.rsase.2024.101442

7. **Kamat, D. K.**, Sharma, S. K., Kumar, K. N., Kumar, P., Saha, S. (2024). Cloud characteristics in the Aravalli ranges of Western India: Insights from ground-based Lidar measurements. *Bulletin of Atmospheric Science and Technology*, 5(1), 11. https://doi.org/10.1007/s42865-024-00075-w

8. Saha, S., **Kamat, D. K.**, Sharma, S., Kumar, P., Kumar, K. N., Bencherif, H., LaL, S., Chandra, S. (2023). Response of the boundary layer clouds to the surface forcings: A case study of western India. *Remote Sensing Applications: Society and Environment*, 32, 101073. https://doi.org/10.1016/j.rsase.2023.101073

9. **Kamat, D. K.**, Sharma, S. K., Kumar, P., Kaushik, N.K., Patel, A., Kumar, K. N., Gunthe, S., Saha, S., Bencherif, H. (2025). Enhancement in Atmospheric Boundary Layer Predictions from WRF Model Using Ground-based Lidar Observations Over an Urban Region in Western India. *Modeling Earth Systems and Environment*. (Under review)

Not included in the thesis

1. Shah, R., Sharma, S., Gadhavi, H., Aniket, Srivastava, R., **Kamat, D. K.**. (2025). Characteristics of uniformly distributed cirrus clouds over the Arabian Sea. *Remote Sensing Letters*, 16(12), pp.1423-1432. https://doi.org/10.1080/2150704X.2025.2578818

2. Shah, R., Sharma, S. K., **Kamat, D. K.**, Kumar, K. N., Kumar, P., Ningombam, S. S., Angchuk, D., Srivastava, R. (2025). Characteristics of multi-layer clouds observed using ceilometer observations over Leh-Ladakh: A high-altitude cold desert region. *Atmospheric Research*, p.108399. `https://doi.org/10.1016/j.atmosres.2025.108399`

3. Shah, R., Sharma, S., **Kamat, D. K.**, Kumar, K. N., Kumar, P., Srivastava, R. (2024). Cloud characteristics and their role in the 2024 United Arab Emirates extreme rainfall events. *Remote Sensing Letters*, 15(11), 1153-1162. `https://doi.org/10.1080/2150704X.2024.2412800`

4. Shukla, K. K., Sharma, S. K., Kumar, K. N., Kumar, P., **Kamat, D. K.**, Attada, R., Saha, S. (2023). Characterization of a Regional Dust Storm Using RAMAN Lidar Over the Western Indian Region. *Journal of the Indian Society of Remote Sensing*, 51(12), 2549-2559. `https://doi.org/10.1007/s12524-023-01778-x`

5. Saha, S., Sharma, S., Chhabra, A., Kumar, P., Kondapalli, N. K., **Kamat, D. K.**, Lal, S. (2023). Atmospheric boundary layer over ahmedabad, western indian region: Impact of COVID-19 nationwide lockdown. *Pure and Applied Geophysics*, 180(3), 1113-1119. `https://doi.org/10.1007/s00024-023-03230-0`

6. Saha, S., Sharma, S., Chhabra, A., Kumar, K. N., Kumar, P., **Kamat, D. K.**, Lal, S. (2022). Impact of dust storm on the atmospheric boundary layer: a case study from western India. *Natural Hazards*, 113(1), 143-155. `https://doi.org/10.1007/s11069-022-05293-z`

7. Saha, S., Sharma, S., Kumar, K. N., Kumar, P., Lal, S., **Kamat, D. K.** (2022). Investigation of atmospheric boundary layer characteristics using ceilometer lidar, COSMIC GPS RO satellite, radiosonde and ERA-5 reanalysis dataset over Western Indian region. *Atmospheric Research*, 268, 105999. `https://doi.org/10.1016/j.atmosres.2021.105999`

8. Sahu, P. J., Pathak, B., Sharma, S. K., Dutta, B., Bhattacharjee, U., Chakraborty,

A., Patel, A., **Kamat, D. K.**, Bhuyan, P. K., Borgohain, A. Bhuyan, K. (2025). Monitoring the Atmospheric Boundary Layer Height Using Ceilometer Lidar Over the Northeast India. *Journal of the Indian Society of Remote Sensing*, 1-15. https://doi.org/10.1007/s12524-025-02375-w

9. Srivastava, S., Singh, S., Sharma, S., Jindal, P., Aparna, C., Kant, Y., Mitra, D., **Kamat, D. K.**, Patel, A., Singh, R.P., Chauhan, P. (2025). Investigation of Atmospheric Boundary Layer Dynamics Over the Himalayan Foothill Region: Insights from Ground-Based LiDAR Observations and WRF Model. *Journal of the Indian Society of Remote Sensing*. 1-20. https://doi.org/10.1007/s12524-025-02400-y

10. Patel, A., Sharma, S. K., Shah, R., **Kamat, D. K.**, Kumar, P., Kumar, K. N., Chotaliy, N. A., Kar, D. K. (2025). Investigation of the Mount Ruang Volcanic Eruption in Indonesia: A Case Study. *Natural Hazards*. (Under review)

Details of the seminars/workshops/conferences attended and presentations made therein

Presentations in international conference/symposium/training school

1. Asia Oceania Geosciences Society (AOGS) 2025 22nd Annual Meeting, Atmospheric boundary layer characteristics over Delhi during heavy air pollution in the post-monsoon and winter season, Singapore, 27 July-1 August 2025. (*Oral, In person*)

2. Asia Oceania Geosciences Society (AOGS) 2025 22nd Annual Meeting, Cloud characteristics over a high-altitude hill station in the Aravalli Range of Western India, Singapore, 27 July-1 August 2025. (*Poster, In person*)

3. 9th international training school on Convective and Volcanic Clouds– CVC– detection, monitoring and modeling, Investigation of the Characteristics and For-

mation Mechanism of Convective Clouds Below and Near the Lifting Condensation Level, Nicolosi, Sicily, Italy, 5-13 October 2024. (*Oral, In person*)

4. European Geosciences Union (EGU) 2024 General Assembly, Exploring the dynamics of the Atmospheric Boundary Layer over the Western-Indian region: Insights and Implications, Vienna, Austria, 14-19 April 2024. (*Oral & Poster, Online*)

5. International Conference on Recent Trends in Geoscience Research and Applications 2023, Investigation of the atmospheric clouds and boundary layer over the western-Indian region, Belgrade, Serbia, 23-27 October 2023. (*Oral, Online*)

6. The International Conference on Regional Climate (ICRC)-CORDEX 2023, Investigation of Atmospheric Clouds over the western-Indian Region, IITM Pune, 25-29 September 2023. (*Poster, In person*)

Presentations in national conference/symposium/training school

1. Frontiers in Geosciences Research Conference (FGRC)-2025, Investigation of atmospheric clouds and the boundary layer characteristics over a semi-arid region in the Aravalli Range of Western India, PRL Ahmedabad, 5-7 February 2025. (*Poster, In person*)

2. National Space Science Symposium (NSSS)-2024, Investigation of the Genesis of Water Vapor, AOT, and Clouds over the Western-Indian Region, Goa University, 26 February- 1 March 2024. (*Poster, In person*)

3. National Symposium ”TROPMET-2023”, Characteristics and formation mechanism of clouds below and near the lifting condensation level over a semi-arid western-Indian region, 22-24 November 2023. (*Oral and Poster, In person*)

4. Frontiers in Geosciences Research Conference (FGRC)-2023, ”Investigations on the impact of aerosol-induced modulation in Cloud and Precipitation Climatology over Ahmedabad, PRL Ahmedabad, 1-3 February 2023. (*Poster, In person*)

5. URSI- RCRS 2022, A Long-term Analysis of Cloud-height and Rainfall using ERA5 Reanalysis, Satellite and Ground Measurements, IIT (Indore), India, 1-4 December 2022. (*Poster, In person*)

6. National Space Science Symposium (NSSS 2022), Finding the Missing Link for 2021 Rainfall: Atlantic Nino, IISER Kolkata, 31 Jan- 4 Feb 2022. (*Poster, Online*)

International short course/training school/workshop attended

1. 9th international training school on Convective and Volcanic Clouds– CVC– detection, monitoring and modeling", 5-13 October 2024, Nicolosi, Sicily, Italy

2. Fourth Short Course on Weather Forecasting Using Numerical Weather Prediction Models, Centre for Space Science and Technology Education in Asia and the Pacific (CSSTEAP), affiliated to the UNITED NATIONS, 14-25 November 2022, Space Applications Centre, Ahmedabad, India

National short course/training school/workshop attended

1. Three days HPC workshop on "Parallel Programming and Concepts of AI", 1-3 July 2024, Physical Research Laboratory, India

2. Workshop on "Atmospheric Research using RADAR", URSI-RCRS 2022, 1-4 December 2022, IIT (Indore), India

3. International workshop on Technical and Scientific Aspects of Lidar Remote sensing of the Atmosphere ITSLRA-2022, 13-15 July 2022, Centre for Remote Sensing and Geo informatics, Sathyabama Institute of Science and Technology, Chennai, India

Recognition/awards/honours

1. Selected as a Student Volunteer for the Asia Oceania Geosciences Society (AOGS) 2025 22nd Annual Meeting and awarded a full registration fee waiver (SGD 480), complimentary meals on duty days during the conference, and AOGS membership for three annual meetings
2. Received a grant of 780 EUROS from the organizers to attend the 9th international training school on Convective and Volcanic Clouds– CVC– detection, monitoring and modeling, Nicolosi, Sicily (Italy), 5-13 October 2024
3. Received financial grant from the Science Engineering Research Board (SERB) International Travel Support (ITS) Scheme for participation in the 9th international training school on Convective and Volcanic Clouds– CVC detection, monitoring and modeling, Nicolosi, Sicily (Italy), 5-13 October 2024
4. Received partial financial support (travel) for in-person participation and presentation in the International Conference on Regional Climate-CORDEX 2023 (ICRC-CORDEX2023), IITM Pune, 25-29 September 2023

Newspaper reportings of our published research work from the thesis

1. ”Solved: How dust storm led to downpour last May”, The Times of India, Ahmedabad Edition. 3 February 2025. https://timesofindia.indiatimes.com/city/ahmedabad/solved-how-dust-storm-led-to-downpour-last-may/articleshow/117865762.cms
2. ”Why is a drier Udaipur cloudier than Ahmedabad”, The Times of India, Ahmedabad Edition. 16 July 2025.
3. ”Why are clouds over A’bad defying gravity and science?”, The Times of India, Ahmedabad Edition. 27 October 2025. https://timesofindia.indiatimes.com/city/ahmedabad/why-are-clouds-over-

abad-defying-gravity-and-science-post-monsoon/articleshow/124833252.cms